Studies on Nano-magnetism of Fe, Co, Ni and Pt based Ferromagnetic Metal and Alloy Nanoparticles Synthesized via Novel Chemical Routes

THESIS

Submitted in partial fulfillment
of the requirements for the degree of

DOCTOR OF PHILOSOPHY

by

DALAVI SHANKAR BALU

Under the Supervision of

Prof. RABI NARAYAN PANDA

BITS Pilani
Pilani | Dubai | Goa | Hyderabad

BIRLA INSTITUTE OF TECHNOLOGY AND SCIENCE, PILANI

2017

BIRLA INSTITUTE OF TECHNOLOGY AND SCIENCE, PILANI

CERTIFICATE

This is to certify that the thesis entitled **Studies on Nano-magnetism of Fe, Co, Ni and Pt based Ferromagnetic Metal and Alloy Nanoparticles Synthesized via Novel Chemical Routes** *and submitted by* **DALAVI SHANKAR BALU** *ID No* **2012PHXF0013G** *for award of Ph.D. of the Institute embodies original work done by him under my supervision.*

Rabi narayan Panda

Signature of the Supervisor

Name in capital letters: **Prof. RABI NARAYAN PANDA**

Designation: **Associate Professor**

Date: 16-10-2017

ACKNOWLEDGEMENTS

I would like to begin by expressing my deepest gratitude to my supervisor, Prof. Rabi Narayan Panda, for his highly inspiring and valuable guidance, genuine interest, continuous encouragement, invaluable advice and kindness during my Ph. D. work.

I would also like to thank the members of Doctoral Advisory Committee; Dr. K. P. Jayadevan and Dr. R. S. Patel, for their valuable advice, motivation and support at various phases of my research work.

I gratefully acknowledge Council of Scientific and Industrial Research (CSIR), New Delhi, for the financial support as Junior Research Fellow (JRF) and Senior Research Fellow (SRF). I also acknowledge BITS Pilani, K. K. Birla Goa campus for providing me Institute Fellowship during Ph. D. program.

I am extremely grateful to Prof. Souvik Bhattacharyya (Vice Chancellor, BITS Pilani), Prof. G. Raghurama (Director, BITS Pilani, K. K. Birla Goa Campus), Prof. A. P. Koley (Associate Dean, Instruction Division), Prof. Neena Goveas (Associate Dean, Academic Registration & Counseling Division), Prof. Prasanta Kumar Das (Associate Dean, Academic Research Division) and Prof. Sunil Bhand (Dean, Sponsored Research and Consultancy Division), for academic and administration facilities during my Ph.D. at BITS Pilani, K. K. Birla Goa Campus.

I am thankful to Prof. A. Chattopadhyay (HOD, Department of Chemistry) for providing the work place, facilities and the help during my Ph. D. work. I would also like to thank Prof. R. N. Behera (Convener, Doctoral Research Committee) and members of DRC for their valuable suggestions, motivation and support during my Ph. D. program. I also acknowledge Maintenance Department, Workshop and Computer Center of BITS Pilani, K.K. Birla Goa Campus for providing necessary facilities.

I am extremely thankful to Dr. M. Manivel Raja (DMRL, Hyderabad) for providing me magnetic measurements facility from his lab and Prof. Sayan Bhattacharyya (IISER, Kolkata) for providing surface area analyzer facility.

I gratefully acknowledge SAIF, IIT Bombay and SAIF, IIT Madras for providing analytical instrumental facilities such as TEM and magnetic measurements.

I am thankful to Mr. Pratap Behera (office staff, ARD) and Mrs. Veena Naik (office staff, SRCD) for cooperation in official work of project and Ph. D. research. I am also thankful to laboratory and office staff of Department of Chemistry- Mr. Digambar, Mrs. Princy, Mrs. Sunayna and Mrs. Reshma, for their help and co-operation.

I express my sincere thanks to my lab Colleagues Mr. J. Theerthagiri and Mrs. Pragnya Mishra for their support and help in research. I am also thankful to all other friends and seniors for their cooperative atmosphere in the lab.

Today, I feel privileged to have this opportunity to thank my beloved parents, Mr. Balu Dalavi and Mrs. Bhagirathi Dalavi, and all family members for being source of my strength always. I express my special thanks to my uncle-Mr. Baburao Dalavi, teacher-Mr. Bhoite Guruji and my all teachers throughout educational career, for their support. Without you all it was never possible to reach this day.

Dalavi Shankar Balu

ABSTRACT

Research carried out in the thesis basically focuses the studies on nano-magnetism in fine particle systems of Fe, Co, Ni and Pt based metals and alloys. Recent literature reports on magnetic nanoparticles confirm their unique magnetic properties and immense technological applications. Materials under study include Fe, Co, Ni, Fe-Co, Co-Ni, Fe-Ni-Co, Fe-Pt, Co-Pt and were selected based on literature survey and gaps in existing research. These nanomaterials were synthesized via novel and modified chemical reduction methods namely (i) sodium borohydride method, (ii) superhydride method and (ii) polyol method. Stabilization, controlled particle size and surface modifications of the nanoparticles were achieved with the help of various capping agents or porous matrix such as oleic acid, oleylamine, CTAB, PEG, PVP and silica matrix.

Modified $NaBH_4$ route in aqueous medium was used to synthesis PEG coated Fe, Co, Ni and Fe-Co-Ni nanoparticles systems. Fe nanoparticles were found to be oxidized after annealing. Co and Ni nanoparticles crystallize in pure fcc phases with crystallite sizes equal to 42.6 nm and 29.1 nm, respectively. Size, shape and surface morphologies of material were studied by SEM and TEM analysis. SEM micrograph shows the particle sizes to be 62 nm and 54 nm whereas TEM studies confirm the sizes to be 43 nm and 48 nm for Co and Ni, respectively. Fe-Ni-Co alloys crystallize in pure fcc phases with crystallite sizes are in the range of 22.8-27.5 nm. SEM particle sizes of Fe-Ni-Co alloys were in the range of 59 nm to 75 nm. The values of saturation magnetization for Co and Ni are 122 and 47 emu/g whereas the coercivity values are 111 and 84 Oe, respectively. The observed values of saturation magnetization for Fe-Ni-Co alloys are in the range of 54.3-41.2 emu/g and coercivity values in the range of 170-122 Oe. These alterations of magnetic characteristics were explained with the help of fine particle size, surface effects, spin canting at the surface and presence of superparamagnetic fractions in the ultrafine materials.

Superhydride reduction route, using oleic acid/oleylamine as capping agents, was used for synthesis of Co, Ni, Fe-Co and Co-Ni nanomaterials. Co crystallizes in mixture of

53% hcp and 47% fcc phases whereas Ni crystallizes in fcc phase. Average crystallite sizes for Co and Ni were found to be 15 nm and 35 nm, respectively. Average TEM particle sizes were equal to 11 nm and 10 nm for Co and Ni, respectively. Both Co and Ni show ferromagnetic behavior at room temperature. The M_S values for Co and Ni are found to be 64 and 29 emu/g, respectively. The H_C values for Co and Ni are 436 Oe and 148 Oe, respectively and indicate high magnetocrystalline anisotropy effect. Fe_xCo_{100-x} alloys (x = 40, 60, 80) prepared via superhydride route crystallize in pure α-Fe-Co alloy phase. The crystallite sizes were found to be in the range of 23-38 nm. Average TEM particle sizes range from 10 to 51 nm. The values of the M_S for Fe-Co alloys range from 93.1-142.2 emu/g which are quite large for Fe-Co nanomaterials. Room temperature Mössbauer studies show change in magnetic structure at the surface of the nanoparticles. Co_xNi_{100-x} alloys (x = 20, 40, 60, 80) crystallize in pure fcc phase. Average crystallite sizes were found to be in the range of 8-11 nm. Average TEM particle sizes range from 7-11 nm with narrow size distributions. The M_S values for annealed Co-Ni alloys are found to be in the range of 25-59.6 emu/g whereas H_C values were 52-314 Oe These results were interpreted with the help of size effects, altered crystal anisotropies and spin canting at the surface of nanomaterials.

Fe-Pt and Co-Pt alloys were synthesized via superhydride reduction route. $Fe_{50}Pt_{50}$ and $Fe_{54}Pt_{46}$ alloys have been coated with oleic acid/oleylamine (route-1) and oleic acid/CTAB (route-2), respectively. The as-prepared Fe-Pt alloys have disordered fcc phase with crystallite sizes of 2.3 nm and 6 nm transformed to ordered fct phase with crystallite sizes of 21nm and 19.5 nm for route-1 and route-2, respectively. SEM studies confirm spherical shape morphologies with SEM particle sizes of 24 nm and 21 nm for route-1 and route-2, respectively. As-prepared Fe-Pt alloys are ferromagnetic with presence of superparamagnetic fractions and average magnetic moments per particle were found to be 753 μ_B and 814 μ_B, for route 1 and 2, respectively. The values of saturation magnetization for annealed Fe-Pt alloys were 4.4 emu/g and 29.6 emu/g whereas maximum values of coercivity were 10000 Oe and 10792 Oe for route-1 and route-2, respectively. $Co_{59}Pt_{41}$ and $Co_{60}Pt_{40}$ alloys have been coated with CTAB (route-1) and oleic acid/CTAB (route-2). Disordered fcc phase of Co-Pt alloys was transformed to ordered fct phase after annealing at 600°C. SEM studies show that annealed Co-Pt nanoparticles have spherical shape morphologies with SEM particle sizes of 38 nm and 59 nm for route-1 and route-2, respectively. The values of M_S and maximum value of H_C for Co-Pt(route-1) are found to be 31.4 emu/g and 1728 Oe, after annealed at 600°C/2h. The values of M_S for Co-Pt(route-2) are found to be 26.9 emu/g, and 22.5 emu/g whereas H_C values are 2525 Oe, and 5027 Oe, for annealed at 600°C/2h, and 600°C/12h, respectively. The observed magnetic properties Fe-Pt and Co-Pt alloys have been interpreted with the help of crystallite sizes, order parameters, size, surface, and composition effects of the nanostructured materials.

Modified polyol method was used for synthesis of Co, $Co_{50}Ni_{50}$ and Co-Pt alloys, and annealing was carried out via route-1 (without NaCl matrix) and route-2 (with NaCl matrix). Co(route-1) crystallizes in hcp phase with crystallite size of 16.4 nm while Co(route-2) crystallizes in fcc phase with crystallite size of 37.1 nm. A TEM micrograph shows that Co(route-1) has chain-like nanostructures whereas Co(route-2) shows nearly spherical morphologies. M_S values of Co(route-1) were 162.7 and 167 emu/g at RT and 100K, respectively. M_S values of Co(route-2) were 29.7 emu/g and 35 emu/g at RT and 100K, respectively. These alterations in the magnetic properties show effects of size, shape, spin canting at the surface, altered crystal anisotropies etc. The H_C values at 100K of Co(route-1) and Co(route-2) were found to be higher than that of RT and indicate the presence of thermal effects. Co-Ni(route-1) and Co-Ni(route-2) crystallize in pure fcc phase with crystallite sizes of 28.1 nm and 30.4 nm, respectively. TEM studies of Co-Ni(route-2) shows spherical morphologies with particle size of 8 nm. M_S and H_C values Co-Ni(route-1) were found to be 116.2-110 emu/g and 93-86 Oe at RT-100K, respectively. M_S and H_C values Co-Ni(route-2) were found to be 45.6-47.4 emu/g and 214-324 Oe at RT-100K, respectively. These magnetic properties show fine particle size effects, anisotropy effects and temperature effects in the materials. After annealing at 700°C, Co-Pt(route-1) possess disordered fcc structure whereas (Co-Pt)route-2 shows ordered fct ($L1_0$) phase. SEM studies confirm spherical shape morphologies with SEM particle sizes of 41 nm and composition as $Co_{58}Pt_{42}$. The values of M_S and H_C for Co-Pt(route-2) are found to be 24 emu/g and 6050 Oe, respectively. The observed magnetic properties have been interpreted with the help of crystallite sizes, order parameters, and composition effects.

Studies of magnetic exchange and dipolar interactions of the embedded and coated nanoparticles system such as Ni/silica, $Co_{50}Ni_{50}$/silica, Co-Ni, Co, Ni, Fe-Co and Fe-Ni-Co. Ni/silica and $Co_{50}Ni_{50}$/silica with various loading (4-12 wt%) have been synthesized by superhydride reduction route. XRD studies and TEM studies confirm that the materials were embedded in amorphous silica matrix. XRD crystallite sizes for Ni/silica and $Co_{50}Ni_{50}$/silica are in the range of 6-10.5 nm and 13.6-16.3 nm, respectively. TEM particle sizes were estimated to be 13.6 nm and 8.9 nm for pure CoNi and 8 wt% CoNi/silica, respectively. Enhancements in the values of magnetizations of Ni/silica and CoNi/silica compared to that of pure materials have been observed. FC/ZFC studies indicate alterations in magnetic structure. These magnetic characteristics have been explained on the basis of fine particle size, surface effects and dipolar interparticle interactions. FC/ZFC measurements of Co_xNi_{100-x} alloys coated by oleic acid and oleyl amine confirm the presence of magnetic irreversibility and superparamagnetic blocking of nanoparticles due to strong dipolar interactions and particle size distribution. Also, magnetic interactions in Co, Ni, Fe-Co and Fe-Ni-Co alloys coated by carbonaceous matter have been studied. FC/ZFC studies of Co and Ni show the wider size distributions and result in shifting of blocking temperature value above 300 K. FC/ZFC magnetization measurements of Fe_xCo_{100-x} alloys show magnetic irreversibility and blocking of nanoparticles due to strong dipolar interparticle magnetic interactions. Fe-Ni-Co alloys show thermo-magnetic irreversibility below 300 K and blocking temperature approximately at 300 K. FC and ZFC magnetic characteristics of Fe-Ni-Co alloys are interpreted on the basis of interparticle interactions among magnetic nanoparticles.

TABLE OF CONTENT

Chapter II: Materials synthesis and characterization techniques

Chapter V: Magnetic properties of nano-crystalline Fe-Pt and Co-Pt alloys synthesized via superhydride route

Chapter VI: Development of newer synthetic route for Co, Co-Ni and Co-Pt nanoparticles by using polyol and studies on their structural and magnetic properties

Chapter VII: Investigations on magnetic exchange and dipolar interactions in some model nanostructured systems: Co and Ni based metals and alloys

LIST OF TABLES

LIST OF SYMBOLS AND ABBREVIATIONS

Symbol	**Description**
a, b, c	Lattice parameters along X, Y, Z axes
Å	Angstrom
C	Curie constant
cc	cubic centimeter
χ	volume susceptibility
χ_m	molar susceptibility
Ci	Curie
cm	centimeter
dB	decibel
°	degree
°C	degree Celsius
deg	degree
δ	isomer shift
ΔE_Q	electric quadrupole splitting
d_{hkl}	spacing between the (hkl) crystallographic planes
emu	electromagnetic unit
eV	Electron Volt
g	gram
Gb	Gigabytes
h	hour
H_{hf}	hyperfine magnetic field
H_z	Hertz
in	inch
J	Joule
K	degree Kelvin

k_B	Boltzmann constant
λ	wavelength
m	meter
M	Molar (concentration)
M'	Molar mass
min	minute
mL	mililitre
mol	mole
μ	magnetic permeability
μ_B	Bohr magneton
μ_{orb}	orbital magnetic dipole moment
μ_s	spin magnetic dipole moment
nm	nanometer
Pa	Pascal
%	percentage
ρ	density
T	Tesla
Tb	Terabytes
θ	diffraction angle
S	order parameter
Abbreviation	**Description**
acac	acetylacetonate
AOT	sodium dioctylsulphosuccinate
At%	Atomic percentage
ATR	attenuated total reflection
aq.	aqueous
BM	Bohr magneton

Bu	Butyl
CTAB	cetyltrimethylammonium bromide
D	physical diameter
D_{cr}	critical diameter
D_m	magnetic diameter
D_t	threshold diameter
DMG	Dimethyl glyoximine
DMF	N, N dimethyl formamide
EDTA	Ethylenediamine tetraacetic acid
EDX	energy dispersive X-ray spectroscopy
e.g.	For example
EMA	electromagnetic wave absorption
emf	electromotive force
Eq.	equation
Et	Ethyl
etc.	etcetera
FC	field cooled
fcc	face centered cubic
fct	face centered tetragonal
H	Applied field
H_C	Coercivity
hcp	hexagonal close packed
He(g)	Helium gas
ICDD	International Centre for Diffraction Data
i.e.	that is
JCPDS	Joint Committee on Powder Diffraction Standards
K_{eff}	effective anisotropy constant
K_i	induced magnetic anisotropy constant

K_s , K_s'	surface anisotropy constant
K_{sh}	shape anisotropy constant
K_u	uniaxial magnetic anisotropy constant
K_V	magnetocrystalline anisotropy constant
LRO	long range order
M	Magnetization
m_{NP}	magnetic moment of a nanoparticle
M_r	remanence or residual magnetization or remanent magnetization
M_S	Saturation Magnetization
$N_2(g)$	Nitrogen gas
$O_2(g)$	Oxygen gas
PEG	Polyethylene glycol
PMR	Perpendicular magnetic recording
PVP	polyvinylpyrrolidone
rpm	Revolutions per minute
RT	room temperature
SAED	selected area electron diffraction
S_{BET}	BET surface area
SDS	sodium dodecylsulphate
SEM	Scanning electron microscopy
SNR	signal to noise ratio
SPM	superparamagnetic
SQUID	Superconducting quantum interference device
T	Temperature
T_B	blocking temperature
T_C	Curie temperature
TEM	Transmission electron microscopy
TEOS	tetraethoxysilane

THF	Tetrahydrofuran
T_{irr}	irreversible temperature
T_N	Neel temperature
V	Particle volume
V_{cr}	critical volume
vs.	versus
VSM	vibrating sample magnetometer
V_t	threshold volume
W	total magnetic energy
W_a	anisotropy energy
W_{ex}	exchange energy
W_H	energy in the external magnetic field
W_m	magnetostatic energy
wt%	weight percent
W_w	energy of the magnetic domain wall
XRD	X-ray diffraction
ZFC	Zero field cooled

CHAPTER 1

Introduction

1.1 Transition metals and alloys

Transition metals and their alloys have tremendous technological applications in various fields such as catalysis, optoelectronic, magnetic and biomedical etc. [1-3]. Recently, transition metals are widely used in the pharmaceutical industries as catalysts for the preparation of various important drugs [1]. Metals and alloys having magnetic characteristics are extensively used for the purpose of magnetic recording, magnetic sensors, high density magnetic storage devices etc. [2]. Newer applications include their use in the field of biomedicine for bio-diagnostics, hyperthermia, drug delivery and magnetic resonance imaging technique [3].

In periodic table, elements present in the group 3 to 12 are referred as transition elements or transition metals. All these transition metals possess partially filled d-subshell in elemental or ionic form, and hence they are also known as d block elements [4]. Typical representation of some selected transition metals is shown in Table 1.1. Transition metals show various attractive properties due to presence of unpaired d electrons in partially filled d shell. More importantly, they can form solid solutions, interstitials and compounds with other metals or non-metals (alloys) which improve the metallic properties for particular applications. Alloy formation in transition metals takes place due to similar atomic sizes and can exchange atomic positions in crystal lattice.

Table 1.1 List of some important transition metals capable of forming alloys.

	Group number									
	3	**4**	**5**	**6**	**7**	**8**	**9**	**10**	**11**	**12**
Period 4	Sc	Ti	V	Cr	Mn	Fe	Co	Ni	Cu	Zn
Period 5	Y	Zr	Nb	Mo	Tc	Ru	Rh	Pd	Ag	Cd
Period 6		Hf	Ta	W	Re	Os	Ir	Pt	Au	Hg

1.2 Important properties of transition metals/alloys

1.2.1 Electronic and optical properties

Transition metals are well known for showing interesting electronic and optical properties due to the presence of free moving valence electrons. However, local electronic structures in the materials change according to chemical and morphological variations [5]. Further, variations in electronic and optical properties are observed for nano-sized metals and alloys arise from size, shape and surface effects. Shape effects on the optical responses are also observed which is known as surface plasmon resonance [5].

1.2.2 Magnetic properties

Transition metals show interesting magnetic properties due to presence of resultant magnetic dipoles. Transition metal compounds and complexes are paramagnetic in nature when they have one or more unpaired d-electrons. Some compounds are diamagnetic due to pairing of all electrons. Some metals (e.g. Fe, Co and Ni) and their alloys show ferromagnetism [6]. Ferromagnetism occurs when magnetic moments of individual species, such as atoms/ions etc. are aligned parallel to each other in a crystalline material. There are few more types of magnetism observed depending on alignment of magnetic moments such as anti-ferromagnetism, ferrimagnetism, superparamagnetism etc.

1.2.3 Catalytic properties

Transition metals and their compounds are used for homogeneous and heterogeneous catalytic activity [1]. These activities are related to their ability to adopt multiple oxidation states and to form complexes. Catalysts in solid form (nanomaterial-based catalysts) involve the formation of bonds between reactant molecules and atoms of the surface of the catalyst. This will lower the activation energy of the reaction and increases the rate of reaction.

1.2.4 Metallic and physical properties

In addition to above, transition metals possess metallic and physical properties, e.g. conductors of electricity and heat, high density, high melting points and boiling points

[7]. These properties are due to metallic bonding by delocalized d-electrons, leading to cohesion which increases with the number of shared electrons.

However, the research work presented in this thesis is focused on few transition metal nanoparticles (i.e. Fe, Co, Ni and Pt) and their alloys in the form of nanomaterials. Hereafter, more detail discussion will be presented about these nanomaterials in further sections of this introduction chapter.

1.3 General methods of synthesis of Fe, Co, Ni and their alloys nanoparticles

Synthesis of transition metals and alloys nanoparticles can be achieved by two approaches, namely, (i) top-down approach and (ii) bottom-up approach. In top-down approach, bigger particles will breakdown into nanomaterials of desired sizes in the range of 1-100 nm. Here, nanomaterials are obtained using high energy particles, deposition techniques, ball milling method and high frequency sonication [8-11]. However, top-down approach has some disadvantages which include possibility of presence of internal stress, surface defects and impurities etc. In bottom-up approach, nanomaterials (nanoparticles or nanostructures) can be precipitated out directly from the solution containing desired metal ions. Bottom-up approach has advantages in synthesis of nanocrystalline materials with fewer defects, homogeneous composition and better short or long range ordering. Synthesis of nanomaterials by bottom-up approach mainly includes chemical synthetic routes which are explained in the following paragraphs.

In chemical synthesis routes, metallic or alloy nanoparticles were obtained by precipitation from the solution. Morphologies of the final products (e.g. size, size distribution and composition) were controlled with the help of various stabilizing or protecting agents [5]. The typical mechanism involved in the chemical routes can be understood with the help of LaMer diagram, i.e. plot of concentration of atoms vs. reaction time [12] as shown in Figure 1.1. The change in phase occurred from homogeneous (solution) to heterogeneous (liquid and nanoparticles) leads to formation of energy barrier. To overcome this barrier, chemical synthesis passes through following three phases (Figure 1.1).

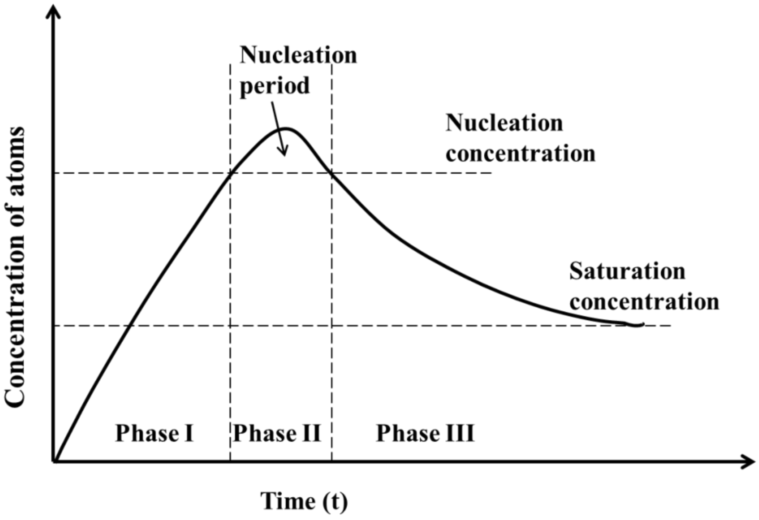

Figure 1.1 LaMer diagram representing different phases involved in chemical routes; phase I, phase II and Phase III. Phase II corresponds to nucleation period [12].

(i) Phase I: Initiation phase - In this phase, concentration of atoms increases with time beyond supersaturation limit to reach energy barrier where spontaneous nucleation occurs.

(ii) Phase II: Nucleation phase - When the degree of supersaturation is higher than energy barrier, nucleation process starts. Here, the formation of stable nuclei of the product and their growth take place. Due to occurrence of simultaneous nucleation and growth, the concentration of atoms decreases up to the level where the nucleation rate becomes zero.

(iii) Phase III: Growth phase - In this phase, the growth of the particle continues till the solution becomes supersaturated with the final product.

The particle sizes and size distribution strongly correlated to phase II where the formation of nanocrystals and nucleation occur together [13]. It shows that kinetics of above processes can be controlled by changing various experimental conditions such as nature of metallic precursor, temperature, pressure, reducing agents or capping agents etc. Accordingly, there can be various chemical synthesis routes developed for the preparation of transition metals/alloys nanoparticles. A few important synthetic routes are described in the following sub-section.

1.3.1 Sol-gel methods

The sol–gel process involves hydrolysis and condensation of metal alkoxides, e.g. $Al(OBu)_3$, $Si(OEt)_4$, $Ti(OEt)_4$ etc. [14]. In the hydrolysis step, the metal alkoxides will be converted to metal hydroxides by reacting with hydroxide group from water. After completion of hydrolysis, sol undergoes condensation reactions (more appropriately, polymerization) to form final gel. In sol-gel process, kinetics, hydrolysis and condensation reactions are directly correlated to the solvent type, temperature, precursors, pH, additives etc. [14]. The resulting gel mainly contains hydroxides of metals which can be converted to metal oxides after calcination at various moderate to high temperatures regime (say, 500-1200°C). Calcination at moderate temperatures results in the formation of crystalline nanomaterials with particular phase. Initially, sol–gel routes were used to prepare monodispersed particles of TiO_2 and SiO_2 [14], and then developed for the synthesis of ultrafine powders of $CoFe_2O_4$ and $NiFe_2O_4$ [15-16]. Further, metal nanoparticles can be prepared via the reduction of metal oxides in hydrogen atmosphere [17]. The narrow particle size distribution can be achieved only when the reaction is carried out through the complexation of the metal ions. For example, iron nanoparticles were distributed in the oxide matrix by sol-gel method without agglomerations [17].

1.3.2 Thermal decomposition method

Thermal decomposition process involves a chemical decomposition of the compounds at high temperatures (say 200-300°C). This method is also known as organometallic route because metal/alloy nanoparticles were obtained by thermal decomposition of organometallic complexes or metal-surfactant complexes at higher temperatures in presence of capping agents. For example, Fe-Pt nanoparticles were prepared by dissolving iron pentacarbonyl ($Fe(CO)_5$) and platinum acetylacetonate ($Pt(acac)_2$) in high boiling solvent such as dioctyl ether. Oleic acid and oleylamine were used as surfactants. Thermal decomposition of these metal precursors was carried out at high temperature (~300°C) which produces monodispersed Fe-Pt nanoparticles in solution. Further, these nanoparticles were purified and dispersed in various solvents [18]. Thermal decomposition method gives high initial supersaturation (burst nucleation) immediately after addition of metal precursor in the hot condition in solution phase. This phenomenon results in the better control on the crystallinity, size and size distribution of the nanocrystals [19-20]. The method has been used for the synthesis of various metallic nanocrystals such as Au, Pt, Fe-Pt, Co-Pt, $CoPt_3$, Fe-Co-Pt etc. [13, 20-21]. However, metal precursors having different decomposition temperatures may produce core-shell structure where metallic complex with lower decomposition temperature forms core and complex with higher decomposition temperature forms shell on the top of the metallic core [22].

1.3.3 Electrochemical and electrodeposition routes

The principle of electrodeposition technique involves the deposition of metal particles on the anode from electrolyte solution by applying voltage across electrodes. Electrochemical and electrodeposition techniques were used to prepare nanowires as well as nanoparticles of the magnetic materials such as Co, Fe-Ni etc. [23-24]. In a typical procedure, suitable substrate material (metal, carbon or semiconductor) was selected on which deposition occurs. One side of substrate was coated with a layer of conducting materials, e.g. Cu, to serve as anode. This anode was placed at the bottom of deposition bath. Pour the solution of metal salts under study in the deposition bath and apply voltage across two electrodes (cathode and anode). The metal nanoparticles were deposited on the surface of substrate (anode). In this method, nuclei formation requires at high overpotentials and low diffusion rates whereas grain growth is occurring at low overpotentials and high surface diffusion rates. Further, grain growth of the nanostructured materials is dependent on the deposition variables such as bath composition, pH, temperature, current density, overpotential, and additives [24]. In electrodeposition method, the nuclei are deposited on the surface of electrode in a random manner [24]. Hence, the size distribution obtained in the randomly nucleated particles is related to the interparticle diffusion coupling. Broadening in the size distribution can be minimized with the help of the slow growth method or H_2 coevolution method [24]. This technique can be used for the preparation of nanowires of Co, Ni, Fe-Pt, Fe-Co, Fe-Ni, Co-Pt, on the varieties of the template materials such as polycarbonate, anodized alumina, and mica [23, 25-28].

1.3.4 Micelle or Microemulsions routes

Micelles or microemulsions are the spherical aggregates formed by the surfactant molecules in the solution. Also, another surfactant can be used in order to enhance surfactant role which is known as cosurfactant. The surfactant molecules contain hydrocarbon chain with polar functional group at one end. Micelle aggregates have sizes ranging from 1–10 nm, while microemulsion aggregates are in the 10–100 nm range in diameter [29]. In the micelles, the hydrophilic end of the surfactant molecules is directed outside from the aggregate and attached to polar solvent molecules (e.g. water). When the hydrophobic end is directed outside from the aggregate and attached to nonpolar solvent molecules (e.g. oil) are called reverse or inverse micelles. Diagrammatic representation of structure of micelles and reverse micelles are shown in Figure 1.2. The volume of cavity formed inside the aggregates is dependent on the nature of surfactants and cosurfactants used.

In micelle route, a solution containing metal ions is reduced inside the micelle by using suitable reducing agents (e.g. sodium borohydride, hydrazine hydrate etc.) to obtain metal or alloy nanoparticles. Size and morphology can be controlled by surfactants; such as: sodium dioctylsulphosuccinate (AOT), cetyltrimethylammonium bromide (CTAB), and sodium dodecylsulphate (SDS). In the case of reverse micelles, water droplets which are stabilized by surfactants, form water-pools dispersed in nonpolar solvent. Here, water-pools acts as ‘nanoreactors’ for the reaction and hence size of the nanoparticles can be in the order of the diameter of the water-pools. Reverse micelle route has already been used for preparation of Co and Co-Pt nanoparticles [30]. This method has great control on average composition of the alloy nanoparticles because both the metallic precursors located at the interface of the micelle simultaneously. However, this method has some limitations which include low yield of nanocrystals and large size distributions (15-24 %).

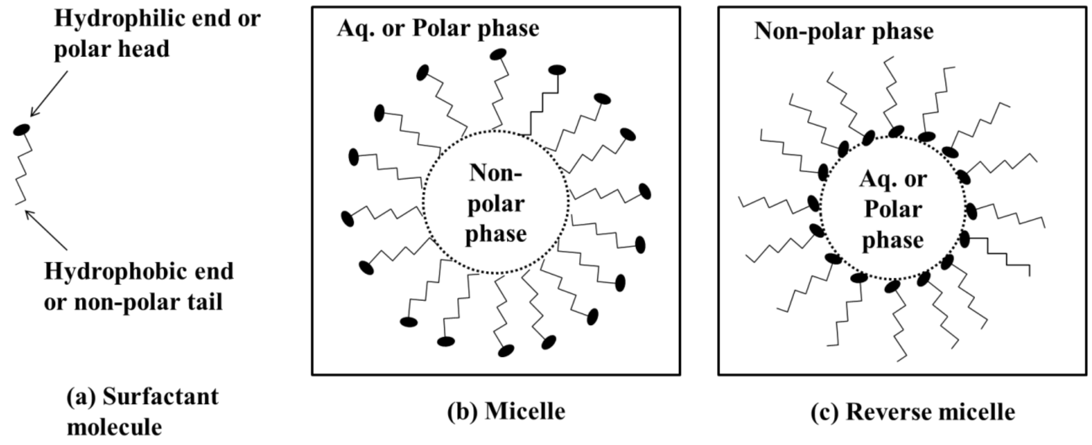

Figure 1.2 Diagrammatic representation of (a) an isolated surfactant molecule and ((b) and(c)) micelle and reverse micelle structures involving surfactant and solvent molecules, respectively.

1.3.5 Chemical reduction methods

Chemical reduction methods use various reducing agents for the synthesis of metal and alloy nanoparticles in solution state. Some of the important reducing agents are as follows.

(a) Sodium borohydride: Synthesis of transition metals, i. e. Fe, Cu, and Ni, using sodium borohydride in aqueous medium have been reported by Glavee et al. and co-workers for the first time [31-32]. Typically, metal sulfates or chlorides are dissolved in distilled water, where it dissociates into M^{n+} cations and SO_4^{2-}or Cl^- anions. The M^{n+} is reduced to M^0 by using a reducing agent, sodium borohydride. The borohydride anion (BH_4^-) is then oxidized to $B(OH)_3$. General reaction scheme is as follows.

$$M^{n+} + nBH_4^- \longrightarrow M^0 + nB(OH)_3 + xH_2(g) \uparrow$$

There is possibility of formation of metal oxides and metal borides by sodium borohydride method due to the presence of acidity and oxygen content in the aq. solution. These problems may be overcome partly, if not fully, by using suitable protecting agents and deoxygenated water.

(b) Superhydride: Lithium triethylborohydride, i.e. $LiB(Et)_3H$, (also known as ‘superhydride’) is a strong reducing agent. Superhydride is found to be easily dissolved in

ether solvents due to which homogenous reduction of metal salts is obtained at various temperatures starting from 25°C [33-35]. The typical synthesis of Fe-Pt includes the dissolution of $FeCl_2$ and $Pt(acac)_2$ metal precursors in diphenyl ether as solvent in the presence of capping agents (i.e. oleic acid, oleylamine) at 100°C. Further, these precursors were reduced by adding 1,2-hexadecanediol and $LiB(Et)_3H$ (1 M in THF) at 200°C, followed by refluxing at 263°C. The method produces monodispersed Fe-Pt nanoparticles of ~4 nm sizes [36]. In addition, a great control over the final composition of Fe-Pt alloy compared to other chemical reduction methods can be achieved.

(c) Polyalcohols: Another reduction method, i.e. polyol process, uses polyalcohol as both solvent and mild reducing agent in presence of a base. The polyol process was first reported by Fievet et al. in 1989 [37-38]. In this process, solid metal precursors (e.g. hydroxides, nitrates, chlorides, acetates) were suspended in a liquid polyol. The suspension was stirred and heated to 100-200°C depending on polyol. The reduction to metal can be obtained by using various polyols such as ethylene glycol, propylene glycol, diethylene glycol, trimethylene glycol, and butylene glycol. General reactions involved in case of ethylene glycol as polyol are as follows.

$$2CH_2OHCH_2OH \longrightarrow 2CH_3CHO + 2H_2O$$

$$2CH_3CHO + M^{n+} \longrightarrow 2CH_3COCOCH_3 + 2H_2O + M^0$$

1.3.6 Multisynthesis processes

Multisynthesis processing routes involve the combination of polyol method and thermal decomposition method [39-41]. In short, the process involves a high temperature solution phase synthesis followed by a size, shape and morphology control step using capping agents and surfactants. For example, monodispersed Fe-Pt nanoparticles of 3-10 nm size have been synthesized via high temperature reduction of $Pt(acac)_2$ using 1-2 hexadecanediol [42]. Also, thermal decomposition of iron carbonyl in the presence of oleic acid and oleyl amine as stabilizing agents can produce Fe-Pt nanoparticles (Figure 1.3) [42]. It has been shown that the composition in the final product can be controlled by the ratio of the iron precursor to the platinum precursor used during the synthesis.

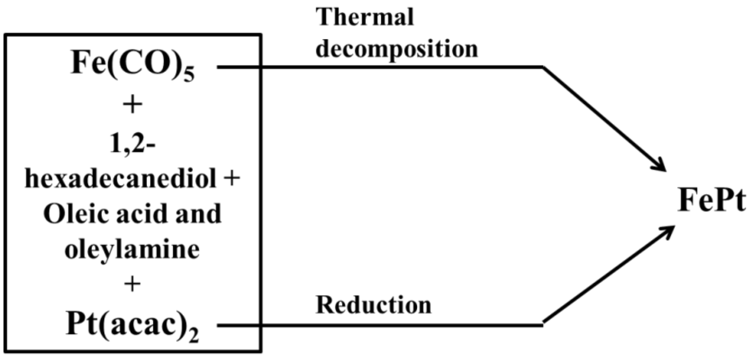

Figure 1.3 A block diagram representing synthesis of Fe-Pt alloy via Multisynthesis process.

1.4 Crystallography of metals and their alloys

The physical and chemical properties of the materials are directly correlated to its crystal structure. This can be studied with the help of various crystallographic parameters. The details of some representative crystal systems with respect to structures, types, and unit cell parameters etc., are discussed in following subsections.

1.4.1 Introduction

The structure of Fe, Co, Ni and their alloys are found to be either amorphous or crystalline in nature. In amorphous materials, all the atoms are randomly arranged in three dimensions. On the other hand, crystalline materials have regular and periodic arrangements of atoms in three-dimensional space where each point represents the position of an atom, a molecule or an ion of the material (Figure 1.4) [43]. This array of points showing an arrangement of atoms, molecules or ions in three-dimensional space is called space lattice and each point is known as lattice point. Further these lattice points can be divided into number of smallest repeating units in space lattice and each unit is named as ‘unit cell’ of the crystal. In Figure 1.4, unit cell is shown by dark lines. Three imaginary axes, i.e. X, Y and Z, are drawn in order to describe the unit cell parameters. This includes the lengths of the edges of the unit cell (i.e. a, b and c) and the angles (i.e. α, β and γ) as shown in Figure 1.4.

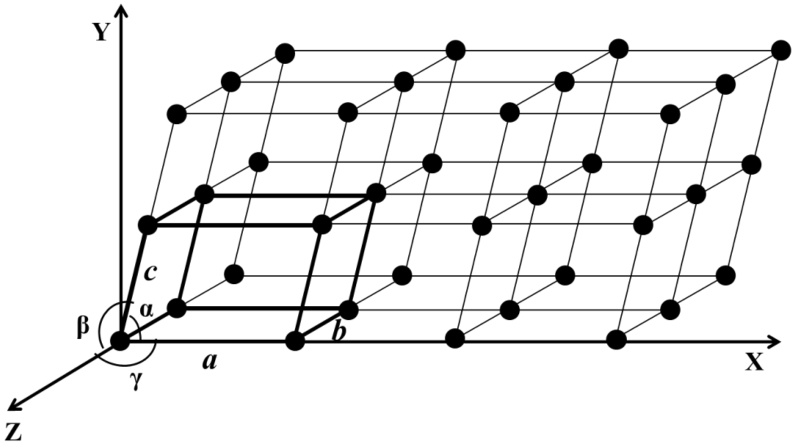

Figure 1.4 The typical representation of arrangement of atoms in unit cell inside an arbitrary space lattice. *a, b, c* and α, β, γ represents lattice parameters and angles, respectively.

According to the French crystallographer Auguste Bravais, there can be only 14 space lattices (or Bravais lattices) in which similar points can be arranged in three-dimensional space. These 14 Bravais lattices have been further divided into seven basic crystal systems [44] which are summarized in Table 1.2. Some crystal systems representatives for metal and alloys are described in detail in the following subsections.

Table 1.2 Crystal systems, examples, no. of Bravais lattices and unit cell characteristics of seven crystal systems.

Sr. No.	Crystal system	Examples	No. of Bravais lattices	Unit cell characteristics	
				Lattice parameters	Crystal angles
1	Cubic	Fe, Co, Ni and their alloys	3	$a = b = c$	$\alpha = \beta = \gamma = 90°$
2	Tetragonal	Fe-Pt, Co-Pt	2	$a = b \neq c$	$\alpha = \beta = \gamma = 90°$
3	Orthorhombic	$BeAl_2O_4$, $Mg_2Si_2O_6$	4	$a \neq b \neq c$	$\alpha = \beta = \gamma = 90°$
4	Monoclinic	$KAlSi_3O_8$, $LiAlSi_2O_6$	2	$a \neq b \neq c$	$\alpha = \gamma = 90^o, \beta \neq 90°$
5	Triclinic	$MnSiO_3$, Al_2SiO_5	1	$a \neq b \neq c$	$\alpha \neq \beta \neq \gamma \neq 90°$
6	Hexagonal	Co, Ni	1	$a = b \neq c$	$\alpha = \beta = 90°, \gamma = 120°$
7	Rhombohedral or Trigonal	$CaCO_3$, Fe_2O_3, Quartz	1	$a = b = c$	$\alpha = \beta = \gamma \neq 90°$

1.4.2 Major classes of crystal systems in Fe, Co, Ni and their alloys

1.4.2.1 Cubic system

The cubic crystal system has three Bravais lattices namely simple or primitive cubic lattice (P), body centered cubic lattice (I) and face centered cubic lattice (F). Arrangements of lattice points corresponding to same species (atoms/ions/molecules) in unit cell of these Bravais lattices are represented in Figure 1.5. The primitive cubic lattice has the lattice points only at the corners of each unit cell. The body centered cubic lattice has the lattice points at the corners as well as in the body center of each unit cell. The face centered cubic lattice has the lattice points at the corners as well as at the center of each of the six faces of the unit cell. The metal and alloy materials are crystallize in one of the Bravais lattices of cubic crystal system.

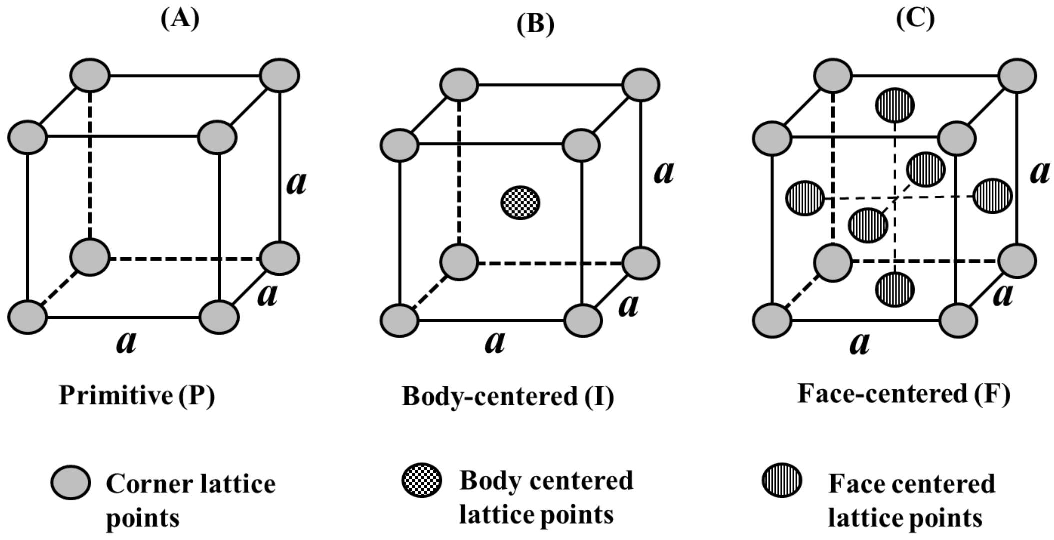

Figure 1.5 Bravais lattices of cubic crystal systems; (A) Primitive, (B) Body centered cubic and (C) Face centered cubic.

Atoms, molecules or ions are arranged in crystal planes in different directions. The orientation of each crystal plane in a lattice may be represented by Miller indices. Miller indices are defined as the reciprocals of the fractional intercepts which the plane makes with the crystallographic axes. Miller indices are generally written in parenthesis as (*hkl*). Distance between two consecutive crystal planes is denoted as *d*-value of that plane (d_{hkl}).

Some of the crystal planes such as (100), (200), (111) and their *d*-spacings are shown in Figure 1.6 for clarity. The *d*-values are directly related to Miller indices (*h*, *k* and *l*) and lattice parameters (*a*, *b* and *c*). Hence *d*-values gives exact information about crystal structure and used for indexing the planes and calculation of lattice parameters.

For cubic crystal system, the relation between *d*-value and lattice parameters is as follows.

$$\frac{1}{d_{hkl}^2} = \frac{h^2 + k^2 + l^2}{a^2} \tag{1.1}$$

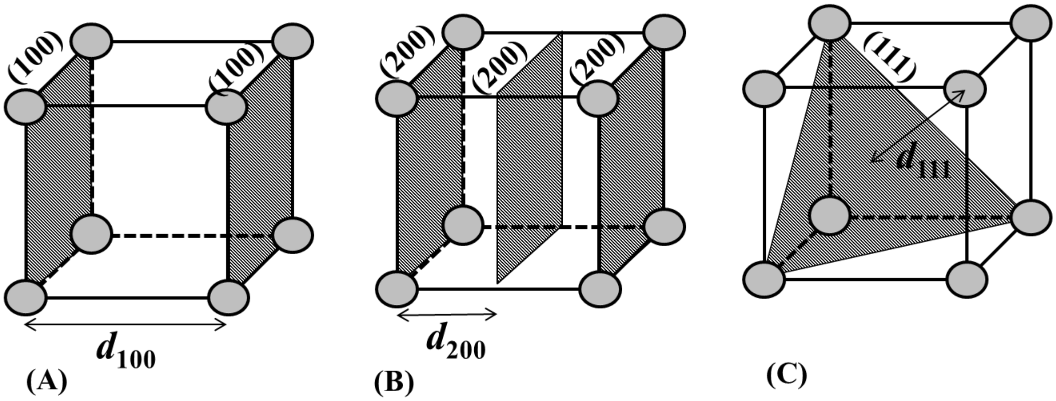

Figure 1.6 Representation of lattice planes; (a) (100), (b) (200) and (c) (111) lattice planes and with their *d*-spacings in simple cubic crystal lattices.

1.4.2.2 Tetragonal system

The tetragonal crystal system has two Bravais lattices namely (i) simple or primitive lattice (P), and (ii) body centered lattice (I). Arrangements of the lattice points in unit cell of these Bravais lattices are represented in Figure 1.7. For example, single metals of Fe, Co, and Pt have body centered cubic, hexagonal close packed, and face centered cubic structure, respectively at room temperature. However, Fe-Pt and Co-Pt alloys have disordered face centered cubic (fcc) structures at room temperature and show transition to face centered tetragonal (fct) crystal structure at higher temperatures. The arrangement of Fe and Pt atoms occurred during the phase transformation from fcc to fct is shown in

Figure 1.8. In case of Co-Pt, Fe atoms can be replaced by Co atoms. For tetragonal crystal system, the relation between d-value and lattice parameters is as follows.

$$\frac{1}{d_{hkl}^2} = \frac{h^2 + k^2}{a^2} + \frac{l^2}{c^2} \tag{1.2}$$

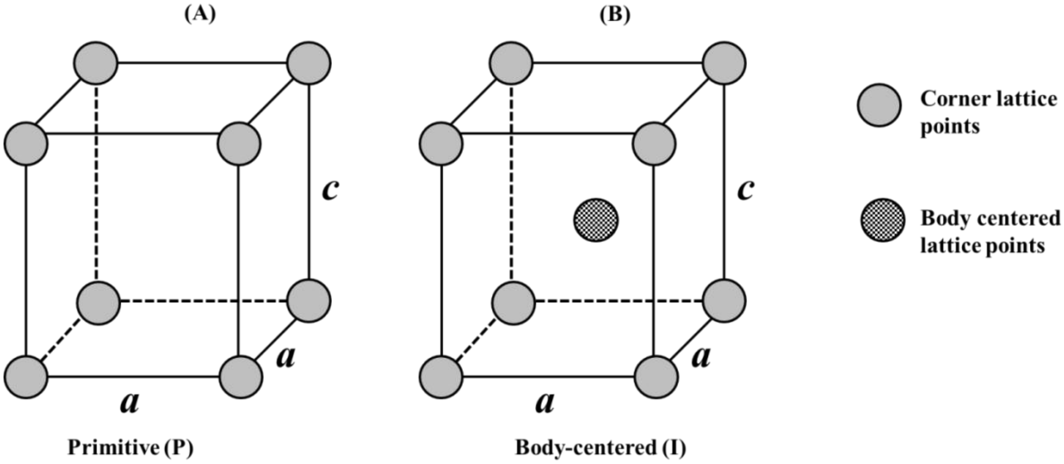

Primitive (P)

Body-centered (I)

Figure 1.7 Bravais lattices of tetragonal crystal system; (A) Primitive and (B) Body centered tetragonal.

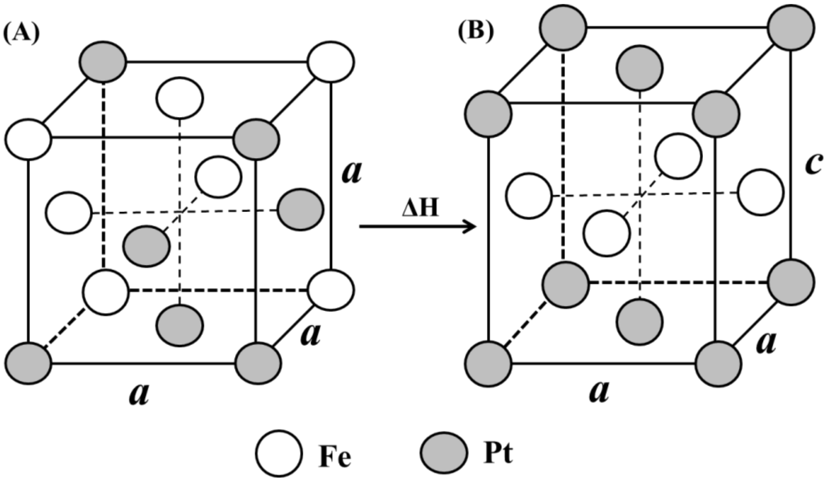

Figure 1.8 Crystal structures of disordered fcc Fe-Pt alloy (A) transforming into ordered fct phase (B). Fe or Pt atoms in disordered fcc structure are occupied in random manner and (A) denotes one of the specific arrangements.

1.4.2.3 Hexagonal system

The hexagonal crystal system has only one Bravais lattice namely simple or primitive lattice (P). Arrangements of lattice points in unit cell of Bravais lattice is represented in Figure 1.9 (A). For example, Co metal crystallizes in hexagonal close packed (hcp) crystal structure at lower temperatures. In case of hcp, additional layer of three lattice points will be incorporated in primitive crystal structure as shown in Figure 1.9 (B). For hexagonal crystal system, the relation between d-value and lattice parameters is as follows.

$$\frac{1}{d_{hkl}^2} = \frac{4}{3}\left(\frac{h^2 + hk + k^2}{a^2}\right) + \frac{l^2}{c^2} \tag{1.3}$$

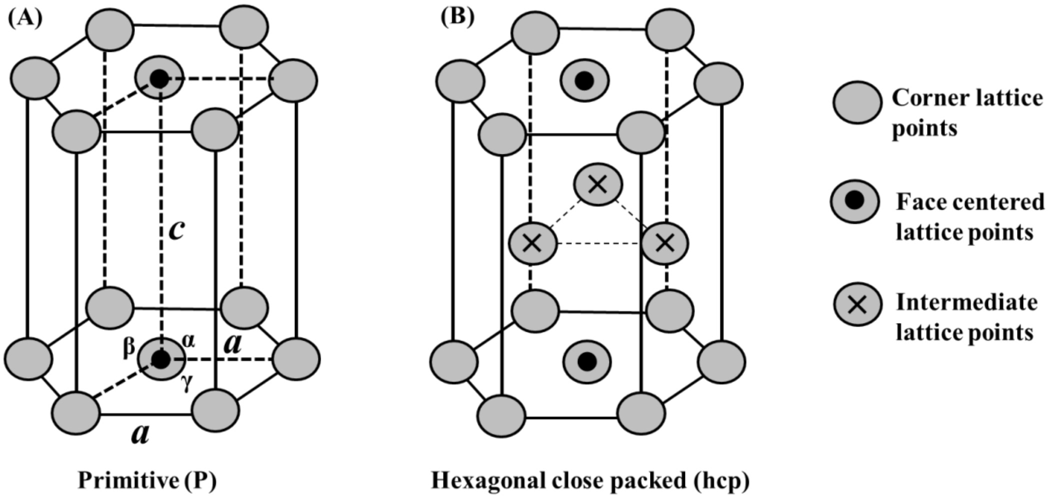

Figure 1.9 (A) Primitive Bravais lattice for hexagonal system and (B) crystal structure for primitive lattice in hcp form.

1.5 General introduction to magnetism

Magnetism in the materials occurs due to the spin and orbital motion of the electrons. Hence, an electron has spin magnetic dipole moment (μ_s) and orbital magnetic dipole moment (μ_{orb}) which are directly related to spin angular momentum and orbital angular momentum of an electron, respectively. Only spin magnetic dipole moment of an electron in z direction is known as the Bohr magneton (BM) and its value is 9.27×10^{-24} JT^{-1}. The fundamental unit of magnetism is Bohr magneton (μ_B). However, the response of magnetic materials in the presence of external magnetic field is expressed in terms of magnetic susceptibility (χ). If M is the magnetization generated in the material at applied field of H, then χ can be expressed by equation 1.4. Here, χ is volume susceptibility because M is magnetic moments per unit volume and also it is dimensionless since M and H. are in same dimensions. Volume susceptibility (χ) can be converted to molar susceptibility (χ_m), (cgs unit is cm^3 mol^{-1}) as shown in equation 1.5.

$$\chi = \frac{\mathrm{M}}{\mathrm{H}} \tag{1.4}$$

$$\chi_m = \chi V_m = \chi \frac{M\prime}{\rho} \tag{1.5}$$

where, M' is molar mass and ρ is density.

1.5.1 Different kinds of magnetic ordering

Depending on behavior of magnetic materials in external magnetic field and the values of χ, they are classified into five basic classes as (i) diamagnetic, (ii) paramagnetic, (iii) ferromagnetic, (iv) ferrimagnetic and (v) antiferromagnetic. The schematic representations of alignments of the magnetic dipole moments exhibiting five major kinds of magnetic behaviors are shown in Figure 1.10 (a), (b), (c) and (d). A brief description of the aforesaid magnetic behaviors is explained in the following subsections.

1.5.1.1 Diamagnetic materials

These materials have completely filled electron shells and hence show no net magnetic moment. However, they can induce magnetic moment in applied magnetic field but in opposite direction to applied field according to Lenz's law. [45] Therefore, diamagnetic materials show negative χ_m values and are in the order of -10^{-6} to -10^{-5} cm^3 mol^{-1}. Examples of diamagnetic transition metals are Cu (χ_m = -5.46×10^{-6} cm^3 mol^{-1}), Ag (χ_m = -1.95×10^{-5} cm^3 mol^{-1}), Au (χ_m = -2.8×10^{-5} cm^3 mol^{-1}) etc. [46].

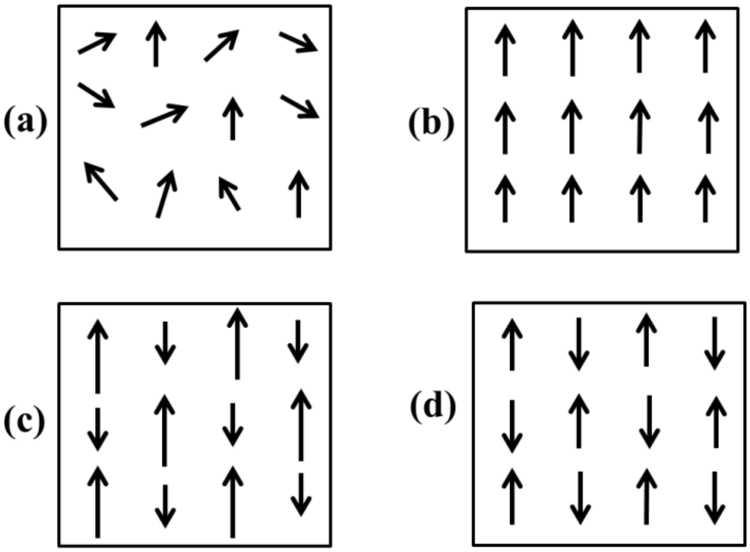

Figure 1.10 Schematic presentations of alignments of atomic magnetic moments for (a) paramagnetic, (b) ferromagnetic, (c) ferrimagnetic and (d) antiferromagnetic materials.

1.5.1.2 Paramagnetic materials

The materials containing unpaired electrons in their atoms, molecules or ions do possess magnetic dipole and may show paramagnetism. In the absence of magnetic field, the atomic magnetic moments are randomly oriented and net magnetic moment becomes zero for paramagnetic materials (Figure 1.10 (a)). When magnetic field is applied, partial alignments of moments occur and give positive χ_m values in the order of 10^{-5} to 10^{-3} cm^3 mol^{-1}. Paramagnetic materials obey Curie law which gives variation of χ with temperature (T′) [43] as shown in equation 1.6. Here C is Curie constant.

$$\chi = \frac{C}{T'} \tag{1.6}$$

Examples for paramagnetic transition metals include W ($\chi_m = 5.3\times10^{-5}$ cm^3 mol^{-1}), Pt ($\chi_m = 1.93\times10^{-4}$ cm^3 mol^{-1}) etc. [46].

1.5.1.3 Ferromagnetic materials

Ferromagnetic materials contain unpaired electrons and possess magnetic dipole like paramagnetic materials. But, these magnetic dipoles strongly interact with magnetic dipoles of neighboring atoms due to exchange fields and the phenomenon is called exchange coupling. Due to exchange coupling, atomic moments are aligned parallel to neighboring moments and hence possess net magnetization (Figure 1.10 (b)). The occurrence of such net magnetization in the absence of field is called spontaneous magnetization. Ferromagnetic materials have higher positive χ_m values than paramagnetic materials in the order of > 10^{-3} cm^3 mol^{-1}. Temperature dependency of χ can be shown by Curie-Weiss law [43] (Eq. 1.7). The value of χ decrease with increasing temperature, loses its ferromagnetic characteristics at critical temperature called Curie temperature (T_C), and becomes paramagnetic above T_C.

$$\chi = \frac{C}{T - \theta} \tag{1.7}$$

where, C and θ are constants and the value of θ is close to T_C.

Examples of the ferromagnetic materials are Fe (χ_m = 1.1×10^5 cm^3 mol^{-1}), Co (χ_m = 132 cm^3 mol^{-1}), Ni (χ_m = 315 cm^3 mol^{-1}) [46].

1.5.1.4 Ferrimagnetic materials

In ferrimagnetic materials, the magnetic moment ordering is composed of two magnetic sublattices (antiparallel arranged) which are separated by oxygen anions as shown in Figure 1.10 (c). The exchange interactions occur through the oxygen anions, called indirect or superexchange interactions. The strongest superexchange interactions were observed for an antiparallel alignment between two sublattices. These materials have similar characteristics like ferromagnetic materials being spontaneously magnetized with T_C at finite temperature. Examples of ferrimagnetic materials include transition metal oxides such as MFe_2O_4 (M = Fe, Mn, Co, Ni etc.) [46]. These materials have normal spinel or inverse spinel structure. M^{2+} ions occupy tetrahedral sites and Fe^{3+} ions occupy either octahedral sites (normal spinel) or both tetrahedral and octahedral sites (inverse spinel). Magnetization of MFe_2O_4 materials depends on nature and concentration of M^{2+} ions. The tetrahedral and octahedral sites form the two magnetic sublattices which are antiparallel to each other with different magnetic moments. Superexchange interactions occurred in these two sublattices and gives ferrimagnetic properties. For Fe_3O_4 spinel, saturation magnetization and Curie temperature are found to be 92 emu/g and 580°C, respectively.

1.5.1.5 Antiferromagnetic materials

The atomic moments in these materials are aligned antiparallel to each other as shown in figure 1.10 (d). Antiferromagnetic materials have χ_m values in the order of 10^{-5} to 10^{-3} cm^3 mol^{-1}. In the materials antiferromagnetic ordering exist at sufficiently low temperatures up to a critical temperature known as Neel temperature (T_N) and above T_N the antiferromagnetic ordering gets disturbed and susceptibility value enters into the paramagnetic regime. Examples of antiferromagnetic materials include hematite (α-Fe_2O_3) (χ_m = 3.5×10^{-3} cm^3 mol^{-1}), Cr (χ_m = 1.8×10^{-4} cm^3 mol^{-1}) etc. [46]. Hematite has corundum (Al_2O_3) crystal structure may be indexed as hexagonal or rhombohedral. Here oxygen ions situated in hexagonal close packed framework and Fe^{3+} ions occupy octahedral interstices. The magnetic moments of the Fe^{3+} ions are ferromagnetically coupled within same c-plane, but antiferromagnetically coupled between the different planes [47].

1.5.2 Ferromagnetism in transition metal and alloys

The transition metal and alloys studied in this thesis are ferromagnetic in nature and are highlights in this sub-section.

The phenomenon of spontaneous ferromagnetism is exhibited by three of the 3d transition metals (i.e. Fe, Co, and Ni), and heavy rare-earth metals such as Gd, Tb, Dy etc. However, the 3d transition metals have high Curie temperatures and exhibit ferromagnetism with large spontaneous magnetizations at room temperature [48]. The magnetic dipole moments exhibited by metals and alloys can be explained based on the band theory of solids [6]. In iron, cobalt and nickel have an inner energy level that is not completely filled, i.e., each atom in the metal has a permanent magnetic moment, equal in strength to the number of unpaired electrons. If the atoms are close to each other so that the electrons can be exchanged between neighboring atoms, a cooperative magnetization may occur which spontaneously aligns all atoms in a lattice and creates a strong magnetic moment. When the spins between neighboring atoms are aligned parallel, the material is said to be ferromagnetic. Slater-Pauling curve describes the variation of the mean atomic magnetic dipole moment as a function of outer electron number in transition metal alloy systems [49]. Fe, Co and Ni exhibit saturation magnetic moments of 2.2, 1.7, and 0.6 Bohr magneton per atom, respectively, at 0 K. Hence, Slater-Pauling curve is an important starting point in deciding the alloy composition for a particular application. Magnetic behavior of ferromagnets involves not only spin coupling between neighboring atoms but the formation of sub-micrometer magnetic domains [50-51]. In ferromagnetic materials, individual magnetic moments form domain in which all moments have parallel orientation. Hence, the resultant magnetization (M) has contribution from all the domains oriented in different directions.

The behavior of ferromagnetic materials under external applied magnetic field (H) is shown in Figure 1.11. In the absence of field (H = 0), all the domains are randomly aligned, cancel magnetization of each other and net magnetization may be negligible. After applying field, magnetization in the material increases slowly and then drastically up to a certain value and then gets saturated (curve a). The saturation magnetization is denoted as M_S, and 'curve a' is called initial magnetization curve. At this stage, the direction of H is reversed, magnetization will not follow initial curve, and instead it will follow the curve b. Some magnetization is retained even at $H\rightarrow0$, which is called remanence or residual magnetization (M_r). The field required to bring magnetization value to zero is called coercive field or coercivity (H_C) of the material. With the further field in opposite direction, magnetization will saturate at negative M_S value. Again increasing field in forward direction (curve c), magnetization will complete loop formation which is called hysteresis loop.

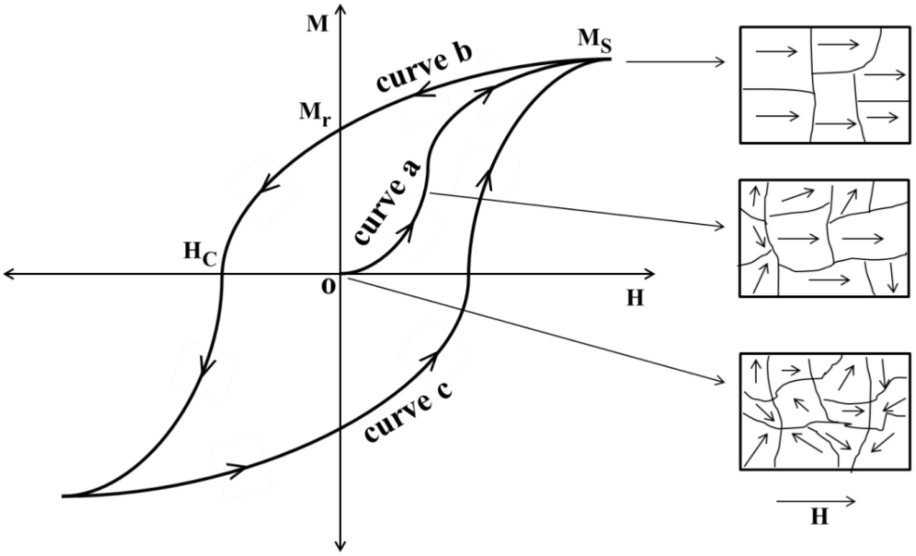

Figure 1.11 Magnetization reversal and domain structure in ferromagnetic materials. Curve a is the initial magnetization plot and curves (b, c) represent hysteresis loops in reverse and forward directions, respectively.

1.5.2.1 Classification of ferromagnetic materials

Depending on the value of coercivity and engineering applications, the magnetic materials are divided into three classes; (a) soft, (b) hard, and (c) semi-hard magnetic materials [52]. Typical M-H plots for these materials are shown in Figure 1.12.

(a) Soft magnetic materials

Soft magnetic materials can be easily magnetized and demagnetized. Hence, they possess high magnetic permeability, low coercivity, and low hysteresis loss. They are used for the cores of the transformers, motors, inductors, and generators. Examples of soft magnetic alloys include Fe-Ni, Fe-Co, Fe-Co-Ni, and Fe-Si alloys.

(b) Hard magnetic materials

Hard magnetic materials require high field to saturate magnetization and hard to demagnetize. They possess high coercivity and high remanence. They are used as permanent magnets in electric meters and loudspeakers. The performance of permanent magnet is its maximum energy density $(BH)_{\max}$ which is a measure of the maximum magnetostatic energy available from a magnet of particular shape. High coercivity and high remanence are required for obtaining large (*BH*)$_{max}$. Examples for hard magnetic materials include Fe-Co-W steel, Fe-C-Al steel, Fe_2NiAl, Fe-Cr-Co alloy, Fe-Pt and Co-Pt alloys.

(c) Semi-hard magnetic materials

They are used in the magnetic recording media which require properties in between soft and hard materials. They are characterized by moderately high coercivity and high remanence magnetization. These properties for specific applications can be designed by synthesizing materials with desired particle sizes. Fine particles or nanoparticles (particle size ≤ 100 nm) of ferromagnetic materials such as Fe, Co, Ni, and their alloys may give properties for magnetic recording media applications.

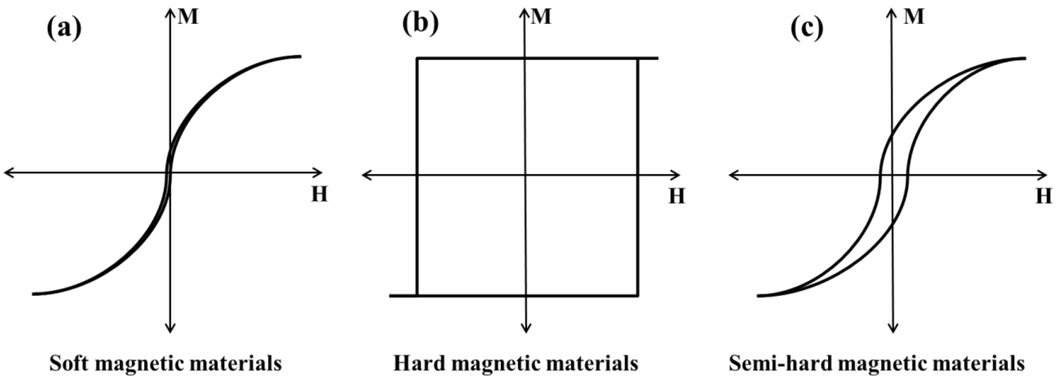

Figure 1.12 Typical representations of M-H plots for soft, hard and semi-hard magnetic materials.

1.6 Fine particle magnetism (Nano-magnetism)

1.6.1 Alteration of magnetic properties of nanostructured materials

Magnetic properties of the materials are generally divided in two types, (i) intrinsic magnetic properties and (ii) extrinsic magnetic properties. Intrinsic magnetic properties do not vary with external parameters, e.g. saturation magnetization (M_S), Magnetocrystalline anisotropy constant (K_V), Curie temperatures (T_C) etc. [53]. Extrinsic magnetic properties depend on the morphology, crystal structure and anisotropies in the system, e.g. magnetic permeability (μ), coercivity (H_C), remanence (M_r) etc. [53].

However, at nano-scale level, intrinsic properties like M_S, K_a, T_C, and extrinsic properties like H_C can change with alloy composition, crystal structure and reduction of particle size [54-57]. The state of lowest free energy for ferromagnetic nanoparticles can be achieved below critical size where it forms single domain particle with uniform magnetization. In such kind of particles, thermal energy (k_BT) plays an important role in the magnetization process and results in magnetic transitions from ferromagnetic to superparamagnetic state with the decrease in particle size [58-59]. Further, variations in magnetic properties such as coercivity value (H_C), blocking temperature (T_B), and effective anisotropy constant (K_{eff}) etc. can also be expected due to interparticle magnetic dipolar interactions [60].

1.6.2 Coercivity of nanoparticles

As the particle size (or particle diameter) of the material is reduced, coercivity is found to increase, reaches to maximum value and then tends towards zero. For example, variation of coercivity with particle sizes in Fe and Fe-Co is reported by Kneller and Luborsky in the size range of 300 nm to 2 nm [61]. Schematic diagram for coercivity variation with particle diameter is shown in Figure 1.13. The diameter at which material reaches to maximum value of the coercivity is called critical diameter (D_{cr}). The particles with diameter above D_{cr} have multi-domains magnetic structure where magnetization is stable and non-uniform. Particles below D_{cr} become single domains with stable and uniform magnetization. As the particle diameter decreases below D_{cr}, coercivity decreases and reaches to zero at threshold diameter (D_t) because of thermal energy exceeds the anisotropy energy barrier. Corresponding particle volumes at critical diameter and threshold diameter are known as critical volume (V_{cr}) and threshold volume (V_t), respectively. In actual practice, there is assembly of particles with different diameters in a system. Hence, resultant properties are estimated from average of all. The particles with diameter below D_t have unstable magnetization, fluctuates in the direction of easy axis, magnetization reverse spontaneously, and are called superparamagnetic particles.

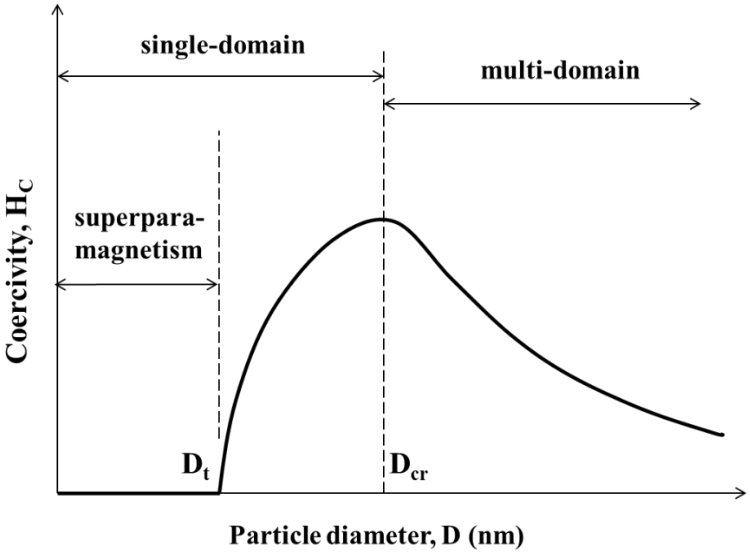

Figure 1.13 Variation of coercivity with the increase in average diameter of nanoparticles.

1.6.3 Magnetic anisotropy in nanoparticle system

The total magnetic energy (W) of nanoparticle system in an external magnetic field (H) can be written as follows:

$$W = W_{ex} + W_m + W_H + W_w + W_a \tag{1.8}$$

Where, W_{ex} is the exchange energy, W_m is the magnetostatic energy, W_H is the energy in the external magnetic field, W_w is the energy of the magnetic domain wall (in case of multi-domain particles), and W_a is the anisotropy energy. Further, the anisotropy energy (W_a) has various components such as: magnetocrystalline anisotropy (W_V), shape anisotropy (W_{sh}), surface anisotropy (W_s), and an induced anisotropy (due to different effects) (W_i). Then, components are described in detail in the following sections.

$$W_a = W_V + W_{sh} + W_s + W_i \tag{1.9}$$

1.6.3.1 Magnetocrystalline anisotropy (W_V) in nanoparticle system

The magnetization of a single crystal in an external magnetic field shows different approach to saturation in different directions along crystallographic axes. This leads to the existence of magnetocrystalline anisotropy [6]. The direction in the crystal in which the magnetization occurs easily is the easy magnetization axis, whereas the direction in which the magnetization occurs in a hard way is the hard magnetization axis. For example, in Fe single crystal, the directions <100>, <010>, and <001>, are easy magnetization axes, and the direction <111> is the hard magnetization axis (Figure 1.14). The mechanical work of magnetization required in order to rotate the spontaneous magnetization vector from the direction of easy magnetization axis to different crystallographic direction is equal to the magnetocrystalline anisotropy energy (W_V).

The symmetry of crystal plays important role in determination of the value of W_V. For example, the magnetocrystalline anisotropy energies for cubic symmetry, $W_{V,c}$, (e.g. Fe, Ni) and for hexagonal uniaxial symmetry, $W_{V,u}$, (e.g. Co) can be written as follows.

$$W_{V,c} = K_1(\alpha_1^2\alpha_2^2 + \alpha_1^2\alpha_3^2 + \alpha_2^2\alpha_3^2) + K_2\alpha_1^2\alpha_2^2\alpha_3^2 + \cdots \tag{1.10}$$

$$W_{V,u} = K_{1u}\sin^2\varphi + K_{2u}\sin^4\varphi + \cdots \tag{1.11}$$

where, α_1, α_2, α_3 are the direction cosines along the crystallographic axes, 'φ' is the angle between the spontaneous magnetization vector and the main axis of symmetry, K_1, K_2, K_3, K_{1u}, and K_{2u} are the magnetocrystalline anisotropy constants.

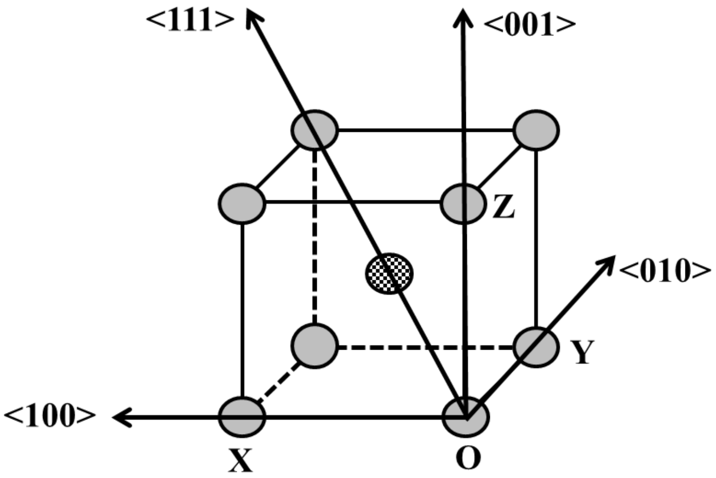

Figure 1.14 Representations of <100>, <010>, <001>, and <111> directions in bcc Fe single crystal.

1.6.3.2 Magnetic shape anisotropy (W_{sh}) in nanoparticle system

The magnetization is dependent on the shape of particles. The shape anisotropy energy (W_{sh}) for a single crystal with ellipsoidal shape (with ellipsoid axes, where, $a >> b = c$), can be defined as follows.

$$W_{sh} = K_{sh}\sin^2\theta \qquad \text{where} \quad K_{sh} = \left(\frac{\mu_0}{2}\right)(N_a - N_b)M_S^2 \qquad (1.12)$$

where, N_a and N_b are demagnetization factors of the ellipsoid axes a and b, respectively (Here, 'a' is major and 'b' and 'c' are minor axes of ellipsoid.). θ is the angle made by the spontaneous magnetization with the major axis, a, of the ellipsoid. K_{sh} is the shape anisotropy constant. For spherical shape, N_a=N_b, therefore K_{sh} = 0, and hence there is no shape anisotropy.

1.6.3.3 Surface magnetic anisotropy (W_s) in nanoparticle system

Surface magnetic anisotropy arises due to incomplete atomic bonding or broken symmetry on the surface of a crystal [62]. For example, the surface anisotropy energy (W_s) for cubic symmetry can be expressed as follows [63-64]:

$$W_s = K_s\cos^2\beta \qquad \text{and} \qquad K_s' = \left(\frac{6}{D}\right)K_s \qquad (1.13)$$

where, K_s and K_s' are the surface anisotropy constant expressed in Jm^{-2} and Jm^{-3}, respectively, and β is the angle between the spontaneous magnetization vector and the direction of the external normal at the surface considered. As the value of K_s' is dependent on particle diameter, surface anisotropy plays significant roles in nanoparticles such as variations in the values of intrinsic magnetization and hyperfine fields [64].

1.6.3.4 Induced magnetic anisotropy (W_i) in nanoparticle system

In nanoparticle systems, magnetic anisotropy can be induced when the equilibrium position of the spontaneous magnetization vector influenced during material preparation and processing. This may result in the occurrence of elastic tensions (stress) in the material or the existence of magnetic exchange coupling between the spins (e.g.

nanoparticle-matrix interface or core–shell). An induced magnetic anisotropy energy can be denoted as W_i and induced magnetic anisotropy constant as K_i.

By considering all four forms of magnetic anisotropy, the total or effective magnetic anisotropy of the nanoparticle systems is the sum of four anisotropies and effective magnetic anisotropy constant (K_{eff}) can be expressed as follows [65].

$$K_{eff} = K_V + K_{sh} + K_s' + K_i \tag{1.14}$$

In actual practice, K_{eff} is more significant because the value of K determined from experimental coercivity value of nanomaterials includes contribution from all four anisotropies as discussed above.

1.6.4 Factors influencing saturation magnetization of nanoparticles

At nano-scale level, surface to volume ratio in nanomaterials is higher than the corresponding bulk materials. This indicates increase in number of surface atoms when compared to bulk atoms. The magnetic structure of bulk atoms and surface atoms are significantly different which leads to interesting magnetic phenomena in nanoparticle systems [66]. Magnetization (M) of the materials is the resultant magnetic moments (μ) per unit volume. However, the variations in M for nanoparticles are dependent on various factors which are discussed below.

1.6.4.1 Size, shape and surface effects

It has been observed that there is reduction in saturation magnetization of nanoparticles compare to corresponding bulk materials and it decreases with decreasing particle size [67-70]. This is related to size, shape and surface effects on magnetization of nanoparticles. As size of particle decreases, the energy that holds the magnetic moment in particular direction (i.e. anisotropy energy) decreases. This leads to the randomization of magnetic moments which may reduce the resultant magnetization [66]. Further, nanoparticles of same volume but different shape have different anisotropy constants as well as proportion of disordered spins at the surface. In case of Fe_3O_4, anisotropy constant for spherical nanoparticles was higher than cubic particles but the higher magnetization was observed for cubic nanoparticles due to presence of less disordered spins [71]. For the nanocrystals of γ-Fe_2O_3 with particle size of 5.9 nm, the spins at the surface of nanoparticle have disordered structure (i.e. canted spin structures) whereas they are ordered in the core [72]. In addition, surface spins may have fix orientation in particular direction because of bonding with organic coating, known as ‘spin pinning’. And spin canted layer may froze into ‘spin-glass-like phase’ at lower temperatures where roughly equal proportion of ferromagnetic and antiferromagnetic atomic orientations are present [73-74]. These surface effects lead to the formation of core-shell magnetic structure in nanoparticles having two kinds of diameters, i.e. physical diameter (D) and magnetic diameter (D_m) as shown in Figure 1.15. Various theoretical models were proposed for explanation of ‘spin canting’ for $NiFe_2O_4$ nanoparticles, ‘spin pinning’ for nanoparticles capped by organic surfactant, and ‘spin-glass-like surface layer’ for ferromagnetic core at low temperatures etc. [73-76]. The surface spin disorder occurs mainly because of the modification of the exchange interactions between surface magnetic ions with incomplete coordination [77]. Reduction in M_S value compare to bulk value ($M_{S\ bulk}$) due to size and surface spin disorderness can be expressed by following relation [78].

$$M_S = M_{S\,bulk}\left(\frac{D_m}{D}\right)^3 \tag{1.15}$$

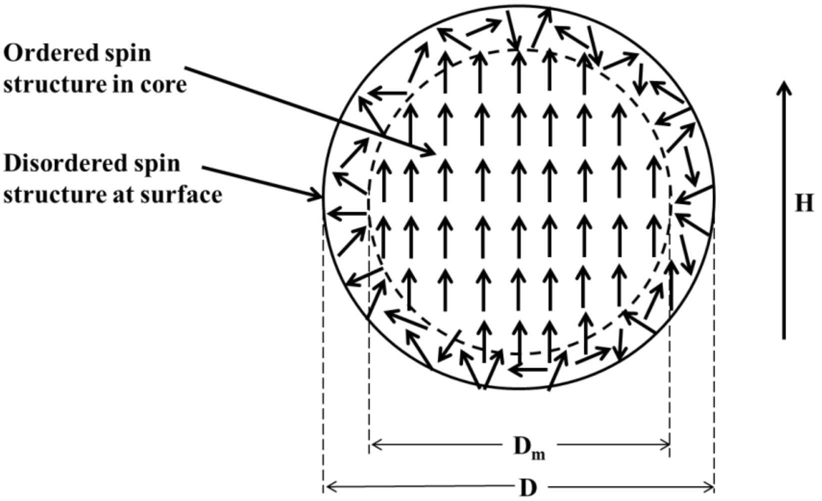

Figure 1.15 Schematic representation of order-disorder spins structure in the nanoparticles. D and D_m are physical and magnetic diameter, respectively.

1.6.4.2 Effects of Temperature

The value of M_S at higher field strengths reduces with the increase in temperature and will reach to zero at Curie temperature (T_C) where ferromagnetic (or ferrimagnetic) materials become paramagnetic. For bulk materials, variation of M_S with temperature can be shown by Bloch law [79] where M_S value found to decrease with increase in temperature. The expression can be represented as follows:

$$M_S(T) = M_S(0)\,(1 - \Lambda T^{3/2}) \qquad (1.16)$$

Where M_S (0) is spontaneous magnetization at 0 K, Λ is a constant that depends on the exchange integral J ($\Lambda \sim 1/J^{3/2}$).

For nanoparticles, it has been observed that T_C decreases as the diameter of nanoparticle decreases [80-82]. In fine particle systems, some systems follow Bloch law while several others show deviation towards larger values from $T^{3/2}$ law [83-85]. However, it has been found that the relative increase of M_S at two different temperatures in fine particles systems is much higher than that of bulk materials in the same temperature range [86]. This increase in magnetization at lower temperatures is due to increase in magnetic diameter and magnetic volume of nanoparticle which has been observed in case of nanoparticles covered by oleic acid [87]. An increase in the magnetic volume will occur when the disordered spins in the surface layer (shell) become magnetically ordered as in the core of particle at low temperatures. This fact has been proved using electron spin resonance spectroscopy and Mossbauer spectroscopy at low temperatures [88-89].

1.6.5 Superparamagnetism in nanoparticles

In case of nanoparticle system, when the particle diameter reduces to below threshold diameter ($D < D_t$), the relaxation time of the magnetic moments at finite temperature is very small and is of the order of 10^{-9} s [90-91]. Under these conditions, the magnetization of single-domain nanoparticles fluctuates rapidly along the easy magnetization axis [90], being always in thermodynamic equilibrium. After applying an external magnetic field, magnetic moments respond instantly to the field variations. This behavior of a system of nanoparticles is magnetically equivalent (i.e. M vs. H response) to a system of paramagnetic atoms (Langevin's paramagnetism) [92], where the non-interacting atomic magnetic moments exist instead of the nanoparticle magnetic moments. Hence, such a system of nanoparticle assembly is called superparamagnetic (SPM) system [93], and the phenomenon is called superparamagnetism.

Thus, the magnetization of a SPM system can be expressed by Langevin formula derived from classical theory of paramagnetism [94].

$$\mathrm{M_{SPM}(H, T) = n m_{NP}}\left(\coth\frac{\mu_0 \mathrm{m_{NP} H}}{\mathrm{k_B T}} - \frac{\mathrm{k_B T}}{\mu_0 \mathrm{m_{NP} H}}\right) \tag{1.17}$$

Where, n is the concentration of nanoparticles in the system, m_{NP} is the magnetic moment of a nanoparticle, and the parenthesis contains the Langevin function. For a system of non-interacting nanoparticles to have a superparamagnetic behavior in the external field, two conditions must be met: (i) the M vs. H plots recorded at different temperatures must show zero coercivity and follow the Langevin function, and (ii) using same magnetization data, curves in the representation of M/M_S vs. H/T should overlap.

In the presence of thermal energy (T > 0 K), when the nanoparticle's size becomes lower than D_t (or particle volume, $V < V_t$), the magnetization of nanoparticle fluctuates along the easy magnetization axis (reversing at 180^o) [90]. In the absence of external magnetic field (H = 0), for the spontaneous magnetization to reverse, considering nanoparticle with uniaxial magnetic anisotropy constant (K_u), the energy barrier must be overcome the value (W_b):

$$\mathrm{W_b = K_u V} \tag{1.18}$$

The probabilities of crossing the potential barrier are higher thermal energy ($k_B T$) and reduction in particle volume (V). The time required to reverse the magnetization is known as Neel relaxation time (τ_N) and the process is known as Neel magnetic relaxation [90].

$$\tau_N = \tau_0 \exp\left(\frac{\mathrm{K_u V}}{\mathrm{k_B T}}\right) \tag{1.19}$$

Where, τ_0 is a time constant which usually has the value 10^{-9} s [95]. In practice of measurements, the time interval taken for Neel relaxation process is called measurement time (t_m). In the case of static measurements, it is generally considered as 100 s [96]. When the relaxation time is equal to the measuring time ($\tau_N = t_m$), above equation 1.19 becomes,

$$K_u V \cong 25 k_B T \tag{1.20}$$

This expression gives temperature up to which spins (magnetic moments) are blocked and are corresponding to the blocking of magnetic moments, known as blocking temperature (T_B).

$$T_B = \frac{K_u V}{25 k_B} \tag{1.21}$$

When the nanoparticles with volume V has a temperature $T < T_B$, the magnetic moments of the nanoparticles are blocked, and when $T > T_B$, the magnetic moments of nanoparticles fluctuate along the axis of easy magnetization (relaxation).

1.6.6 Long-range crystalline order (LRO)

In crystalline solids, arrangement of atoms or lattice periodicity is maintained over a distance to obtain crystal symmetry or correlations. This translational ordering over a long distance compare to interatomic distances is known as long range crystalline order. The perfect long range order (LRO) in Fe-Pt or Co-Pt system means all the Pt-sites are occupied by Pt atoms and the Fe-sites by Fe atoms (or Co sites by Co atoms) in fct crystal structure. However, the actual chemical order may not be perfect and to characterize the degree of order, LRO parameter (S) can be defined by following expression [97]:

$$S = r_{Pt} + r_{Fe} - 1 \tag{1.22}$$

where, r_{Pt} and r_{Fe}, are the fractions of Pt- and Fe-sites occupied by a correct atom, Pt or Fe, respectively. When the order is perfect, the order parameter S reaches unity, while for a completely random atom arrangement S is equal to zero. Thus, the order parameter can reach its maximum ($S = 1$) only for a stoichiometric composition. For non-stoichiometric compositions, S is always less than unity. Generally, powder XRD is used to calculate the long-range chemical order parameter (S) in Fe-Pt and Co-Pt alloys.

1.7 Literature Survey

1.7.1 Recent reports on Fe, Co and Ni metal nanoparticles

Investigations on physical properties of nano-magnetic materials have become important topic of research because of their variations in the properties at the nano-scale level [98-99]. It has been studied in the literature that magnetic nanoparticles show size and surface dependent magnetism and magnetic transition from ferromagnetism to superparamagnetism [100]. The magnetic properties of metal nanoparticles have already been studied in order to explain their applicability in the technological and biological fields [100]. The self-assembled nanocrystals of metal nanoparticles which can show ferromagnetism at room temperature, such as Fe, Co and Ni, are widely used in the fabrication of nano-devices [102-103]. The metal nanoparticles of Fe, Co, and Ni have great interest due to their potential technological applications; such as magnetic recording, magnetic storage devices, magnetic refrigeration systems, catalysis, ferro-fluids, magnetic carriers for drug delivery, magnetic resonance imaging etc. [104-107]. Especially, metallic magnetic materials at nano-dimension, e. g. cobalt and nickel nanoparticles, are used in the microwave absorption devices due to their high relative complex permeability in the frequency range of 1-5 GH_z [108]. Metallic and alloy magnetic materials have high permeability, large saturation magnetization and high Snoek limit at high frequency band. Therefore, they are especially promising for the excellent electromagnetic wave absorption (EMA) performances in gigahertz range [109]. Recently, metal and alloy magnetic nanoparticles are used in the development of radar-absorbing materials for commercial and military applications instead of carbon based materials, ferrites and carbonyl iron powder [109-110].

1.7.2 Recent reports on binary alloys of Fe, Co and Ni

Recently, research on Fe-Co alloys has received increasing attention of scientists because of their technological properties; such as large permeability, high saturation magnetization and Curie temperature [111-112]. In nanometer scale, Fe-Co alloys are important for their applications as building units for functional nanomaterials, magnetic resonance imaging, magnetic recording, biomedical applications and microwave absorbing materials [113-117]. Size, shape, surface and compositions dependence of physical and chemical properties of the nano-structured Co-Ni alloy materials, such as magnetic and catalytic properties, have been studied in the literature [118-120]. Co-Ni alloys nanomaterials are soft magnetic systems even though they were least focused for their investigations on magnetic properties when compared to other soft magnetic systems such as, Fe-Co and Fe-Ni [121]. Co-Ni nanomaterials with desired size, shape, surface morphologies and compositions have specific applications in technological fields [122]. These nanomaterials have extensive applications in the field of magnetic recording media, ferrofluids, magnetic inks, magnetic resonance imaging, sensors etc. [2, 123]. In biomedical sciences, magnetic nanoparticles are used as probes and vectors for medical diagnosis, hyperthermia treatment, drug delivery systems etc. [124-125]. In addition, Co-Ni alloys are effective electromagnetic wave absorption materials used in fabricating electronic devices for various applications [126].

1.7.3 Recent reports on ternary alloys of Fe, Co and Ni

Fe-Ni-Co ternary alloys can be used successfully for high density magnetic recording [127-129]. The substituted alloys can have improved magnetostrictive properties and can have varieties of applications including magnetoresistance sensor [130]. Further Fe-Ni-Co alloy with compositions (i.e. 29% Ni, 17% Co and balanced Fe) is termed as Kovar and is of technological importance in electronic industry, e.g. power tubes, X ray tubes, seal materials etc. [130-132]. The Kovar alloy possesses soft magnetic properties having coercivity in the range of approximately 50-100 Oe. The curie temperature of the Kovar alloy has a value of 435°C. As stated earlier, the microstructure and magnetic properties of the Kovar alloys are sensitive to shape and size of the alloy particles. Synthesis and characterization of Kovar alloys have already reported in nano-crystalline form by using gaseous reduction method [130]. Fe-Ni-Co alloys have been receiving technological importance due to their size and shape sensitive magnetic and microstructural properties [133-134]. Especially, these alloys are widely used as EMA materials for commercial and military applications [109]. In electronic industries, these materials are used for recording, storage devices, material’s sealing, press working, photo-etching and thermal resistance purposes due to their unique magnetic and thermo-physical properties [130].

Further, it has been observed that doping of small amount of cobalt in Fe-Ni alloys show enhancement in magnetic properties with small hysteresis loss [135]. Greve et al. have studied nano-structured $Fe_{54}Ni_{27}Co_{19}$ and PTFE nanocomposites for their magnetic high frequency applications in GH_z range [136]. It has been reported that structure and magnetic properties Fe-Ni-Co ternary alloys depend on the synthetic methodology and subsequent heat treatments of the materials [137].

1.7.4 Recent reports on Fe-Pt and Co-Pt alloys

Modern permanent magnet materials are based on intermetallic compounds of rare-earths and 3*d* transition metals with very high magnetocrystalline anisotropy, such as $Nd_2Fe_{14}B$ and $SmCo_5$ [138]. $L1_0$ phases of Fe-Pt and Co-Pt alloys also possess high magnetocrystalline anisotropy constants (K_u), i.e. 6.6-10 × 10^6 Jm^{-3} and 4.9 × 10^6 Jm^{-3}, respectively [139]. However, Fe-Pt and Co-Pt alloys have more advantage compared to the rare-earth-transition-metal-based compounds due to their ductility and chemical inertness. High magnetocrystalline anisotropies of Fe-Pt and Co-Pt alloys results in higher H_C values ranges from 4-20 kOe. Fe-Pt alloys with H_C values of 4-8 kOe with significant values of saturation magnetization, M_S (40-60 emu/g) are required in order to make stable storage device with maximum signal to noise ratio (SNR) [140]. SNR can be increased by decreasing grain size, but magnetizations of smaller grains below critical size may fluctuate due to thermal energy known as superparamagnetic effects. However, stable magnetization can be achieved by using high anisotropy materials. Due to the unique combination of excellent intrinsic magnetic properties and good corrosion resistance, $L1_0$-based thin films and nanoparticles of Fe-Pt alloys are promising candidates for ultra-high-density magnetic storage media [42, 139].

1.7.5 Recent reports on metal/alloy nanoparticles dispersed in silica matrix

Recently, research in nanochemistry mainly focuses on synthetic techniques meant for precise control on the morphology of nanoparticles [141]. In order to control the particle size, size distribution and morphology, silica matrix is an excellent candidate who provides cavities having well defined size, geometry and regularity in special arrangements [142]. Generally, metal precursors were adsorbed on the mesoporous template and then reduced in H_2 (g) flow. Such kind of approach is called “host-guest” synthesis [143]. The methodology gives highly dispersed system of metal nanoparticles in silica matrix. It has been reported that silica matrix is an excellent candidate for transferring magnetic exchange interactions among particles and hence enhanced magnetic properties at macro scale can be expected [144]. At present, syntheses of Ni nanoparticles dispersed in silica matrix have been reported by sol-gel method and chemical reduction by aqueous hydrazine [143, 145].

These materials have potential applications in various fields; just to name a few: catalysis [146], biomedical [147], magnetic recording media [148], microwave absorption materials [126] etc. Alloy nanoparticles embedded in silica matrix show altered magnetic properties (M_S, H_C, K_{eff} etc.). The values of the M_S can be different from that of the bulk materials [149-150]. Co, Ni and their alloys nanoclusters in silica host show an enhancement in the magnetic moment and decrease in coercivity due to the superparamagnetic behavior [151]. Significant changes in effective anisotropy constant (K_{eff}) are also reported for metal/alloy nanostructures [149]. These variations in the magnetic properties of nanomaterials embedded in silica matrix have already been attributed to several aspects such as high surface area to volume ratio, electronic structure, interaction between nanomaterials and matrix, or interparticle interactions [150, 152-153]. In order to control size, dispersion, stability and interparticle interactions among nanoparticles, nano-composites of alloys (e.g. Co-Ni, Ni-Cu, Co-Cu, Fe-Co etc.) in silica matrix have been synthesized by various synthesis techniques such as sol-gel method [150], high temperature hydrogen reduction method [153], ion implantation method [149], mechanical milling [155] etc.

1.8 Gaps in existing research

According to above literature survey, there are several reports on the synthesis of magnetic nanoparticles by different synthetic routes. Magnetic properties of metal and alloy nanoparticles can be different for materials synthesized via different synthetic routes. Each synthetic strategy produces nanomaterials with particular dimensions, morphologies, and unique properties. Capping agents play important role in controlling size of nanomaterials and induce surface effects in magnetic characteristics. Tailoring of particle size of the nanomaterials to obtain desired magnetic properties can be achieved by designing synthetic strategies. Hence the novel and modified synthetic routes give a platform for designing and achieving properties which are useful for specific applications.

1. For biomedical applications, it is imperative that these nanoparticles to be dispersed in aqueous medium by using various biocompatible capping agents which may enhance fluid flow characteristics. Hence, study of synthesis and characterization of ferromagnetic metal/alloy nanoparticles stabilized in aqueous medium is a necessary topic of research. It is required to develop new synthetic strategy based on sodium borohydride reduction method to obtain thermally stable nanoparticles, characterizations and study for the magnetic properties.
2. As superhydride reduction method in suitable organic medium is useful for synthesis of ultrafine nanoparticles using various capping agents. Investigations on the magnetic properties of many important capped metal/alloy systems have not been reported by superhydride reduction route. Some notable capping agents are oleic acid, oleylamine, hexadecylamine, N-cetyltrimethylammonium bromide etc. There exists limited information in literature so far in this regard.
3. It has been demonstrated that air stable magnetic nanoparticles can be synthesized by polyol method using PEG-200. The polyol method can be modified for the synthesis of nanomaterials coated with new capping agents which may not be possible when polyol as solvent. The magnetic materials included in the objectives have some useful for future technological applications due to coating and have not been studied by polyol method. Further, exhaustive characterizations and explorations on fine particle magnetism need further investigation.
4. There is scant literature available on dispersion of magnetic nanoparticles in Silica or polymer matrix using various chemical reduction routes. Dispersion of nanoparticles in silica matrix increases interparticle separation than coated by silica. Interparticle interactions play an important role towards magnetic properties of the materials. To be noted several fundamental magnetic parameters can be estimated with nano-

particle assembly with well-defined interparticle separation. This will be possible by development of novel chemical synthetic methods.

1.9 Scope of the present research work (Defination) and objectives

This investigation focused on the synthesis, characterization and magnetic properties of selected transition metal and binary/ternary alloy nanoparticles (Fe, Co, Ni, Pt and Pd Based) with novel chemical reduction routes. These materials have been synthesized via three different methodologies namely, (i) modified $NaBH_4$ reduction route, (ii) superhydride route and (iii) modified polyol method. Synthesized materials were characterized by various instrumental techniques, such as Fourier transform infrared spectroscopy, elemental analysis, X-ray diffraction, scanning electron microscopy and transmission electron microscopy. Further, room temperature and low temperature magnetic properties of the materials have been studied in detail. Observed magnetic properties show fine particle size, shape and surface effects dominantly. Also, studies on the inter-particle dipolar magnetic interactions among magnetic nanoparticles have been carried out for magnetic nanoparticles dispersed mesoporous silica matrix.

The following objectives of the present research work have been proposed.

1. Synthesis, characterization and magnetic properties of selected transition metal and binary/ternary alloy nanoparticles (Fe, Co and Ni Based) using modified NaBH4 reduction route in aqueous medium.

2. Synthesis, characterization and magnetic properties of selected transition metal and binary/ternary alloy nanoparticles (Fe, Co, Ni, Pt and Pd based) using superhydride reduction route in suitable organic medium.

3. Synthesis, characterization and magnetic properties of selected transition metal and binary/ternary alloy nanoparticles (Fe, Co, Ni, Pt and Pd) using modified polyol method.

4. Studies on the inter-particle dipolar magnetic interactions among magnetic nanoparticles dispersed in thin film polymer matrix and mesoporous silica matrix.

1.10 Outlay of the Thesis

The thesis is divided into eight chapters.

In chapter I, an introduction to transition metal/alloys, synthesis methods, crystal structures, magnetism, fine particle magnetism (nano-magnetism), literature survey, identification of research gaps based on literature survey and the objectives of the present research work have been discussed.

Chapter II describes the details of synthesis methodologies and methods of instrumental characterizations used in this research work.

Chapter III describes synthesis, characterizations and studies on magnetic properties of PEG coated nanocrystalline Fe, Co, Ni and Fe-Ni-Co alloys synthesized via modified $NaBH_4$ route in aqueous medium.

Chapter IV describes synthesis, characterizations and studies on magnetic properties of oleic acid/oleylamine coated nanocrystalline Co, Ni, Fe-Co and Co-Ni alloys synthesized via modified superhydride route in organic medium.

Chapter V describes synthesis, characterizations and studies on magnetic properties of nanocrystalline Fe-Pt and Co-Pt alloys synthesized via modified superhydride route in organic medium. Here, combinations of oleic acid, oleylamine and CTAB were used as capping agents

Chapter VI describes synthesis, characterizations and studies on magnetic properties of PVP coated nanocrystalline Co, $Co_{50}Ni_{50}$ and Co-Pt alloys synthesized via modified polyol method in organic medium.

Chapter VII describes the studies on magnetic exchange and interparticle dipolar interactions among nanoparticles embedded in silica matrix and coated with organic matter. The systems under study include Ni/silica, $Co_{50}Ni_{50}$/silica, Co-Ni coated with oleic acid/oleylamine, Co, Ni, Fe-Co and Fe-Ni-Co coated with carboneous matter.

Chapter VIII includes summary and future scope of research.

References

1. M. L. Crawley and B. M. Trost, Eds., Applications of Transition Metal Catalysis in Drug Discovery and Development: An Industrial Perspective, John Wiley & Sons, NJ, 2012.
2. R. Ferrando, J. Jellinek and R. L. Johnston, Chem. Rev., 108 (2008) 845-910.
3. N. T. K. Thanh and L. A. W. Green, Nano Today, 5 (2010) 213-230.
4. F. A. Cotton, G. Wilkinson, C. A. Murillo and M. Bochmann, Advanced Inorganic Chemistry, 6th ed., John Wiley & Sons, SG, 2003.
5. D. Alloyeau, C. Mottet and C. Ricolleau, Eds., Nanoalloys: Synthesis, Structure and Properties, Springer, UK, 2012.
6. B. D. Cullity and C. D. Graham, Introduction to Magnetic Materials, 2nd ed., John Wiley & Sons, NJ, 2009.
7. J. D. Lee, Concise Inorganic Chemistry, 5th ed., Chapman & Hall, NY, 1996.
8. H. Gleiter, Prog. Mater. Sci., 33 (1989) 223-315.
9. P. V. Satyam, J. Kamila, S. Mohapatra, B. Satpati, D. K. Goswami, B. N. Dev, R. E. Cook, L. Assoufid, J. Wang and N. C. Mishra, J. Appl. Phys., 93 (2003) 6399-6403.
10. G. F. Goya, Solid State Commun., 130 (2004) 783-787.
11. S. Mornet, S. Vasseur, F. Grasset and E. Duguet, J. Mater. Chem., 14 (2004) 2161-2175.
12. V. K. LaMer and M. D. Barnes, J. Colloid Sci., 1 (1946) 71-77.
13. J. Park, J. Joo, S. G. Kwon, Y. Jang and T. Hyeon, Angew. Chem. Int. Ed., 46 (2007) 4630-4660.
14. C. J. Brinker and G. W. Scherrer, Sol-Gel science, Academic Press, NY, 1990.
15. J. G. Lee, H. M. Lee, C. S. Kim and Y. J. Oh, J. Magn. Magn. Mater., 177-181 (1998) 900-902.
16. D-H. Chen and X-R. He, Mater. Res. Bull., 36 (2001) 1369-1377.
17. J-P. Wang and H-L. Luo, J. Appl. Phys., 75 (1994) 7425-7428.
18. J. Kim, C. Rong, J. Ping Liu and S. Sun, Adv. Mater., 21 (2009) 906-909.
19. S. G. Kwon, and T. Hyeon, Acc. Chem. Res., 41 (2008) 1696-1709.

20. S. Sun, Adv. Mater., 18 (2006) 393-403.
21. K. Philippot and B. Chaudret, C. R. Chimie, 6 (2003) 1019-1034.
22. S. U. Son, Y. Jang, J. Park, H. B. Na, H. M. Park, H. J. Yun, J. Lee and T. Hyeon, J. Am. Chem Soc., 126 (2004) 5026-5027.
23. H. R. Kahn and K. Petrikowski, J. Magn. Magn. Mater., 215-216 (2000) 526-528.
24. R. M. Penner, J. Phys. Chem. B, 106 (2002) 3339-3353.
25. H. Zeng, M. Zheng, R. Skomski, D. J. Sellmyer, Y. Liu, L. Menon and S. Bandyopadhyay, J. Appl. Phys., 87 (2000) 4718-4720.
26. R. Ferre, K. Ounadjela, J. M. George, L. Piraux and S. Dubois, Phys. Rev. B, 56, (1997) 14066-14075.
27. Y. H. Huang, H. Okumura, G. C. Hadjipanayis and D. Weller, J. Appl. Phys., 91 (2002) 6869-6871.
28. H. R. Khan and K. Petrikowski, Mater. Sci. Eng. C, 19 (2002) 345-348.
29. M. P. Pileni and N. Duxin, Chem. Innov., 30 (2000) 25-33.
30. C. Petit, S. Rusponi and H. Brune, J. Appl. Phys., 95 (2004) 4251-4260.
31. G. N. Glavee, K. J. Klabunde, C. M. Sorensen and G. C. Hadjapanayis, Langmuir, 8 (1992) 771-773.
32. G. N. Glavee, K. J. Klabunde, C. M. Sorensen, G. C. Hadjipanayis, Z. X. Tang and L. Yiping, Nanostruct. Mater., 3 (1993) 391-398.
33. H. Bonnemann, W. Brijoux and T. Joussen, Angew. Chem. Int. Ed. Engl., 29 (1990) 273-275.
34. H. Bonnemann, R. Brinkmann, R. Koppler, P. Neiteler and J. Richter, Adv. Mater., 4 (1992) 804-806.
35. S. Sun and C. B. Murray, J. Appl. Phys., 85 (1999) 4325-4330.
36. S. Sun, S. Anders, T. Thomson, J. E. E. Baglin, M. F. Toney, H. F. Hamann, C. B. Murray and B. D. Terris, J. Phys. Chem. B, 107 (2003) 5419-5425.
37. F. Fievet, J. P. Lagier, B. Blin, B. Beaudoin and M. Figlarz, Solid State Ionics, 32-33 (1989) 198-205.
38. B. Blin, F. Fievet, D. Beaupere, M. Figlarz, Nouv. J. Chim., 13 (1989) 67-72.
39. V. F. Puntes, K. M. Krishnan and A. Paul Alivisatos, Science, 291 (2001) 2115-2117.

40. V. F. Puntes, K. Krishnan and A. Paul Alivisatos, Top. Catal., 19 (2002) 145-148.
41. V. F. Puntes, K. M. Krishnan and P. Alivisatos, Appl. Phys. Lett., 78 (2001) 2187-2189.
42. S. Sun, C. B. Murray, D. Weller, L. Folks and A. Moser, Science, 287 (2000) 1989-1992.
43. B. R. Puri, L R. Sharma and M. S. Pathania, Principles of Physical Chemistry, 46th ed., Vishal Publishing Co., India, 2013.
44. B. D. Culity, Elements of X ray Diffraction, Addison-Wesley: Reading, MA, 1956.
45. D. Halliday, R. Resnick and J. Walker, Fundamentals of Physics, 5th ed. Extended, John Wiley & Sons, NY, 1997.
46. J. F. Schenck, Med. Phys., 23 (1996) 815-850.
47. A. H. Morris, Canted antiferromagnetism: Hematite, World Scientific Publishing, SG, 1994.
48. S. Chikazumi and S. H. Charap, Physics of Magnetism, Krieger Publishing Co., NY, 1978.
49. R. M. Bozorth, Ferromagnetism, Van Nostrand, Prinston, NJ, 1951.
50. W. F. Brown Jr., Rev. Mod. Phys., 17 (1945) 15-19.
51. F. Bloch, Z. Phys., 74 (1932) 295-335.
52. S. Chikazumi, Physics of Ferromagnetism, Oxford University Press, NY, 1997.
53. M. E. McHenry, M. A. Willard and D. E. Laughlin, Prog. Mater. Sci., 44 (1999) 291-433.
54. J. P. Chen, C. M. Sorensen, K. J. Klabunde, G. C. Hadjipanayis, E. Devlin, and A. Kostikas, Phys. Rev. B, 54 (1996) 9288-9296.
55. R. N. Panda, and N. S. Gajbhiye, J. Appl. Phys., 81 (1997) 335-339.
56. A. A. El-Gendy, E. M. M. Ibrahim, V. O. Khavrus, Y. Krupskaya, S. Hampel, A. Leonhardt, B. Buchner, and R. Klingeler, Carbon, 47 (2009) 2821-2828.
57. O. Margeat, C. Amiens, B. Chaudret, P. Lecante, and R. E. Benfield, Chem. Mater., 17 (2005) 107-111.
58. K. Haneda, Can. J. Phys., 65 (1987) 1233-1244.
59. C. Kittel, Phys. Rev., 70 (1946) 965-971.

60. F. C. Fonseca, G. F. Goya, R. F. Jardim, R. Muccillo, N. L. V. Carreno, E. Longo and E. R. Leite, Phys. Rev. B, 66 (2002) 104406.
61. E. F. Kneller and F. E. Luborsky, J. Appl. Phys., 34 (1963) 656.
62. J. M. D. Coey, Magnetism and Magnetic Materials, Cambridge University Press, UK, 2010.
63. L. Neel, J. Phys. Radium, 15 (1954) 225-239.
64. F. Bodker, S. Mørup and S. Linderoth, Phys. Rev. Lett., 72 (1994) 282-285.
65. C. Caizer, J. Magn. Magn. Mater., 320 (2008) 1056-1062.
66. A. G. Kolhatkar, A. C. Jamison, D. Litvinov, R. C. Willson and T. R. Lee, Int. J. Mol. Sci., 14 (2013) 15977-16009.
67. H. Kachkachi, J. Magn. Magn. Mater., 316 (2007) 248-254.
68. T. Kim and M. Shima, J. Appl. Phys., 101 (2007) 09M516.
69. C. Caizer, M. Stefanescu, J. Phys. D: Appl. Phys., 35 (2002) 3035-3040.
70. C. Caizer, Mater Sci. Eng. B, 100 (2003) 63-68.
71. G. Zhen, B. W. Muir, B. A. Moffat, P. Harbour, K. S. Murray, B. Moubaraki, K. Suzuki, I. Madsen, N. Agron-Olshina, L. Waddington, P. Mulvaney and P. G. Hartley, J. Phys. Chem. C, 115 (2011) 327-334.
72. J. M. D. Coey, Phys. Rev. Lett., 27 (1971) 1140-1142.
73. A. E. Berkowitz, J. A. Lahut, I. S. Iacobs, L. M. Levinson and D.W. Forester, Phys. Rev. Lett., 34 (1975) 594-597.
74. S-D. Li, H. Bi, J-L. Fang, W. Zhong and Y-W. Du, Chin. Phys. Lett., 21 (2004) 737-740.
75. A. E. Berkowitz, J. A. Lahut, C. E. VanBuren, IEEE Trans. Magn., MAG-16 (1980) 184-190.
76. R. H. Kodama, A. E. Berkowitz, E. J. McNiff Jr. and S. Foner, Phys. Rev. Lett., 77 (1996) 394-397.
77. A. E. Berkowitz, R. H. Kodama, S. A. Makhlouf, F. T. Parker, F. E. Spada, E. J. McNiff Jr. and S. Foner, J. Magn. Magn. Mater., 196-197 (1999) 591-594.
78. Y-W. Jun, J-W. Seo and J. Cheon, Acc. Chem. Res., 41 (2008) 179-189.
79. F. Bloch, Z. Phys., 61 (1930) 206-219.
80. J. Wang, W. Wu, F. Zhao and G. Zhao, Appl. Phys. Lett., 98 (2011) 083107.

81. H. M. Lu, Z. H. Cao, C. L. Zhao, P. Y. Li and X. K. Meng, J. Appl. Phys., 103 (2008) 123526.
82. J. Mazo-Zuluaga, J. Restrepo and J. Mejia-Lopez, J. Phys.: Condens. Matter, 20 (2008) 195213.
83. R. H. Kodama, J. Magn. Magn. Mater., 200 (1999) 359-372.
84. S. Linderoth, L. Balcells, A. Labarta, J. Tejada, P. V. Hendriksen, S. A. Sethi, J. Magn. Magn. Mater., 124 (1993) 269-276.
85. P. V. Hendriksen, S. Linderoth, P. A. Lindgard, Phys. Rev. B, 48 (1993) 7259-7273.
86. C. Caizer, Appl. Phys. A, 80 (2005) 1745-1751.
87. C. Caizer and I. Hrianca, Ann. Phys., 12 (2003) 115-122.
88. R. V. Upadhyay, D. Srinivas and R. V. Mehta, J. Magn. Magn. Mater., 214 (2000) 105-111.
89. E. Tronc, A. Ezzir, R. Cherkaoui, C. Chaneac, M. Nogues, H. Kachkachi, D. Fiorani, A. M. Testa, J. M. Greneche and J. P. Jolivet, J. Magn. Magn. Mater., 221 (2000) 63-79.
90. L. Neel, Ann. Geophys., 5 (1949) 99-136.
91. J. Mejia-Lopez, D. Altbir and I. K. Schuller, Appl. Phys. Lett., 83 (2003) 332-334.
92. P. Langevin, Ann. Chim. Phys., 5 (1905) 70-127.
93. C. P. Bean, L. D. Livingston, J. Appl. Phys., 30 (1959) S120.
94. I. S. Jacobs, C. P. Bean, in Magnetism, vol. III, G. T. Rado and H. Suhl, Eds., Academic Press, NY, 1963.
95. C. H. Back, D. Weller, J. Heidmann, D. Mauri, D. Guarisco, E. L. Garwin and H. C. Siegmann, Phys. Rev. Lett., 81 (1998) 3251-3254.
96. L. Neel, Adv. Phys., 4 (1955) 191-243.
97. B. E. Warren, X-ray Diffraction, Dover Publications, Inc., NY, 1990.
98. M. Makarewicz, M. Podsiadly and M. Balanda, Acta Phys. Pol. A, 115 (2009) 568-571.
99. P. Boyer, D. Menard and M. Meunier, J. Appl. Phys., 112 (2012) 063910.
100. S. Zhang, J. Lee and S. Sun, The Open Surface Science Journal, 4 (2012) 26-34.

101. Q. A. Pankhurst, J. Connolly, S. K. Jones and J. Dobson, J. Phys. D: Appl. Phys., 36 (2003) R167-R181.
102. G. Cheng, D. Romero, G. T. Fraser and A.R. Hight Walker, Langmuir, 21 (2005) 12055-12059.
103. M. P. Pileni, J. Phys. Chem. B, 105 (2001) 3358-3371.
104. M. Kasture, S. Singh, P. Patel, P. A. Joy, A. A. Prabhune, C. V. Ramana, and B. L. V. Prasad, Langmuir, 23 (2007) 11409-11412.
105. B. Stahl, N. S. Gajbhiye, G. Wilde, D. Kramer, J. Ellrich, M. Ghafari, H. Hahn, H. Gleiter, J. Weiumuller, R. Würschum and P. Schlossmacher, Adv. Mater., 14 (2002) 24-27.
106. M. Giersig and M. Hilgendorff, J. Phys. D: Appl. Phys., 32 (1999) L111-L113.
107. P. Tartaj, M. P. Morales, S. Veintemillas-Verdaguer, T. Gonzalez-Carreno and C. J. Serna, J. Phys. D: Appl. Phys., 36 (2003) R182-R197.
108. Y. Kato, S. Sugimoto, K. Shinohara, N. Tezuka, T. Kagotani and K. Inomata, Mater. Trans., 43 (2002) 406-409.
109. S. J. Yan, L. Zhen, C. Y. Xu, J. T. Jiang, W. Z. Shao, L. Lu, and J. Tang, J. Appl. Phys., 109 (2011) 07A320.
110. J. R. Liu, M. Itoh, and K. Machida, Appl. Phys. Lett., 88 (2006) 062503.
111. G. S. Chaubey, C. Barcena, N. Poudyal, C. Rong, J. Gao, S. Sun and J. P. Liu, J. Am. Chem. Soc., 129 (2007) 7214-7215.
112. C. Jo, J. Lee and Y. Jang, Chem. Mater., 17 (2005) 2667-2671.
113. H. Zeng, J. Li, J. P. Liu, Z. L. Wang and S. Sun, Nature, 420 (2002) 395-397.
114. W. S. Seo, J. H. Lee, X. Sun, Y. Suzuki, D. Mann, Z. Liu, M. Terashima, P. C. Yang, M. V. McConnell, D. G. Nishimura and H. Dai, Nat. Mater., 5 (2006) 971-976.
115. N. Takano, N. Hosoda, T. Yamada and T. Osaka, J. Electrochem. Soc., 146 (1999) 1407-1411.
116. S. Behrens, H. Bonnemann, N. Matoussevitch, A. Gorschinski, E. Dinjus, W. Habicht, J. Bolle, S. Zinoveva, N. Palina, J. Hormes, H. Modrow, S. Bahr and V. Kempter, J. Phys.: Condens. Matter, 18 (2006) S2543-S2561.
117. X. G. Liu, D. Y. Geng and Z. D. Zhang, Appl. Phys. Lett., 92 (2008) 243110.

118. D. Mercier, J. C. S. Levy, G. Viau, F. Fievet-Vincent, F. Fievet, P. Toneguzzo and O. Acher, Phys. Rev. B, 62 (2000) 532-544.
119. S. Talapatra, X. Tang, M. Padi, T. Kim, R. Vajtai, G. V. S. Sastry, M. Shima, S. C. Deevi and P. M. Ajayan, J. Mater. Sci., 44 (2009) 2271-2275.
120. T. Ishihara, N. Horiuchi, T. Inoue, K. Eguchi, Y. Takita and H. Arai, J. Catal., 136 (1992) 232-241.
121. X-M. Liu, S-Y. Fu and C-J. Huang, Mater. Lett., 59 (2005) 3791-3794.
122. H. Li, J. Liao, Y. Feng, S. Yu, X. Zhang and Z. Jin, Mater. Lett., 67 (2012) 346-348.
123. K. V. P. M. Shafi, A. Gedanken and R. Prozorov, Adv. Mater., 10 (1998) 590-593.
124. J. Chatterjee, M. Bettge, Y. Haik and C. J. Chen, J. Magn. Magn. Mater., 293 (2005) 303-309.
125. C. Sun, J. S. H. Lee and M. Zhang, Adv. Drug Delivery Rev., 60 (2008) 1252-1265.
126. N. Li, C. Hu and M. Cao, Phys. Chem. Chem. Phys., 15 (2013) 7685-7689.
127. X. Liu, G. Zangari and L. Shen, J. Appl. Phys., 87 (2000) 5410-5412.
128. X. Liu, P. Evans and G. Zangari, IEEE Trans. Magn., 36 (2000) 3479-3481.
129. X. Liu and G. Zangari, J. Appl. Phys., 90 (2001) 5247-5252.
130. M. Bahgat, M-K. Paek, C-H. Park and J-J. Pak, Mater. Trans., 49 (2008) 208-214.
131. J-W. Yoon and S-B. Jung, Microelectron. Eng., 84 (2007) 2634-2639.
132. Z. Yu, P. Yang, K. Qi and R. Li, Rare Metal Mat. Eng., 37 (2008) 2118-2121.
133. K. Ikeda, K. Kobayashi and M. Fujimoto, J. Appl. Phys., 92 (2002) 5395-5400.
134. R. Ramprasad, P. Zurcher, M. Petras, M. Miller and P. Renaud, J. Appl. Phys., 96 (2004) 519-529.
135. S. K. Vajpai, R. K. Dube and A. Tewari, Metall. Mater. Trans. A, 39A (2008) 2725-2735.
136. H. Greve, C. Pochstein, H. Takele, V. Zaporojtchenko, F. Faupel, A. Gerber, M. Frommberger and E. Quandt, Appl. Phys. Lett., 89 (2006) 242501.
137. E. Jartych, J. Magn. Magn. Mater., 323 (2011) 209-216.
138. J. M. D. Coey, Eds., Rare-Earth Iron Permanent Magnets, Clarendon Press, Oxford, UK, 1996.

139. D. Weller, A. Moser, L. Folks, M. E. Best, W. Lee, M. F. Toney, M. Schwickert, J-U. Thiele and M. F. Doerner, IEEE Trans. Magn., 36 (2000) 10-15.
140. I. Zafiropoulou, V. Tzitzios, D. Petridis, E. Devlin, J. Fidler, S. Hoefinger and D. Niarchos, Nanotechnology, 16 (2005) 1603-1607.
141. J. C. Park and H. Song, Nano. Res., 4, (2011) 33-49.
142. M. Tadic, D. Markovic, V. Spasojevic, V. Kusigerski, M. Remskar, J. Pirnat and Z. Jaglicic, J. Alloys Compd., 441, (2007) 291-296.
143. C-M. Yang, P-H. Liu, Y-F. Ho, C-Y. Chiu and K-J. Chao, Chem. Mater., 15 (2003) 275-280.
144. M. Wu, Y. D. Zhang, S. Hui, T. D. Xiao, S. Ge, W. A. Hines, J. I. Budnick and M. J. Yacaman, J. Appl. Phys., 92 (2002) 6809-6812.
145. A. G. Boudjahem, S. Monteverdi, M. Mercy and M. M. Bettahar, J. Catal., 221, (2004) 325-334.
146. L. Li, P. Lu, Y. Yao and W. Ji, Catal. Commun., 26 (2012) 72-77.
147. A. Hutten, D. Sudfeld, I. Ennen, G. Reiss, K. Wojczykowski and P. Jutzi, J. Magn. Magn. Mater., 293 (2005) 93-101.
148. T. Lutz, C. Estournes and J. L. Guille, J. Sol-Gel Sci. Technol., 13 (1998) 929-932.
149. C. de Julian Fernandez, C. Sangregorio, G. Mattei, C. Maurizio, G. Battaglin, F. Gonella, A. Lascialfari, S. Lo Russo, D. Gatteschi, P. Mazzoldi, J. M. Gonzalez and F. D. Acapito, Nucl. Instrum. Methods Phys. Res. B, 175-177 (2001) 479-484.
150. G. Ennas, A. Falqui, S. Marras, C. Sangregorio and G. Marongiu, Chem. Mater., 16 (2004) 5659-5663.
151. G. Mattei, C. de Julian Fernandez, P. Mazzoldi, C. Sada, G. De, G. Battaglin, C. Sangregorio and D. Gatteschi, Chem. Mater., 14 (2002) 3440-3447.
152. I. M. L. Billas, A. Chatelain and W. A. de Heer, J. Magn. Magn. Mater., 168 (1997) 64-84.
153. J. L. Dormann, D. Fiorani and E. Tronc, Adv. Chem. Phys., 98 (1997) 283-494.
154. A. Casu, M. F. Casula, A. Corrias, A. Falqui, D. Loche, S. Marras and C. Sangregorio, Phys. Chem. Chem. Phys., 10 (2008) 1043-1052.
155. G. Ennas, G. Marongiu, S. Maras and G. Piccaluga, J. Nanopart. Res., 6 (2004) 99-105.

CHAPTER II

Materials synthesis and characterization techniques

2.1 Synthesis methodology

The nanocrystalline magnetic metals and alloys under this thesis work were synthesized by novel or modified chemical synthetic strategies using reducing agents such as: sodium borohydride, superhydride and polyol. The typical synthetic approaches have been described below.

2.1.1 Sodium borohydride reduction method

This methodology was used to synthesize Fe, Co, Ni nanoparticles as well as Fe_xNi_{80-x}-Co_{20} ternary alloy nanoparticles (x = 0.2, 0.3, 0.4, 0.5). As this synthesis was carried out in air atmosphere, oxidation of metal nanoparticles was observed at pH above 6.5 during the reaction. This is because of the nanoparticle surface being highly reactive with hydroxyl ions at pH above 6.82 [1]. To prevent this oxidation, the reactions have been carried out at pH below 6.5 by using 1 M HCl. Also the nanomaterials were capped by polyethylene glycol (PEG) properly. For the synthesis of air stable nanomaterials in aqueous medium, the new modified methodology has been reported with reference to previously reported sodium borohydride route [2]. During modifications of synthetic strategies, the parameters such as concentrations of metal ions and reducing agent, pH of reaction mixture and PEG capping, were controlled appropriately. A schematic representation of experimental methodology is shown in Figure 2.1. In step 1, stoichiometric amount metal salts were charged in 500 mL capacity round bottom flask and added 1 M HCl for dissolution. Concentration total metal ions present in reaction bath were maintained around 0.1 M. Temperature of the reaction mixture was kept around 25-30°C. In step 2, reducing agent (1 M aq. $NaBH_4$ solution) was added to reduce metal ions. Reaction mixture changes into black color dispersion, indicating the formation of metal/alloy nanoparticles takes place. Finally in step 3, solids were separated by filtration, washed with water and subjected to capping with PEG-200. After capping, samples were dried at room temperature (RT) and subjected to annealing at 600°C under high purity N_2(g) flow for 2h.

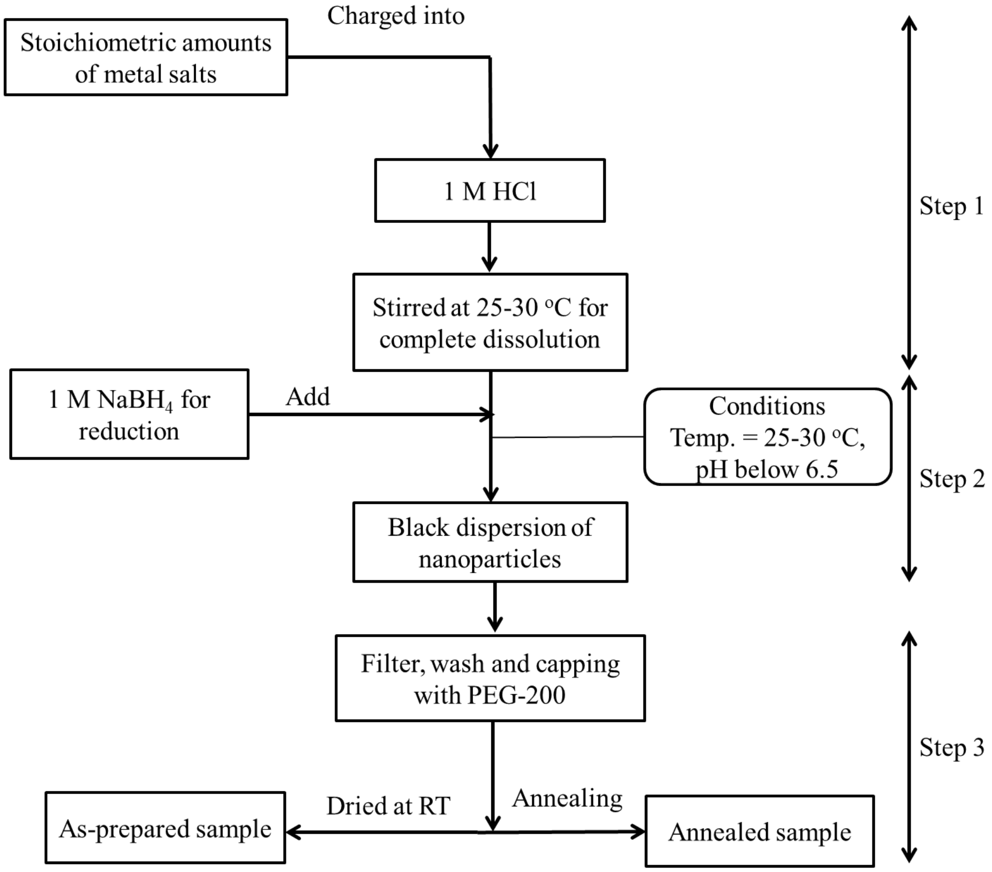

Figure 2.1 Schematic representation of modified sodium borohydride reduction method.

2.1.2 Superhydride reduction method

(a) Synthesis of metal/alloy nanoparticles:

This methodology was used to synthesize Co, Ni, Fe_xCo_{1-x} (x = 0.2, 0.4, 0.6, 0.8), Co_xNi_{1-x} (x = 0.2, 0.4, 0.6, 0.8), Fe-Pt, and Co-Pt etc. The superhydride reduction process is well known in order to prepare nano-meter sized particles of transition metal/alloys with controlled size and shape morphologies [3-4]. The resulting controlled size and shape may be obtained by using different concentrations of metal ions in organic solvents along with the suitable capping agents. The modifications were applied to previously reported superhydride reduction method [4] to achieve above mentioned properties in the materials. A schematic representation of modified experimental steps is shown in Figure 2.2. In step 1, stoichiometric amounts metal salts were charged into 250 mL capacity round bottom flask containing 25 mL diphenyl ether. High purity N_2(g) was purged for 2 h to keep inert atmosphere. Then, mixture was heated to 100°C and capping agents were added. In step 2, reduction was carried out at 200°C by addition of superhydride solution (Lithium triethylborohydride, 1 M in THF). Solution was turns into black color indication formation of metal/alloy nanoparticles. Reaction mixture was stirred at 200°C for 30 min followed by heating to 240°C for 30 min in order to get uniform growth of nanocrystals. In step 3, reaction mixture cooled to RT, products were separated by centrifugation, washed with ethanol. Solids were dried at RT for as-prepared samples and annealed at 400-600°C under N_2(g) flow.

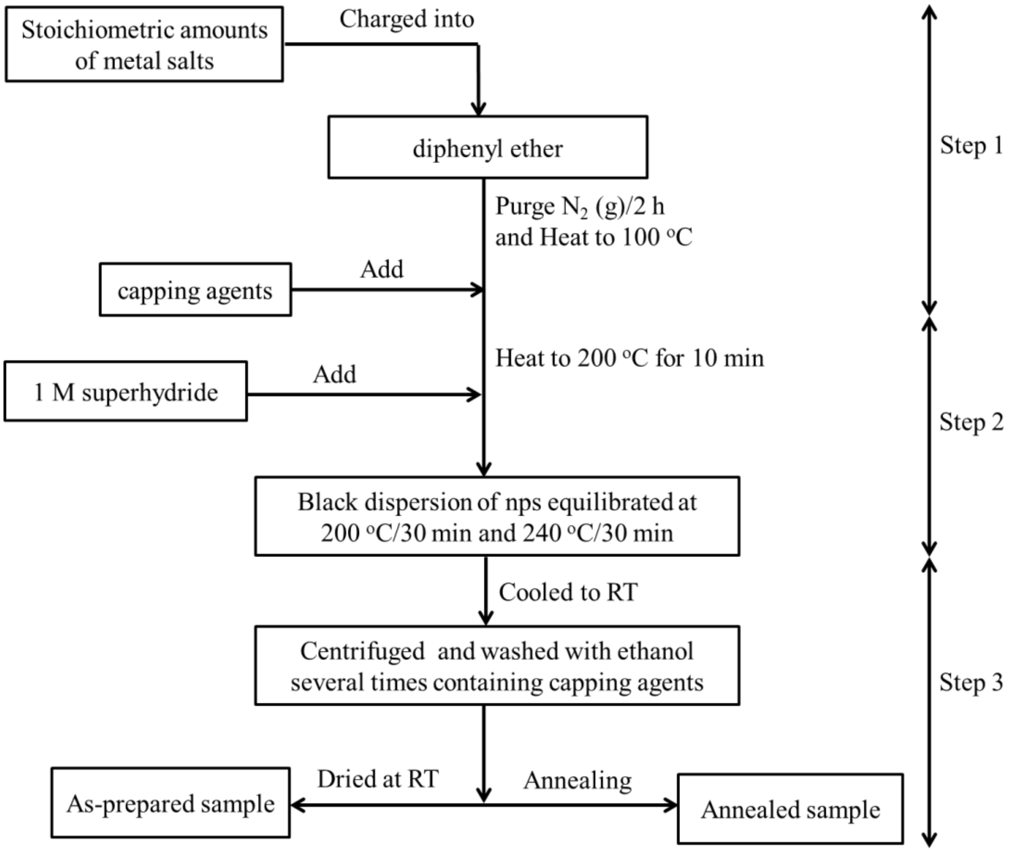

Figure 2.2 Schematic representation of modified superhydride reduction method.

(b) Synthesis of Ni and CoNi nanoparticles dispersed in silica matrix:

For the synthesis of Ni and CoNi alloy nanoparticles dispersed in silica matrix (KIT-6) with various loading wt% (4-12 wt%), the superhydride reduction method has been used with oleic acid and oleylamine as capping agents. The chemicals and experimental procedure were similar to superhydride reduction method. Additional changes in synthetic procedure are described as follows. Firstly, mesoporous silica matrix (KIT-6) was prepared as per the literature reported procedure [5] for obtaining cubically ordered phase. In a typical synthesis batch with tetraethoxysilane (TEOS), 6.5 g of Pluronic P123 (EO20PO70EO20, MW = 5800) was dissolved in 250 g of distilled water and added 13 g of conc. HCl (35 %). Then, 6.5 g of n-Butanol was added under stirring at 35°C. After 1 h stirring, 14.5 g of TEOS was added at 35°C. The mixture was stirred for 24 h at 35°C. The solid product was filtered and dried at 100°C without washing followed by calcination at 550°C for 6 h in order to get KIT-6 matrix as starting materials for further synthesis.

2.1.3 Polyol reduction method

This methodology was used to synthesize Co, $Co_{50}Ni_{50}$ and $Co_{50}Pt_{50}$ etc. The previously reported polyol reduction methods use polyol (e.g. ethylene glycol, 1,2-propanediol etc.) as both solvent and reducing agents without any capping agents [6, 7]. Further, a report was found on usage of diphenyl ether as solvent and reduction was carried out by 2 mL PEG-200 at 150°C [8]. But, diphenyl ether has limited solubility for various capping agents, e.g. polyvinylpyrrolidone (PVP). In this work, polyol method was modified by introducing N, N dimethyl formamide (DMF) which can be used for capping agents such as PVP. A schematic representation of modified experimental steps is shown in Figure 2.3. In step 1, stoichiometric amount metal salts were charged in 250 mL capacity round bottom flask containing and 20 mL DMF. Solution was stirred up to complete dissolution of salts. Appropriate amount PVP as capping agent and PEG-200 as reducing agent were added in above solution and heated to 100-110°C for 5 min. In step 2, reduction was achieved by addition of NaOH pellets. Solution turns into black color which indicates formation of metal/alloy nanoparticles. Solution was maintained at 100-110°C for 15 min. There is formation of NaCl takes place along with product. In step 3, reaction mixture cooled to RT and added acetone for precipitation. Products were separated by centrifugation. For as-prepared materials, solids washed with distilled water to remove excess NaOH and NaCl. Further, annealing of the materials was done by two routes. In annealing route-1, as-prepared materials were annealed at 600°C for 6 h (i.e. without NaCl matrix). And in annealing route-2, solids obtained after centrifugation were annealed at 600°C for 6 h (i.e. with NaCl matrix) and then washed with water.

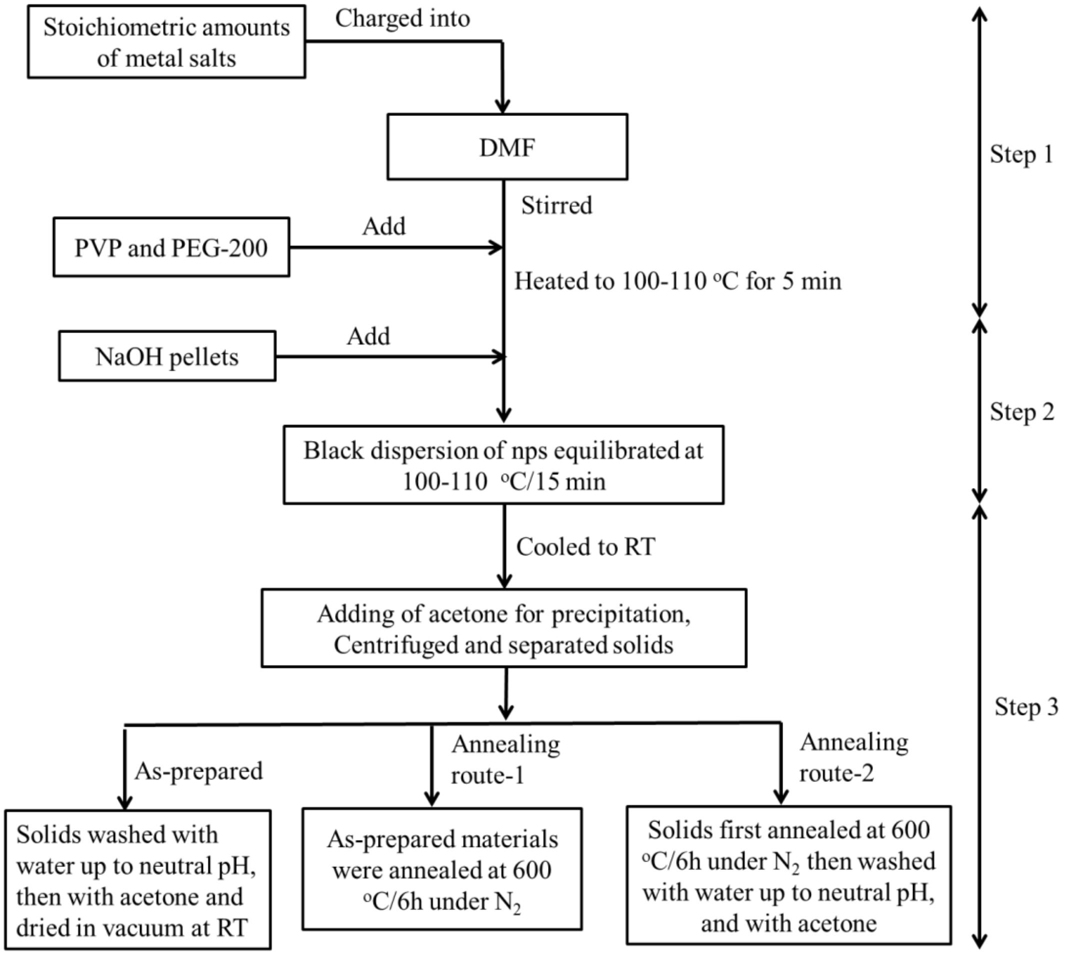

Figure 2.3 Schematic representation of modified polyol reduction method.

2.2 Materials processing: Heat treatments in N_2(g) atmosphere

Materials processing involved in this research work is the annealing of synthesized materials or as-prepared materials at various temperatures (400-600°C) under the flow of high purity N_2(g). Typical experimental setup for annealing is shown in Figure 2.4. Sample was taken in an alumina boat and kept at the middle position of the quartz tube. High purity N_2(g) was passed through quartz tube for 4 h to create inert atmosphere. Annealing temperature, heating rate, holding time and cooling rate were adjusted in programmed controller. After running temperature program, annealed sample was removed at RT.

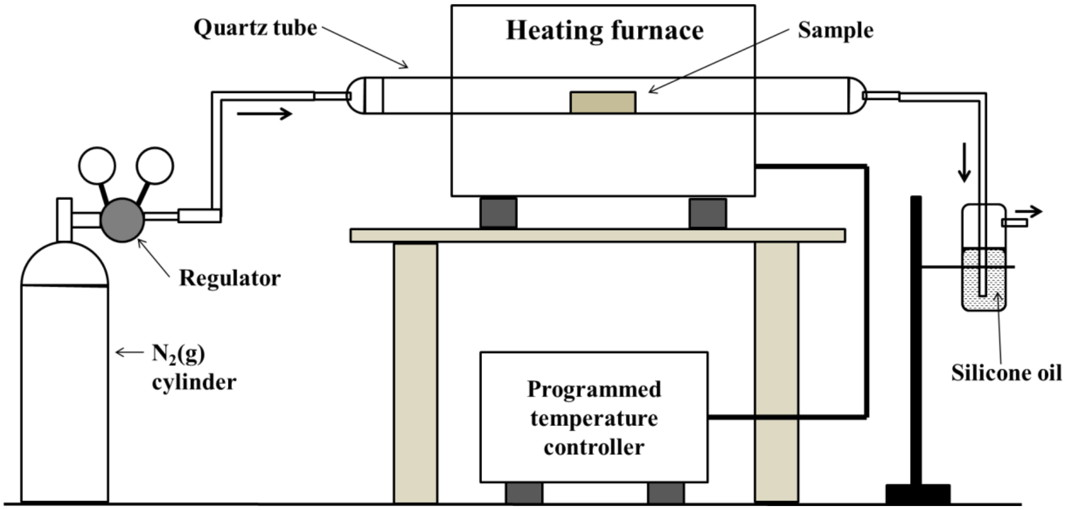

Figure 2.4 Block diagram representing setup for annealing in inert gas flow atmosphere.

2.3 Elemental analysis and sorption studies of nanomaterials

The syntheses of nanomaterials in this study involve stabilization of nanoparticles by using various capping agents such as: PEG-200, PVP, oleic acid, oleylamine, CTAB etc. The presence of capping agents on the surface of nanomaterials (i.e. as-prepared as well as annealed) was confirmed with the help of suitable analysis methods as described below. Further, distribution of metal/alloy nanoparticles in silica matrix was confirmed with the help of Electron micrographs and BET surface area analysis method more appropriately.

2.3.1 Chemical analysis

Selected elements in the materials used in this research work were subjected to chemical analysis as per technical requirements. In specific, elements such as Fe and Ni present in the materials have been analyzed quantitatively using conventional chemical methods [9]. For analysis of Fe, Fe from the sample converted to Fe (III) ions. These ions form deep-colored complex with salicylic acid. The complex was spectrophotometrically titrated with standard ethylenediaminetetraacetic acid (EDTA) solution at pH ~2.4. At end point, color of solution disappears due to formation of Fe-EDTA stable complex. Hence, from the concentration of Fe, one can calculate the amount of Fe in the sample. Ni can be analyzed gravimetrically by precipitating Ni in the form of Ni-DMG complex. Acidic solution of Ni salt was heated to 70-80°C. Excess amount of ethanolic solution of dimethylglyoxime (DMG) was added followed by immediate addition of dilute ammonia solution to form Ni-DMG red precipitate. This precipitate was filtered through sintered glass crucible, washed with cold water to dissolve chlorides and dried at 120°C. The amount of Ni in the sample can be calculated by measuring the weight of the Ni-DMG complex.

2.3.2 CHNS elemental analyzer

The presences of C, H, N and S in selected samples were confirmed by CHNS elemental analyzer (Model: Elementar, Vario Micro cube, Germany) which gives the weight percentage of C, H, N and S elements present in the materials. The basic principle lies in the fact that the elements, i.e. C, N, H and S of the samples are converted to their corresponding oxides by purging O_2(g) at 1150°C. Further N-oxides are reduced to N_2(g) at 850°C. The evolved gases are passed through the separating chamber and separated at different temperatures. Detector will detect each gas separately to produce elemental analysis results. The capping agents used in the synthesis have definite percentage of C, H, N and S. The results thus obtained from the elemental analyzer can be used for analysis of organic matter present at the surface of nanomaterials.

2.3.3 UV-Visible spectroscopy

The reactions in which color change occurred after reduction can be monitored by using UV-Visible spectroscopy technique (Model: JASCO, V-570, Japan). It is based on the principle that compounds containing π-electrons or non-bonding electrons (n-electrons) can absorb or reflect UV-visible light (wavelength range ~ 200-800 nm) due to electronic transitions from ground state to excited state. The basic instrumental arrangement includes the light source, sample holder and detector which measure intensity of transmitted light. The absorption of UV and visible light by compounds obeys Beer-Lambert law which states that the absorbance of a solution is directly proportional to the concentration of the absorbing compound in the solution and the path length. Resulting spectrum shows absorption peaks at different wavelengths correspond to particular electronic transitions. UV-Visible spectroscopy of solid samples in the form of pellet can be studied by measuring reflectance as a function of wavelength.

2.3.4 FTIR spectroscopy

FTIR spectra of materials were recorded using FTIR spectrophotometer (Model: SHIMADZU, IRAffinity-1, Japan) in order to analyze organic coating on the surface. For solid samples, KBr pellet containing sample (concentration < 10%) was prepared and liquid samples were done using attenuated total reflection (ATR) cell. The chemical bonds in a molecule vibrate with particular vibrational frequency. In FTIR spectroscopy, radiations from infrared (IR) region (wavenumber ~ 400-4000 cm^{-1}) are absorbed by bonds when the IR frequency matches with vibrational frequency of the bond and there is change in dipole moment of a molecule. Each functional group or bond in the compound absorbs IR radiations of particular frequency expressed in wavenumber (cm^{-1}). In a FTIR spectrum, peaks at various wavenumbers correspond to functional groups or chemical bonds present in the capping material. After comparing positions of peak obtained in FTIR spectrum of sample with standard values, one can confirm the presence of particular capping agents or its compound qualitatively.

2.3.5 BET surface area analysis

Nitrogen adsorption-desorption experiments were carried out using surface area analyzer (Model: Micromeritics, Gemini VII, USA). Initially samples were outgassed (or activated) by heating to 150-250°C for 3h in high purity He(g) atmosphere. The amount of gas adsorbed was measured by volumetric method at various relative pressures (P/P^o) and adsorption curve was obtained with point-by-point data. Similarly, desorption curve can also be obtained while reducing the gas pressure. Assuming the formation close packed monolayer of N_2(g) at 77 K with molecular cross-sectional area of 0.162 nm^2, the BET surface area, pore volumes and pore sizes were determined. The BET surface area studies were done in order to calculate surface areas, pore volumes and pore sizes distribution of pure silica matrix (KIT-6) as well as metal/alloy loaded silica matrix.

2.4 Instrumental characterization techniques

The crystal structure, microstructure, size, shape, and magnetic properties of the nanomaterials were determined by using following instrumental techniques.

2.4.1 X-ray diffraction (XRD)

(i) Basic components of XRD instrument

XRD patterns were recorded on powder X-ray diffractometer (Model: Rigaku, Mini Flex II, Japan). Typical block diagram for XRD instrument is shown in Figure 2.5.

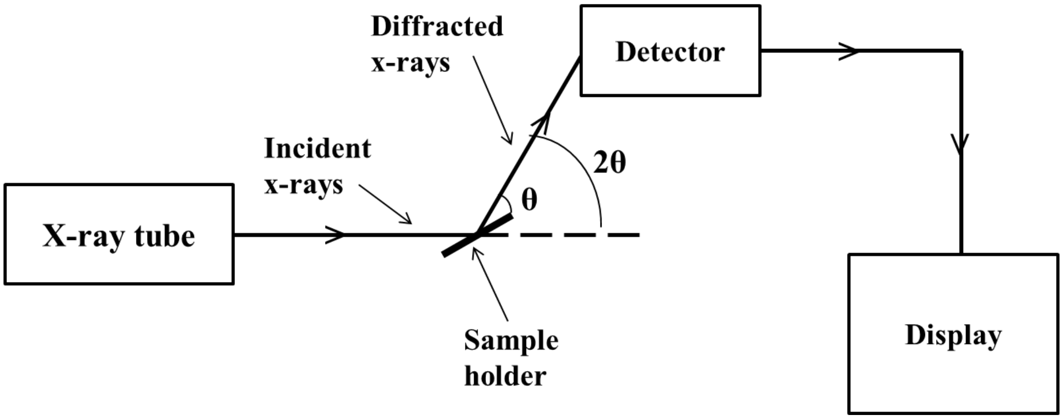

Figure 2.5 Block diagram representing various components of powder XRD diffractometer.

X-ray tube produces X-rays by bombarding a beam of high energetic electrons to a metal target in an evacuated tube. These energetic electrons excite the target atoms and then return back to ground state by emitting high frequency electromagnetic i.e. X-rays. The emitted X-rays are the characteristic of the target metal. For example, the most widely used target metals are Cu and Mo. For Cu as a target metal, the resulting beam is passed through Ni filter which absorbs K_{β} X-rays and passes the $K_{\alpha1}$ and $K_{\alpha2}$ X-rays with wavelengths (λ) of 1.5405 Å and 1.5443 Å respectively [10]. For the calculation, the value of λ for X-rays is taken as 1.5405 Å. These X-rays (incident X-rays) fall on the sample place on sample holder. X-rays get diffracted by the atomic planes of sample in an angle 'θ' to the sample and 2θ with respect to incident X-rays. Diffracted X-rays are collected in the detector system at various diffraction angles. The measured diffraction intensities as a function of 2θ will be displayed on the screen of computer.

(ii) Bragg's law

When a material is irradiated with X-rays, they will be diffracted from the atomic planes in the crystalline materials. These diffracted X-rays form constructive interference in particular directions based upon the type of crystal structure and show diffraction peak in the XRD pattern. The condition for constructive interference is that the diffracted X-rays should obey Bragg's law [10].

$$2d_{hkl}\ \sin\theta = n\lambda \tag{2.1}$$

Where λ is the wavelength of the X-ray beam, d_{hkl} is the spacing between the (hkl) crystallographic planes contributing to the diffraction peak, θ is the angle of diffraction, and n is an order of diffraction (usually, n=1). If the materials do not obey Bragg conditions then the interference will be non-constructive and will show low intensity diffraction peaks.

(iii) Analysis of XRD pattern

The phase purity of the synthesized materials can be analyzed by XRD studies. Crystalline materials have sharp diffraction lines in their XRD patterns due to ordered atomic arrangements while amorphous materials have more diffuse diffraction lines due to a lack of atom-to-atom long range ordering. The typical XRD patterns for amorphous and crystalline materials (Fe_3O_4 and Ni mixture) are represented in Figure 2.6.

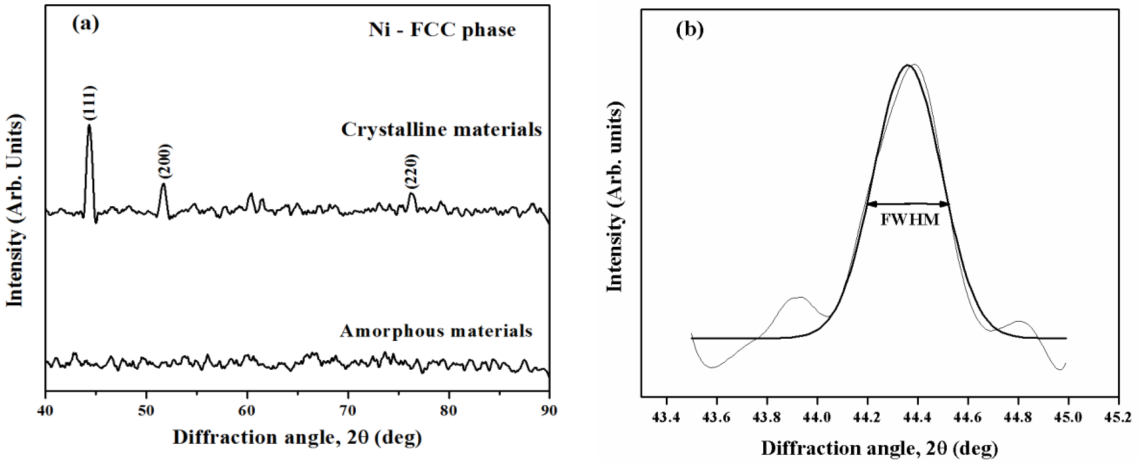

Figure 2.6 (a) Typical (arbitrary sketch) XRD patterns for amorphous and crystalline materials. (b) Single peak fitting for calculation of FWHM [10].

X-ray diffraction peaks were found to be broadening with decreasing crystallite size. This fact can be used for calculation of crystallite size of the materials. Peak broadening due to crystallite size varies inversely with crystallite size. The crystallite size (t) can be calculated by Scherrer equation,

$$t = \frac{K'\lambda}{B\cos\theta} \tag{2.2}$$

where, B refers to the full width at half maximum (FWHM) of the diffraction peak in radian, K′ is the shape factor (K′ = 0.9 for spherical particles with cubic symmetry), λ is the wavelength of X-rays irradiation and θ is half the diffraction angle. There are also some other factors that are responsible for broadening of diffraction lines. For example, instrumental broadening, microstrain (lattice strain), crystallite size and temperature are a few factors.

The broadening due to crystallites is most pronounced at large diffraction angles (2θ); however, lattice strain and instrumental broadening are significantly larger at a larger 2θ. Also, peak intensity is usually weak at larger 2θ. Hence, crystallite size is calculated more accurately by considering diffraction peaks at 2θ values between 20° to 50° [11].

2.4.2 Transmission electron microscopy (TEM)

(i) Basic components of TEM

TEM measurements were carried out on PHILIPS CM200 (USA) microscope. In transmission electron microscopy, electrons are used as source of radiation. These electrons were accelerated and focused by using electromagnetic lenses and apertures. Next, they interact with sample and form image on a fluorescent screen or CCD camera. Typically, a TEM can be divided into three primary components namely the electron source, the electromagnetic lenses with apertures and the projection chamber [12]. Typical block diagram for TEM microscope is presented in Figure 2.7.

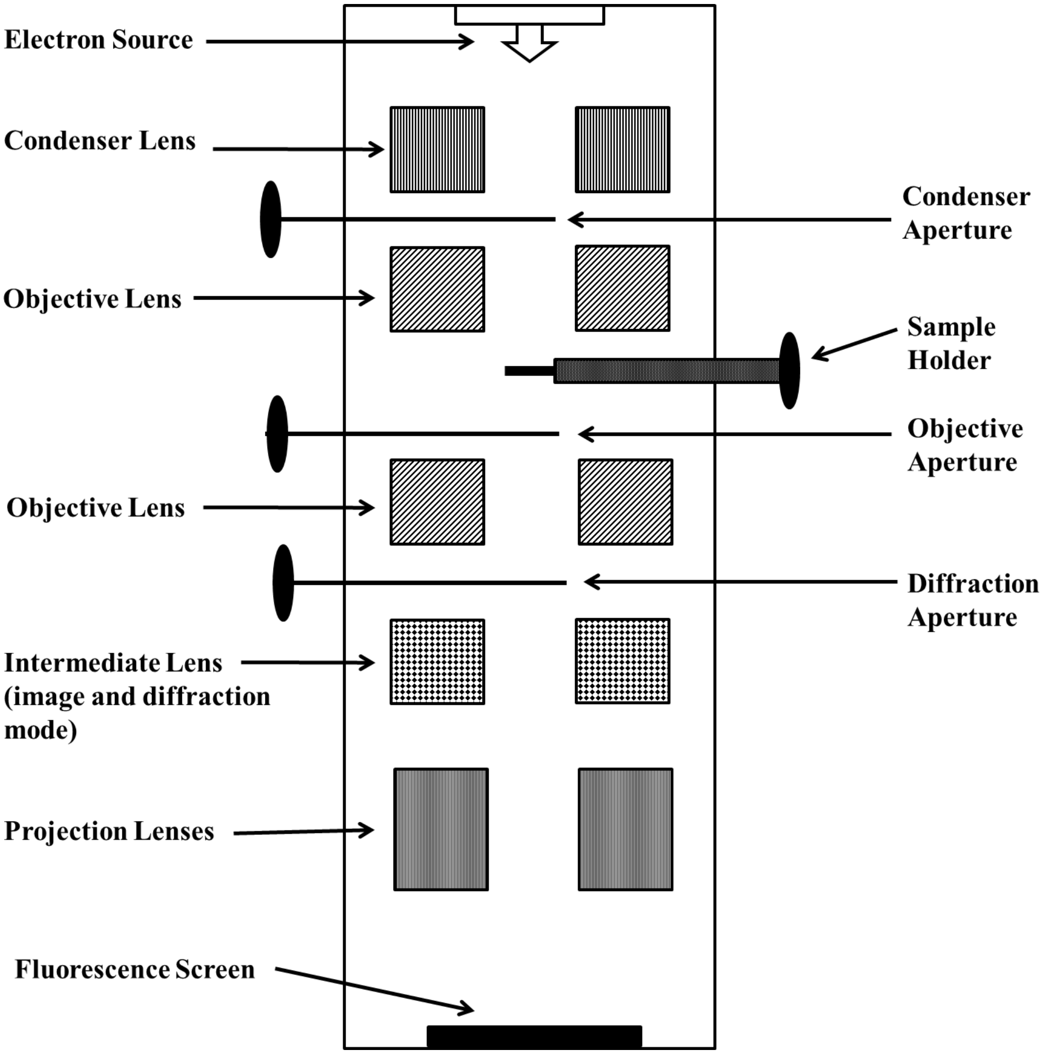

Figure 2.7 Typical block diagram showing various components in TEM microscope.

The electron source produces electrons by either thermionic emission or field emission process at cathode. The electrons from cathode are pulled away by an extraction anode and accelerated down the microscope column by acceleration anode which is at 100-300 kV higher than the extraction anode. For better electron beam, TEM microscopes are kept under a very high vacuum 10^{-4}-10^{-8} Pa. This electron beam pass through electromagnetic lenses which are made up of pole pieces (made by iron) and copper coil. Electrons pass through the hole or bore of electromagnetic lens subjected to magnetic field, generated by passing current in the coil, which control the focus of beam by varying magnetic field. Condenser lenses are used to control intensity or brightness of the beam and condenser aperture allows only those electrons which are in certain angles. There are two poles of objective lenses, i.e. upper and lower poles, and sample holder is situated in between them to insert sample for imaging. Upper pole helps in analyzing emitted X-rays and lower pole is used for imaging and diffraction purpose. Objective lens is used for magnifying image whereas numbers of objective apertures are used to resolve an image. The intermediate lens has two operating modes, i.e. image mode and diffraction mode. Image mode used to get image of sample while diffraction mode is used to observe selected area electron diffraction (SAED) pattern. Diffraction aperture is used for selection of area for diffraction. Projection lenses controls the final magnification and resolution of the image which is viewed on the fluorescence screen.

(ii) Sample preparation

For powder samples, the sample was dispersed in suitable solvent (water or ethanol) by sonication. A drop of stable dispersion was put on copper grid or carbon coated copper grid. Carbon coated copper grid provide support to small species in the samples such as: nanoparticles or biological species. Then a grid was dried under IR lamp to form thin layer of particles. Finally sample grid was mounted in TEM column with the help of sample holder.

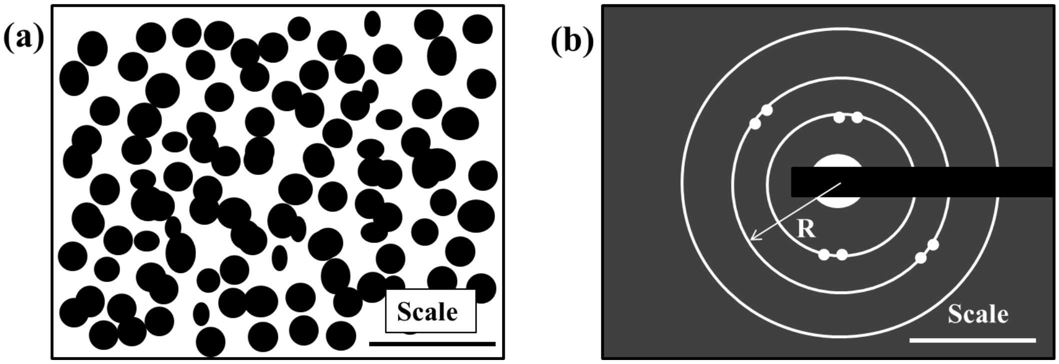

Figure 2.8 A typical representation of (a) TEM image and (b) SAED pattern for polycrystalline nanoparticles [12].

(iii) Imaging and diffraction

This sample is mounted on the sample holder and inserted in the instrument. When electron beam is irradiated on the sample, the beam interacts with electron clouds in the atoms and gets transmitted or diffracted. In transmitted beam, elastically scattered electrons are used for imaging and diffraction purpose. In-elastically scattered electrons and emitted X-rays are used for various spectroscopic techniques e.g. energy dispersive X-ray spectroscopy (EDX). Typical TEM image and SAED pattern for polycrystalline nanomaterials are shown in Figure 2.8. TEM micrograph for nanoparticles shows the distribution of particles with various sizes, also presence of any agglomerations in them (Figure 2.8(a)). SAED pattern for polycrystalline nanoparticles contains diffraction circles with bright spot at center which corresponds to direct beam (Figure 2.8(b)).

(iv) TEM data analysis

In TEM analysis of the sample, electron beam is transmitted through the sample and hence light and dark areas are visible in bright field TEM image. At the lighter areas, the material is less dense (less electron density) and more electrons have passed through. The darker areas contain the material with greater electron density and fewer electrons have been transmitted. In case of inorganic nanoparticles, TEM micrograph will show black dots dispersed in some area which are attributed to nanomaterials. The TEM particle size of the nanomaterials can be determined by using image analyzing software (e.g. Image J) whereas shape and arrangement nanoparticles can be observed from image. SAED pattern is used to determine crystal structure and lattice parameters of the sample. Similar to X-ray diffraction, electron diffraction is also results from interference of electron wave and obeys Bragg's law. In SAED pattern, intense spots (for single crystal) or rings (for polycrystalline materials) are due to constructive interference whereas dark regions form due to destructive interference. Amorphous sample does not show any diffraction pattern. In SAED pattern, each spot in case of single crystal and ring for polycrystalline material represents particular lattice plane (*hkl*). If distance of spot or ring from the center is denoted by R then d-values can be calculated by following formula,

$$d_{hkl} \approx \frac{\lambda L}{R} \tag{2.3}$$

Where, λ is the wavelength of electron beam and L is camera length.

2.4.3 Scanning electron microscopy (SEM)

(i) Basic components of SEM

SEM measurements were carried out using JEOL JSM 6390 (USA). SEM has similar functional components compared with that of TEM but the image formation takes place by secondary electrons emitted by the sample surface following excitation by the primary electron beam. Further, SEM can be extended to energy disperse X-ray microanalysis (EDX) [13]. A block diagram of SEM has been shown in Figure 2.9. The electron gun generates an electron beam of energy ranging from 0.2-40 keV. This beam can be focused with the help of two condenser lenses. Then, the beam passes through pairs of deflection coils which deflect the beam in the directions of *x* and *y* axes so that it can scan over a rectangular area of the sample surface. The magnification in SEM is controlled by voltage supplied to deflection coils. As the primary electron beam interacts with the sample, the electrons lose energy by repeated random scattering and absorption within the volume of the specimen. This volume is known as interaction volume. The size of the interaction volume depends on the electron beam energy, the atomic number and density of the specimen. This interaction produces secondary electrons and X-rays are detected in secondary electron detector and X-ray detector, respectively.

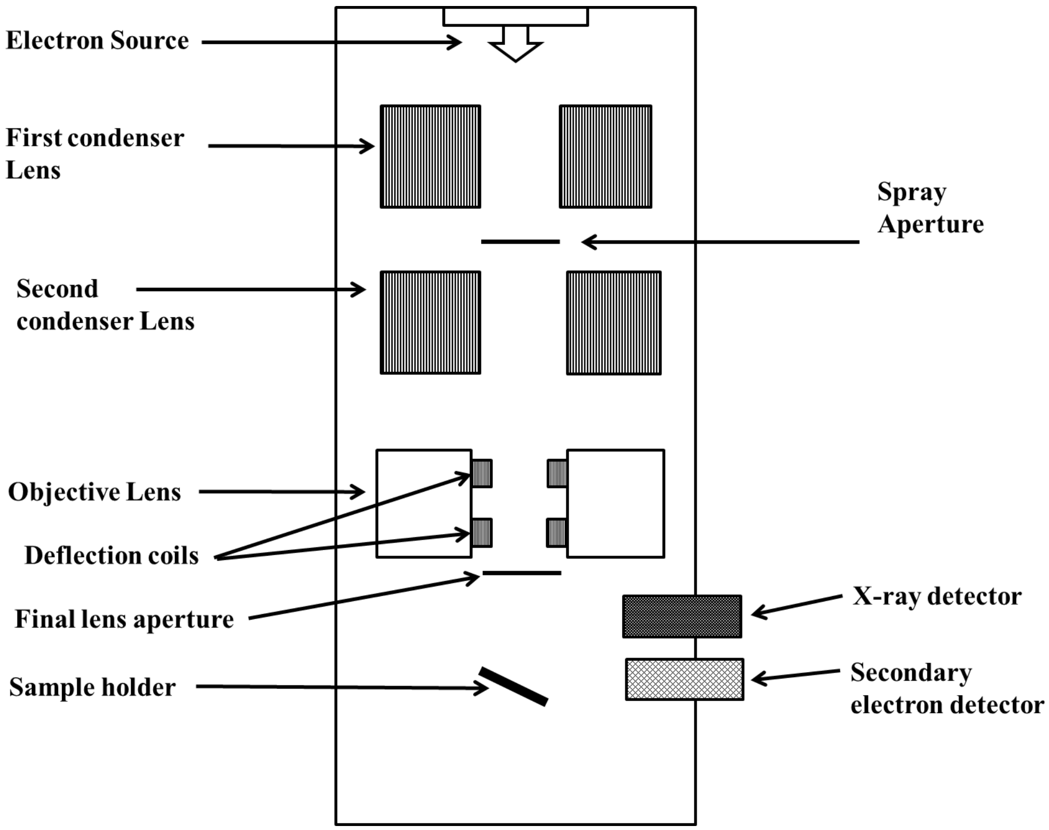

Figure 2.9 Typical block diagram of components in SEM microscope.

(ii) Sample preparation

For the samples like bulk metal piece, pellets etc., surface must be cleaned using solvents or compressed gas, dried and mounted on the holder using double-sided conductive tapes (i.e. carbon or copper tapes). In case of powder samples of nanoparticles, the finely grinded dry powder was spread on a carbon or copper tape, press lightly to hold. This carbon strip was mounted on sample holder for imaging. If the samples are less conductive then charge will building on the surface resulting in the image distortion. For elimination of such a charge effect, samples should be coated with a conductive metal (e.g. silver, gold etc.) by using sputtering coater.

(iii) Imaging in SEM and EDX

SEM images are formed by secondary electrons ejected from the surface of sample due to inelastic scattering. Although SEM images have lower resolution (2 nm, 100000X) than TEM (0.2 nm, 1000000X), SEM is better for imaging bulk samples and has a greater depth of view, giving rise to better 3D images of the sample. Typical SEM micrograph is shown in Figure 2.10(a). The energies of X-rays emitted from the surface of sample carry information about elements. These X-rays are generated in a region about few nanometers in depth and used for EDX spectroscopy technique. A typical EDX spectrum is shown in Figure 2.10(b) for the material $Co_{0.8}Ni_{0.2}$ alloy. Each element present in sample gives their corresponding peaks in EDX spectrum.

(iv) SEM and EDX data analysis

In SEM micrograph, one can identify microstructure, size and shape of nanomaterials. The SEM particle size of the nanoparticles can be determined by using image analyzing software (e.g. Image J). EDX spectroscopy uses X-rays emitted from sample and these are correlated to characteristics of the materials. A particular element emits X-rays of particular energy in keV. The chemical composition of the elements present in the sample can be analyzed by EDX spectrum.

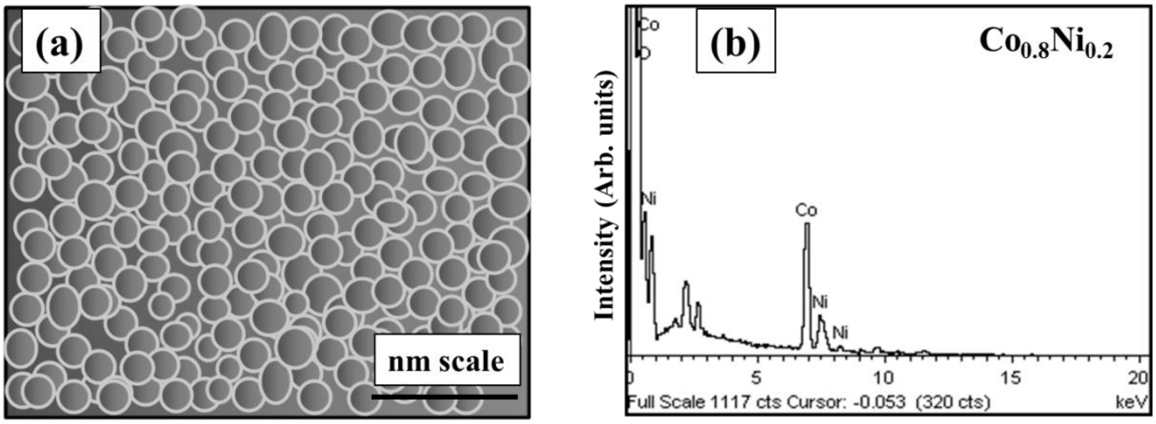

Figure 2.10 (a) Typical SEM micrograph of nanomaterials showing spherical particles and (b) EDX spectrum for $Co_{0.8}Ni_{0.2}$ alloy.

2.5 Magnetic measurements

Magnetic properties of the materials were studied using vibrating sample magnetometer (VSM), Superconducting quantum interference device (SQUID) magnetometer and Mössbauer spectroscopy. Details of instrumentation and measurement have been discussed below.

2.5.1 Basic principle and components of VSM and SQUID

(i) Basic principle and components of VSM

The magnetic measurements were performed using VSM. Depending upon sensitivity and requirements, different instrument models were used such as: ADE-EV9 (USA), Quantum Design PPMS-261(USA) and Lakeshore VSM 7410 (USA). The principle of VSM is based on the fact that the change in magnetic flux occurred in the pickup coils when the magnetic sample is vibrated between coils. The typical components of VSM are shown in Figure 2.11 [14].

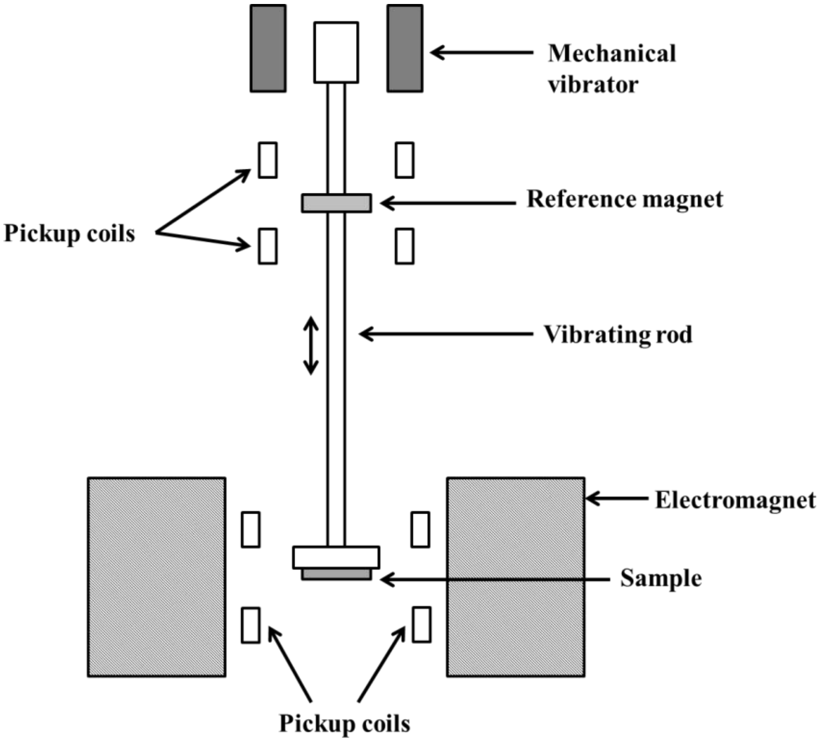

Figure 2.11 Block diagram representing components of VSM. In actual practice sample chamber is housed inside an outer chamber in vacuum/inert gas atmosphere.

The vibrating rod (non-magnetic) is attached to mechanical vibrator. Sample is attached to other end of rod which is placed in between pickup coils. Also reference magnet is attached to vibrating rod and surrounded by another set of pickup coils. Reference magnet is used to calibrate the apparatus provided it must of the similar size, shape and permeability as sample. Electromagnets are used to apply external magnetic field (H) to sample which generates magnetic field in the sample (B). As the sample vibrates, the oscillating magnetic field of sample induces an alternating electromotive force (*emf*) in the pickup coils. The *emf* thus generated is further amplified using a lock-in amplifier which specifically senses the signals at the vibrational frequency.

(ii) Basic principle and components of SQUID

SQUID magnetic measurements were performed on Quantum Design (USA) magnetometer. SQUID magnetometer also measures same magnetic parameters like VSM, but the principle of sensing magnetic field is done by superconducting coils instead of pickup coils in VSM. A sample is passed through superconducting coils separated by Josephson junction i.e. thin insulating layer. This insulating layer of 2-3 nm thickness is fabricated using aluminum oxide (Al_2O_3). The electron pairs in superconductor (Cooper pairs) can jump through the Josephson junction due to quantum tunneling effect [15]. A typical DC-SQUID is made up of two Josephson junctions (A and B) connected parallel as shown in Figure 2.12.

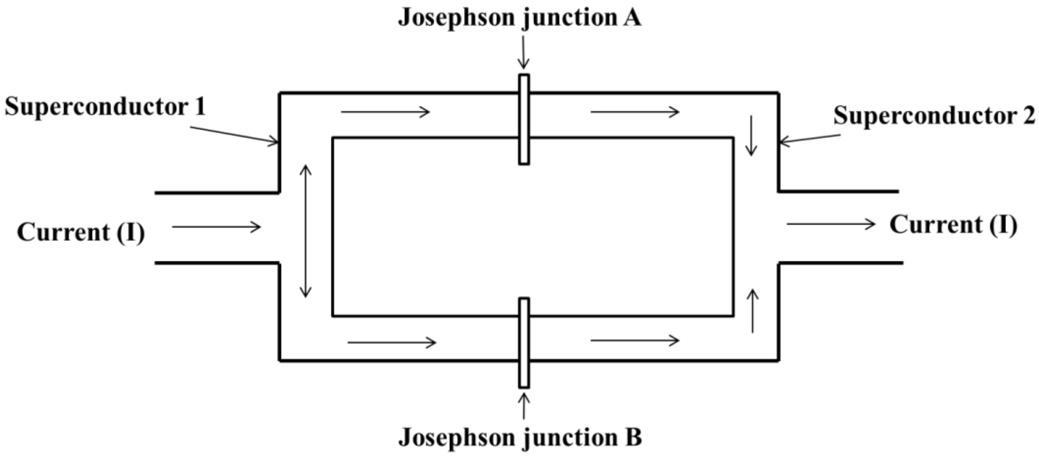

Figure 2.12 Block diagram of superconducting coil used in SQUID magnetometer.

When a current passes through superconductors without magnetic sample, Cooper pairs have weak interference (or phase shifts, δ_A and δ_B) at Josephson junctions A and B. However, as magnetic sample passes through SQUID device, there will be change in interference (or phase shift) due to magnetic flux (B) of sample. This results in the change in current (I) passing through superconducting loop and expressed as [16],

$$\mathrm{I} = 2I_0 \sin\delta_0 \cos\left(\frac{2\pi e}{h}\int B\, dS\right) \tag{2.4}$$

Where, I_0 is the initial current, δ_0 is a constant phase shift, *e* is the charge of an electron, h is Planck's constant and *S* is area of the superconducting loops. The resulting current is amplified by other coils to make final data. SQUID magnetometers have more precision and sensitivity when compared with VSM because of the superconducting coils which are having quantum level sensing.

2.5.2 Sample preparation and measurement techniques

For measurements, solid powder samples should be pelletized into cylindrical shape with dimensions of 4 mm diameter and 6 mm height using Teflon mold. In case of small quantity samples, powder were weighed and packed in Teflon tape to form cylindrical shape pellet. This sample pellet was tightly attached to vibrating rod at sample position mark using glue or Teflon tape. And magnetic measurements were carried out with appropriate instrument parameters. The VSM can be used to measure magnetization (M) generated in the materials with varying applied field (-20 kOe $< H <$ 20 kOe). The hysteresis loops (i.e. M vs. H plots) can be obtained at various temperatures ranging from lower limit of ~5 K to higher limit of ~800 K. The VSM has magnetization sensitivity up to 10^{-5} emu which corresponds to magnetization of 0.04 µg of iron and hence, VSM is applicable for both weak and strong magnetic materials. However, SQUID has more sensitivity (~10^{-8} emu) and accuracy of sensing weak signals and hence it can use for less quantity of samples or very weak magnetic moments. Temperature dependent magnetic properties of the nanomaterials, especially superparamagnetism, can be studied by measuring magnetization in the temperature range of 5-300 K (M vs. T plot). These measurements will be carried out in field cooled (FC) and zero field cooled (ZFC) conditions by applying small magnetic field (~50-500 Oe). The sample was first cooled down to 5 K in the absence of external magnetic field and then heated up to 300 K in the presence of external magnetic field and the magnetization is recorded as ZFC. The FC measurements were done after ZFC measurements and the magnetization is recorded while cooling the sample down from 300 K to 5 K with same applied field.

2.5.3 Estimation of magnetic parameters

The typical M-H plot is shown in Figure 2.13 (a). From M-H plot, one can determine the values of magnetic parameters such as: M_S, M_r, and H_C. The values of M_S of the materials can be determined by 1/H law i.e M vs. 1/H plot of H values near saturation field [17]. Then, the value of M_S is equal to the intercept on the magnetization axis of M vs. 1/H plot as shown in inset of Figure 2.13 (a). Typical M-T plot is shown in figure 2.13 (b). For SPM particles, ZFC curve shows maximum magnetization at blocking temperature, T_B. The divergence in magnetization of FC and ZFC curves below T_B is due to magnetic anisotropy energy barrier and spin relaxation. SPM particles have low anisotropy barrier and can be overcome by thermal energy (k_BT). Thermal energy causes the random flipping of the magnetic moments above T_B which results in the decrease of magnetization.

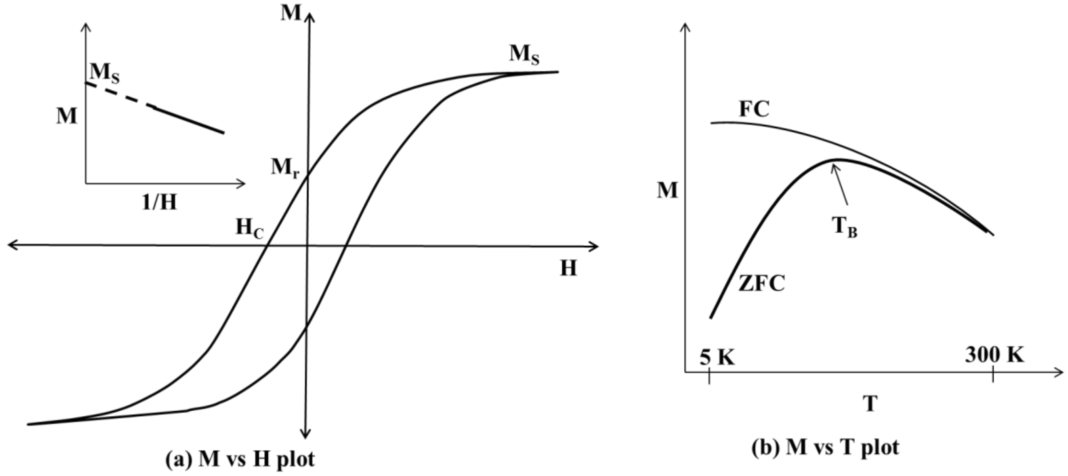

(a) M vs H plot (b) M vs T plot

Figure 2.13 Typical plots of magnetic measurements; (a) M vs. H plot and (b) M vs. T under FC/ZFC conditions, using VSM.

2.6 Mössbauer spectroscopy

Mössbauer effect was discovered by R. L. Mössbauer in 1957 and he was awarded by Nobel Prize in 1961 [18, 19]. Further, Mössbauer effect has been observed in various isotopes such as ^{57}Fe, ^{129}I, ^{119}Sn, ^{121}Sb etc. However, ^{57}Fe is most repeatedly used isotope since its discovery in 1959 [20, 21]. Mössbauer spectroscopy can be used to study electronic, magnetic, and structural properties within the materials. Mössbauer measurements in this research were carried out using ^{57}Fe isotope.

(i) Basic principle of Mössbauer spectroscopy

Mössbauer spectroscopy is based on the principle of recoil free emission and absorption of γ radiations by similar nuclei. γ rays source for ^{57}Fe is radioactive ^{57}Co ($t_{1/2}$ = 270 days) which decays to the excited state of ^{57}Fe (i.e. ^{57}Fe*) by capturing electron. ^{57}Fe* decays to stable ^{57}Fe by emission of delayed γ rays with energy of 14.4 keV which is known as γ ray fluorescence. These γ rays can be resonantly absorbed by another Fe nucleus in the crystal lattice of the sample (Figure 2.14(a)). In order to achieve resonance condition, a γ rays source subjected to Doppler motion with velocity (*v*, mm/s). The detector measures γ ray counts at various Doppler velocities and resulting plot shows absorption of γ rays at *v* = 0 for equivalent nucleus (Figure 2.14(b)).

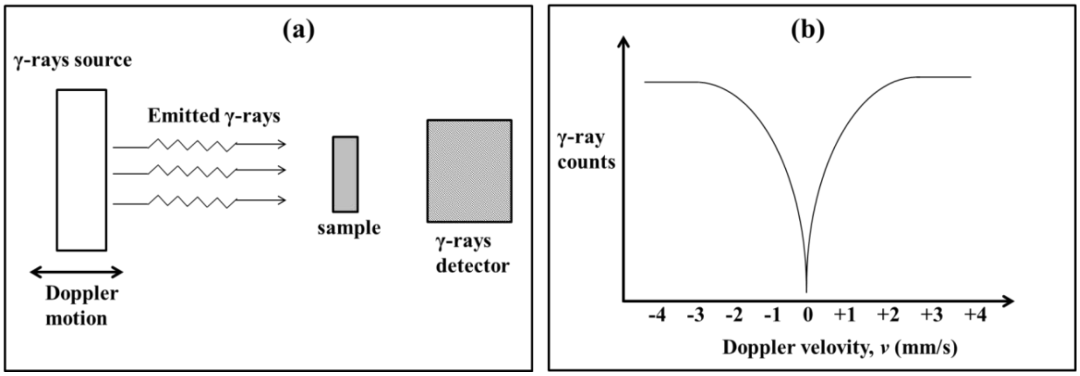

Figure 2.14 Gamma resonance in Fe nucleus; (a) Basic principle and (b) typical Mössbauer spectrum showing absorption.

(ii) Block diagram of Mössbauer spectrometer

The spectrometer used for Mössbauer study was FastCom Tech (Germany). Basic components in Mössbauer spectroscopy involves the γ rays source, sample holder and detection system as shown in Figure 2.15. Source generates γ rays of specific energy (14.4 keV of ^{57}Fe source). This energy can be tuned by moving the source in to-and-fro motion (with velocity *v*) using motor and motor controller which produces Doppler shift in γ rays energy. For example, a velocity of 10 mm/s produces an energy shift of 4.8×10^{-7} eV to a 14.4 keV γ ray of ^{57}Fe. An energy range of 10 mm/s is sufficient to tune the full Mössbauer spectrum of ^{57}Fe [22]. The γ rays fall on the sample may be absorbed or transmitted depending on energy. Transmitted γ rays are collected by detector in the detection system and converted to proper signal of γ rays counts as a function of energy. Amplifier arrangements are used to make signal more accurate and resolved. These measurements were repeated several times with fix time interval, stored in memory and supplying feedback to motor controller to maintain constant acceleration. Finally, results will be displayed on computer screen.

(iii) Effect of magnetic field in Mössbauer spectroscopy

In magnetic materials, e.g. ^{57}Fe, the nuclear states have magnetic dipole moments which can be oriented with different projections along a magnetic field. If the nucleus is in a magnetic field, the energy states of nuclear transitions split into sub-states analogous to 'nuclear Zeeman effect'. In ^{57}Fe, Zeeman splitting of the nuclear energy levels is occurred due to an internal (or a hyperfine) magnetic field in Fe. Thus the ground state (I = 1/2) splits into two levels (m_I = 1/2 and -1/2) and the excited state (I = 3/2) splits into four levels (m_I = 1/2, -1/2, 3/2 and -3/2). All these energy levels and their six allowed transitions are shown in Figure 2.16(a). Therefore, the resonance line of iron will splits into six lines, i.e. sextet (Figure 2.16(b)).

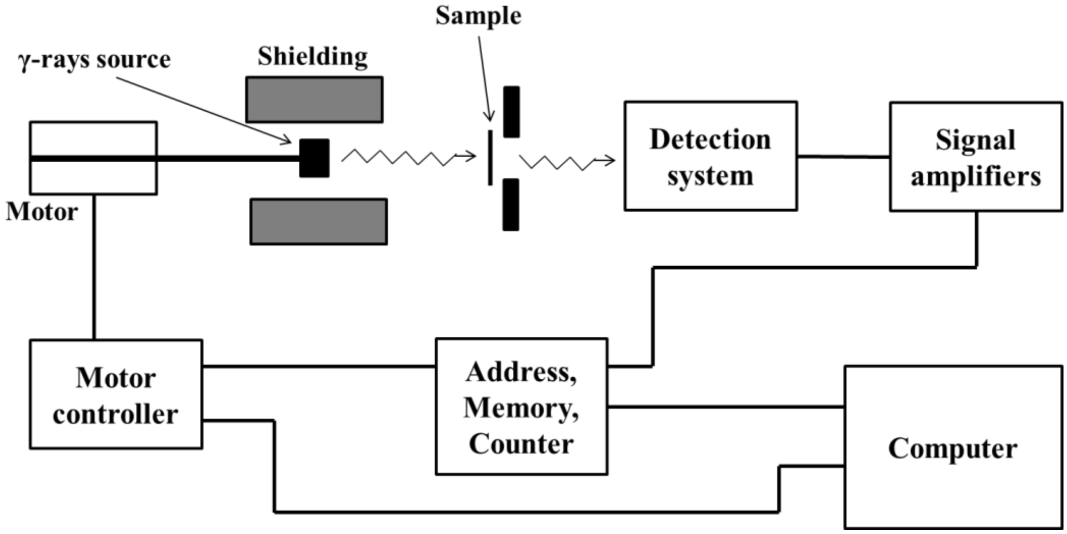

Figure 2.15 A typical block diagram representing components in Mössbauer spectrometer.

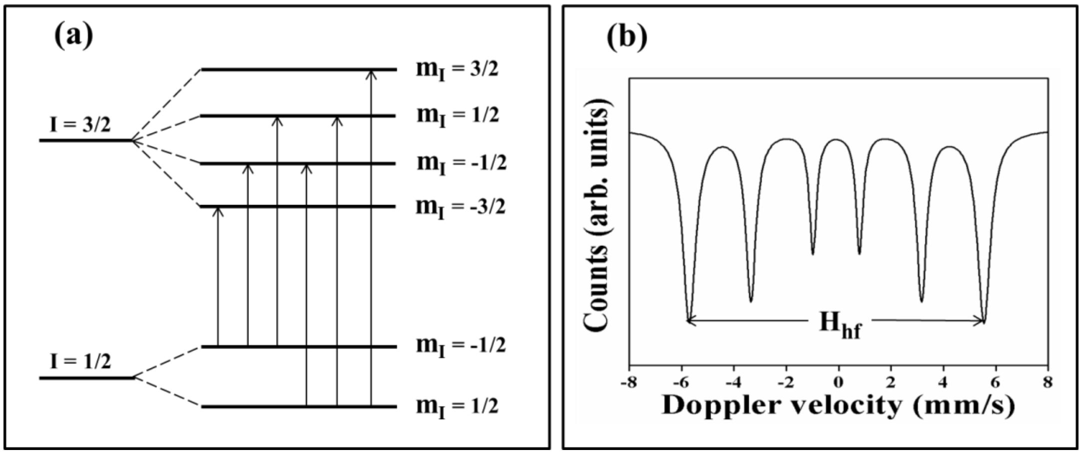

Figure 2.16 (a) Representations of the Zeeman splitting of nuclear energy levels and allowed transitions in ^{57}Fe. (b) Corresponding Mössbauer spectrum of sextet in ^{57}Fe.

(iv) Sample preparation and measurement techniques

The powder samples were packed in Mössbauer sample holder and placed perpendicular to the γ-ray beam. The Mössbauer spectra were recorded at room temperature using a constant acceleration spectrometer with a 25 mCi ^{57}Co(Rh) gamma ray source. The values of the isomer shifts were reported with respect to natural iron (Fe) foil.

(v) Estimation of Mössbauer parameters

The experimental spectrum was analyzed using the PCMOS II least-squares fitting program which gives the values of Mössbauer parameters such as: isomer shift (δ), electric quadrupole splitting (ΔE_Q), hyperfine magnetic field (H_{hf}), line width and relative intensities of the fitted sub-spectra. An isomer shift is the shift in absorption energy due to the electrostatic interactions between the nucleus and s-electron density around it. Hence, δ-values give information about valency of Fe in the sample. Quadrupole splitting in Mossbauer spectrum provides information about symmetric or asymmetric electric field gradient around nucleus. Asymmetric field gradient splits excited state energy level ($I = 3/2$) into two energy levels ($m_I = \pm3/2$ and $\pm1/2$) with energy difference of ΔE_Q while symmetric field gradient (e.g. cubic structure) shows no splitting. The values of the hyperfine field indicate Zeeman splitting of the nuclear energy levels by internal magnetic field in Fe.

References

1. A. Alqudami, S. Annapoorni, Plasmonics, 2 (2007) 5-13.
2. C. W. Kim, Y. H. Kim, H. G. Cha, H. W. Kwon and Y. S. Kang, J. Phys. Chem. B, 110 (2006) 24418-24423.
3. S. S. Parhizgar and S. A. Sebt, J. Theor. Appl. Phys., 7 (2013) 44.
4. C-M. Shen, C. Hui, T-Z. Yang, C-W. Xiao, S-T. Chen, H. Ding and H-J. Gao, Chin. Phys. Lett., 25 (2008) 1479-1481.
5. F. Kleitz, S. H. Choi and R. Ryoo, Chem. Commun., (2003) 2136-2137.
6. P. Karipoth, A. Thirumurugan and R. J. Joseyphus, J. Colloid Interface Sci., 404 (2013) 49-55.
7. B. Liu, J-G. Guan, Q. Wang and Q-J. Zhang, Mater. Trans., 46 (2005) 1865-1867.
8. V. Tzitzios, D. Niarchos, G. Margariti, J. Fidler and D. Petridis, Nanotechnology, 16 (2005) 287-291.
9. J. Mendham, R. C. Denney, J. D. Barnes, M. J. K. Thomas, Vogel's Textbook of Quantitative Chemical Analysis, 6th ed., Prentice Hall, NJ, 2000.

10. B. D. Cullity, Elements of X ray Diffraction, Addison-Wesley: Reading, MA, 1956.
11. A. Monshi, M. R. Foroughi and M. R. Monshi, World J. Nanosci. Eng., 2 (2012) 154-160.
12. P. J. Goodhew, J. Humphreys, R. Beanland, Electron Microscopy and Analysis, 3rd ed., Taylor & Francis, UK, 2001.
13. J. I. Goldstein, D. E. Newbury, P. Echlin, D. C. Joy, C. E. Lyman, E. Lifshin, L. Sawyer and J. R. Michael, Scanning Electron Microscopy and X-ray Microanalysis. 3rd ed., Springer, NY, 2003.
14. B. D. Cullity and C. D. Graham, Introduction to Magnetic Materials, 2nd ed., John Wiley & Sons, NJ, 2009.
15. M. G. Castellano, Fortschr. Phys., 51 (2003) 288-294.
16. H. Ibach and H. Luth, Solid-State Physics: An Introduction to Principles of Materials Science, 4th ed., Springer, NY, 2009.
17. C. P. Bean and I. S. Jacobs, J. Appl. Phys., 31 (1960) 1228-1230.
18. R. L. Mössbauer, Z. Physik, 151 (1958) 124-143.
19. http://www.nobelprize.org/nobel_prizes/physics/laureates/1961/mossbauer-lecture.pdf
20. R. V. Pound and G. A. Rebka, Jr., Phys. Rev. Lett., 3 (1959) 554-556.
21. J. P. Schiffer and W. Marshall, Phys. Rev. Lett., 3 (1959) 556-557.
22. B. Fultz, Mössbauer Spectrometry, in Characterization of Materials, E. Kaufmann, Eds., John Wiley & Sons, NY, 2011.

CHAPTER III

Magnetic properties of Fe, Co, Ni and Fe-Ni-Co nanoparticles synthesized via $NaBH_4$ route in aqueous medium

3.1 Introduction

The magnetic behavior of fine particles is of considerable interest both from a scientific and practical point of view [1, 2]. Fine particle magnetism involves both size effect and surface effect. In such kind of particles, thermal energy, k_BT, plays an important role in magnetic characteristics. The magnetic parameters such as M_S, H_C, T_C etc. changes with alteration of particle dimensions. Several reports have been established in the literature on fine particle magnetic properties [3-5]. The decrease in the M_S values of nanoclusters when compared with the bulk values with decreasing size is a consequence of fluctuations due to thermal and rotational effects (also known as size and surface effects). Fine particles in the form of core-shell structures, variations in the H_C values can be observed due to interactions between core, interface and surface anisotropies.

The synthesis, characterization and application of ferromagnetic metal nanoparticles and their alloys has attracted a great deal of attention due to their potential technological applications [6, 7]. Magnetic nanoparticles with 2-20 nm size have applications in the high density magnetic storage devices, ferrofluids, magnetic refrigeration systems, and contrast agents in magnetic resonance imaging, magnetic carriers for drug targeting and catalysis [6]. Further, nanostructure magnetic materials with controllable size, shape and morphology (e.g. core-shell, composites etc.) have large applications in above mentioned fields [7]. The recent interest lies on the iron group alloys because of their interesting magnetic and thermal properties. The altered magnetic properties can be expected for fine particles with high and low crystal anisotropies for cobalt and nickel provided that shape or stress anisotropies are not predominant [8-10]. However, stability of nanoparticles against air oxidation is more in the form of their alloys compare to single metals. Desired magnetic properties of alloys can be tuned by varying compositions of alloys. Among binary and ternary alloys, Fe-Ni-Co alloys are least focused for their magnetic characteristics studies. Fe-Ni-Co alloys having 29% of Ni and 17 wt% of Co is known as KOVAR and it has wider usage, such as sealing of metal and hard glass parts, in the electronic industries [11]. Soft magnetic properties of Fe-Co-Ni are related to the fcc cubic structure with no or little anisotropy in the materials. In addition, in nanocrystalline form, the soft magnetic properties are closely related to microstructural effects such as grain size, dispersion of crystal axes, non-magnetic layer, order-disorder phase transformation etc. [12-13].

For biomedical applications, it is imperative that these nanoparticles are dispersed in the aqueous solutions. Especially, the synthesis and stabilization of Fe, Co and Ni nanoparticles to an aqueous medium in addition to magnetic properties pose major bottleneck in this field [14]. Because the nanoparticles of iron group metals (i.e. Fe, Co and Ni) are prone to oxidation at room temperature, limited practical applications can be achieved. Hence, the stabilization of nanoparticles is necessary and can be achieved by using suitable stabilizing agents. In this chapter, we have given more emphasis on stabilization of ultrafine Fe, Co, Ni and Fe-Ni-Co nanoparticles in the size range of 20 nm to 50nm in aqueous medium by encapsulating the particles with a chemically stable species (e.g. polyethylene glycol). Sodium borohydride is used as reducing agent in order to achieve the controlled reduction of metal ions in aqueous medium. The nanomaterials were subjected to characterizations and fine particle magnetism was studied in detail.

3.2 Experimental

The chemicals used for synthesis of above materials include Ferric chloride hexahydrate ($FeCl_3{\cdot}6H_2O$), Cobalt chloride hexahydrate ($CoCl_2{\cdot}6H_2O$), Nickel chloride hexahydrate ($NiCl_2{\cdot}6H_2O$), Sodium borohydride ($NaBH_4$) and Polyethylene glycol (PEG-200) from Molychem, India. The chemicals were of analytical grade and have been used without further purification.

3.2.1 Synthesis of capped Co and Ni nanoparticles

The details of materials, moles and weights of materials taken for the synthesis of Co and Ni nanoparticles are tabulated in Table 3.1. In a typical method, 4.5 mmol of $CoCl_2{\cdot}6H_2O$

(or $NiCl_2{\cdot}6H_2O$) were dissolved in 50 mL of 1 M HCl to keep pH of reaction mixture below 6.5 and transferred in 500 mL three necks round bottom flask. Total metal ions concentration were kept approximately 0.1 M because lower concentration gives particles in nano-size range. Reaction mass stirred till complete dissolution at 25-30°C. In this mixture, added 50 mL 1 M $NaBH_4$ solution in time duration 20 minutes with vigorous stirring at 25-30°C. Black colored solids of metal or alloy were precipitated out with evolution of H_2 gas. Solids were separated by filtration on Whatmann filter paper no. 1. Then solids were drawn in 1 ml PEG-200 for capping and separated after 1 h. Portion of the sample was dried in vacuum desiccator over night at room temperature (i.e. as-prepared sample) and some portion was used for annealing. All samples except Fe were annealed at 600°C for 2 hours under N_2(g) flow. Iron sample was not annealed because iron nanoparticles are pyrophoric in nature and oxidizes to Fe_3O_4 after annealing.

Table 3.1 Details of moles and weights of metal salts used for synthesis of Fe, Co and Ni nanoparticles via sodium borohydride reduction method.

Materials	$FeCl_3{\cdot}6H_2O$		$NiCl_2{\cdot}6H_2O$		$CoCl_2{\cdot}6H_2O$	
	Moles (mmol)	weight (g)	Moles (mmol)	weight (g)	Moles (mmol)	weight (g)
Fe	4.5	1.216	---	---	---	---
Co	---	---	---	---	4.5	1.07
Ni	---	---	4.5	1.07	---	---

3.2.2 Synthesis of capped Fe-Ni-Co ternary alloys nanoparticles

The details of materials, moles and weights of materials taken for the synthesis of Fe-Ni-Co alloys nanoparticles are tabulated in Table 3.2. In a typical method, stoichiometric amount of $FeCl_3{\cdot}6H_2O$, $NiCl_2{\cdot}6H_2O$ and $CoCl_2{\cdot}6H_2O$ salts were dissolved in 50 mL of 1 M HCl to keep pH of reaction mixture below 6.5 and transferred in 500 mL three necks round bottom flask. Total metal ions concentration were kept approximately 0.1 M because lower concentration gives particles in nano-size range. Further reduction procedure was similar as given above in section 3.2.1 for the synthesis of Co and Ni nanoparticles. In case of Fe-Ni-Co ternary alloys, final compositions of the alloys have been confirmed from chemical analysis methods.

Table 3.2 Details of moles and weights of metal salts used for synthesis of Fe-Ni-Co alloy nanoparticles via sodium borohydride reduction method.

Materials	$FeCl_3·6H_2O$		$NiCl_2·6H_2O$		$CoCl_2·6H_2O$	
	Moles (mmol)	weight (g)	Moles (mmol)	weight (g)	Moles (mmol)	weight (g)
$Fe_{0.2}Ni_{0.6}Co_{0.2}$	0.9	0.243	2.7	0.642	0.9	0.214
$Fe_{0.3}Ni_{0.5}Co_{0.2}$	1.35	0.365	2.25	0.535	0.9	0.214
$Fe_{0.4}Ni_{0.4}Co_{0.2}$	1.8	0.486	1.8	0.428	0.9	0.214
$Fe_{0.5}Ni_{0.3}Co_{0.2}$	2.25	0.608	1.35	0.320	0.9	0.214

3.3 Results and Discussion

Results and discussion has been presented separately for single metal (Fe, Co, and Ni) and Fe-Ni-Co materials in subsections 3.3.1 and 3.3.2 respectively.

3.3.1 Characterizations and magnetic properties of Fe, Co and Ni nanoparticles

3.3.1.1 XRD studies

The XRD patterns of as-prepared materials of Fe, Co and Ni are shown in Figure 3.1. They have amorphous nature at as-prepared state. The ‘as-prepared’ materials were heat treated in N_2(g) atmosphere at various temperatures (200-600°C) for 2 h duration. After annealing even at 200°C in N_2(g) atmosphere, Fe gets oxidized to Fe-oxides and hence it has not included in further characterizations. The XRD patterns for Co and Ni heat treated at 600°C are shown in Figure 3.2. Co and Ni form pure crystalline phases after heat treatments. Although, Co crystallizes at 600°C and Ni at around 300°C, we carried out heat treatments at same temperature in order to address fine particle magnetism of the materials more appropriately. This also ensures uniformity in the surface structures as the materials are being prepared using the same route. Both Co and Ni crystallize in fcc crystal structure (JCPDS card no. 89-4307 and 70-0989 for Co and Ni, respectively) (Table 3.3).

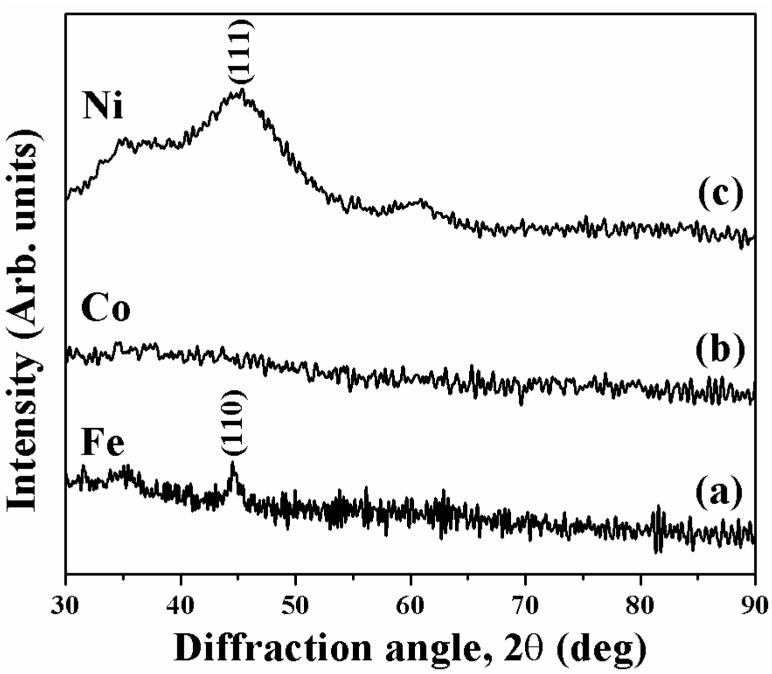

Figure 3.1 XRD patterns for as-prepared (a) bcc Fe, (b) amorphous Co, and (c) fcc Ni nanoparticles.

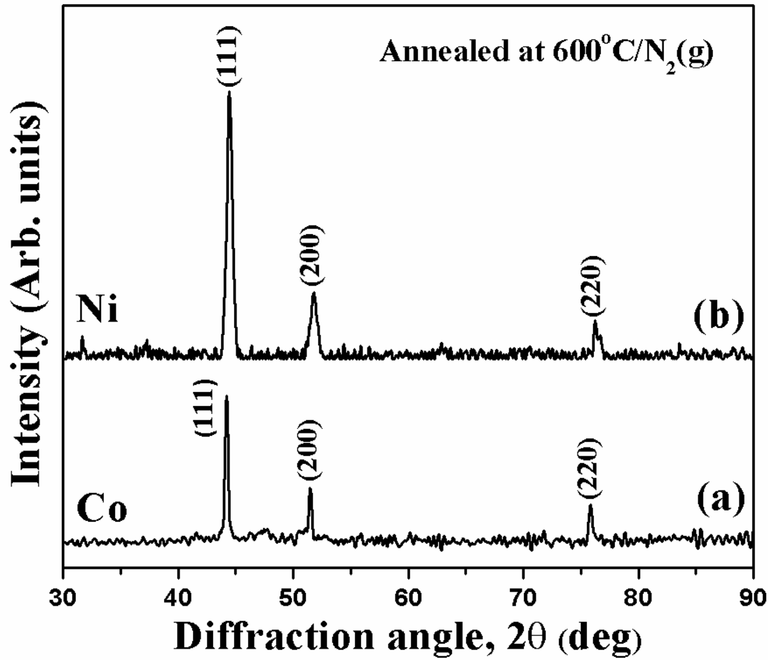

Figure 3.2 XRD patterns for fcc (a) Co, and (b) Ni nanoparticles annealed at 600°C in N_2(g) atmosphere for 2 h duration.

Table 3.3 Crystalline phase, *d*-spacing, lattice parameters, and crystallite sizes of Co and Ni heated at 600°C for 2 h.

Materials	Crystalline phase	*d*-spacing (Å)			Lattice parameters, *a* (Å)	Crystallite size (nm)
		(hkl)	Observed	Theoretical		
Co	fcc	(111)	2.0463	2.0467	3.54(±1)	42.6(±1)
		(200)	1.7728	1.7723		
		(220)	1.2529	1.2532		
Ni	fcc	(111)	2.0354	2.0340	3.52(±1)	29.1(±1)
		(200)	1.7628	1.7620		
		(220)	1.2461	1.2460		

The peaks observed in the XRD pattern of fcc Co at 2θ value of 44.2°, 51.5° and 75.8° correspond to the (111), (200) and (220) crystal planes, respectively. Similarly, peaks observed in the XRD pattern of fcc Ni at 2θ value of 44.5°, 51.9° and 76.4° correspond to the (111), (200) and (220) crystal planes, respectively. The observed and theoretical values of *d*-spacing of indexed Co and Ni peaks were shown in Table 3.3. The estimated values of lattice parameters (*a*) of Co and Ni were found to be 3.54(±1) Å and 3.52(±1) Å, respectively (Table 3.3). The broadening of the most intense peak with Miller indices (111) has been used for determination of crystallite sizes. The average crystallite sizes from Scherrer formula for Co and Ni were found to be 42 nm and 29 nm, respectively (Table 3.3). These results indicate nano-size nature of our materials.

3.3.1.2 SEM studies

Figure 3.3(a, b, c) represents the SEM micrographs with different magnifications for Co nanoparticles heat treated at 600°C in N_2(g) atmosphere. SEM particle size distribution is shown Figure 3.3(d). The estimated value of average SEM particle size is tabulated in Table 3.4. SEM micrographs of micron size area (Figure 3.3 (a, b)) show that nanomaterials get agglomerated to form bigger particles. However, magnified SEM micrograph to 30000X (i.e. Figure 3(c)) confirms the presence of nanomaterials hence used for further analysis. Figure 3.3(c) confirmed that Co nanoparticles have nearly spherical shape morphologies. The average SEM particle size for Co nanoparticles estimated from micrograph in Figure 3.3(c) was found to be 62±5 nm. SEM studies indicate that synthesized Co nanoparticles have large size distribution and SEM particle size is found to be larger than the XRD crystallite size. These discrepancies can be attributed to the presence of aggregates or clusters consisting of several crystallites.

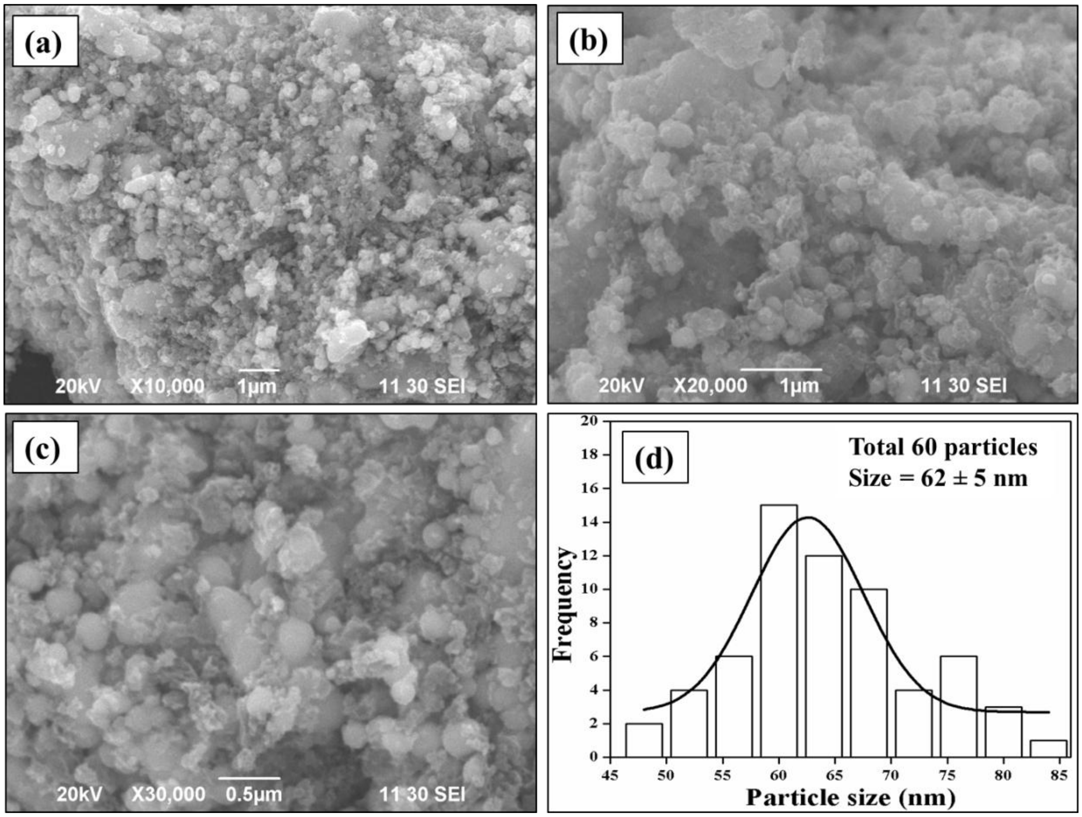

Figure 3.3 (a), (b), (c) SEM micrographs with various magnifications for Co nanoparticles, heat treated at 600°C for 2 h under N_2 (g) flow atmosphere and (d) size distribution for micrograph 'c'.

SEM micrographs with different magnifications for Ni nanoparticles heat treated at 600°C in N_2(g) atmosphere are shown in Figure 3.4(a, b, c). SEM particle size distribution is shown Figure 3.4(d). The estimated value of average SEM particle size of Ni is tabulated in Table 3.4. SEM micrograph of Ni having micron size area (Figure 3.4(a)) shows the presence of nanostructures having nearly spherical shape morphologies. However, in order to observe nanostructures more clearly and for the estimation of accurate particle sizes, SEM micrographs of higher magnifications (30000X-40000X) have been presented (Figure 3.4(b, c)). SEM studies confirm the presence of monodispersed Ni nanoparticles without any agglomerations. The average SEM particle size for Ni nanoparticles estimated from micrograph in Figure 3.4(c) was found to be 54±3 nm. SEM studies indicate that synthesized Ni nanoparticles have large size distribution. Average SEM particle size of Ni is larger than the XRD crystallite size and may be attributed to the presence of aggregates or clusters consisting of several crystallites.

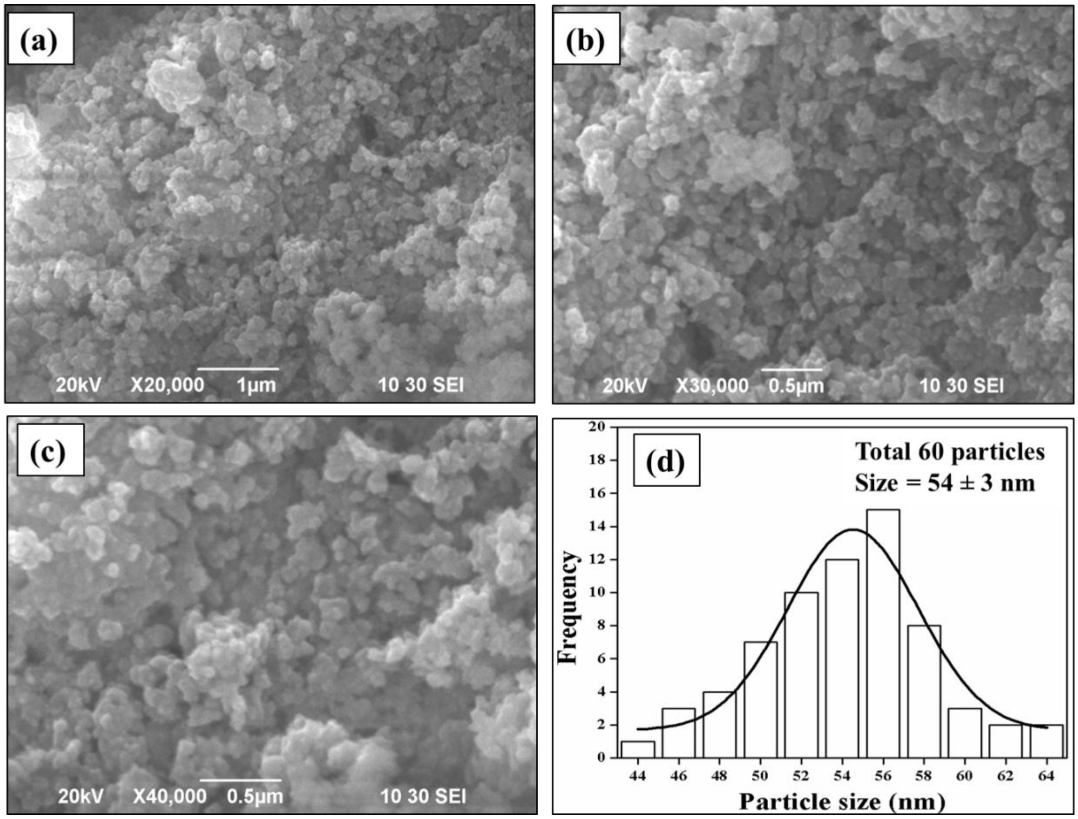

Figure 3.4 (a), (b), (c) SEM micrographs with various magnifications for Ni nanoparticles heat treated at 600°C for 2 h under N_2 (g) flow atmosphere and (d) size distribution for micrograph ‘c’.

Table 3.4 SEM particle sizes and TEM particle sizes of Co and Ni heated at 600°C for 2 h.

Materials	Average SEM particle size (nm)	Average TEM particle size (nm)
Co	62 ± 5	43 ± 4
Ni	54 ± 3	48 ± 5

3.3.1.3 TEM studies

TEM micrographs for annealed Co and Ni nanoparticles are shown in Figure 3.5. The estimated values of average TEM particle sizes are tabulated in Table 3.4. TEM micrographs of Co and Ni confirmed that nanoparticles have nearly spherical shape. The average TEM particle sizes were found to be 43±4 nm and 48±5 nm for Co and Ni, respectively. TEM particle sizes are found to be larger than the XRD crystallite sizes but more accurate than SEM particle sizes.

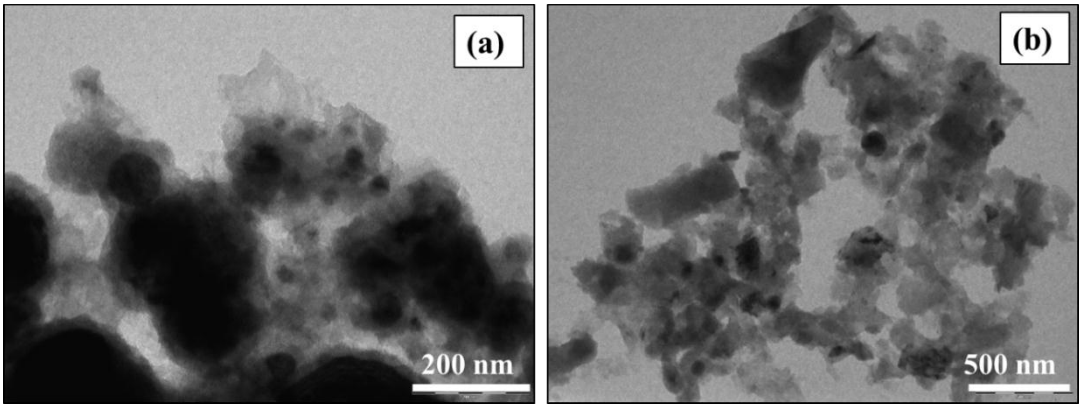

Figure 3.5 TEM micrographs of (a) Co and (b) Ni nanoparticles heat treated at 600°C for 2 h under N_2 atmosphere.

3.3.1.4 Magnetic studies

The magnetic properties of the Co and Ni nanoparticles were studied by measuring room temperature hysteresis (M-H) curves. The field dependence of specific magnetizations of Co and Ni are shown in the Figure 3.6. The inset of the Figure 3.6 represents the corresponding values of coercivity. However, approach to saturation magnetization of the nanoparticles has a form very similar to 1/H law employed for the bulk material [15]. In summary, specific magnetization values in the field strength of 10-15 kOe are taken. The extrapolated values at M axis in the M vs. 1/H plots were taken as M_S (Figure 3.7). The values of saturation magnetization (M_S) are 122 and 47 emu/g whereas the coercivity values (H_C) are 111 Oe and 84 Oe for Co and Ni, respectively (Table 3.5).

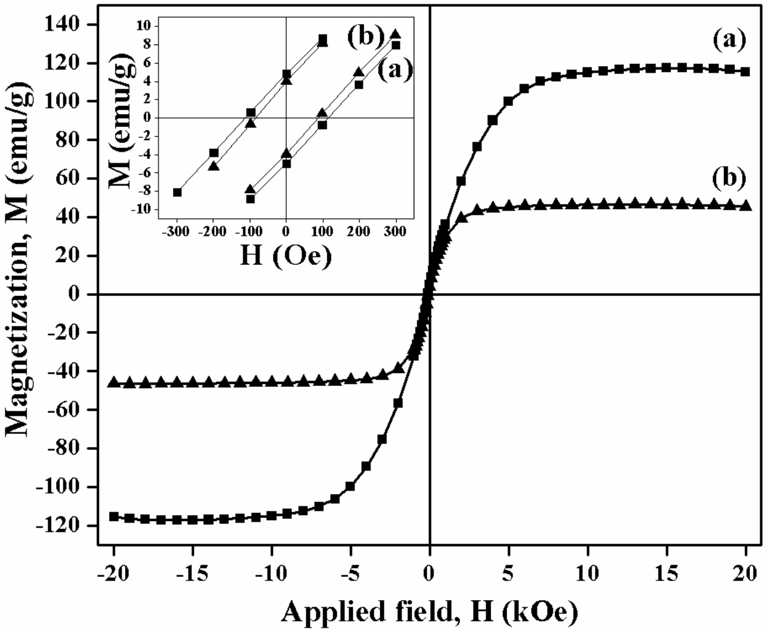

Figure 3.6 Plot of specific magnetizations versus applied field for (a) Co and (b) Ni nanoparticles heat treated at 600°C for 2 h under N_2 atmosphere. Inset (a) and (b) shows the corresponding values of coercivities for Co and Ni, respectively.

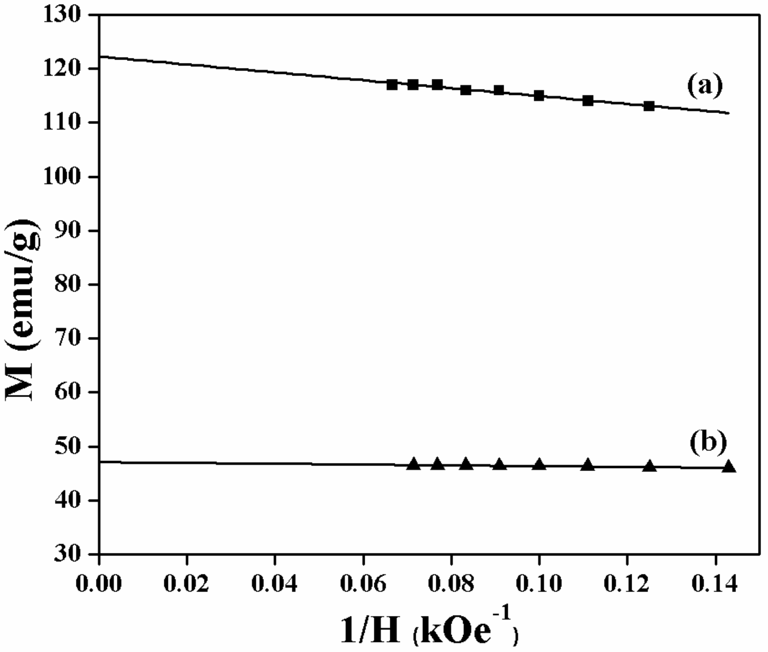

Figure 3.7 Plot of M vs. 1/H representing approach to saturation magnetization of (a) Co and (b) Ni nanoparticles.

Magnetic-hysteresis (M-H) curve of Co and Ni confirms ferromagnetic nature of the materials (Figure 3.5). The values of M_S for Co and Ni are 122 emu/g and 47 emu/g, respectively which are slightly lower than the values of M_S for bulk Co (162 emu/g) and Ni (55.4 emu/g) [16]. The decrease in the values of M_S in our materials may be attributed to the decrease in particle size, increase in surface area and crystalline disorder at the surface layers which might create magnetic interfaces and results in lower values of magnetization [17]. Further, degrees of spin canting at the surface of the nano-crystallites may be significantly larger and may contribute towards lower magnetizations. In spin canting, magnetic moments at the surface have random orientation whereas bulk magnetic moments orient in the direction of applied field. Hence actual magnetic volume contributing towards magnetization is less and results in the reduction in M_S value [18]. In the case of Ni, saturation magnetization can be achieved at lower applied field strength i.e. below 5 kOe whereas Co is not saturated completely up to 10 kOe (Figure 4). The values of coercivity for Co (i.e. 111 Oe) and Ni (i.e. 84 Oe) are in the range of soft magnetic behavior. It has been reported that coercivity value for Co and Ni increases with decreasing particle size, goes through maximum at critical size and then decreases below critical size. In the case of Co, the multidomain structure can be obtained at particle size of ~15 nm with coercivity value of ~190 Oe [19]. As average particle size of Co nanoparticles in this study is larger than 15 nm, the decrease in H_C value in case of Co may be related to particle size and multidomain structure. Critical size for Ni nanoparticles is reported as 86 nm with coercivity value equal to 203.5 Oe [20]. Also, coercivity values of Co and Ni nanomaterials are slightly greater than the value where superparamagnetic behavior will occur. These results are matching well with the literature reported data [20].

Table 3.5 XRD phase, saturation magnetization and coercivity of Co and Ni heated at 600°C for 2 h under N_2(g) flow.

Materials	XRD phase	Saturation Magnetization, M_S (emu/g)	Coercivity, H_C (Oe)
Co	fcc	122	111
Ni	fcc	47	84

3.3.2 Characterizations and magnetic properties of Fe-Ni-Co alloy nanoparticles

3.3.2.1 XRD studies

The XRD patterns for $Fe_{20}Ni_{60}Co_{20}$, $Fe_{30}Ni_{50}Co_{20}$, $Fe_{40}Ni_{40}Co_{20}$ and $Fe_{50}Ni_{30}Co_{20}$ ternary alloys synthesized by sodium borohydride reduction route and heat treated at 600°C (under N_2 atmosphere) are shown in Figure 3.8. The composition, lattice parameters and crystallite sizes have been summarized in Table 3.6. The XRD lines were broadened and indicate fine particle nature of the materials. The average crystallite size is defined as the diameter of the core of the nanocrystal having periodicity of lattice and does not include thickness of the surface capping agent [21]. Further, the crystallite size obtained by XRD may not correspond to nanoparticle size because of agglomeration of several crystallites forming clusters. Such kinds of results have already been reported in the literature [22]. Also, it has been observed that XRD lines can be broaden due to lattice strain in the nanoparticles [23]. However, in our investigation line broadening due to lattice strain effect has not been considered. As the formation of nanocrystals in the present synthesis occurs through nucleation and growth mechanism and not by mechanical activation (such as ball milling and mechanical alloying), Scherrer equation concerns regarding the broadening due to crystallite size only [23]. The XRD line broadening of the Fe-Ni-Co ternary alloy materials increases with the increase of Fe content in the materials. The alloys crystallize in fcc structure with lattice parameter (*a*) equal to 3.546(±1), 3.546(±1), 3.555(±1), and 3.558(±1) Å for $Fe_{20}Ni_{60}Co_{20}$, $Fe_{30}Ni_{50}Co_{20}$, $Fe_{40}Ni_{40}Co_{20}$ and $Fe_{50}Ni_{30}Co_{20}$ alloys, respectively. The estimated crystallite sizes for $Fe_{20}Ni_{60}Co_{20}$, $Fe_{30}Ni_{50}Co_{20}$, $Fe_{40}Ni_{40}Co_{20}$ and $Fe_{50}Ni_{30}Co_{20}$ alloy materials were found to be 27.5(±1), 27.0(±1), 24.0(±1), and 22.8(±1) nm, respectively. For $Fe_{50}Ni_{30}Co_{20}$ alloy, we observed very low intensity (<5%) spinel oxide, i.e. $(FeNiCo)_3O_4$ phase (Figure 3.8). For high percentage of Fe in the alloy, oxide formation takes place due to small grain size of the materials. This may be due to higher oxidation potential of Fe compared to Co and Ni. The phase boundaries of Fe-Ni-Co have been well studied and our results corroborates well with the reported literature [24]. It should be noted that the surface of the nanoparticles may be encapsulated with thin oxide layers and are not detected by X-ray diffraction. The surface oxidation in air may be expected in Fe and Fe based nanomaterials due to highly reactive or pyrophoric nature of Fe. Such kind of results has already been reported in the literature [22].

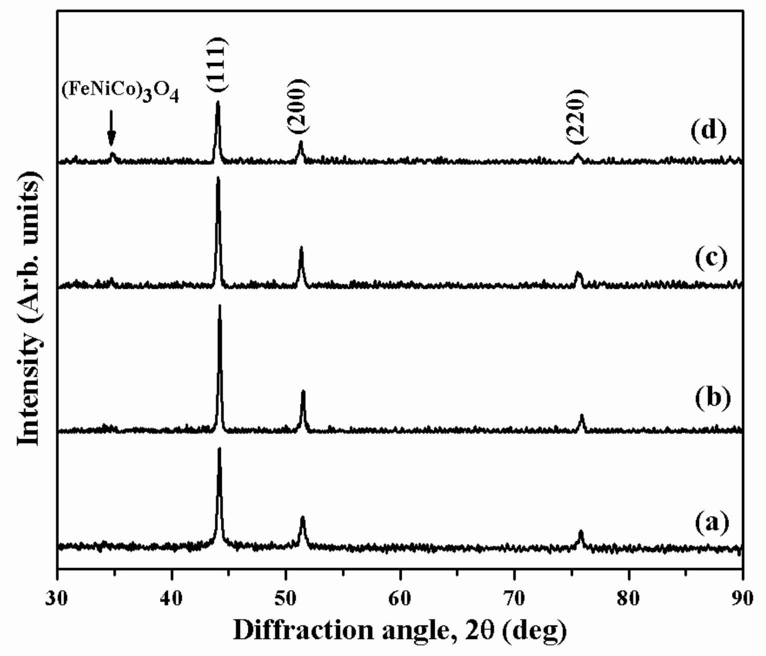

Figure 3.8 XRD patterns for (a) $Fe_{20}Ni_{60}Co_{20}$, (b) $Fe_{30}Ni_{50}Co_{20}$, (c) $Fe_{40}Ni_{40}Co_{20}$ and (d) $Fe_{50}Ni_{30}Co_{20}$ ternary alloys heat treated at 600°C under N_2(g) atmosphere. The XRD patterns are indexed in accordance with fcc structure.

Table 3.6 Crystalline phase, annealing conditions, lattice parameters, and crystallite sizes of Fe-Ni-Co ternary alloys with various compositions heated at 600°C for 2 h.

Alloy Composition	Crystalline Phase	Annealing conditions temp/h (°C/h)	Lattice parameter, *a* (Å)	Crystallite size by XRD (nm)
$Fe_{20}Ni_{60}Co_{20}$	fcc	600/2	3.546(±1)	27.5(±1)
$Fe_{30}Ni_{50}Co_{20}$	fcc	600/2	3.546(±1)	27.0(±1)
$Fe_{40}Ni_{40}Co_{20}$	fcc	600/2	3.555(±1)	24.0(±1)
$Fe_{50}Ni_{30}Co_{20}$	fcc	600/2	3.558(±1)	22.8(±1)

The variations of the lattice parameters and crystallite sizes for Fe-Ni-Co ternary alloys are shown in Figure 3.9. With the increase of Fe content in the ternary alloy, the diffraction peaks shift to lower angle and the values of lattice parameters increase from

3.546 Å to 3.558 Å. This result can be attributed to the difference in the values of atomic radius of cobalt, nickel and iron, i.e. 1.67 Å, 1.62 Å and 1.72 Å respectively [25]. It should be noted that lattice expansion is found for ultrafine particle systems due to size and surface effects. The calculated crystallite sizes of the ternary alloys (i.e. $Fe_{20}Ni_{60}Co_{20}$, $Fe_{30}Ni_{50}Co_{20}$, $Fe_{40}Ni_{40}Co_{20}$ and $Fe_{50}Ni_{30}Co_{20}$) decreases with the increase of Fe content in the materials (Figure 3.9). It may be interpreted that in our synthesized ternary alloy, Fe atoms are embedded in the fcc Co-Ni alloy matrix [26].

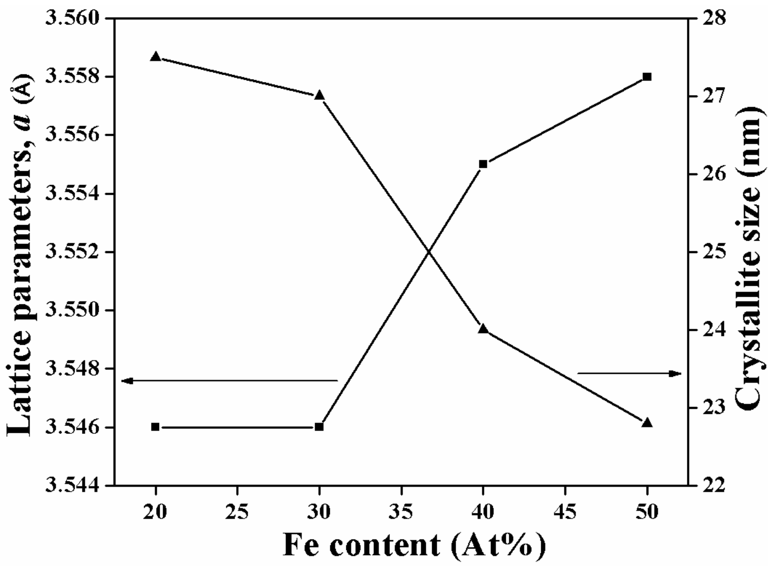

Figure 3.9 Variation of lattice parameters and crystallite sizes with increasing Fe content in $Fe_xNi_{80-}xCo_{20}$ alloys heat treated at 600°C under $N_2(g)$ atmosphere.

3.3.2.2 SEM studies

The typical SEM micrographs with different magnifications (10000-30000X) for $Fe_xNi_{80-x}Co_{20,}$ x =20, 30, 40 and 50 alloys are presented in Figures 3.10 and Figure 3.11. Average SEM particle sizes were estimated from SEM micrograph taken at 30000X magnification (Figure 3.11). The average SEM particle sizes estimated from the most probable value in particle size distribution plots shown as insets of Figure 3.11. The estimated SEM particle sizes are tabulated in Table 3.7. SEM micrographs at lower magnifications (≤ 20000) show the presence of nanomaterials in agglomerated form. In order to see more clear nanostructures, SEM micrographs with higher magnifications (≥ 30000) (Figure 3.11) were measured which confirm a uniform distribution of nanoparticles having nearly spherical shape. The estimated average SEM particle sizes are found to be 72±7 nm, 75±5 nm, 72±4 nm, and 59±6 nm for $Fe_{20}Ni_{60}Co_{20}$, $Fe_{30}Ni_{50}Co_{20}$, $Fe_{40}Ni_{40}Co_{20}$, and $Fe_{50}Ni_{30}Co_{20}$, respectively. The SEM particle sizes are found to be bigger than the estimated crystallite sizes (Table 3.6). It should be noted that several crystallites can form aggregates. The nanoparticle size determined by SEM may be larger compared to crystallite size. Such kinds of results are not uncommon in the literature for ferromagnetic crystallites [22].

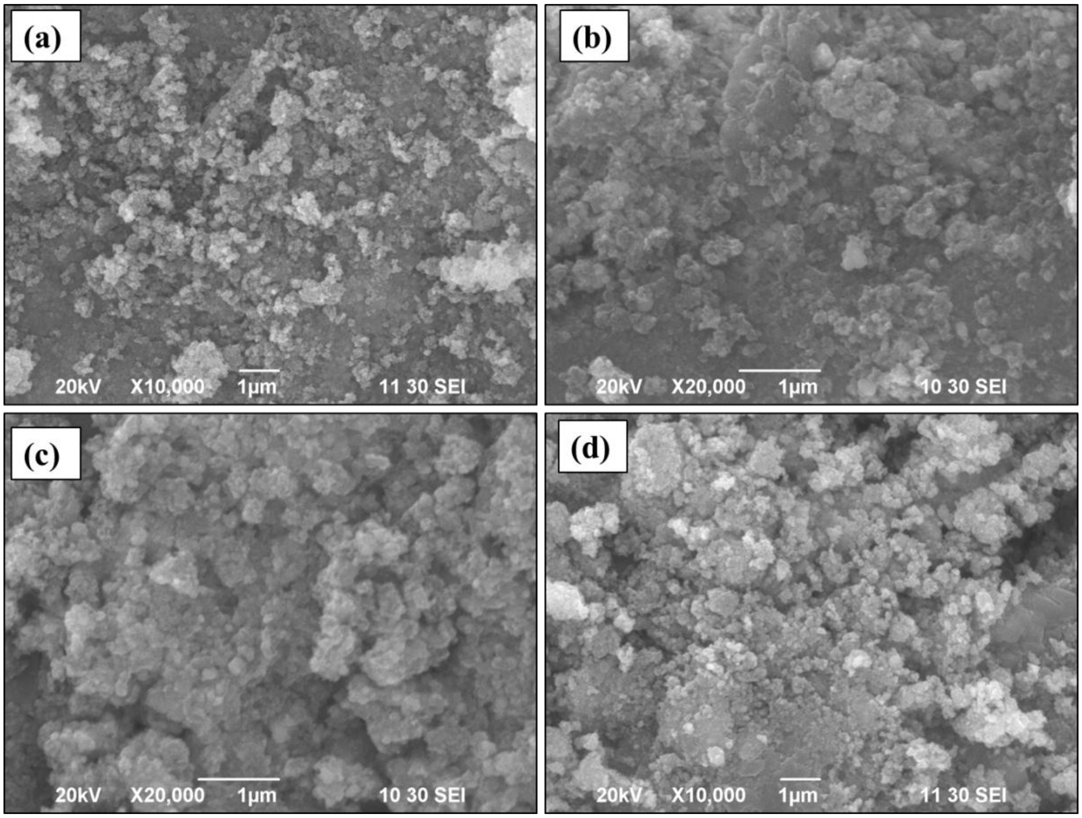

Figure 3.10 SEM micrographs at low magnifications of (a) $Fe_{20}Ni_{60}Co_{20}$, (b) $Fe_{30}Ni_{50}Co_{20}$, (c) $Fe_{40}Ni_{40}Co_{20}$ and (d) $Fe_{50}Ni_{30}Co_{20}$ ternary alloys heat treated at 600°C under N_2(g) atmosphere.

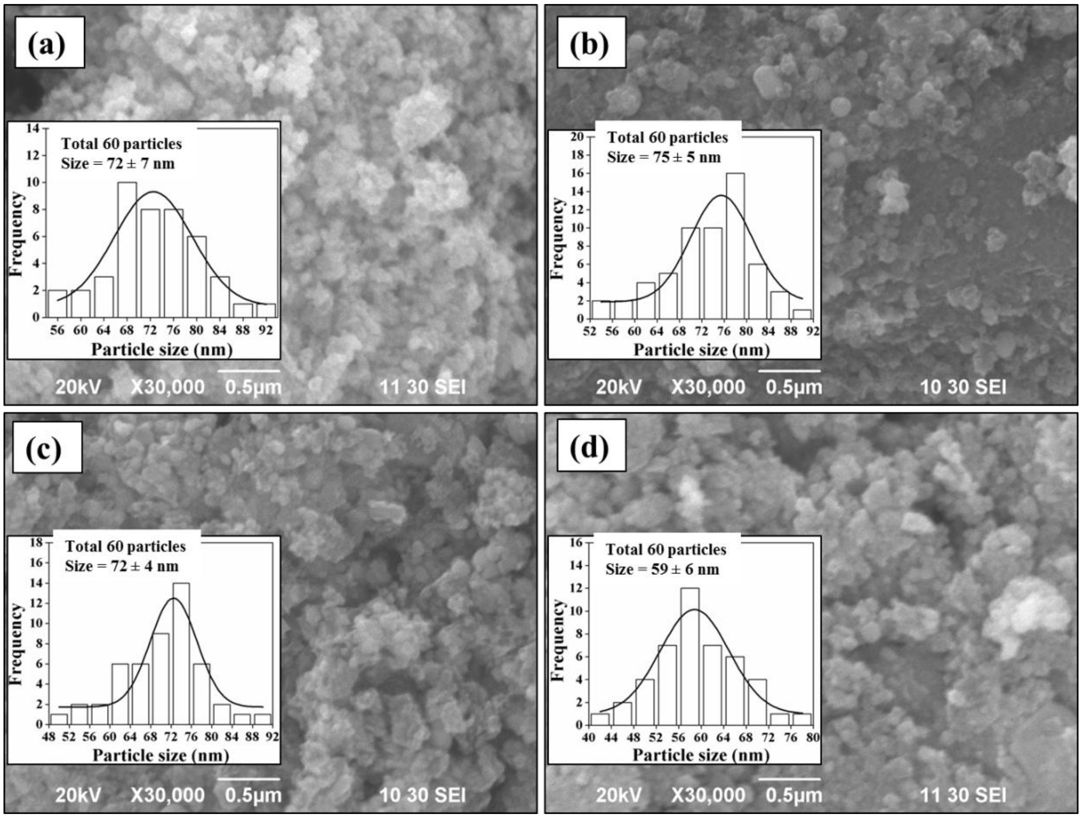

Figure 3.11 SEM micrographs at high magnification of (a) $Fe_{20}Ni_{60}Co_{20}$, (b) $Fe_{30}Ni_{50}Co_{20}$, (c) $Fe_{40}Ni_{40}Co_{20}$ and (d) $Fe_{50}Ni_{30}Co_{20}$ ternary alloys heat treated at 600°C under N_2(g) atmosphere.

Table 3.7 SEM particle sizes and TEM particle sizes of Fe-Ni-Co ternary alloys with various compositions heat treated at 600°C for 2 h.

Alloy Composition	Annealing condition temp/h (°C/h)	Average SEM particle size (nm)	Average TEM particle size (nm)
$Fe_{20}Ni_{60}Co_{20}$	600/2	72 ± 7	15 ± 2
$Fe_{30}Ni_{50}Co_{20}$	600/2	75 ± 5	--
$Fe_{40}Ni_{40}Co_{20}$	600/2	72 ± 4	22 ± 3
$Fe_{50}Ni_{30}Co_{20}$	600/2	59 ± 6	--

3.3.2.3 TEM studies

In order to investigate particle size distributions and phase purity, we examined two selected materials, $Fe_{20}Ni_{60}Co_{20}$ and $Fe_{40}Ni_{40}Co_{20}$, for TEM and SAED studies. The typical TEM micrographs for $Fe_{20}Ni_{60}Co_{20}$ and $Fe_{40}Ni_{40}Co_{20}$ alloys, heat treated at

600°C, are shown in Figure 3.12(a) and Figure 3.12(b), respectively. Insets of Figure 3.12 represent corresponding TEM particle size distribution plots. The SAED patterns of $Fe_{20}Ni_{60}Co_{20}$ and $Fe_{40}Ni_{40}Co_{20}$ are shown in Figure 3.13. The estimated average TEM particle sizes for Fe-Ni-Co alloys from TEM micrographs are summarized in Table 3.7. TEM micrograph studies confirm that the synthesized Fe-Ni-Co alloys have nearly spherical morphology having average TEM particle sizes of 15±2 nm and 22±3 nm for $Fe_{20}Ni_{60}Co_{20}$ and $Fe_{40}Ni_{40}Co_{20}$ alloys, respectively. Although, there is indication of the presence of some agglomerated fractions of the nanomaterials in TEM micrographs, the TEM particle sizes, i.e. 15 nm and 22 nm, are comparable with the average XRD crystallite sizes, i.e. 27.5 nm and 24 nm, for $Fe_{20}Ni_{60}Co_{20}$ and $Fe_{40}Ni_{40}Co_{20}$, respectively. In our TEM investigation, the micrographs indicate broader distribution of particle sizes. The reason can be majorly due to the chemical methodology adopted for synthesis and surface modifications by dissolved species leading to agglomeration [27]. As in the present synthesis methodology, we have used high concentration of borohydride (i.e. 1 M) in presence of Cl^- ions, PEG etc. in order to reduce metal ions; grain growth leading to agglomeration is dominant.

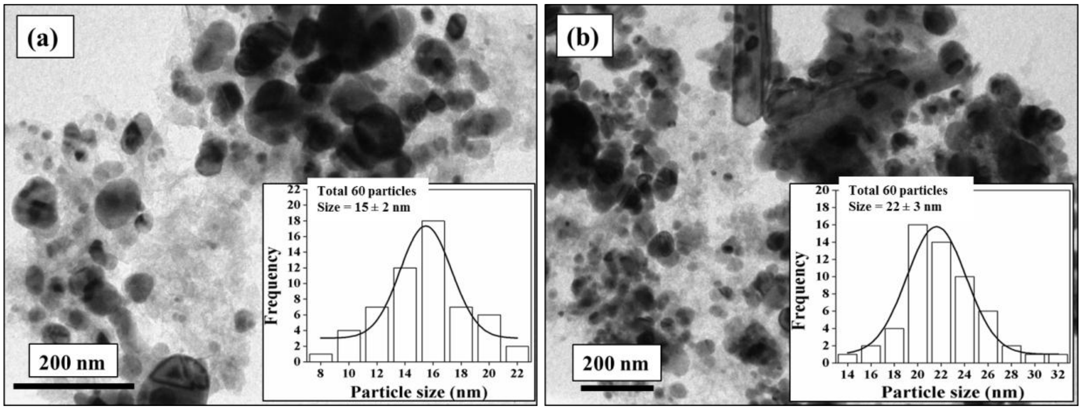

Figure 3.12 TEM micrographs of (a) $Fe_{20}Ni_{60}Co_{20}$ and (b) $Fe_{40}Ni_{40}Co_{20}$ alloys nanoparticles and corresponding insets (Fig. (a) and (b)) represent corresponding size distributions.

In SAED pattern, the formation of diffraction rings indicates polycrystalline nature of the materials (Figure 3.13). The interplanar spacing (*d*-value) for (111) and (200) crystal planes from SAED patterns were found to be 2.0449 Å and 1.7667 Å for $Fe_{20}Ni_{60}Co_{20}$

and 2.0576 Å and 1.7921 Å for $Fe_{40}Ni_{40}Co_{20}$, respectively. The interplanar spacing obtained for (111) and (200) planes from SAED patterns matches well with the corresponding values obtained from XRD results. These results indicate the formation of pure fcc Fe-Ni-Co ternary alloy phases.

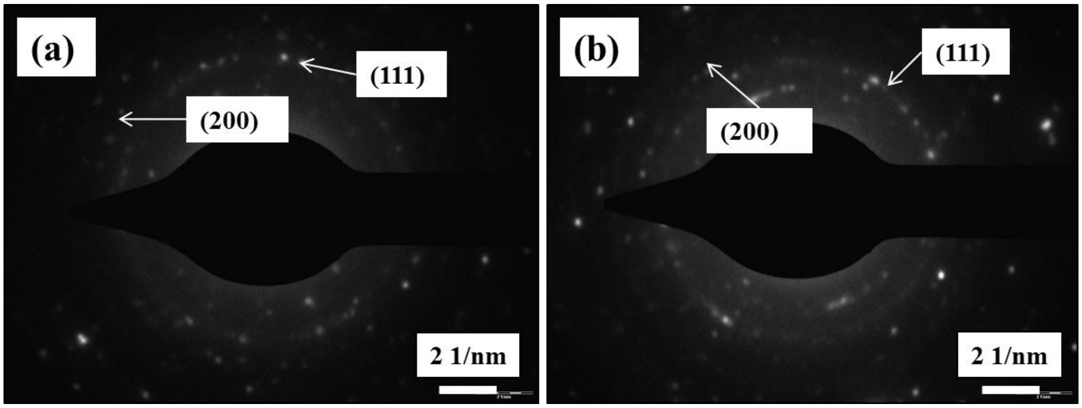

Figure 3.13 SEAD patterns of (a) $Fe_{20}Ni_{60}Co_{20}$ and (b) $Fe_{40}Ni_{40}Co_{20}$ alloys nanoparticles. Major diffraction rings are indexed in accordance with fcc crystal structure.

3.3.2.4 Magnetic studies

Figure 3.14 shows a typical M vs. H characteristics plot of Fe-Ni-Co materials under study. However, for more clarity, specific magnetizations as a function of increasing field strength (0-20 kOe) of $Fe_{20}Ni_{60}Co_{20}$, $Fe_{30}Ni_{50}Co_{20}$, $Fe_{40}Ni_{40}Co_{20}$ and $Fe_{50}Ni_{30}Co_{20}$ alloys having particle sizes 27.5 nm, 27.0 nm, 24.0 nm, 22.8 nm respectively are shown in Figure 3.15. The inset of Figure 3.15 represents the values of coercivity for corresponding alloys. An approach to calculate the values M_S of Fe-Ni-Co alloys is represented in Figure 3.16. The compositions, XRD phases, saturation magnetizations and the values of coercivity are summarized in Table 3.8. The specific magnetization as a function of field does not exhibit saturation up to 20 kOe and indicates superparamagnetic fractions in the materials. The values of coercivity are found in the range of 122 Oe to 170 Oe for $Fe_{20}Ni_{60}Co_{20}$, $Fe_{30}Ni_{50}Co_{20}$, $Fe_{40}Ni_{40}Co_{20}$ and $Fe_{50}Ni_{30}Co_{20}$ alloys. The saturation magnetization and coercivity values as a function of Fe content have been presented in Figure 3.17.

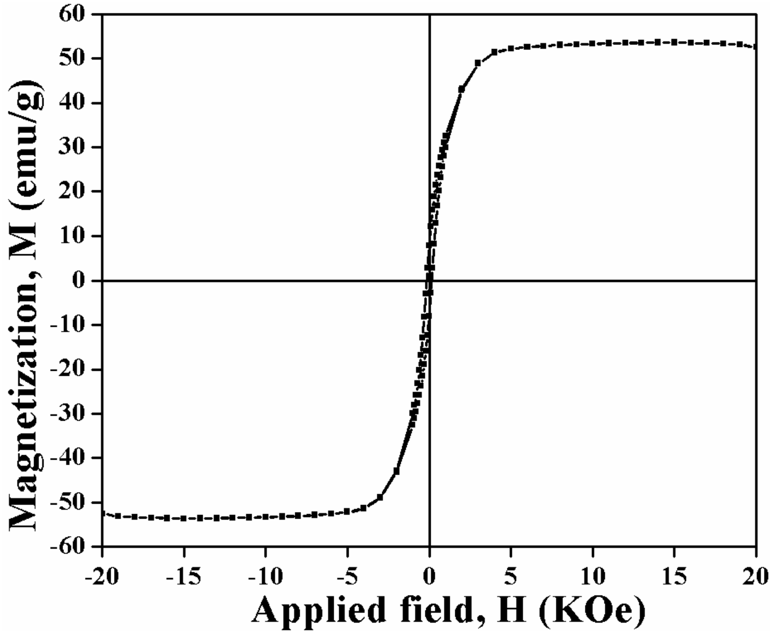

Figure 3.14 A typical M vs. H plot of $Fe_{20}Ni_{60}Co_{20}$ alloy heat treated at 600°C under N_2(g) atmosphere.

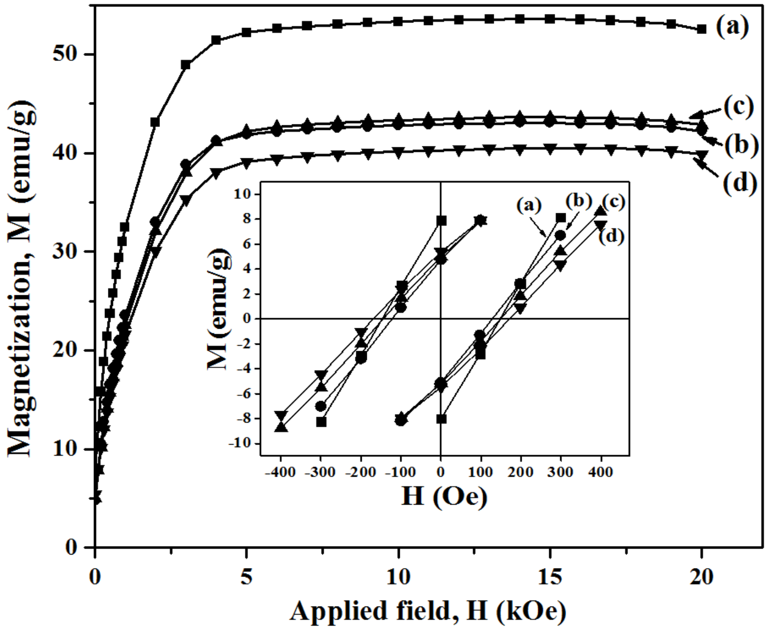

Figure 3.15 Plots of Specific magnetizations as a function of field for (a) $Fe_{20}Ni_{60}Co_{20}$, (b) $Fe_{30}Ni_{50}Co_{20}$, (c) $Fe_{40}Ni_{40}Co_{20}$ and (d) $Fe_{50}Ni_{30}Co_{20}$ ternary alloys heat treated at 600°C under N_2 (g) atmosphere. Inset shows coercivity for corresponding compositions.

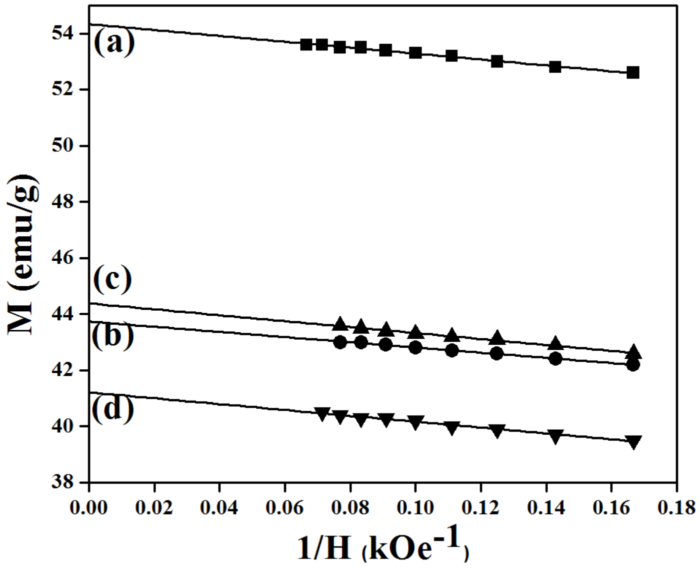

Figure 3.16 Plot of specific magnetization as a function of 1/H for various Fe-Ni-Co nanomaterials; (a) $Fe_{20}Ni_{60}Co_{20}$, (b) $Fe_{30}Ni_{50}Co_{20}$, (c) $Fe_{40}Ni_{40}Co_{20}$ and (d) $Fe_{50}Ni_{30}Co_{20}$ alloys.

The observed values of saturation magnetization for $Fe_{20}Ni_{60}Co_{20}$, $Fe_{30}Ni_{50}Co_{20}$, $Fe_{40}Ni_{40}Co_{20}$ and $Fe_{50}Ni_{30}Co_{20}$, i.e. 54.3-41.2 emu/g, are significantly lower than the reported bulk values (160-171 emu/g) measured at room temperature [28]. These results indicate fine particle nature of our materials. The size range of our nano-particles seems to be larger than the expected range for which we can observe a decrease in saturation magnetization. But, magnetocrystalline anisotropy plays an important role in inducing size effects of the nano-crystals. If the magnetocrystalline anisotropy is lower, one can get size effects even for larger crystallites. Thus the magnetocrystalline anisotropy of our materials may be lower in order to induce the size effects. The effective magnetic moments of ultrafine ferromagnetic transition metal particles are found much below the bulk value. Further, degrees of spin canting at the surface of the nano-crystallites may be significantly larger and may contribute towards lower magnetizations. Such kind of results has already been reported in literature for γ-Fe_2O_3, $NiFe_2O_4$ and CrO_2 materials [3, 18, 29]. The reduction in magnetization can also be due to surface effects. Surface oxidation of the nanoparticles may play the role for the reduction of the specific magnetization. The above stated arguments have been supported by the observed line broadening in the X-ray diffraction patterns. Further it can be seen that the increase of Fe content, the values of saturation magnetization decreases which is of opposite trend found in the literature [30]. However we have observed reduction in particle size as a function of Fe content in our alloys. Therefore the reduction of magnetization as a result of surface oxidation and surface effects is more dominant over the increase in Fe content in the ternary alloys. Finally ferrimagnetic or antiferromagnetic impurities at the surface of the nanoparticles can also decrease the total magnetization. It should be noted that Fe-Ni-Co alloys with larger Fe content are prone to surface oxidation to a larger extent. The values of coercivity decrease from 170 Oe to 122 Oe with decrease in Fe content (increase in Ni content) in the ternary alloys (Figure 3.17). The coercivity is relatively high because the particle size is not in the range where the anisotropy is averaged and coercivity is small.

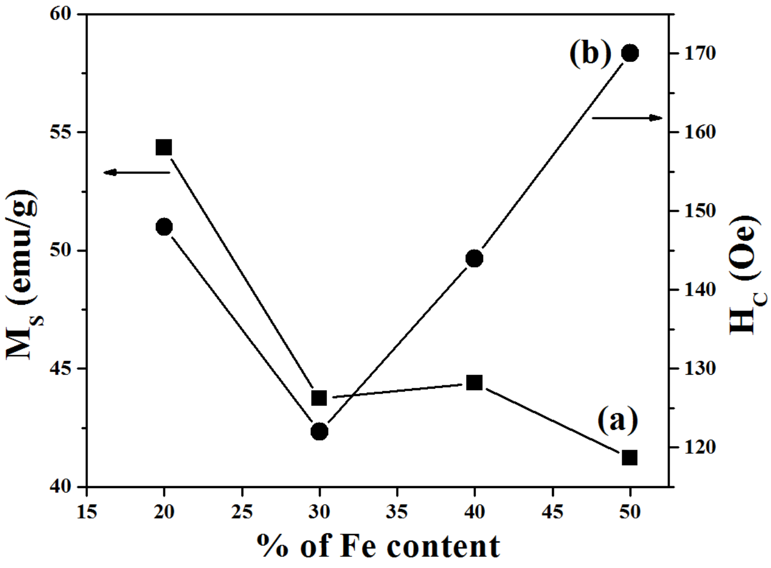

Figure 3.17 Variation of (a) saturation magnetization and (b) coercivity as a function of increasing Fe content in the Fe-Ni-Co ternary alloys.

Table 3.8 Composition, XRD phase, saturation magnetization and coercivity of Fe-Ni-Co ternary alloys heat treated at 600°C for 2 h under N_2(g) flow.

Composition	XRD phase	Saturation magnetization, Ms (emu/g)	Coercivity, Hc (Oe)
$Fe_{20}Ni_{60}Co_{20}$	fcc	54.3	148
$Fe_{30}Ni_{50}Co_{20}$	fcc	43.7	122
$Fe_{40}Ni_{40}Co_{20}$	fcc	44.3	144
$Fe_{50}Ni_{30}Co_{20}$	fcc	41.2	170

3.4 Conclusions

In summary, PEG coated Fe, Co and Ni nanoparticles have been stabilized in aqueous medium by modified $NaBH_4$ reduction route. Fe nanoparticles were found to form oxides after annealing whereas Co and Ni nanoparticles form pure crystalline phase. We have prepared pure fcc phases of Co and Ni with lattice parameters 3.54(±1) Å and 3.52(±1) Å whereas crystallite sizes are equal to 42.6(±1) nm and 29.1(±1) nm, respectively. SEM and TEM studies confirm the formation of nano-spheres of Co and Ni by this methodology. Size, shape and surface morphologies of material were studied by SEM and TEM analysis. SEM micrograph shows the particle sizes to be 62±5 nm and 54±3 nm whereas TEM studies confirm the sizes to be 43±4 nm and 48±5 nm for Co and Ni, respectively. These particle sizes are larger than crystallite sizes estimated by XRD studies due to the agglomeration of the nano-particles. Fine particle magnetism in our material is explained by the plot of specific magnetization versus applied field which shows the signature of the size and surface effects. The values of saturation magnetization are 122 emu/g and 47 emu/g whereas the coercivity values are 111 Oe and 84 Oe for Co and Ni, respectively. These magnetic parameters indicate excellent soft magnetic behavior of Co and Ni nanoparticles. The decrease in saturation magnetization of Co and Ni compared to the bulk values have been explained on the basis of size, surface effects and spin canting at the surface of the ultrafine materials. The synthesized high moment Co and Ni nano-structured materials may be useful for soft magnetic applications.

A new synthetic strategy is also applied for the preparation of nanocrystalline $Fe_{20}Ni_{60}Co_{20}$, $Fe_{30}Ni_{50}Co_{20}$, $Fe_{40}Ni_{40}Co_{20}$ and $Fe_{50}Ni_{30}Co_{20}$ alloys. The synthetic method produces uniform and spherical nano-dimensional systems. It could prepare pure fcc phases of the ternary alloys with lattice parameters in the range of 3.546-3.558 Å and crystallite sizes are in the range of 22.8-27.5 nm. The increases in the values of lattice parameters were observed with the increase of Fe content in the ternary alloys. SEM studies indicate the presence of aggregates or clusters consisting of several crystallites. SEM particle sizes of Fe-Ni-Co alloys were in the range of 59±6 nm to 75±5 nm. TEM studies confirm that synthesized materials have spherical morphologies with minute fractions of agglomerations. Estimated values of TEM particle sizes were found to be 15±2 nm and 22±3 nm for $Fe_{20}Ni_{60}Co_{20}$ and $Fe_{40}Ni_{40}Co_{20}$, respectively. The observed values of saturation magnetization for our ternary alloys are in the range of 54.3-41.2 emu/g and coercivity values in the range of 170-122 Oe. The above results indicate excellent soft magnetic behavior of the synthesized ternary alloys. The alterations of magnetic characteristics were explained on the basis of size, surface effects, spin canting at the surface and presence of superparamagnetic fractions in the ultrafine materials.

References

1. J. Forsman, U. Tapper, A. Auvinen and J. Jokiniemi, J. Nanopart. Res., 10 (2008) 745-759.
2. Y. Hou, H. Kondoh, T. Ohta and S. Gao, Appl. Surf. Sci., 241 (2005) 218-222.
3. S. N. Khanna and S. Linderoth, Phys. Rev. Lett., 67 (1991) 742-745.
4. L. Yiping, G. C. Hadjipanayis, C. M. Sorensen and K. J. Klabunde, J. Magn. Magn. Mater., 104-107 (1992) 1545-1546.
5. J. P. Chen, C. M. Sorensen, K. J. Klabunde, G. C. Hadjipanayis, E. Devlin and A. Kostikas, Phys. Rev. B, 54 (1996) 9288-9296.
6. T. Hyeon, Chem. Commun., (2003) 927-934.
7. Q. Wang, A. Wu, L. Yu, Z. Liu, W. Xu and H. Yang, J. Phys. Chem. C, 113 (2009) 19875–19882.
8. F. C. Fonseca, G. F. Goya, R. F. Jardim, R. Muccillo, N. L. V. Carreno, E. Longo and E. R. Leite, Phys. Rev. B, 66 (2002) 104406.
9. A. A. El-Gendy, E. M. M. Ibrahim, V. O. Khavrus, Y. Krupskaya, S. Hampel, A. Leonhardt, B. Buchner and R. Klingeler, Carbon, 47 (2009) 2821-2828.
10. O. Margeat, C. Amiens, B. Chaudret, P. Lecante and R. E. Benfield, Chem. Mater., 17 (2005) 107-111.
11. M. Bahgat, M-K. Paek, C-H. Park and J-J. Pak, Mater. Trans., 49 (2008) 208-214.
12. G. Herzer, IEEE Trans. Magn., 26 (1990) 1397-1402.

13. S. K. Vajpai, B. V. Mahesh and R. K. Dube, J. Alloys Compd., 476 (2009) 311-317.
14. M. Kasture, S. Singh, P. Patel, P. A. Joy, A. A. Prabhune, C. V. Ramana and B. L. V. Prasad, Langmuir, 23 (2007) 11409-11412.
15. C. P. Bean and I. S. Jacobs, J. Appl. Phys., 31 (1960) 1228-1230.
16. A. Wu, X. Yang and H. Yang, J. Alloys Compd., 513 (2012) 193-201.
17. K. Srinivasa Rao, T. Balaji, Y. Lingappa, M. R. P. Reddy and T. L. Prakash, Phase Transitions, 85 (2012) 235-243.
18. A. H. Morrish and K. Haneda, J. Magn. Magn. Mater., 35 (1983) 105-113.
19. J. J. Host, J. A. Block, K. Parvin, V. P. Dravid, J. L. Alpers, T. Sezen and R. LaDuca, J. Appl. Phys., 83 (1998) 793-801.
20. J. D. Lee, H. S. Kim, S. Y. Jeong, K. H. Kim, J. J. Lee, B. Y. Ahn and S. I. Kim, J. Korean Phys. Soc., 46 (2005) 1142-1147.
21. X. Sun, Z. Y. Jia, Y. H. Huang, J. W. Harrell, D. E. Nikles, K. Sun and L. M. Wang, J. Appl. Phys., 95 (2004) 6747-6749.
22. R. N. Panda and N. S. Gajbhiye, J. Appl. Phys., 81 (1997) 335-339.
23. A. Monshi, M.R. Foroughi and M.R. Monshi, World Journal of Nano Science and Engineering, 2 (2012) 154-160.
24. R. M. Bozorth, Ferromagnetism, Wiley IEEE Press, NJ, 1993.
25. S. J. Yan, L. Zhen, C. Y. Xu, J. T. Jiang, W. Z. Shao, L. Lu and J. Tang, J. Appl. Phys., 109 (2011) 07A320.
26. E. Jartycht, J. Olchowik, J.K. Zurawicz and M. Budzynski, J. Phys.: Condens. Matter, 5 (1993) 8921-8926.
27. K. J. Carroll, D. M. Hudgins, L. W. Brown III, S. D. Yoon, D. Heiman, V. G. Harris and E. E. Carpenter, J. Appl. Phys., 107 (2010) 09A303.
28. D. A. Colling, J. Appl. Phys., 41 (1970) 1038-1039.
29. W. A. de Heer, P. Milani and A. Chatelain, Phys. Rev. Lett., 65 (1990) 488-491.
30. S. U. Jen, H. P. Chiang, C. M. Chung and M. N. Kao, J. Magn. Magn. Mater., 236 (2001) 312-319.

CHAPTER IV

Magnetic properties of some Co and Ni based metal/alloy nanoparticles synthesized via superhydride route

In this chapter, we have focused on synthesis, characterization and magnetic properties of Co, Ni, Fe-Co and Co-Ni alloys systems.

4.1 Introduction

The development of metal and alloys nanoparticles with high permeability for high temperature applications has become a subject of intensive research and cannot be achieved by the existing soft magnetic materials; for example: ferrites [1]. Magnetic properties of nanomaterials depend on particle size, shape, surface morphologies, crystal anisotropies and inter-particle interactions. It has been reported that chemical reduction carried out using superhydride as a reducing agent in organic medium can produce monodispersed nanoparticles of size <10 nm [2]. Advantages of superhydride over sodium borohydride mainly include facile reduction of metal ions at its atomic level with controlled size and shape which may be expected to arise from the flexibility of using different concentrations of metal ions in organic solvents along with the capping agents [2].

Single metal magnetic nanoparticles, e.g. Co and Ni, shows unique magnetic properties provided these nanoparticles must have air stability towards surface oxidation [3]. Hence, synthesis methodology which produces stable Co and Ni nanoparticles is needed in order to study their nanocrystalline properties. Further, it has been noted that intermetallic alloys of Fe, Co, Ni are more stable compare to single metal. Among all alloys, Fe-Co alloys are important soft magnetic materials due to their high saturation magnetization and low coercivity [4]. Amongst various binary alloys, Co-Ni alloys are more stable with respect to air oxidation and composition. Further, Co-Ni alloys are highly applicable in the field of catalysis because doping of transition metal in another transition metal could alter the d band electron filling and hence greatly alter the surface morphologies as well as catalytic efficiency of the materials [5, 6]. However the cobalt rich alloys have high manufacturing cost and their applications are limited. The issues need to be addressed is how to improve material stability and surface protection around magnetic nanomaterials. Therefore, synthesis, characterization and magnetic properties of Fe-Co and Co-Ni alloy nanomaterials are important topics for investigation. Several attempts have been undertaken for the preparation of oxide free and chemically stabilized metal or alloy nanoparticles [7-9]. The stabilization of these nanoparticles includes encapsulation with carbon or silica, coating with organic ligand such as oleic acid, oleylamine, n-trioctylphosphine or triphenylphosphine etc. It should be noted that capping with oleic acid and oleylamine could help in synthesis of stable, monodispersed nanoparticles with narrow size distribution [10, 11].

However, there is scanty literature available on the synthesis of oleic acid and oleylamine capped nanoparticles by superhydride route. The chemical nature of organic capping on the surface of alloy nanoparticles by oleic acid and oleylamine has not been explored in detail till to date. Therefore, motivation in our study lies on surface functionalization by oleic acid and oleylamine on the surface nanomaterials. We have adopted a modified synthetic strategy for stabilizing nanomaterials during the synthesis.

4.2 Experimental

The chemicals used for synthesis of above materials include ferric chloride hexahydrate ($FeCl_3 \cdot 6H_2O$), cobalt chloride hexahydrate ($CoCl_2 \cdot 6H_2O$), nickel chloride hexahydrate ($NiCl_2 \cdot 6H_2O$) and oleic acid, oleylamine, diphenyl ether and superhydride ($LiBEt_3H$, 1 M in THF) from Sigma Aldrich, USA. The chemicals were of analytical grade and have been used without further purification.

4.2.1 Synthesis of capped Co and Ni nanoparticles

Amount of metal salts used for synthesis of Co and Ni nanoparticles are tabulated in Table 4.1. In a typical synthesis, $CoCl_2 \cdot 6H_2O$ (or $NiCl_2 \cdot 6H_2O$) were added into 25 mL diphenyl ether in the 250 mL flask and stirred under high purity N_2(g) gas atmosphere for duration of 2 h at room temperature. Then, the resulting mixture was heated to 100°C and appropriate amount of capping agents were added. Further, this solution was heated to 200°C for the time duration 10 min and 3 mL/mmol superhydride solution ($LiBEt_3H$, 1 M in THF) was added into the hot solution drop-wise for a duration of approximately 5 min. Black dispersion of product nanoparticles was formed. The solution was stirred at 200°C for 30 min and at 240°C for 30 min in order to remove excess THF (boiling point = 157°C). The mixture was cooled down to room temperature and added 15 mL ethanol containing some amount of corresponding capping agents. The black solids were separated by centrifugation at 6000 rpm for 5 min and decanted out upper clear liquid. Black solids were again dispersed in 10 ml ethanol containing capping agents and centrifuged. Separated solids were dried at RT in vacuum (i.e. as-prepared materials). Finally, these as-prepared materials were heat treated in high purity N_2(g) atmosphere at higher temperatures (600°C) and used for further characterizations and magnetic properties study.

Table 4.1 Details of moles and weights of metal salts taken as starting materials for synthesis of Co and Ni nanoparticles via superhydride reduction method.

Materials	Metal salts	Moles (mmol)	weight (g)
Co (*, **)	$CoCl_2·6H_2O$	1	0.238
Ni (*, **)	$NiCl_2·6H_2O$	1	0.238

* Total metal ions concentration = 0.04 M.
** Capping agents - Oleic acid (0.32 ml) and Oleylamine (0.34 ml).

4.2.2 Synthesis of capped Fe-Co alloys nanoparticles

The synthesis method described in the above subsection (4.2.1) has been adopted for synthesis of Fe-Co binary alloys. For the synthesis of Fe_xCo_{100-x} alloys (x= 20, 40, 60, 80), stoichiometric amounts of metal salts were taken and are tabulated in Table 4.2. In a typical synthesis of Fe-Co binary alloys, stoichiometric amount $FeCl_3·6H_2O$ and $CoCl_2·6H_2O$ salts were added into 25 mL diphenyl ether in the 250 mL flask and stirred under high purity N_2(g) gas atmosphere for duration of 2 h at room temperature. The reduction procedure using superhydride was similar to the procedure described above in section 4.2.1 for the synthesis of Co and Ni nanoparticles. After final centrifugation, all Fe_xCo_{100-x} alloy samples were dried at RT in vacuum (i.e. as-prepared materials) and annealed in high purity N_2(g) atmosphere at higher temperature (600°C) and used for further characterizations and magnetic properties study.

Table 4.2 Details of moles and weights of metal salts used for synthesis of Fe-Co alloys via superhydride reduction method.

Materials	x	Metal salts	Moles (mmol)	weight (g)
Fe_xCo_{100-x} (*, **)	20	$FeCl_3 \cdot 6H_2O$	0.2	0.054
		$CoCl_2 \cdot 6H_2O$	0.8	0.190
	40	$FeCl_3 \cdot 6H_2O$	0.4	0.108
		$CoCl_2 \cdot 6H_2O$	0.6	0.143
	60	$FeCl_3 \cdot 6H_2O$	0.6	0.162
		$CoCl_2 \cdot 6H_2O$	0.4	0.095
	80	$FeCl_3 \cdot 6H_2O$	0.8	0.216
		$CoCl_2 \cdot 6H_2O$	0.2	0.047

* Total metal ions concentration = 0.04 M.

** Capping agents - Oleic acid (0.32 mL) and Oleylamine (0.34 mL).

4.2.3 Synthesis of capped Co-Ni alloys nanoparticles

Similarly, for the synthesis of Co_xNi_{100-x} binary alloys (x= 20, 40, 60, 80), stoichiometric amounts of metal salts were taken and are tabulated in Table 4.3. In a typical synthesis, stoichiometric amount $NiCl_2 \cdot 6H_2O$ and $CoCl_2 \cdot 6H_2O$ were added into 25 mL diphenyl ether in the 250 mL flask and stirred under high purity N_2(g) gas atmosphere for 2 h at room temperature. The reduction procedure using superhydride was similar to the procedure described above in section 4.2.2 for the synthesis of Fe-Co alloys. After final centrifugation, all Co_xNi_{100-x} alloy samples were dried at RT in vacuum (i.e. as-prepared materials) and also annealed in high purity N_2(g) atmosphere at higher temperature (400°C) and used for further characterizations and magnetic properties study.

Table 4.3 Details of moles and weights of metal salts taken for synthesis of Co-Ni alloys via superhydride reduction method.

Materials	x	Metal salts	Moles (mmol)	weight (g)
Co_xNi_{100-x} (*, **)	20	$CoCl_2 \cdot 6H_2O$	0.2	0.047
		$NiCl_2 \cdot 6H_2O$	0.8	0.190
	40	$CoCl_2 \cdot 6H_2O$	0.4	0.095
		$NiCl_2 \cdot 6H_2O$	0.6	0.143
	60	$CoCl_2 \cdot 6H_2O$	0.6	0.143
		$NiCl_2 \cdot 6H_2O$	0.4	0.095
	80	$CoCl_2 \cdot 6H_2O$	0.8	0.190
		$NiCl_2 \cdot 6H_2O$	0.2	0.047

* Total metal ions concentration = 0.04 M.

** Capping agents - Oleic acid (0.32 mL) and Oleylamine (0.34 mL).

4.3 Results and Discussion

4.3.1 Characterizations and magnetic properties of Co and Ni nanoparticles

4.3.1.1 FTIR spectroscopy studies of organic capping on Co and Ni nanoparticles

In order to prove the presence of organic capping on the surface of Co and Ni nanomaterials, FTIR spectroscopy studies were carried out. FTIR spectra for as-prepared (280°C) and heat treated (600°C) oleic acid/oleylamine coated Co and Ni nanoparticles are shown in Figure 4.1(a, b, c and d). For comparison, FTIR spectra of pure oleic acid and oleylamine were recorded and shown in Figure 4.2. The observed characteristics peak positions and assignments of vibrational modes are summarized in Table 4.4.

The characteristic peaks for pure oleic acid are located at 2850-3000 cm^{-1}, 1708 cm^{-1} and 2679 cm^{-1} due to oleyl group, $\nu(C{=}O)$ stretch and $\nu(O{-}H)$ stretch, respectively. Similarly, the characteristic peaks for pure oleylamine are located at 2850-3000 cm^{-1}, 1655 cm^{-1}, 1579 cm^{-1} and 3333 cm^{-1} which can be assigned due to oleyl group, $\nu(C{=}C)$ stretch, NH_2 scissoring mode and $\nu(N{-}H)$ stretch, respectively. The above mentioned values for the peak positions for oleic acid and oleylamine are in accordance with those reported by Shukla et al. [12].

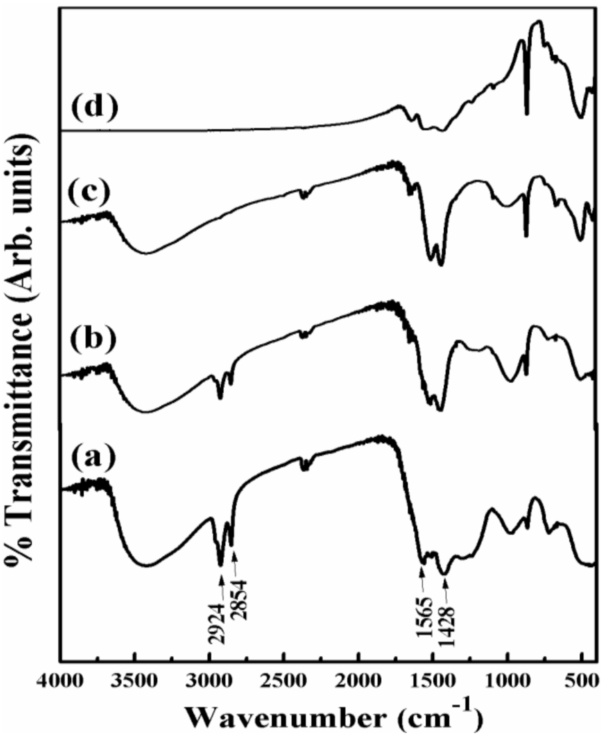

Figure 4.1 FTIR spectra of oleic acid and oleyl amine capped Co and Ni nanoparticles synthesized via superhydride route; (a) as-prepared Co, (b) as-prepared Ni, (c) Co heat treated at 600°C and (d) Ni heat treated at 600°C.

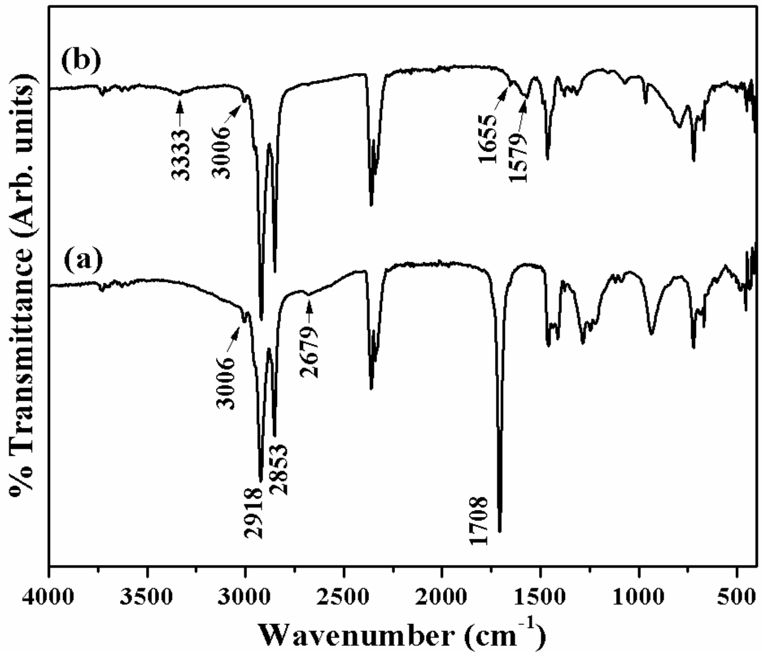

Figure 4.2 FTIR spectra of commercial (Sigma-Aldrich) (a) oleic acid and (b) oleylamine.

Table 4.4 FTIR frequencies and assignments for coated Co and Ni nanoparticles along with those of commercial (Sigma-Aldrich) oleic acid and oleylamine.

As-prepared Co nanoparticles, $\bar{\upsilon}$ (cm^{-1})	As-prepared Ni nanoparticles, $\bar{\upsilon}$ (cm^{-1})	Pure oleic acid, $\bar{\upsilon}$ (cm^{-1})	Pure oleylamine, $\bar{\upsilon}$ (cm^{-1})	Assignments
—	—	—	3333 w	N—H stretch
—	—	3006 w	3006 w	C—H stretch
2924 s	2924 s	2918 s	2918 s	asym. CH_2 stretch
2854 m	2854 m	2853 s	2853 s	sym. CH_2 stretch
—	—	2679 w	—	O—H stretch
—	—	1708 s	—	C═O stretch
—	—	1655 w	1655 w	C═C stretch
—	—	—	1579 b	NH_2 scissoring
1565 w	1565 w	—	—	asym COO^{-} stretch
1428 b	1428 b	—	—	sym COO^{-} stretch

Abbreviations: b-broad, s-strong, m-medium, w-weak, sym-symmetric, asym-asymmetric.

In case of as-prepared Co and Ni nanoparticles, the absence of peaks at 1708 cm^{-1}, 1592 cm^{-1} and 3325 cm^{-1} confirm the absence of pure oleic acid and oleylamine on the surface of nanoparticles. The peaks at 2924 cm^{-1} and 2854 cm^{-1} corresponds to oleyl group in the capping materials. The peaks in range of 1430-1565 cm^{-1} for the as-prepared Co and Ni nanomaterials can be assigned to carboxylate ($–COO^{-}$) group. The above mentioned result indicates capping of oleic acid and oleylamine in the form of their acid-base complex consisting of $–COO^{-}$ and $–NH_3^{+}$ ions. The peaks for olefinic C—H (3007 cm^{-1}) and ν(C═C) stretch (1654 cm^{-1}) mode are absent in the FTIR spectra. These results indicate some sort of feeble bonding interactions between metal nanoparticles and oleic acid-oleylamine mixture either via carboxylate ion or olefinic double bond [12, 13]. Several peaks are found in the finger print region (1450-400 cm^{-1}) for as-prepared Co and Ni. These lines may be interpreted as complex combinations of the ν(C—C) stretch, ν(C—O) stretch, CH_2 deformation and some other modes.

FTIR spectra for heat treated Co and Ni in N_2(g) atmosphere show the absence of oleic acid and oleylamine capping. The peaks in the region of 2854-2924 cm^{-1} were absent in case of heat treated materials which indicates decomposition of oleyl group into some other simpler organic compound(s). However, we have observed several peaks in the finger print region, the frequencies of which were different compared with the peaks in as-prepared materials (Figure 4.1). These results indicate the presence of thin organic capping of unknown materials at the surface of heat treated Co and Ni nanoparticles at 600°C.

4.3.1.2 XRD studies

The XRD patterns of Co and Ni heat treated at 600°C under N_2(g) atmosphere are presented in Figure 4.3(a, b). The XRD patterns for as-prepared Co and Ni nanomaterials are presented in inset of Figure 4.3. The as-prepared Co and Ni nanomaterials contain amorphous fractions majorly and the structural parameters for the heat treated nanomaterials were examined. The metallic phases of the materials were found to be oxide free. The XRD lines were broadened consistent with a nano-scale crystallite size. The lattice parameters and crystallite sizes of Co and Ni have been summarized in Table 4.5. Co crystallizes in the mixture of hexagonal close packed (hcp) (α) and face centered cubic (fcc) (β) crystal structures (JCPDS # 05-0727 (α-Co) and 15-0806 (β-Co)) [14]. The calculated lattice parameters for α-Co are a = 2.5049 Ǻ and c = 4.0856 Ǻ whereas for β-Co are a = 3.5383 Ǻ. Ni crystallizes in fcc crystal structure with lattice parameters value, a = 3.5273 Ǻ (JCPDS # 70-0989). Average crystallite sizes for Co and Ni were found to be 15 nm and 35 nm, respectively.

The amorphous nature of the as-prepared Co and Ni nanomaterials can be correlated with inhibition of grain growth during synthesis of the materials due to the presence of surfactants. Therefore, the structural and magnetic properties are expected to be different due to poor crystallization and surface functionalization of the nanomaterials. Generally, α-Co phase is stable at lower temperatures while β-Co phase is stable at temperatures above 450°C. However, the presence of both phases at 600°C is mainly due to the synthetic conditions used in chemical reduction route and fine particle nature of the materials [15]. The hcp crystal structure is the most stable structure in cobalt and the presence of fcc structure indicates the stabilization of a less stable structure. Evidence for such kind of stabilization of fcc phase has been reported for cobalt metal encapsulated within copper matrix [16].

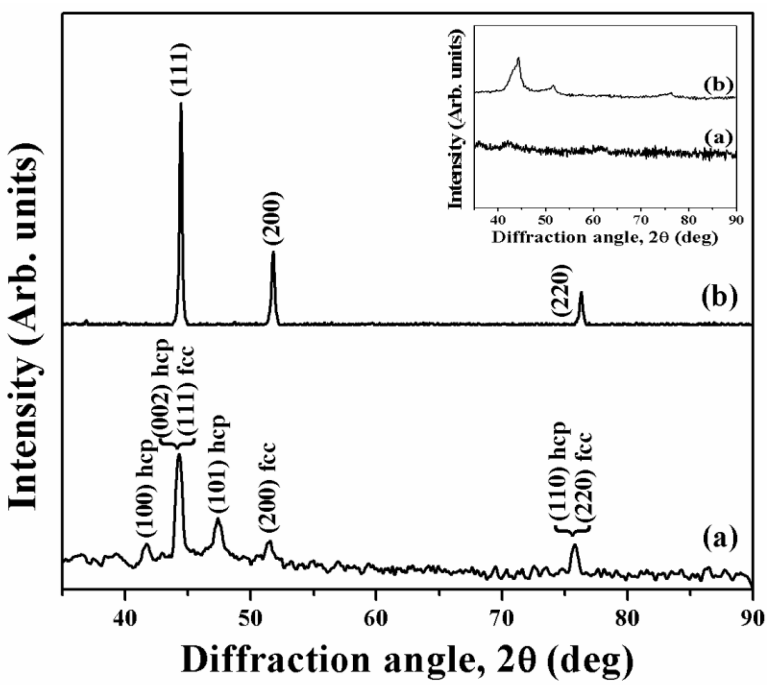

Figure 4.3 XRD patterns of (a) Co and (b) Ni nanoparticles heat treated at 600°C for 2 h duration under N_2 atmosphere. Inset represents the XRD patterns of as-prepared nanomaterials; (a) Co and (b) Ni.

The fraction of hcp and fcc phases present in Co sample were determined by using following equations 4.1 and 4.2 [17]:

$$P_{hcp} + P_{fcc} = 1 \tag{4.1}$$

$$P_{hcp} = \frac{I_{hcp}}{(I_{hcp} + 0.908\, I_{fcc})} \tag{4.2}$$

where, P_{hcp} and P_{fcc} are the fractions of hcp and fcc phases in Co, respectively; I_{hcp} and I_{fcc} are the intensities of (101) peak of hcp Co and (200) peak of fcc Co in the XRD patterns, respectively.

The XRD patterns for synthesized Co material indicate the presence of 53% α-Co and 47% β-Co phase (Figure 4.3(a)). The lattice parameters were determined from (002) and (101) peaks for α-Co whereas (111) peak in case of β-Co. The values of lattice parameters for α-Co and β-Co phases are in well agreement with reported values of a = 2.5088 Å, c = 4.0762 Å for α-Co and a = 3.5448 Å for β-Co [18]. The XRD pattern for Ni confirms the presence of stable fcc crystal phase (Figure 4.3(b)). The calculated value of lattice parameters, i.e. a = 3.5273 Å, is matching with reported value of a = 3.5242 Å [18].

4.3.1.3 TEM studies

TEM micrographs, with different magnifications, for Co and Ni heat treated at 600°C are shown in Figure 4.4(a, b, c, d). The TEM particle size distributions (frequency of occurrence vs. nano-size range) for Co and Ni nanoparticles have been shown in Figure 4.5(a, b). The average TEM particle sizes for Co and Ni determined from TEM micrographs are summarized in Table 4.5. TEM micrographs with magnifications 135000X and 225000X of Co and Ni, respectively (Figure 4.4 (a) and (c)) confirm that both Co and Ni have monodispersed nanostructures with nearly spherical morphologies. However, there are very few cases of irregular shaped particles observed at the surface of the nanomaterials. In order to get more accurate view and for particle size estimations, images at higher magnifications (310000X) were taken (Figure 4.4 (b) and (d)).

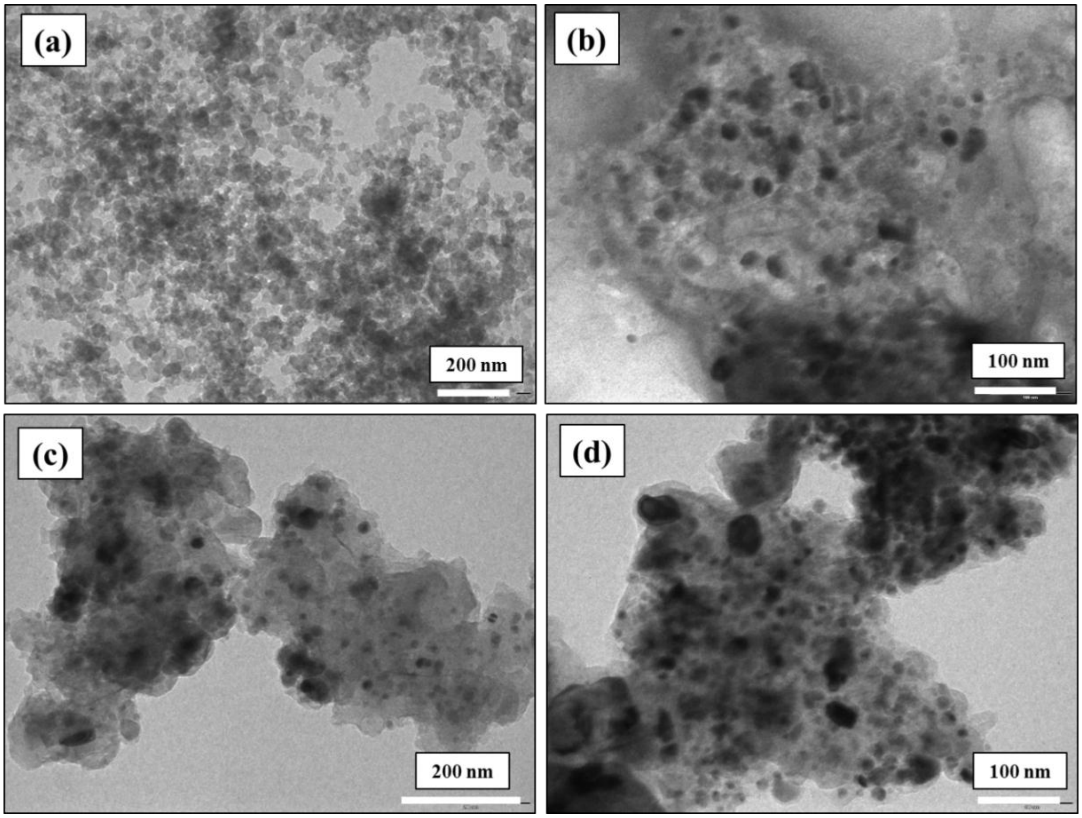

Figure 4.4 (a), (b) TEM micrographs with different magnifications of Co nanoparticles and (c), (d) of Ni nanoparticles, heat treated at 600°C for 2 h under N_2(g) atmosphere.

Particle size distribution plots of Co and Ni (Figure 4.5) show presence of particles in the size range of 6-16 nm. However, average TEM particle sizes for Co and Ni were estimated to be 11±2 nm and 10±2 nm, respectively. The estimated TEM particle sizes are smaller than crystallite sizes, i.e. 15 nm and 35 nm, for Co and Ni respectively. These results might be due to the fact that TEM particle size corresponds to local probe which contains smaller particles only while crystallite size corresponds to the average of the whole mass including larger crystallites [19]. It indicates the fine particle nature of synthesized materials with relatively narrow particle size distributions.

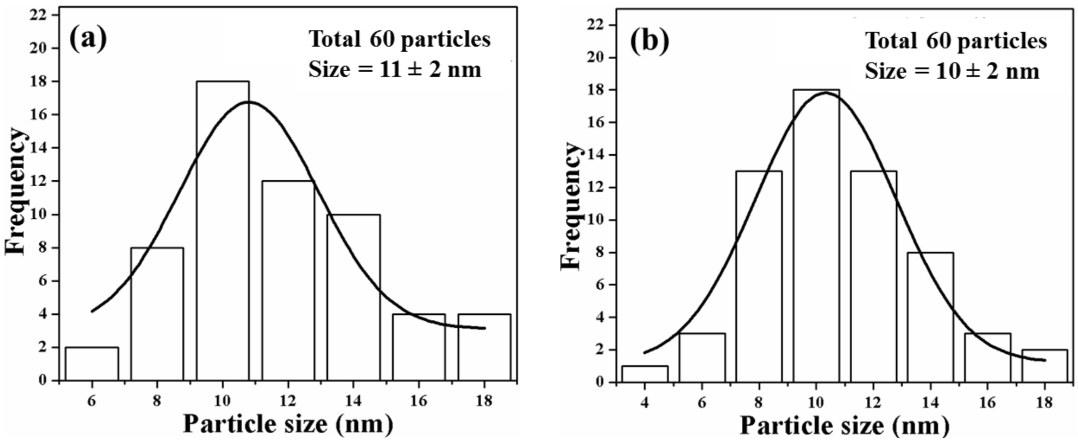

Figure 4.5 TEM particle size distributions plots for (a) Co and (b) Ni nanoparticles.

Table 4.5 Crystallite size, TEM particle size, saturation magnetization and coercivity of Co and Ni nanoparticles heat treated at 600°C for 2 h under N_2(g) atmosphere.

Materials	Crystallite size (nm)	TEM particle size (nm)	Saturation magnetization, M_S (emu/g)	Coercivity, H_C (Oe)
Co	15	11 ± 2	64	436
Ni	35	10 ± 2	29	148

4.3.1.4 Investigation of magnetic properties

The magnetic properties of materials have been investigated from the studies of room temperature magnetic hysteresis loop (M-H curve). Field dependence of the magnetization for Co and Ni are shown in Figure 4.6. The inset of the Figure 4.6 represents M vs. 1/H plots of Co and Ni nanoparticles. The M_S were determined from the intercept of M vs. 1/H plot. The estimated values of M_S and H_C for Co and Ni are summarized in Table 4.5. The values of M_S are found to be 64 and 29 emu/g whereas the values H_C are 436 Oe and 148 Oe for Co and Ni, respectively.

The magnetic hysteresis loops confirm that both Co and Ni show ferromagnetic behavior at room temperature (Figure 4.6). The values of M_S for Co and Ni, i.e. 64 and 29 emu/g, respectively, were found to be smaller than the values for bulk Co (162 emu/g) and Ni (55.4 emu/g) [3]. It has been reported that hcp Co phase is stable at ambient conditions whereas fcc Co phase is formed after annealing above 450°C. However, fcc Co phase can be obtained at ambient conditions in nanomaterials with controlled synthesis [14]. Further, bulk hcp Co is magnetically hard phase compare to fcc Co phase with M_S value equal to 162 emu/g and H_C value greater than 100 Oe. While bulk fcc Co is soft magnetic phase with M_S value equal to 172 emu/g and H_C value less than 100 Oe [14, 20]. Also, magnetization of the materials was not saturated up to 4000 Oe field which confirms the presence of superparamagnetic fractions. It indicates that magnetic properties of nanocrystalline materials are dependent on size, shape, spin canting at the surface, altered crystal anisotropies and magnetic dipole interactions etc. [21, 22]. These aspects have already been explained in the chapter I, subsection 1.6.4. The decrease in saturation magnetization value may be attributed to the above mentioned parameters. Further, non-magnetic layers present on the surface of nanoparticles may also result in the reduction of saturation magnetization value [23]. Further, reduction of saturation magnetization in our Co nanomaterials may also be due to presence of fcc phase (47%) which show reduction in magnetization in nanoparticle systems [24].

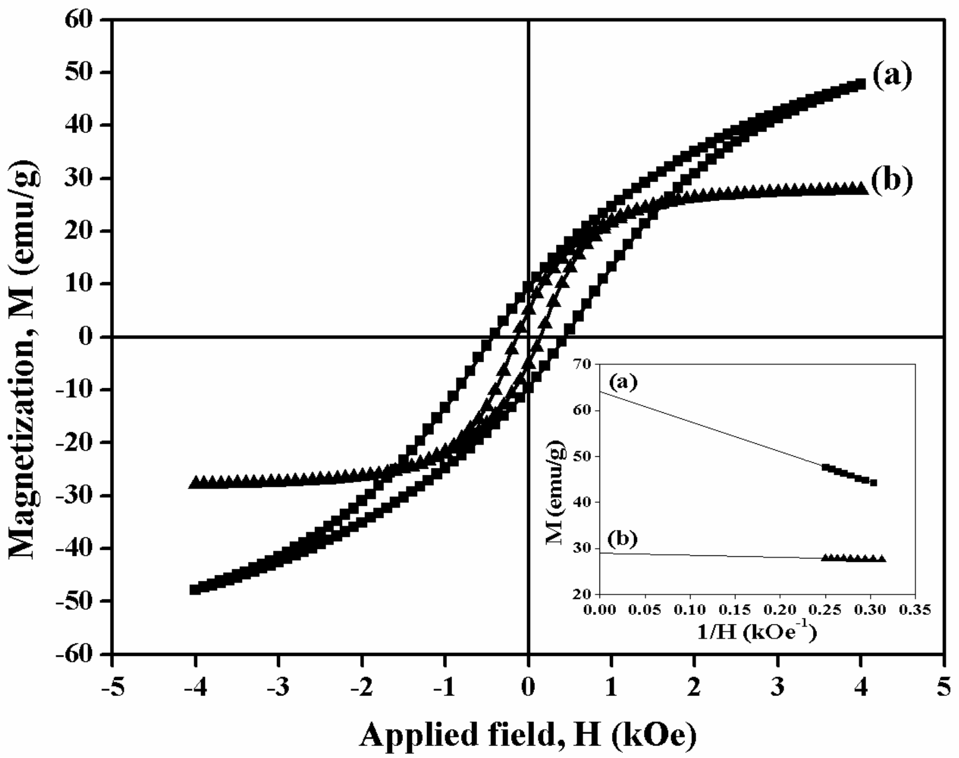

Figure 4.6 Room temperature magnetic hysteresis loops for (a) Co and (b) Ni heat treated at 600°C for 2 h under $N_2(g)$ atmosphere. Inset represents corresponding M vs. 1/H plots and its extrapolated portions towards $1/H \rightarrow 0$.

The coercivity values of Co and Ni, i.e. 436 Oe and 148 Oe, respectively, are higher than the values corresponding to superparamagnetic behavior. In particular, the value of saturation magnetization (64 emu/g) is significantly less and coercivity (436 Oe) is quite higher for Co nanomaterials than that of Wang et al. (110.8 Oe) observed for Co nanoplatelets [17]. It is expected that shape anisotropy contribution in our material is less significant. Therefore, the higher values of coercivity can be due to the presence of magnetically hard hcp Co phase. Also, small ferromagnetic fractions having larger particles, as indicated by particle size distribution studies, can results in larger H_C values for Co and Ni nanoparticles. This variation can be understood as altered synthesis methodology and material structures in the current study.

4.3.2 Characterizations and magnetic properties of Fe-Co nanoparticles

4.3.2.1 CHN analysis and FTIR spectroscopy studies of organic capping on Fe-Co nanoparticles

For Fe-Co alloys, in order to ascertain the chemical nature of the capping layer, we have performed organic content analysis by CHN and FTIR on the samples, heat treated at 600°C under N_2(g) atmosphere. The CHN content for various Fe-Co samples are tabulated in Table 4.6. The CHN contents were found to be 35.00, 32.82 and 23.53 wt% for $Fe_{40}Co_{60}$, $Fe_{60}Co_{40}$ and $Fe_{80}Co_{20}$ alloy compositions, respectively. The major fraction of materials in the organic capping layer were carbon, i.e. 33.39, 31.17 and 21.42 with C:H ratios 21.0:1, 19.8:1 and 10.4:1 for $Fe_{0.4}Co_{0.6}$, $Fe_{0.6}Co_{0.4}$ and $Fe_{0.8}Co_{0.2}$, respectively. To be noted that C:H ratio used during the synthesis was 6:1. The observation of higher C:H ratios in the capping layers indicate the presence of unknown carbonaceous materials which are chemically and structurally different from the oleic acid, oleylamine and/or their complex combinations. FTIR spectra of heat treated samples of $Fe_{40}Co_{60}$, $Fe_{60}Co_{40}$ and $Fe_{80}Co_{20}$ are shown in Figure 4.7. These results are quite similar to the nature of capping on the pure Co and Ni nanoparticles irrespective of the alloy compositions. The FTIR study confirms the absence of pure oleic acid and oleylamine at the surface of the nanoparticles. The presence of organic capping layer after the heat treatment of the as-prepared oleic acid/oleylamine capped particles is believed to be playing a role in stabilizing from surface oxidation of nanoparticles even at room temperature.

Table 4.6 Atomic % of N, C and H present in the Fe-Co alloys with various compositions.

Materials	at % of N	at % of C	at % of H	Total CHN content (at %)	C/H ratio
$Fe_{40}Co_{60}$	0.02	33.39	1.59	35.00	21.0
$Fe_{60}Co_{40}$	0.08	31.17	1.57	32.82	19.8
$Fe_{80}Co_{20}$	0.06	21.42	2.05	23.53	10.4

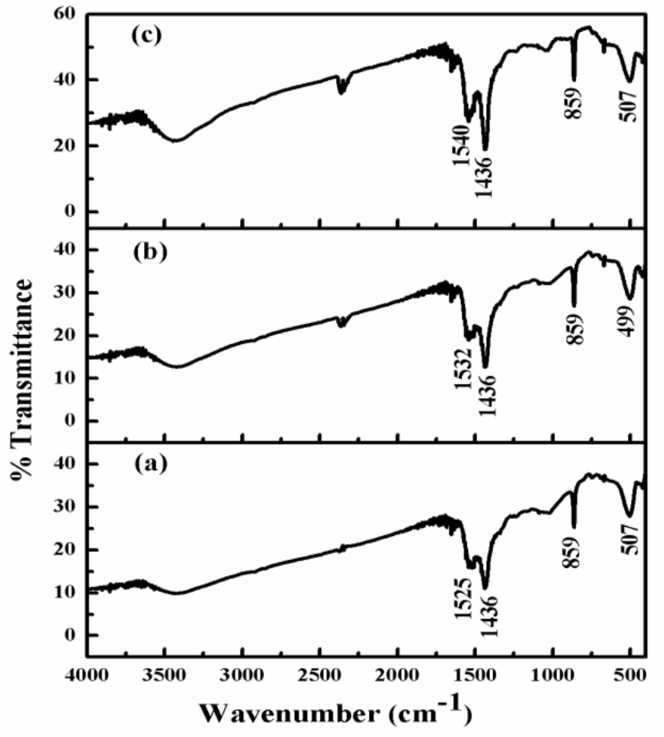

Figure 4.7 FTIR spectra of oleic acid and oleylamine capped Fe-Co nanoparticles synthesized via superhydride route and heat treated at 600°C under N_2(g) atmosphere; (a) $Fe_{40}Co_{60}$, (b) $Fe_{60}Co_{40}$ and (c) $Fe_{80}Co_{20}$.

4.3.2.2 Solid state reactivity and XRD studies of Fe-Co nanoparticles

Fe_xCo_{100-x} ($20 \leq x \leq 80$) alloys with different compositions were synthesized under similar experimental conditions as mentioned earlier (section 4.2.2). The as-synthesized alloys were heat treated at various temperatures (400-600°C) under high purity N_2(g) atmosphere in order to increase the crystallinity of the materials and to observe any order-disorder phase transformation. However, we have optimized the minimum temperature, i.e. 600°C, required for the crystallization of Fe-Co alloys in order to obtain ultrafine particles. XRD patterns of Fe-Co alloys having different compositions, i.e. Fe_xCo_{100-x} ($20 \leq x \leq 80$), heat treated at 600°C are shown in Figure 4.8. It is observed that $Fe_{20}Co_{80}$ alloy contains major bcc (α) and minor fcc (γ) whereas Fe-Co alloy phases having Fe content (x) above 40, show single α-Fe-Co alloy phase. The observations of various phases in different compositions of Fe_xCo_{100-x} are shown in phase diagram (Figure 4.9). Our results of obtaining α-Fe-Co phase for $x > 40$ are in accordance with the phase diagram [25, 26] where it has been observed that Co can diffuse into the α-Fe structure in order to form Fe-Co solid solution. Thus, the presence of mixture of α and γ phases simultaneously in $Fe_{20}Co_{80}$ alloy may be because of large Co content that exceeds the solubility limit (72-90 % of Co content) for the formation of Fe-Co solid solution at room temperature.

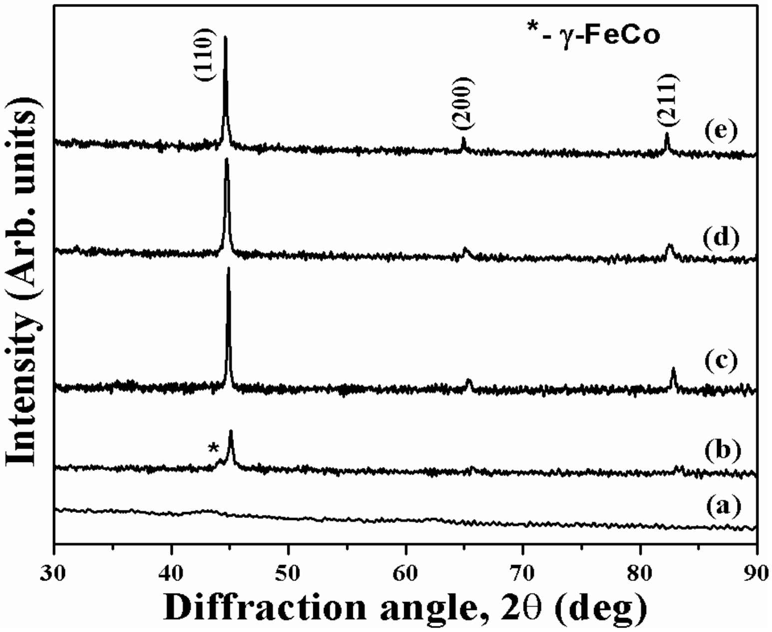

Figure 4.8 XRD patterns of (a) $Fe_{20}Co_{80}$, (b) $Fe_{40}Co_{60}$, (c) $Fe_{60}Co_{40}$ and (d) $Fe_{80}Co_{20}$ alloys nanoparticles annealed at 600°C.

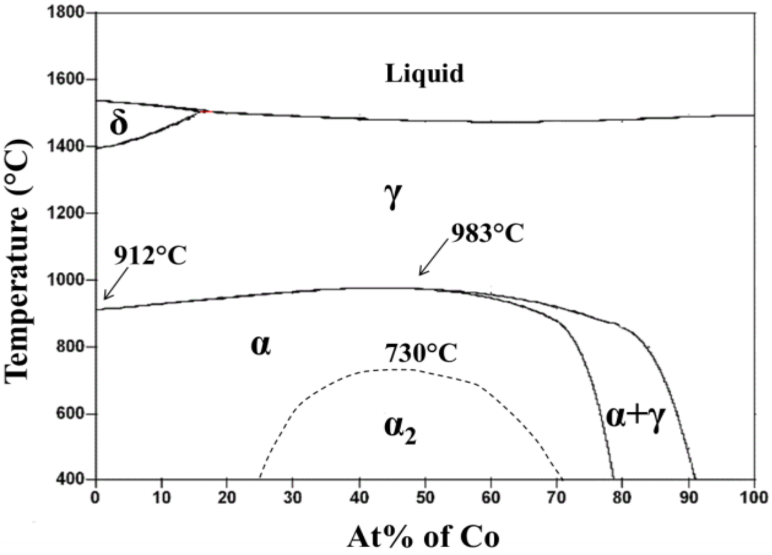

Figure 4.9 Phase diagram for Fe-Co alloys with various compositions [25, 26].

The XRD peaks were broad in nature. This result indicates the signature of nano-crystalline nature of the materials. Crystallite sizes for Fe-Co alloys are represented in Table 4.7. The observed XRD peak positions are indexed in accordance with JCPDS card for α-Fe-Co alloy (JCPDS # 49-1567).

The compositions (i.e. Fe_xCo_{100-x} ($40 \leq x \leq 80$) studied in the present work are within the regime where one can expect order-disorder transformation above 400^oC. However, the (100) super lattice peak position at 2θ values of $\sim 36.4^o$ is not observed in the XRD patterns of the annealed Fe-Co materials up to a temperature of 600°C [27]. Suppression of phase transformation in ultrafine nano-materials have been reported in the literature [28, 29], however, for Fe-Co systems using the present synthetic strategy is the first time report.

The calculated values of lattice parameters (a) for α- Fe_xCo_{100-x} alloys are 2.836(±4) Å, 2.852(±2) Å, 2.859(±1) Å and 2.868(±1) Å for x = 20, 40, 60 and 80, respectively (Table 4.7). The shift in the peak positions and increase in the lattice parameters were observed with the increase in Fe content in Fe-Co alloys. These results confirm the formation of α-Fe-Co alloy solid solution where Fe atoms are in bcc phase [30, 31]. The calculated lattice parameters for Fe-Co alloys are comparable, but slightly less than the value for bulk α-Fe, i.e. 2.866 Å [32]. Average crystallite sizes for the synthesized Fe-Co alloys were found to be in the range of ≈ 23-38 nm for the heat treated materials.

Table 4.7 Compositions, crystalline phase, lattice parameters and crystallite sizes for Fe-Co alloy nanoparticles with different compositions. Figure(s) in parentheses include error bars.

Composition	Crystalline phase	Lattice parameters (Å)	Crystallite size (nm)
$Fe_{20}Co_{80}$	bcc + fcc	2.836(±4)	23.30(±3)
$Fe_{40}Co_{60}$	bcc	2.852(±2)	37.93(±1)
$Fe_{60}Co_{40}$	bcc	2.859(±1)	26.06(±2)
$Fe_{80}Co_{20}$	bcc	2.868(±1)	38.27(±2)

4.3.2.3 TEM microstructural studies of Fe-Co nanoparticles

TEM micrographs at various magnifications for Fe-Co alloys annealed at 600°C are shown in Figure 4.10. TEM particle size distribution plots are represented in Figure 4.11. Figure 4.12 shows SAED patterns for Fe-Co alloys. The estimated average particle sizes for Fe-Co alloys from TEM micrographs are summarized in Table 4.8. TEM micrograph studies confirm that the synthesized Fe-Co alloys have nearly spherical morphologies. Average particle sizes for Fe-Co alloys, estimated from TEM micrographs ranges from 10 nm to 51 nm and are comparable with the average crystallite sizes obtained using XRD technique, i.e. 23 to 38 nm. TEM particle size distributions are reasonably narrow and are evident from the estimated size deviation of 0.6-2.2 nm from average values (Table 4.8).

SAED pattern shows the formation of broader diffraction rings which indicates polycrystalline nature of the materials. The diffraction from the crystalline planes, i.e. (110), (200), (211) etc. in SAED pattern for Fe-Co alloys for all compositions matches exactly with the XRD results and confirm the formation of α-Fe-Co alloy phase. In addition, the lattice parameters values obtained from SAED patterns, i.e. 2.79(±1), 2.845(±7), 2.856(±5) and 2.80(±2) Ǻ for Fe_xCo_{100-x}, x = 20, 40, 60 and 80, respectively, agrees well with the corresponding values obtained from XRD results.

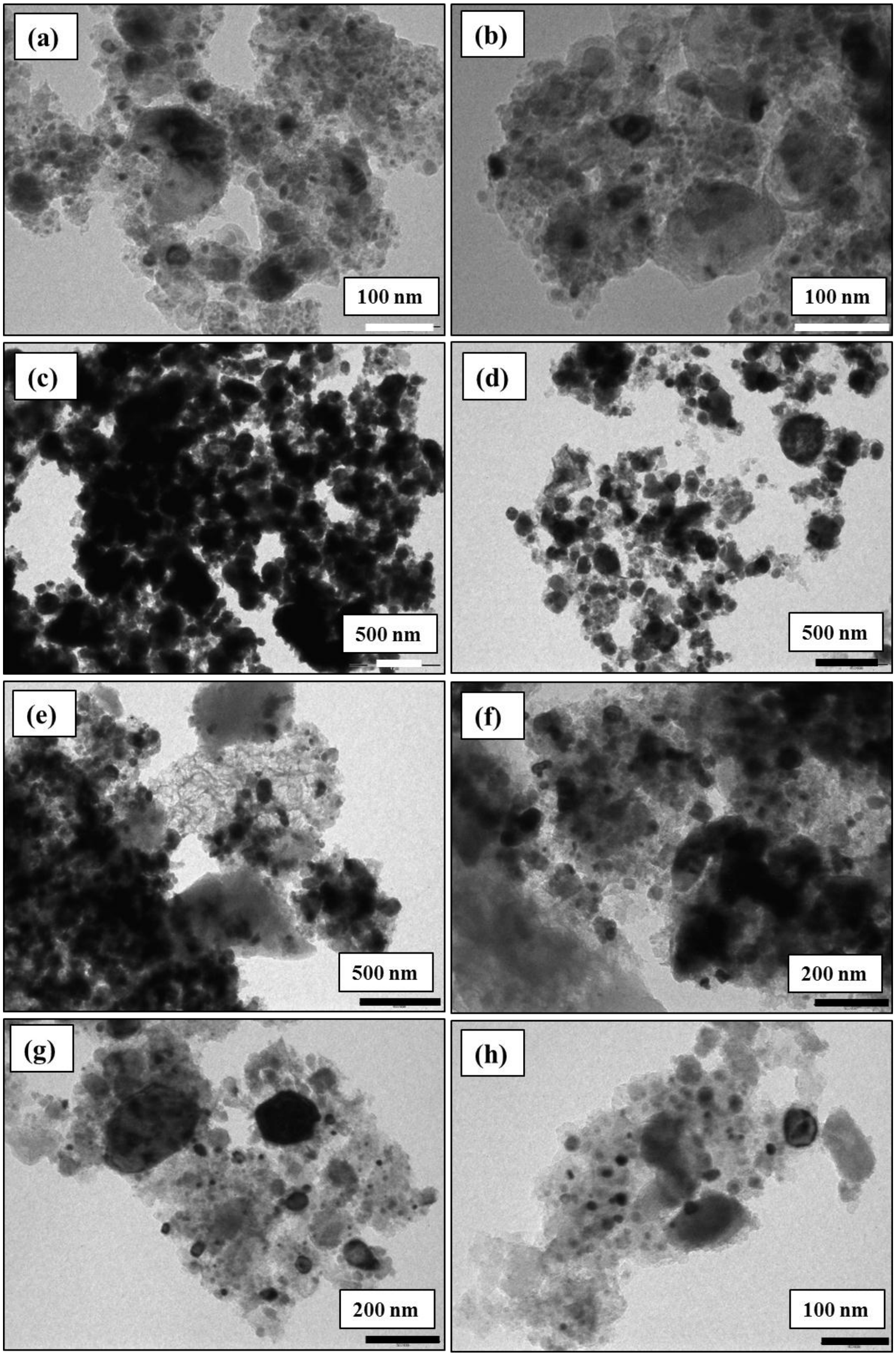

Figure 4.10 TEM micrographs with various magnifications of (a) (b) $Fe_{20}Co_{80}$; (c) (d) $Fe_{40}Co_{60}$; (e) (f) $Fe_{60}Co_{40}$ and (g), (h) $Fe_{80}Co_{20}$ alloys nanoparticles annealed at 600°C under $N_2(g)$ atmosphere.

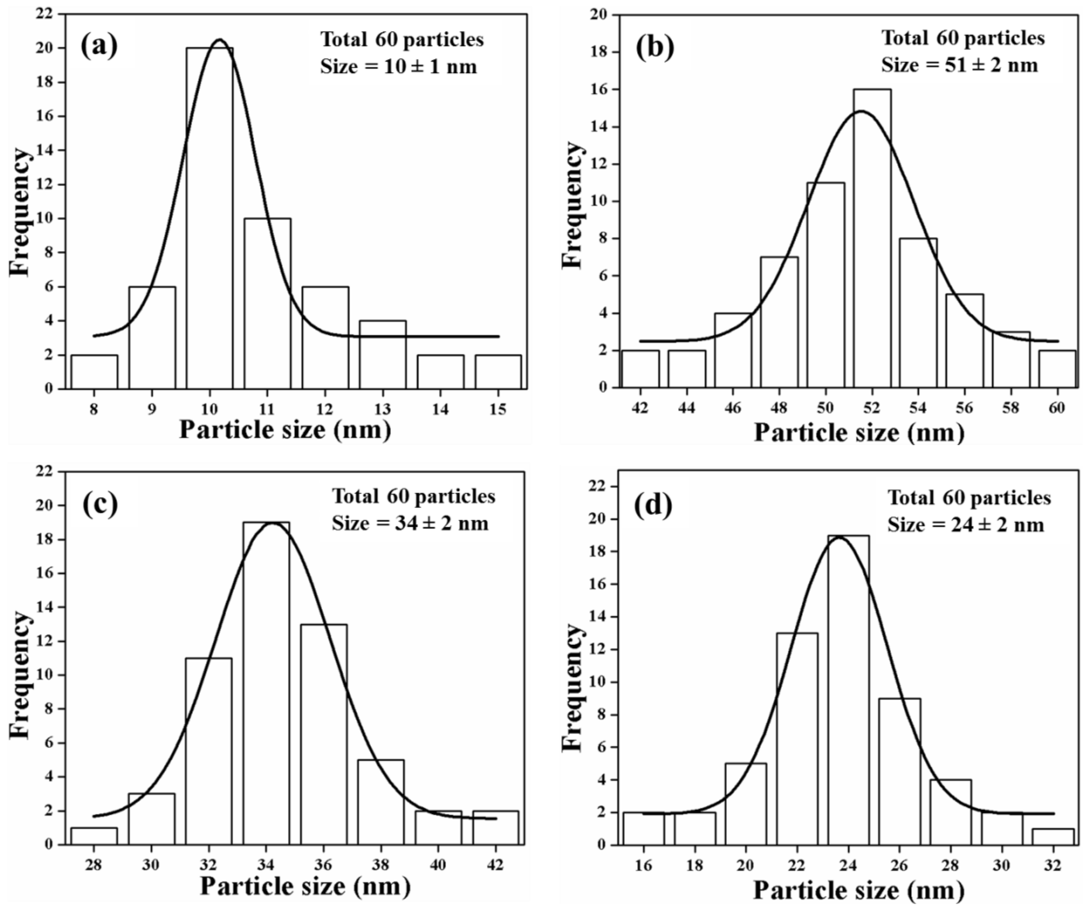

Figure 4.11 TEM particle size distribution plots of (a) $Fe_{20}Co_{80}$, (b) $Fe_{40}Co_{60}$, (c) $Fe_{60}Co_{40}$ and (d) $Fe_{80}Co_{20}$ alloys nanoparticles annealed at 600°C under N_2(g) atmosphere.

Table 4.8 Compositions, TEM particle sizes, saturation magnetizations (M_S), corrected saturation magnetizations (M'_S), remanent magnetizations (M_r) and coercivity (H_C) values for Fe-Co alloy nanoparticles with different compositions.

Composition	TEM Particle size (nm)	M_S (emu/g)	M'_S (emu/g)	M_r (emu/g)	H_C (Oe)
$Fe_{20}Co_{80}$	10 ± 1	--	--	--	--
$Fe_{40}Co_{60}$	51 ± 2	92.5(±1)	142.2	2.2	244
$Fe_{60}Co_{40}$	34 ± 2	67.1(±1)	100.1	9.3	400
$Fe_{80}Co_{20}$	24 ± 2	71.1(±0.5)	93.1	10.4	472

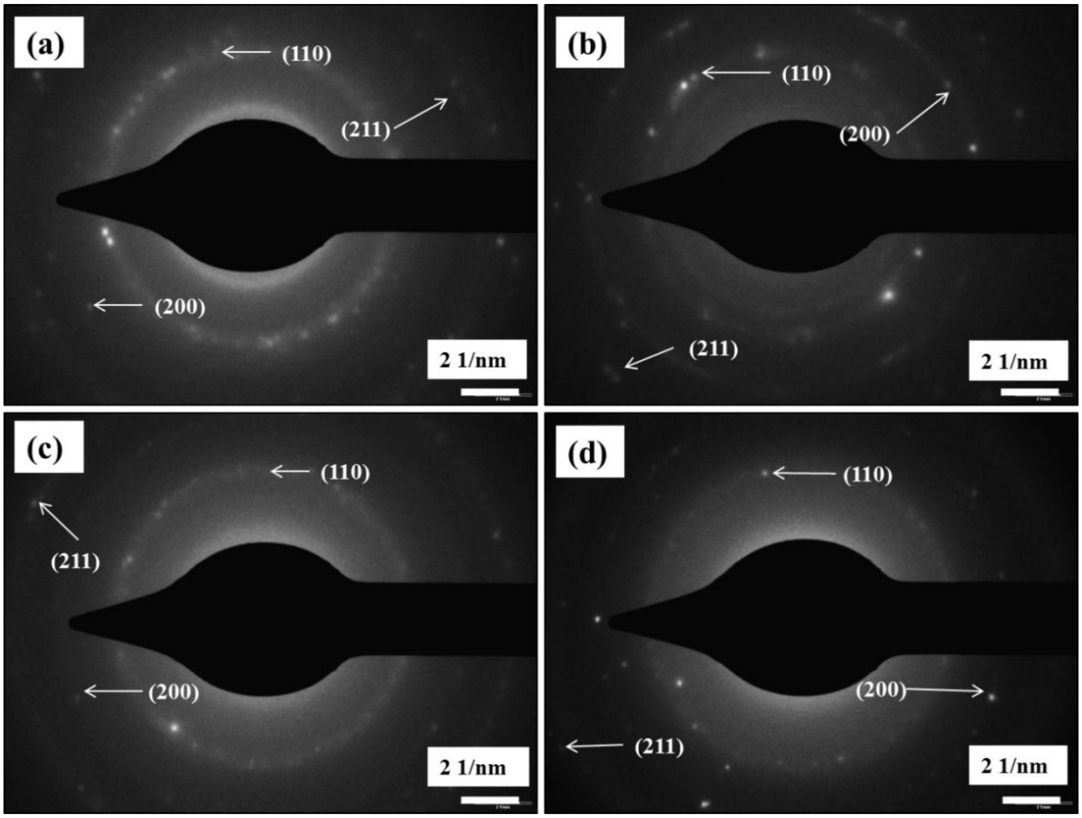

Figure 4.12 SAED patterns of (a) $Fe_{20}Co_{80}$, (b) $Fe_{40}Co_{60}$, (c) $Fe_{60}Co_{40}$ and (d) $Fe_{80}Co_{20}$ alloys nanoparticles annealed at 600°C under N_2(g) atmosphere. Observed diffraction rings are indexed in accordance with bcc crystal structure.

4.3.2.4 Magnetic properties of Fe-Co nanoparticles

M vs. H curves for Fe_xCo_{100-x} alloys (x = 40, 60, 80) have been shown in Figure 4.13 and the inset represents the corresponding values of the M_S. As $Fe_{20}Co_{80}$ alloy crystallizes with mixture of two phases, i.e. fcc and bcc, the material is excluded while investigating the composition dependent of magnetization. Fe-Co alloys annealed at 600°C, contain organic coating at the surface. Therefore, two different values of M_S are reported herewith, i.e. one denotes M_S without considering wt% of organic layer and the other, M'_S , after wt% corrections corresponding to CHN content. Considering the very high values of C/H ratios, the oxygen content is assumed to be negligibly small and not considered while estimating the corrected values for M_S. The values of the M_S of the materials were determined by M vs. 1/H law. The estimated extrapolated values of the M_S, M_r and H_C for Fe-Co alloys are tabulated in Table 4.8. The values of M_S, M_r and H_C

for Fe_xCo_{100-x} alloys (x = 40, 60, 80) are found to be in the range of 71.1-92.5 emu/g, 2.2-10.4 emu/g and 244-472 Oe, respectively. After corrections employed for wt% of organic coatings, the values of the M_S are estimated in the range of 93.1-142.2 emu/g for Fe_xCo_{100-x} alloys (x = 40, 60, 80).

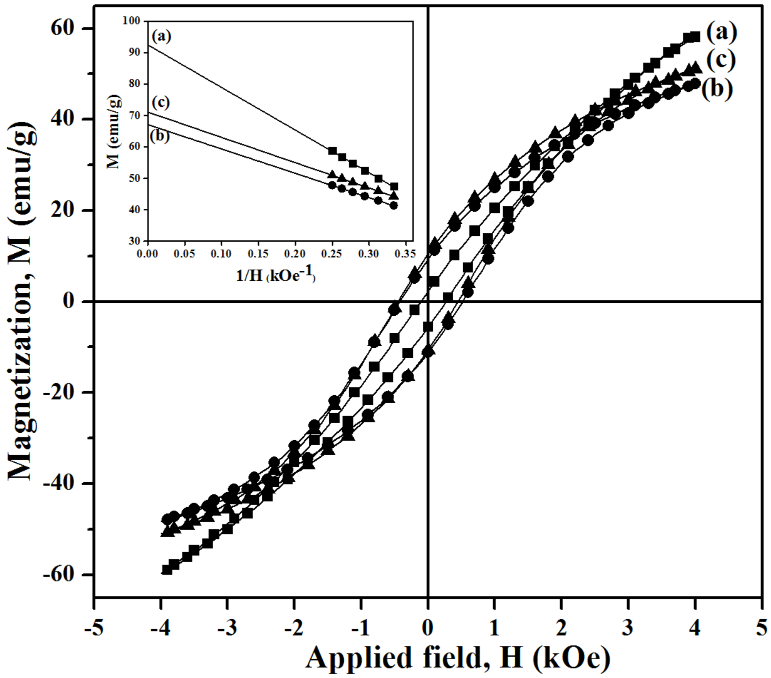

Figure 4.13 Room temperature magnetic hysteresis loops for (a) $Fe_{40}Co_{60}$, (b) $Fe_{60}Co_{40}$ and (c) $Fe_{80}Co_{20}$ alloys nanoparticles heat treated at 600°C for 2 h under N_2 atmosphere. Inset represents the corresponding M vs 1/H plots and its extrapolated portions towards $1/H \rightarrow 0$.

The magnetic hysteresis loops confirm that Fe-Co alloys exhibit ferromagnetic behavior at room temperature (Figure 4.13). The values of M_S, i.e. 71.1-92.5 emu/g, and 93.1-142.2 emu/g, for Fe-Co alloys having organic coating and after correction for wt% for organic coating are smaller than the values reported for bulk ordered materials (i.e. 245 emu/g) [33]. This may be attributed to the combined effects of altered crystal anisotropies, disordered structure, reduction in particle size and spin canting at the surface of nanomaterials [34]. It has been established by Zeng et al. [33] that reduction of M_S (say maximum up to ≈15 emu/g) is observed as a result of disordering in the distribution of Fe and Co atoms in the crystal structure. The disordered structure has already been established by our XRD results. Although, almost constancy in magnetic anisotropy may be observed at least up to room temperature for ideal Fe-Co bulk magnetic materials, significant alteration may not be over ruled for nano materials. Therefore, additional reduction in magnetization at room temperature may be attributed to thermal effects at our measurement temperature, i.e. 298K. The estimated maximum value of M_S, i.e. 143emu/g, for $Fe_{40}Co_{60}$ alloy composition after correction for organic capping, is still significantly lower than the bulk saturation, i.e. 245 emu/g. This result indicates the signature of onset of fine particle size and surface effects including superparamagnetism in Fe-Co alloys synthesized by the present strategy and such reduction has already observed in several magnetic materials [28, 35].

It should be noted that specific magnetization vs. field plots of Fe-Co alloys at room temperature do not saturate up to an applied field of 4000 Oe. These results confirm the presence of superparamagnetic fractions in the alloy materials. Also, it is observed that there is alteration of M_S values with Fe content in the Fe_xCo_{100-x} alloys (Figure 4.14). It should be noted that magnetic saturation is related to positions and arrangements of atoms in the crystal structure and resultant magnetization may be dependent on magnetic exchange interactions among atomic moments [36]. Also, it is reported that M_S values for Fe-Co alloys are composition dependent and may vary with concentration of Fe in the Fe_xCo_{100-x} ($40 \leq x \leq 80$) nanomaterials [37]. With the increase in Fe at% (x) in Fe-Co alloys, the values of M_S, initially increases, shows a maximum ($\approx x = 50$) and thereafter decreases. The shifting of the maximum is dependent on materials structure obtained by using alternative synthetic methods [37, 38]. In our study, we obtained gradual decrease in the values of M_S with increase in the Fe at% (x) (from $x = 40$ to 80) measured at room temperature from M vs. H plots and after applying the corrections for CHN content (Figure 4.14(b)). Although, particle size distribution and presence of superparamagnetic fractions may influence the values of M_S, in the present study, effect of composition of the Fe-Co alloys is dominant for the decreasing trend of the M_S values. It should be noted that the wt% correction abruptly increases the values of M'_S compared to M_S with the increase of Co content. The abrupt changes may result from the small variation of organic content due to different chemical affinity of nano-materials with different composition, even though the synthetic parameters are similar. The variation of H_C of Fe_xCo_{100-x} ($40 \leq$

$x \leq 80$) nanomaterials with gradual increase in the values of x has been shown in Figure 4.14(c) and the values of M_r are presented in Table 4.8. The gradual increase in the values of H_C with increasing Fe content may be attributed to different size and surface morphologies along with composition [38, 39]. It has been reported in the literature that H_C values are inversely proportional to the grain size of the material above a critical size and our results are in accordance with the literature reports [33]. The reduced values of the ratios of remanent magnetization and saturation magnetization, i.e. M_r/M_S, of the Fe_xCo_{100-x} alloys are found to be 0.02, 0.13 and 0.14 for x equal to 40, 60 and 80, respectively. This indicates that crystal anisotropies increase with the increase in Fe content and supports the increasing trend in the values of the coercivities. Such kinds of results have already been reported in the literature for Fe-Co system [40].

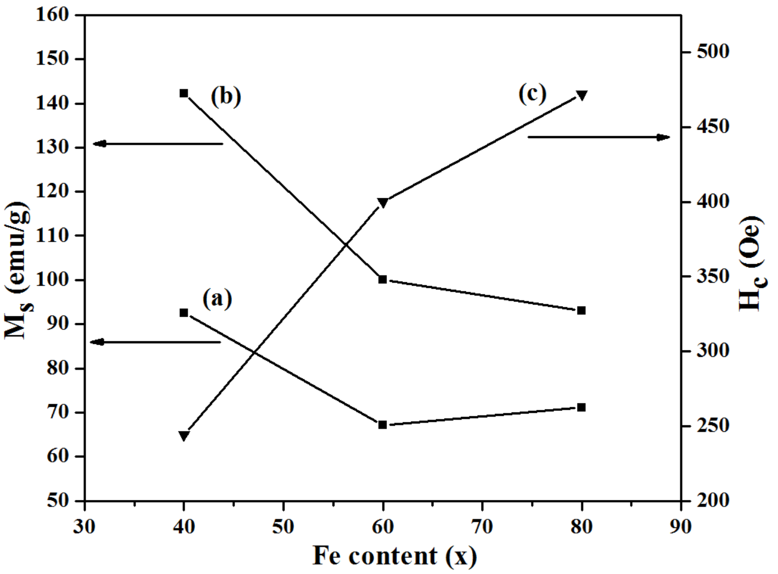

Figure 4.14 Plot of variations in values of (a) M_S, (b) M'_S and (c) H_C with respect to increasing Fe content in the Fe_xCo_{100-x} alloys ($40 \leq x \leq 80$).

4.3.2.5 Mössbauer Spectroscopic studies of Fe-Co alloys

The room temperature Mössbauer spectra of Fe_xCo_{100-x} alloys (x = 40, 60, 80) have been shown in Figure 4.15 along with its fitted sub-spectra for clarity reason. The values of hyperfine field (H_{hf}), isomer shift (δ), line width and relative intensities of the fitted sub spectra are summarized in Table 4.9. The Mössbauer spectrum of $Fe_{20}Co_{80}$ did not show well defined Mössbauer absorption. This may be attributed to the presence of less amount of Fe content and mixture of two phases in the structure of the alloy. The Mössbauer spectra of $Fe_{40}Co_{60}$, $Fe_{60}Co_{40}$ and $Fe_{80}Co_{20}$ having crystallite sizes of 38 nm, 26 nm and 38 nm, respectively, were deconvoluted into ferromagnetic sextet and superparamagnetic doublet of Fe-Co material. The relative intensity of the sextet:doublet in $Fe_{40}Co_{60}$, $Fe_{60}Co_{40}$ and $Fe_{80}Co_{20}$ alloys are 80:20, 90:10 and 80:20, respectively.

As the relative intensity of the doublet and sextet is related to the fraction of superparamagnetic nanoparticles present in the materials, saturation magnetizations in the alloys may differ significantly. This indicates the fine particle nature of our materials with particle size distribution. The presence of one sextet indicates single Fe site with equivalent chemical environment in Fe-Co alloys. Interpretation of Mössbauer data of Fe-Co alloys with one sextet has already been reported for materials synthesized by sonochemical method [41]. The line widths of the Mössbauer spectra are broadened, i.e. 0.44 mm/s, 0.52 mm/s and 0.54 mm/s. This may be attributed to the random substitution of Fe atoms by Co ones with hyperfine field distributions. It has been reported in the literature that Mössbauer spectra of $Fe_{50}Co_{50}$ powders are characterized by broadened line-width with a shoulder of the outmost lines [42, 43]. However, in the Mössbauer spectra, we did not observe such shoulder in the outmost lines which indicates pure phase nature of the materials.

Table 4.9 Deconvoluted Mössbauer parameters for fitted subspectra of various Fe-Co alloys. Hyperfine field not relevant for doublet subspectra are marked with dashes.

Composition	Sub Spectrum	Mössbauer Parameters			
		H_{hf} (T)	Isomer Shift, δ (mm/s)	Line widths, (mm/s)	Relative Intensity (%)
$Fe_{40}Co_{60}$	Sextet	33.8	0.005	0.44	80
	Doublet	---	0.342	0.60	20
$Fe_{60}Co_{40}$	Sextet	34.9	0.017	0.52	90
	Doublet	---	0.255	0.45	10
$Fe_{80}Co_{20}$	Sextet	34.4	0.033	0.54	80
	Doublet	---	0.329	0.45	20

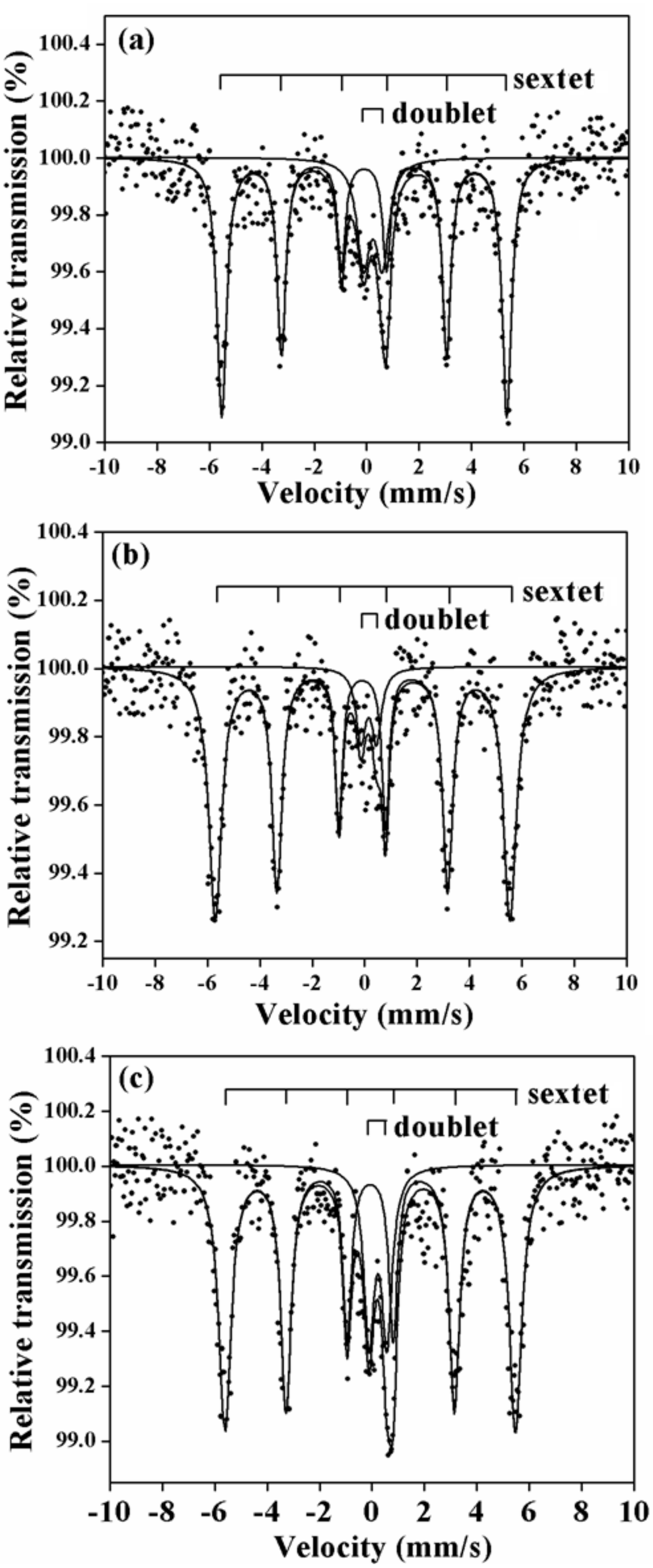

Figure 4.15 Room temperature Mössbauer spectra of (a) $Fe_{40}Co_{60}$, (b) $Fe_{60}Co_{40}$ and (c) $Fe_{80}Co_{20}$ alloy nanoparticles. Solid lines represent fitted resultant spectra along with deconvoluted subspectra of various Fe sites in the materials.

The values of the H_{hf} for sextet (i.e. 33.8 T, 34.9 T and 34.4 T for $Fe_{40}Co_{60}$, $Fe_{60}Co_{40}$ and $Fe_{80}Co_{20}$, respectively are higher than that of pure α-Fe (H_{hf} = 33.3 T) [44] and comparable with the literature reported values i.e. 33.8 T, 35.4 T and 36.4 T for $Fe_{40}Co_{60}$, $Fe_{60}Co_{40}$ and $Fe_{80}Co_{20}$, respectively [45]. This confirms the formation of pure Fe-Co alloys. In the materials under study, we have obtained variation in H_{hf} values with respect to composition of Fe-Co alloy with maximum value for $Fe_{60}Co_{40}$ alloy. These variations may be attributed to the change in magnetic environment at the Fe nucleus in Fe-Co alloys with composition. Further, the discrepancies in H_{hf} values may be attributed to the disordered magnetic structures at the surface of nanomaterials. These kinds of surface effects on the hyperfine field have been reported in literature [46]. Kodama et al. have already reported that the H_{hf} value equal to 36 T for $Fe_{48}Co_{52}$ alloy nanoparticles which is greater than the value for ordered $Fe_{50}Co_{50}$ alloy (i.e. 35 T) [37]. However, H_{hf} values, i.e. 33.8-34.9 T, for the Fe-Co alloys in the present study are in the range where one can expect disordered Fe-Co alloys characteristics [47]. One can expect increase in magnetic moment of Fe atom with increase of Fe content in the Fe-Co alloys. However, referring to magnetic study, we do not observe such trend in the M_S values. This is attributed to presence of reduced size, surface effects and superparamagnetic fractions in the materials. Thus, the Mössbauer study appropriately corroborates the magnetic characteristics.

The Mössbauer parameter, isomer shift (δ) is related to chemical bonding associated with Fe in a solid [46]. The values of δ for sextet sub-spectra were found to be 0.005 mm/s, 0.017 mm/s and 0.033 mm/s for $Fe_{40}Co_{60}$, $Fe_{60}Co_{40}$ and $Fe_{80}Co_{20}$, respectively. These values of δ are smaller but comparable to the value reported for disordered $Fe_{50}Co_{50}$ alloy (i.e. 0.035 mm/s) [48]. The values of δ for doublet sub-spectra were found to be 0.342 mm/s, 0.255 mm/s and 0.329 mm/s for $Fe_{40}Co_{60}$, $Fe_{60}Co_{40}$ and $Fe_{80}Co_{20}$, respectively. Although, δ values indicate Fe to be in higher oxidation state, we do not observe Fe-oxide phase in our XRD and Mössbauer investigation. Thus, the doublet spectrum is attributed to the presence of superparamagnetic fractions present in the materials.

4.3.3 Characterizations and magnetic properties of Co-Ni nanoparticles

4.3.3.1 CHN analysis and FTIR spectroscopy studies of organic capping on Co-Ni nanoparticles

In case of Co-Ni alloys, CHN analysis and FTIR spectroscopic investigations show interesting results. The CHN analysis results for several Co-Ni compositions were tabulated in Table 4.10. The wt% of organic matter (majorly C and H) for annealed Co_xNi_{100-x} alloys were found to be 56.02 %, 60.03 %, 42.97 % and 52.89 % for x = 20, 40, 60 and 80, respectively. Typical FTIR spectra for as-prepared and annealed at 400°C $Co_{40}Ni_{60}$ alloy are shown in Figure 4.16. Similar to Fe-Co alloys, as-prepared as well as annealed $Co_{40}Ni_{60}$ did not cap with pure oleic acid and oleylamine on the surface of nanoparticles. The peaks at 2918 cm^{-1} and 2854 cm^{-1} in as-prepared and annealed materials corresponds to oleyl group in the capping materials. The peaks in range of 1444-1580 cm^{-1} for the as-prepared and annealed Co-Ni alloy materials may be due the presence of carboxylate ($–COO^{-}$) function. These results indicate that both as-prepared as well as annealed $Co_{40}Ni_{60}$ alloy capped with oleic acid and oleylamine in the form of their acid-base complex consisting of $–COO^{-}$ and $–NH_3^{+}$ ions.

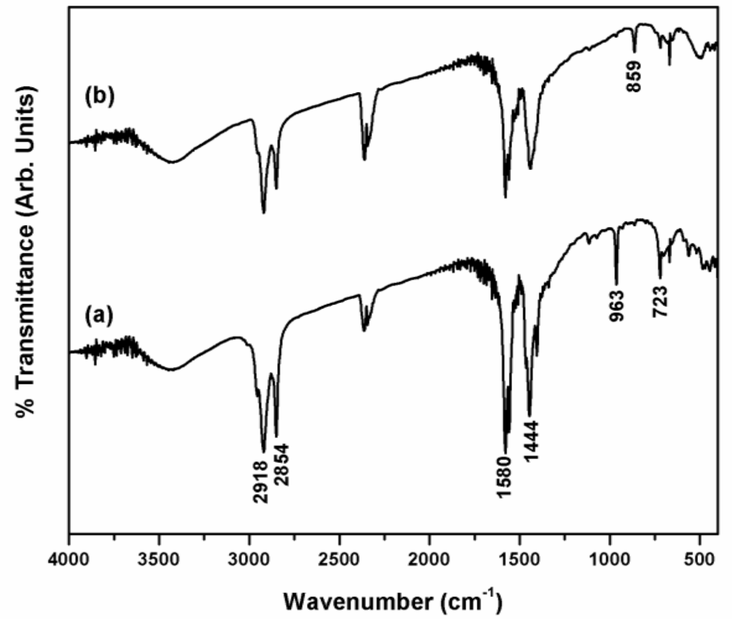

Figure 4.16 FTIR spectra for oleic acid and oleylamine capped $Co_{40}Ni_{60}$ alloys; (a) as-prepared and (b) annealed at 400°C for 2 h.

Table 4.10 Annealing conditions, At % of N, C, H, total CHN content and C/H ratios for annealed oleic acid and oleylamine coated Co-Ni alloys with various compositions.

Materials	Annealing conditions (°C/h)	at % of N	at % of C	at % of H	Total CHN content (at %)	C/H ratio
$Co_{40}Ni_{60}$	As-prepared	0.02	58.60	9.14	67.76	6.41
$Co_{20}Ni_{80}$	400/2	0.01	49.54	6.47	56.02	7.65
$Co_{40}Ni_{60}$	400/2	0.01	53.06	6.96	60.03	7.62
$Co_{60}Ni_{40}$	400/2	0.00	37.59	5.38	42.97	6.98
$Co_{80}Ni_{20}$	400/2	0.02	47.13	5.74	52.89	8.21

4.3.3.2 Solid state reactivity and XRD studies of Co-Ni nanoparticles

As-prepared Co_xNi_{100-x} alloys (x = 20, 40, 60, 80) alloys were amorphous in nature as examined by XRD patterns (Typical XRD pattern for as-prepared $Co_{40}Ni_{60}$ is shown in Figure 4.17 (a)). Hence, they were annealed at various temperatures (300-600°C) under high purity nitrogen gas atmosphere in order to increase the crystallinity of the materials. Finally, we have optimized the minimum temperature, i.e. 400°C, required for crystallization of Co-Ni alloys in order to obtain crystalline materials. XRD patterns for annealed Co_xNi_{100-x} alloys (x = 20, 40, 60, 80) at 400°C are shown in Figure 4.17. The peaks can be indexed to three planes, i.e. (111), (200) and (220) for fcc phase of Co-Ni alloy with no other impurity peaks were observed (JCPDS # 04-8490) [49]. The peak broadening in the XRD pattern is attributed to fine particle nature of the materials. Estimated values of crystallite sizes of synthesized Co-Ni alloys are summarized in Table 4.11.

As-prepared as well as annealed Co-Ni alloys crystallize in pure fcc structure. Lattice parameters value and crystallite size for as-prepared $Co_{40}Ni_{60}$ alloy is found to be 3.545(±7) Ǻ and 9 nm, respectively. And the values of lattice parameters for Co_xNi_{100-x} alloys (x = 20, 40, 60, 80) annealed at 400°C are found to be 3.534(±2) Ǻ, 3.537(±4) Ǻ, 3.548(±2) Ǻ, and 3.569(±4) Ǻ, respectively. The values of lattice parameters for Co_xNi_{100-x} alloys (x = 20, 40, 60, 80) increase with increase in Co content. These results indicate the formation of Co-Ni alloys with high homogeneity [50]. Average crystallite sizes for the synthesized Co_xNi_{100-x} alloys (x = 20, 40, 60, 80) were found to be 8 nm, 10 nm, 11 nm and 11 nm, respectively. The slight increase in crystallite size is observed as Co content increases in Co-Ni alloys.

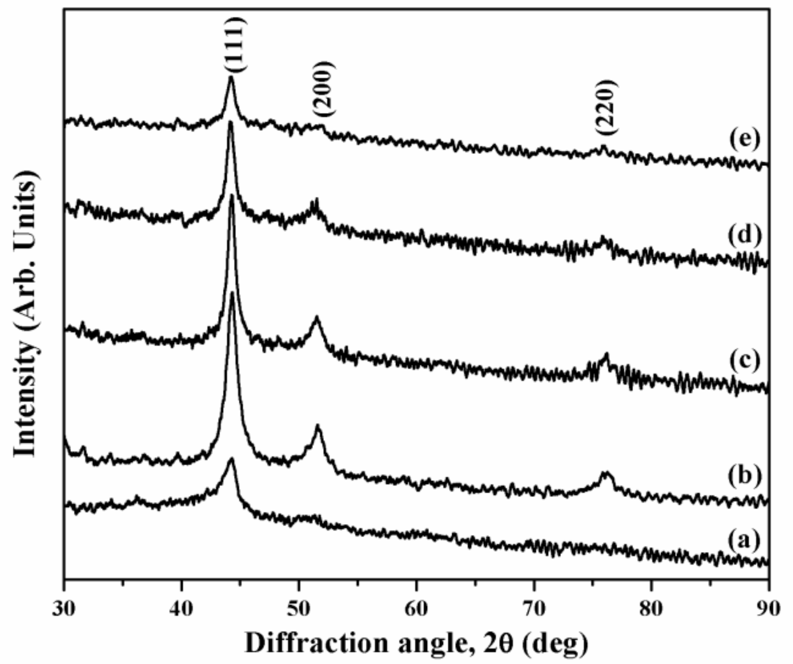

Figure 4.17 XRD patterns of (a) as-prepared $Co_{40}Ni_{60}$ and (b) $Co_{20}Ni_{80}$, (c) $Co_{40}Ni_{60}$, (d) $Co_{60}Ni_{40}$ and (e) $Co_{80}Ni_{20}$ alloys obtained after heat treatment at 400°C for 2 h, each.

Table 4.11 Compositions, annealing condition, crystalline phase, lattice parameters and crystallite sizes for Co-Ni alloy nanoparticles with different compositions. Figure(s) in parentheses include error bars.

Composition	Annealing conditions (°C/h)	Crystalline phase	Lattice parameters (Å)	Crystallite size (nm)
$Co_{40}Ni_{60}$	As-prepared	fcc	3.545(±7)	9.0(±4)
$Co_{20}Ni_{80}$	400/2	fcc	3.534(±2)	8.0(±4)
$Co_{40}Ni_{60}$	400/2	fcc	3.537(±4)	10.0(±3)
$Co_{60}Ni_{40}$	400/2	fcc	3.548(±2)	11.0(±4)
$Co_{80}Ni_{20}$	400/2	fcc	3.569(±4)	11.0(±4)

4.3.3.3 TEM microstructural studies of Co-Ni nanoparticles

The as-prepared and annealed (400°C) Co-Ni alloys were examined by TEM technique for microstructure. A Typical TEM micrograph for as-prepared $Co_{40}Ni_{60}$ and size distribution is shown in Figure 4.18. TEM micrographs for annealed Co_xNi_{100-x} alloys (x = 20, 40, 60, 80) and corresponding size distribution plots are shown in Figure 4.19. Also, typical SAED patterns for Co-Ni alloys are shown in Figure 4.20. TEM micrographs of as-prepared as well as annealed Co-Ni alloys confirm narrow size distribution of nanostructures with spherical morphologies. Average TEM particle size for as-prepared $Co_{40}Ni_{60}$ alloy is found to be 7 nm.

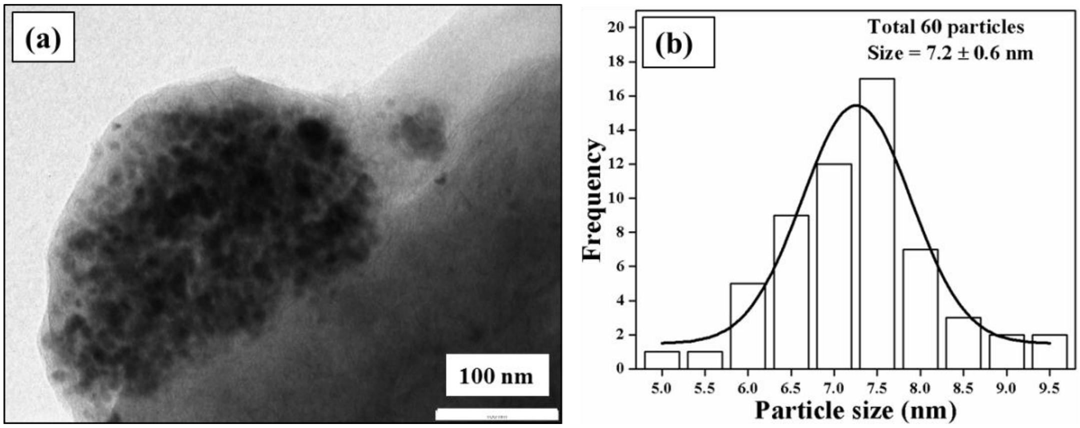

Figure 4.18 (a) A typical TEM micrographs of as-prepared $Co_{40}Ni_{60}$ and (b) its particle size distribution plot.

Average TEM particle sizes for Co_xNi_{100-x} alloys (x = 20, 40, 60, 80) were found to be in the range of 9-11 nm (Table 4.12). These results match well with the crystallite sizes range (8-11 nm), calculated from powder XRD profile. SAED patterns of Co_xNi_{100-x} alloys (x = 20, 40, 60, 80) show the formation of diffraction rings which indicates polycrystalline nature of the materials. The diffraction rings were indexed to crystalline planes, i.e. (111), (200) and (220), in SAED pattern according to d-values which matches exactly with the XRD results and confirm the formation of fcc Co-Ni alloy phase.

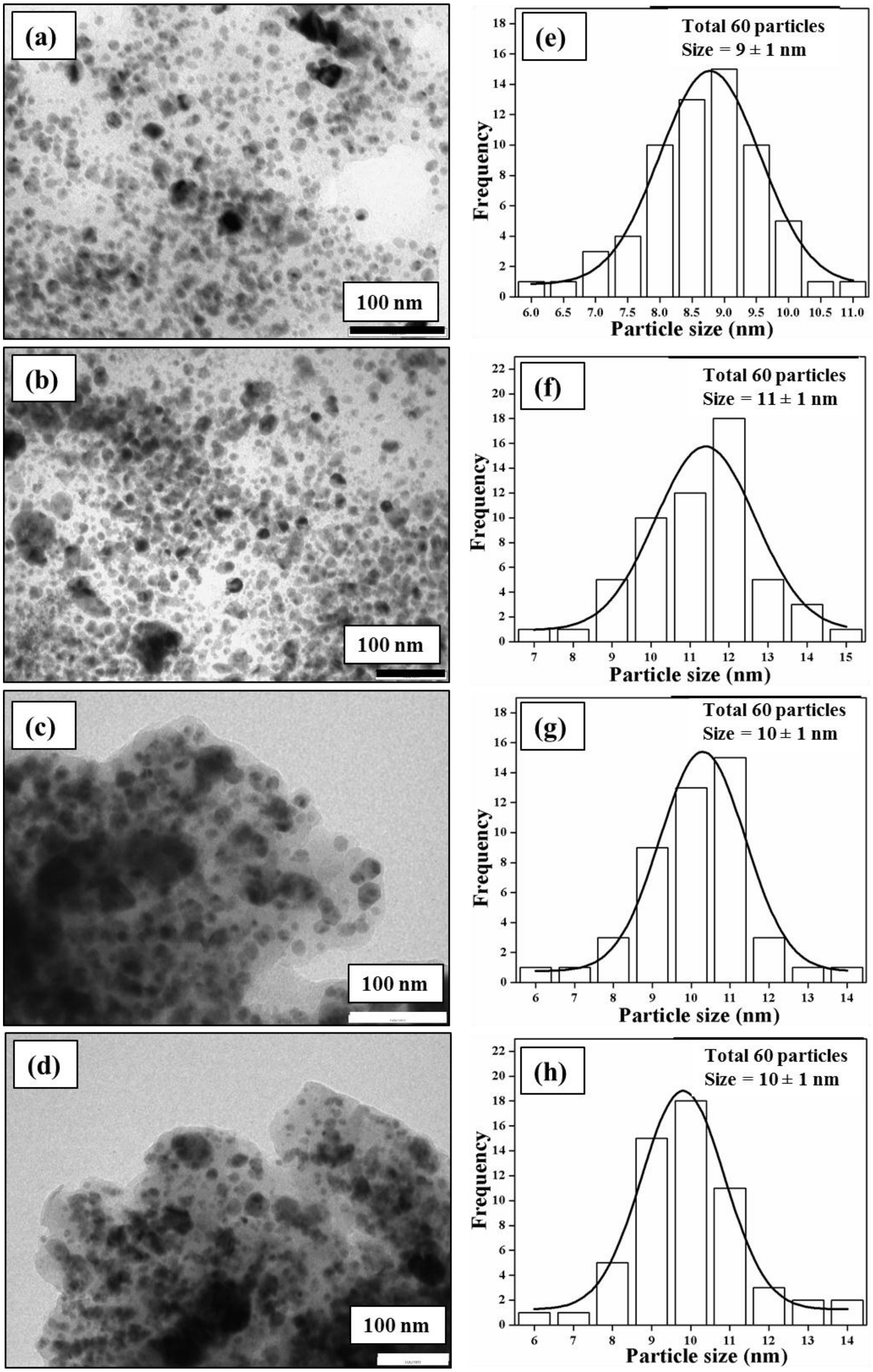

Figure 4.19 TEM micrographs of annealed (400°C/2h) (a) $Co_{20}Ni_{80}$, (b) $Co_{40}Ni_{60}$, (c) $Co_{60}Ni_{40}$, and (d) $Co_{80}Ni_{20}$ and their (e), (f), (g) and (h) corresponding particle size distribution plots.

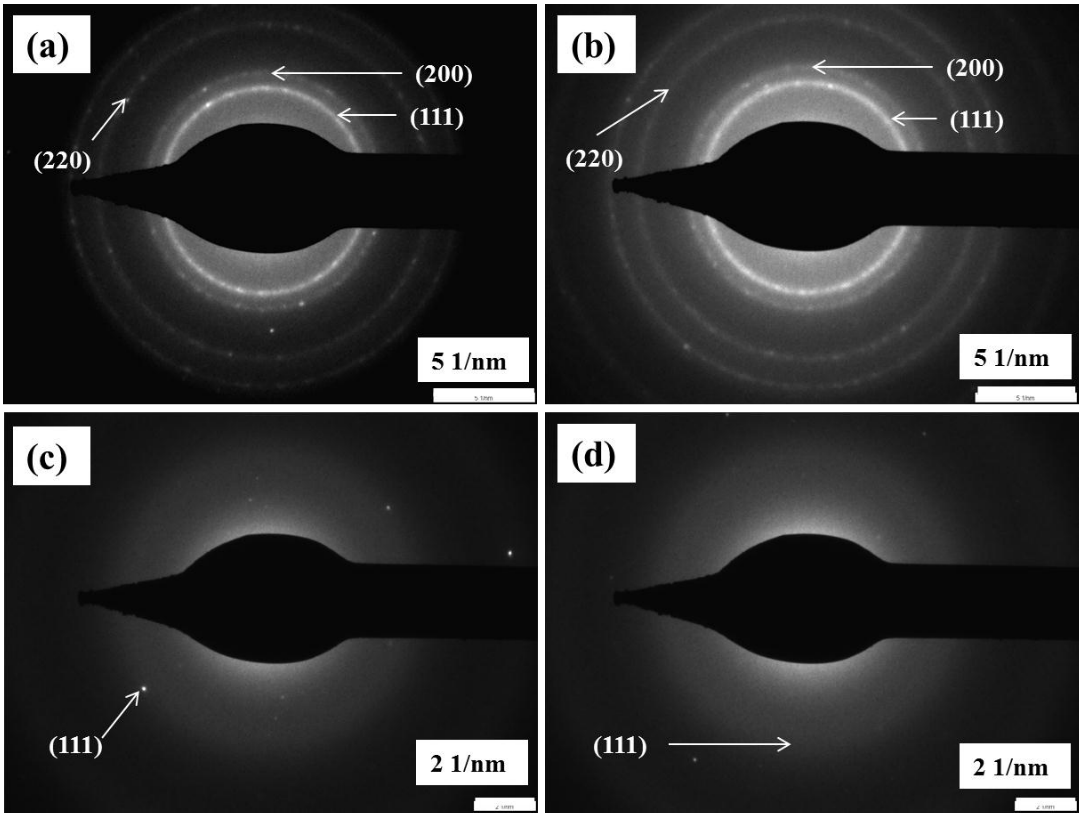

Figure 4.20 SAED patterns of (a) $Co_{20}Ni_{80}$, (b) $Co_{40}Ni_{60}$, (c) $Co_{60}Ni_{40}$, and (d) $Co_{80}Ni_{20}$ alloys annealed at 400°C for 2 h. The observed diffraction rings are indexed in accordance with fcc structure.

Table 4.12 Compositions, TEM particle sizes, saturation magnetizations (M_S), corrected saturation magnetizations (M'_S), remanent magnetizations (M_r) and coercivity (H_C) values for Co-Ni alloy nanoparticles with different compositions. Figure(s) in parentheses include error bars.

Composition	TEM Particle size (nm)	M_S (emu/g)	M'_S (emu/g)	M_r (emu/g)	H_C (Oe)
As-prepared $Co_{40}Ni_{60}$	7 ± 1	3.0(±1)	--	0.07	25
$Co_{20}Ni_{80}$	9 ± 1	11.0(±5)	25	1.04	52
$Co_{40}Ni_{60}$	11 ± 1	14.0(±4)	35	1.78	123
$Co_{60}Ni_{40}$	10 ± 1	18.0(±1)	31.6	3.01	221
$Co_{80}Ni_{20}$	10 ± 1	28.0(±1)	59.6	5.48	314

4.3.3.4 Magnetic properties of Co-Ni nanoparticles

M vs. H curves for Co_xNi_{100-x} alloys (x = 20, 40, 60, 80) have been shown in Figure 4.21. The estimated extrapolated values of the M_S, M_r and H_c for Co-Ni alloys are tabulated in Table 4.12. Co-Ni alloys annealed at 400°C contain organic coating at the surface. Therefore, two different values of M_S are reported herewith, i.e. one denotes M_S without considering wt% of organic layer and the other, M'_S , after wt% corrections corresponding to CHN content. The values of the M_S of the materials were determined by M vs. 1/H law. The values of M_S, M_r and H_C for as-prepared $Co_{40}Ni_{60}$ alloy were found to be 3 emu/g, 0.07 emu/g and 25 Oe, respectively. The values of M_S, M_r and H_C for annealed Co_xNi_{100-x} alloys (T=400^{o}C) (x = 20, 40, 60, 80) were found to be in the range of 11-28 emu/g, 1.04-5.48 emu/g and 52-314 Oe, respectively. Thus, after weight correction, the M_S values for Co_xNi_{1-x} alloys are found to be 25, 35, 31.6 and 59.6 emu/g, for x = 20, 40, 60 and 80, respectively.

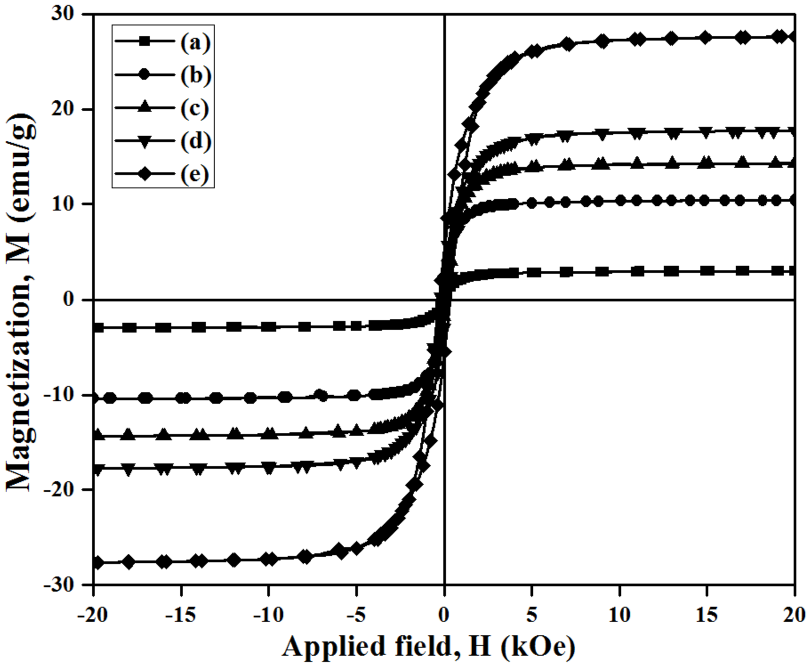

Figure 4.21 Room temperature magnetic hysteresis loops for (a) as-prepared $Co_{40}Ni_{60}$ and (b) $Co_{20}Ni_{80}$ (c) $Co_{40}Ni_{60}$ (d) $Co_{60}Ni_{40}$ and (e) $Co_{80}Ni_{20}$ annealed at 400°C for 2 h.

M vs. H plots of Co-Ni alloys shown in Figure 4.21 indicate that the ‘as-prepared’ and annealed Co-Ni nanocrystalline alloys are ferromagnetic in nature. Observed values of M_S and H_C for as-prepared $Co_{40}Ni_{60}$ (3 emu/g and 25 Oe) show soft magnetic properties. Smaller value of M_S for as prepared $Co_{40}Ni_{60}$ alloy may be attributed to the presence of amorphous fraction in the materials as confirmed by XRD studies. The M_S values for annealed Co_xNi_{100-x} alloys (x = 20, 40, 60, 80), i.e. 11, 14, 18 and 28 emu/g are remarkably smaller than the reported values for bulk Co-Ni alloy materials, i.e. 75, 95, 113 and 143 emu/g, respectively [51]. The reduction in M_S values can be explained on the basis of size, surface effects and weight fraction of organic matter present on the surface of the particles. The contribution of organic matter coated on the surface of Fe-Co nanomaterials towards reduction in M_S has already been explained above. Thus, after weight correction, the M_S values for Co_xNi_{100-x} alloys are found to be 25, 35, 31.6 and 59.6 emu/g, for x = 20, 40, 60 and 80, respectively. The increasing trend in M_S values with the increase of Co content (Figure 4.22) is in accordance to Slater-Pauling curve observed for bulk Co-Ni alloys [51, 52]. Further these results may be attributed to the alteration of crystal anisotropies along with canted spin present at the surface of the nanomaterials. The H_C value for annealed $Co_{40}Ni_{60}$ alloy was found to be larger than the H_C values for as-prepared $Co_{40}Ni_{60}$ alloy. It may be attributed to larger grain sizes of annealed samples than as-prepared materials. The H_C values for annealed Co_xNi_{100-x} alloys (52-314 Oe) were higher than the typical range for soft magnetic materials (Figure 4.22). These results indicate the presence of fine particle size effects in the materials. The reduced values of remanent magnetization (M_r/M_S) of the Co_xNi_{100-x} alloys were found to be 0.09, 0.12, 0.16 and 0.19 for x equal to 20, 40, 60 and 80, respectively. This indicates that crystal anisotropies increase with the increase in Co content and supports the increasing trend in the values of the coercivities. Also, the values of M_r/M_S are less than 0.5 and may be attributed to the presence of randomly oriented single domain particles [53].

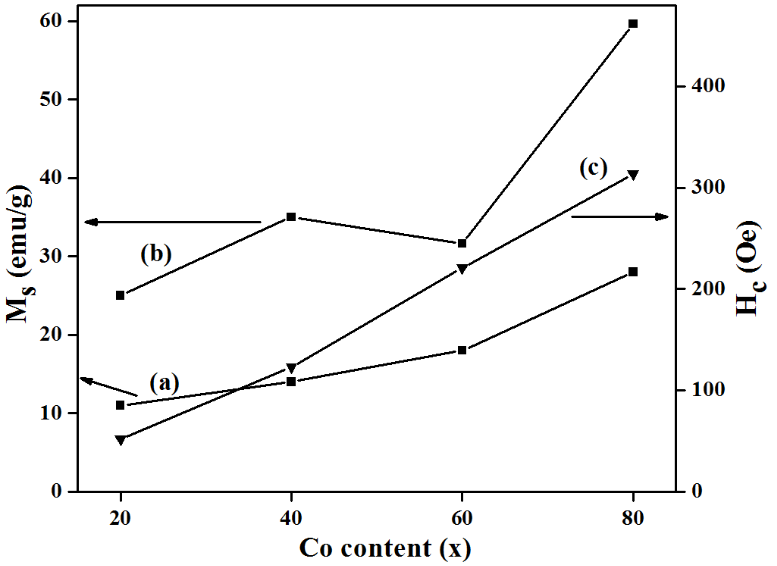

Figure 4.22 Plot of variations in values of (a) M_S, (b) M'_S and (c) H_C with respect to increasing Co content(x) in the Co_xNi_{100-x} alloys ($20 \leq x \leq 80$).

4.4 Conclusions

In summary, Co, Ni, Fe-Co and Co-Ni nanoparticles have been successfully synthesized by superhydride reduction route and surface functionalization was obtained by using oleic acid and oleylamine as capping agents. Capping on as-prepared materials was confirmed by FTIR study. Crystalline phases of the materials were obtained by annealing under high purity nitrogen atmosphere.

XRD patterns confirm that Co crystallizes in mixture of 53% hcp and 47% fcc phase whereas Ni crystallizes in fcc phase only. Average crystallite sizes for Co and Ni were found to be 15 nm and 35 nm, respectively. TEM studies indicate the fine particle nature and spherical shape morphologies of synthesized materials. Average TEM particle sizes from TEM micrographs analysis are equal to 11 nm and 10 nm for Co and Ni, respectively. Magnetic properties of Co and Ni were studied by field dependence of magnetization plots. Both Co and Ni show ferromagnetic behavior at room temperature. The magnetization-field (M-H) characteristics show the presence of superparamagnetic fractions in the ferromagnetic materials. The M_S values for Co and Ni are found to be 64 emu/g and 29 emu/g, respectively. The H_C values for Co and Ni are 436 Oe and 148 Oe, respectively and indicate high magnetocrystalline anisotropy effect and/or the presence of particle size distribution in our materials.

Fe_xCo_{100-x} alloys (x = 40, 60, 80) crystallize in pure α-Fe-Co alloy phase. The crystallite sizes were found to be in the range of ≈ 23-38 nm. TEM micrograph studies prove nearly spherical morphologies with narrow particle size distribution of the synthesized Fe-Co alloys. Average particle sizes estimated from TEM micrographs range from 10 nm to 51 nm. The values of the M_S for Fe-Co alloys range from 93.1-142.2 emu/g after corrections for organic wt % at the surface of the materials. These values are quite large for Fe-Co materials while considering the small size nature of the materials and may be useful for potential technological applications. Variation of saturation magnetization with compositions was interpreted on the basis of varied compositions, reduction in particle size, altered crystal anisotropies and spin canting at the surface of nanomaterials. Room temperature Mössbauer studies show presence of ferromagnetic sextet and superparamagnetic doublet in Fe-Co materials. The variations in the values of H_{hf} in Fe-Co alloys may be attributed to the change in magnetic structure at the Fe nucleus with composition and disordered magnetic structures at the surface of the nanoparticles.

Co_xNi_{100-x} alloys (x = 20, 40, 60, 80) crystallize in pure fcc phase. Average crystallite sizes were found to be in the range of 8-11 nm. TEM micrograph studies show nearly spherical morphologies with narrow particle size distribution for the synthesized Co-Ni alloys. Average TEM particle sizes range from 7-11 nm. As-prepared as well as annealed Co-Ni alloys exhibit ferromagnetic behavior at room temperature with soft magnetic properties. The M_S values for annealed Co-Ni alloys are found to be in the range of 25-59.6 emu/g. The observed H_C values for annealed Co-Ni alloys (52-314 Oe) were found higher than the typical range for soft magnetic materials. These results were interpreted with the help of size effects, altered crystal anisotropies and spin canting at the surface of nanomaterials.

References

1. X. Gao, S. C. Tan, A. T. S. Wee, J. Wu, L. Kong, X. Yu and H. O. Moser, J. Electron Spectrosc. Relat. Phenom., 150 (2006) 11-14.

2. S. S. Parhizgar and S. A. Sebt, J. Theor. Appl. Phys., 7 (2013) 44.
3. A. Wu, X. Yang and H. Yang, J. Alloys Compd., 513 (2012) 193-201.
4. C. W. Kim, Y. H. Kim, H. G. Cha, H. W. Kwon and Y. S. Kang, J. Phys. Chem. B, 110 (2006) 24418-24423.
5. J. G. Chen, C. A. Menning and M. B. Zellner, Surf. Sci. Rep., 63 (2008) 201-254.
6. Q. Liu, X. Guo, T. Wang, Y. Li and W. Shen, Mater. Lett., 64 (2010) 1271-1274.
7. K. P. Donegan, J. F. Godsell, D. J. Otway, M. A. Morris, S. Roy, J. D. Holmes, J. Nanopart. Res., 14 (2012) 670.
8. M. Aslam, L. Fu, S. Li and V.P. Dravid, J. Colloid Interface Sci., 290 (2005) 444-449.
9. H. T. Yang, Y. K. Su, C. M. Shen, T. Z. Yang and H. J. Gao, Surf. Interface Anal., 36 (2004) 155-160.
10. C-M. Shen, C. Hui, T-Z. Yang, C-W. Xiao, S-T. Chen, H. Ding and H-J. Gao, Chin. Phys. Lett., 25 (2008) 1479-1481.
11. G. S. Chaubey, C. Barcena, N. Poudyal, C. Rong, J. Gao, S. Sun and J. P. Liu, J. Am. Chem. Soc., 129 (2007) 7214-7215.
12. N. Shukla, C. Liu, P. M. Jones and D. Weller, J. Magn. Magn. Mater., 266 (2003) 178-184.
13. M. Kasture, S. Singh, P. Patel, P. A. Joy, A. A. Prabhune, C. V. Ramana and B. L. V. Prasad, Langmuir, 23 (2007) 11409-11412.
14. V. M. Maksimovic, N. D. Nikolic, V. B. Kusigerski and J. L. Blanusa, J. Serb. Chem. Soc., 80 (2015) 197-207.
15. B. Stahl, N. S. Gajbhiye, G. Wilde, D. Kramer, J. Ellrich, M. Ghafari, H. Hahn, H. Gleiter, J. Weibumuller, R. Wurschum and P. Schlossmacher, Adv. Mater., 14 (2002) 24-27.
16. P. Anil Kumar, S. Mitra and K. Mandal, Indian J. Pure Appl. Phys., 45 (2007) 21-26.
17. H. Wang, L. Zhang, J. Huang and J. Li, J. Nanopart. Res., 13 (2011) 1709-1715.
18. A. S. Kurlov, A. I. Gusev and A. A. Rempel, Rev. Adv. Mater. Sci., 32 (2012) 52-60.

19. A. Ponrouch, M. P. Bichat, S. Garbarino, C. Maunders, G. Botton, P. L. Taberna, P. Simon and D. Guay, ECS Trans., 25(41) (2010) 3-11.
20. M-I. Baraton and I. V. Uvarova, Eds., Functional Gradient Materials and Surface Layers Prepared by Fine Particles Technology, Springer, UA, 2001.
21. A. G. Kolhatkar, A. C. Jamison, D. Litvinov, R. C. Willson and T. R. Lee, Int. J. Mol. Sci., 14 (2013) 15977-16009.
22. J. M. D. Coey, Phys. Rev. Lett., 27 (1971) 1140-1142.
23. R. Kaiser and G. Miskolczy, J. Appl. Phys., 41 (1970) 1064-1072.
24. J. Ahmed, S. Sharma, K. V. Ramanujachary, S. E. Lofland and A. K. Ganguli, J. Colloid Interface Sci., 336 (2009) 814–819.
25. A. Zelenakova, D. Oleksakova, J. Degmova, J. Kovac, P. Kollar, M. Kusy and P. Sovak, J. Magn. Magn. Mater., 316 (2007) e519-e522.
26. T. Sourmail, Prog. Mater. Sci., 50 (2005) 816-880.
27. G. B. Chon, K. Shinoda, S. Suzuki and B. Jeyadevan, Mater. Trans., 51 (2010) 707-711.
28. R. N. Panda and N. S. Gajbhiye, J. Appl. Phys., 86 (1999) 3295-3302.
29. H. H. Hsiao, R. N. Panda, J. C. Shih and T. S. Chin, J. Appl. Phys., 91 (2002) 3145-3149.
30. P. Karipoth, A. Thirumurugan and R. J. Joseyphus, J. Colloid Interface Sci., 404 (2013) 49-55.
31. M. Kaur, Q. Dai, M. Bowden, M. Engelhard, Y. Wu, J. Tang and Y. Qiang, Appl. Phys. Lett., 103 (2013) 202407.
32. R. S. Sundar and S. C. Deevi, Int. Mater. Rev., 50 (2005) 157-192.
33. Q. Zeng, I. Baker, V. McCreary and Z. Yan, J. Magn. Magn. Mater., 318 (2007) 28-38.
34. M. Kaur, J. S. McCloy, W. Jiang, Q. Yao and Y. Qiang, J. Phys. Chem. C, 116 (2012) 12875-12885.
35. S. Morup, E. Brok and C. Frandsen, J. Nanomater., 2013 (2013) Article ID 720629.
36. A. Azizi, S. K. Sadrnezhaad and A. Hasani, J. Magn. Magn. Mater., 322 (2010) 3551-3554.

37. D. Kodama, K. Shinoda, K. Sato, Y. Konno, R. J. Joseyphus, K. Motomiya, H. Takahashi, T. Matsumoto, Y. Sato, K. Tohji and B. Jeyadevan, Adv. Mater., 18 (2006) 3154-3159.
38. G. H. Lee, S. H. Huh, J. W. Jeong, S. H. Kim, B. J. Choi, J. H. Jeong, H. I. Lee and H-C. Ri, J. Korean Phys. Soc., 42 (2003) 367-370.
39. X-W. Wei, G-X. Zhu, Y-J. Liu, Y-H. Ni, Y. Song and Z. Xu, Chem. Mater., 20 (2008) 6248-6253.
40. D. Ung, G. Viau, C. Ricolleau, F. Warmont, P. Gredin and F. Fievet, Adv. Mater., 17 (2005) 338-344.
41. Q. Li, H. Li, V. G. Pol, I. Bruckental, Y. Koltypin, J. Calderon-Moreno, I. Nowik and A. Gedanken, New J. Chem., 27 (2003) 1194-1199.
42. H. Moumeni, S. Alleg and J. M. Greneche, J. Alloys Compd., 386 (2005) 12-19.
43. J. Zarpellon, H. F. Jurca, N. Mattoso, J. J. Klein, W. H. Schreiner, J. D. Ardisson, W. A. A. Macedo and D. H. Mosca, J. Colloid Interface Sci., 316 (2007) 510-516.
44. M. F. Casula, G. Concas, F. Congiu, A. Corrias, A. Falqui and G. Spano, J. Phys. Chem. B, 109 (2005) 23888-23895.
45. C. E. Johnson, M. S. Ridout and T. E. Cranshaw, Proc. Phys. Soc., 81 (1963) 1079-1090.
46. R. N. Panda and N. S. Gajbhiye, J. Appl. Phys., 81 (1997) 335-339.
47. J. E. Frackowiak, Hyperfine Interact., 60 (1990) 757-760.
48. H. H. Hamdeh, B. Fultz and D. H. Pearson, Phys. Rev. B, 39 (1989) 11233-11240.
49. S. Olvera, J. Sanchez-Marcos, F. J. Palomares, E. Salas, E. M. Arce and P. Herrasti, Mater. Charact., 93 (2014) 79-86.
50. Y. D. Li, L. Q. Li, H. W. Liao and H. R. Wang, J. Mater. Chem., 9 (1999) 2675-2677.
51. P. Elumalai, H. N. Vasan, M. Verelst, P. Lecante, V. Carles and P. Tailhades, Mater. Res. Bull., 37 (2002) 353-363.
52. M. Y. Rafique, L. Pan and A. Farid, J. Alloys Compd., 656 (2016) 443-451.
53. N. Galvez, E. Valero, M. Ceolin, S. Trasobares, M. Lopez-Haro, J. J. Calvino and J. M. Dominguez-Vera, Inorg. Chem., 49 (2010) 1705-1711.

CHAPTER V

Magnetic properties of nano-crystalline Fe-Pt and Co-Pt alloys synthesized via superhydride route

This chapter deals with the studies on magnetic properties of hard magnetic materials of Fe-Pt and Co-Pt alloys nanoparticles synthesized via superhydride reduction route.

5.1 Introduction

In last few decade, plenty of research carried out in the field of longitudinal magnetic recording media in order to increase areal density of recording and reached the maximum limit up to 20 Gb/in^2 at laboratory research level [1, 2]. Recently, research is more focused towards increasing the recording and storage capacity limit up to 1 Tb/in^2 which is known as ultrahigh density recording media. Perpendicular magnetic recording (PMR) method is used for high density recording media other than longitudinal recording method. In PMR, alignments of the poles of the magnetic elements, which represent bits, were kept perpendicular to the surface of the disk platter. This kind of alignment takes lesser platters than the horizontal alignment used in longitudinal magnetic recording. Hence, large numbers of smaller grains were placed in unit area to increase areal density. One bit of magnetic recording may contain few grains hence areal density increases with smaller grain size. And number of magnetic grains per bit is known as signal-to-noise ratio (SNR) [3]. In order to achieve such a high areal density with adequate SNR (25-30 dB), it is reported that nanomaterials of grain size of ~10 nm with coercivity (H_C) values of about 4-8 kOe can be suitable for applications [4-6]. Such kinds of nanoparticle systems are observed to be thermally unstable due to superparamagnetic limit of size. However, according to Stoner–Wohlfarth model, thermal stability can be achieved when the ratio K_uV/k_BT is greater than 60 [7]. This condition of thermal stability at nano-dimensions can be easily obtained in the materials such as Fe-Pt, Co-Pt alloys etc. because they possess high value of K_u in the order of 10^6 Jm^{-3}.

Various physical and chemical methods have been employed for Fe-Pt and Co-Pt alloys in order to get particular morphology and properties. Conventional physical deposition methods, such as physical vapor deposition, have less control on the composition, particle size and morphology at the nucleation and growth step [8]. On the other hand, chemical methods can meet the above stated requirements including surface effects [9-13]. Monodispersed Fe-Pt alloy nanoparticles (~10 nm) assemblies with proper interparticle separation via polyol process have been established in the literature [9, 10]. In another development, Fe-Pt alloy nanoparticles can also be synthesized by thermal decomposition of precursors of Fe and Pt in octyl ether without using a reducing agent [11].

It has been observed that reaction conditions, such as precursors, reducing agent, surfactants, and reaction parameters (e.g. temperature and time), have great influence on composition, structural and magnetic properties of final Fe-Pt product [12, 14, 15]. The precursors such as $Fe(CO)_5$ and $Pt(acac)_2$ used in decomposition method produces nanoparticles of 4 nm with narrow size distribution but less control on composition. While reduction carried out in the absence of extra reducing agent (e.g. 1-2 hexadecanediol) in above method can form larger particles with well control composition [12]. Reducing agents play important role in controlling composition, e.g. superhydride method forms Pt nuclei first and then instantaneous reduction of Fe precursor at 200°C to form Fe nuclei which control the composition due to uniform availability of Fe for incorporation into the Pt seeds [14]. Surfactants also help in engineering the nucleation and growth to control the size and composition distribution of the nanoparticle dispersion. For example, n-butylamine and trioctylphosphine stabilizes higher and lower valence states of Fe species, respectively, which controls the formation of Fe nuclei [15]. Further, refluxing temperature and time helps in order to obtain narrow distribution in final size and composition. Hence, investigation on the synthesis of capped Fe-Pt nanoparticles in order to improve quality of the final product with regard to purity, composition, size and magnetic characteristics has become an important topic of interest.

In this chapter, we are reporting a newer modified synthetic strategy with respect to precursors, concentration of surfactants and reducing agent for the synthesis of Fe-Pt and

Co-Pt nanocrystals. Fe-Pt and Co-Pt alloys nanoparticles were synthesized *in situ* using superhydride as reducing agent with the presence of various capping agents such as oleic acid, oleylamine and CTAB. Effects of reaction parameters on structure, morphology and magnetic properties of the synthesized Fe-Pt and Co-Pt alloys were studied in detail.

5.2 Experimental

The chemicals used for synthesis of Fe-Pt and Co-Pt nanomaterials include ferric chloride hexahydrate ($FeCl_3 \cdot 6H_2O$), cobalt chloride hexahydrate ($CoCl_2 \cdot 6H_2O$), and CTAB from Molychem, India; oleic acid, oleylamine, diphenyl ether and superhydride ($LiBEt_3H$, 1 M in THF) from Sigma Aldrich, USA. The chemicals were of analytical grade and have been used without further purification. There is scanty literature found on the study of surfactants or capping agents based modifications in superhydride methodology to achieve narrow size and composition distribution. Among various capping agents, oleic acid, oleylamine and CTAB may be suitable in order to achieve above objectives because of their strong binding ability to metal species [16, 17]. In this chapter, combinations of above capping agents are used for study.

5.2.1 Synthesis of Fe-Pt alloys nanoparticles

The typical experimental steps for the synthesis of Fe-Pt alloys using superhydride method is same as described in chapter IV, section 4.2.2 by using the stoichiometric amounts of metal salts (Fe salt and Pt salt) and capping agents. The details of amount of metal salts used for synthesis of Fe-Pt alloys are tabulated in Table 5.1. Two different routes using different capping agents have been used for preparation Fe-Pt alloys, i.e. route 1 (oleic acid and oleylamine capped) and route 2 (oleic acid and CTAB capped). Hereafter, Fe-Pt alloys prepared via route-1 and route-2 are denoted as FePt(route-1) and FePt(route-2), respectively. Finally, as-prepared materials were heat treated in high purity $N_2(g)$ atmosphere at higher temperatures (500°C and 600°C) and used for further characterizations and magnetic properties study.

5.2.2 Synthesis of Co-Pt alloys nanoparticles

The typical experimental steps for the synthesis of Co-Pt alloys using superhydride method is same as described in chapter IV, section 4.2.2 by using the stoichiometric amounts of metal salts (Co salt and Pt salt) and capping agents. The details of amount of metal salts used for synthesis of Co-Pt alloys are tabulated in Table 5.1. Similarly, two different routes have been used for preparation Co-Pt alloys, i.e. route 1 (CTAB capped) and route 2 (oleic acid and CTAB capped). Hereafter, Co-Pt alloys prepared via route-1 and route-2 are denoted as CoPt(route-1) and CoPt(route-2), respectively. Finally, as-prepared materials were heat treated in high purity N_2(g) atmosphere at moderately higher temperatures (500°C-600°C) and used for further characterizations and magnetic properties study.

Table 5.1 Details of moles and weights of metal salts taken for synthesis of Fe-Pt and Co-Pt alloys nanoparticles via superhydride reduction method.

Materials	Metal salts (Min assay)	Moles (mmol)	weight (g)	Capping agents (volume; molar ratio)	
				Route 1	Route 2
Fe-Pt *	$FeCl_3 \cdot 6H_2O$	0.2	0.054	Oleic acid (0.13 ml; 2);	Oleic acid (0.13 ml; 2); CTAB (292 mg, 2)
	$PtCl_2$ (73% Pt)	0.2	0.053	Oleylamine (0.14 ml; 2)	
Co-Pt *	$CoCl_2 \cdot 6H_2O$	0.2	0.049	CTAB (292 mg, 2)	Oleic acid (0.13 ml; 2); CTAB (292 mg, 2)
	$PtCl_2$ (73% Pt)	0.2	0.053		

* Total metal ions concentration was 0.016 M.

** molar ratio = Moles of capping agent / Total no. of moles of metal ions.

5.3 Results and Discussion

5.3.1 Characterizations and magnetic properties of Fe-Pt alloy nanoparticles via route-1 and route-2

5.3.1.1 XRD studies of Fe-Pt alloy nanoparticles

(A) Route-1

As-synthesized and annealed Fe-Pt(route-1), were subjected to XRD measurements and the corresponding diffraction patterns were presented in Figure 5.1((a) and (b)). The materials processing parameters and results from XRD patterns are tabulated in Table 5.2. Oleic acid and oleylamine coated Fe-Pt nanoparticles (route-1) possesses disordered fcc crystal structure in 'as-synthesized stage' (Figure 5.1(a)). Broad peaks for as-synthesized materials indicate majorly amorphous nature of Fe-Pt nanocrystals with crystallite sizes of ~2.3 nm. After annealing at 600°C for 2 h, as-synthesized Fe-Pt alloys were transformed into long range ordered fct ($L1_0$) phase. The materials were phase pure and the peaks were indexed in accordance with the fct (L1o) phase (JCPDS # 43-1359) [18]. The presence of peaks corresponding to superlattice reflections, i.e. (001), (110), and (200)/(002) doublet peaks in XRD pattern of Fe-Pt materials (Figure 5.1(b)) [19]. Average crystallite size of annealed Fe-Pt alloy was found to be 21 nm. Long range order parameters (S) was calculated from the intensities of (001) and (002) diffraction peaks by using the equation 5.1 and found to be 0.73 [20].

$$S \cong 0.85\left[\frac{I_{001}}{I_{002}}\right]^{1/2} \tag{5.1}$$

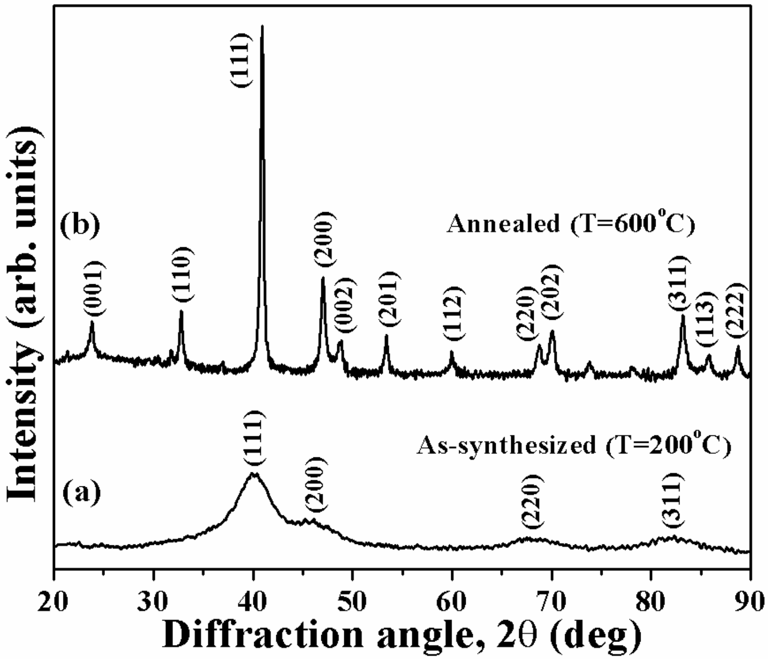

Figure 5.1 XRD patterns of Fe-Pt nanoparticles via route-1, (a) As-synthesized (T=200°C), (b) annealed (T=600°C).

The calculated values of the lattice parameters from (001) and (110) peaks for L10 Fe-Pt were c = 3.7363 Å and a = 3.8600 Å with c/a = 0.9679 (Table 5.2). These lattice parameters are comparable with the values for pure L10 Fe-Pt alloy, i.e. c = 3.7133 Å and a = 3.8525 Å with c/a = 0.9638 [21], and confirms the formation of L10 Fe-Pt alloy.

(B) Route-2

XRD patterns of as-synthesized and annealed Fe-Pt(route-2), were presented in Figure 5.2(a and b). The materials processing parameters and results from XRD patterns are tabulated in Table 5.2. The XRD results for Oleic acid and CTAB coated Fe-Pt nanoparticles (route-2) were analyzed in a similar manner as stated above for as-synthesized and annealed materials. The as-synthesized Fe-Pt alloy by route-2 do have disordered fcc structure with crystallite size of 6 nm suggesting more crystalline characteristics compared to as-synthesized Fe-Pt alloy from route-1. Phase transformation to $L1_0$ Fe-Pt alloy from route-2 was also observed at 600°C with long range parameter of 0.77 and crystallite size of 19.5 nm.

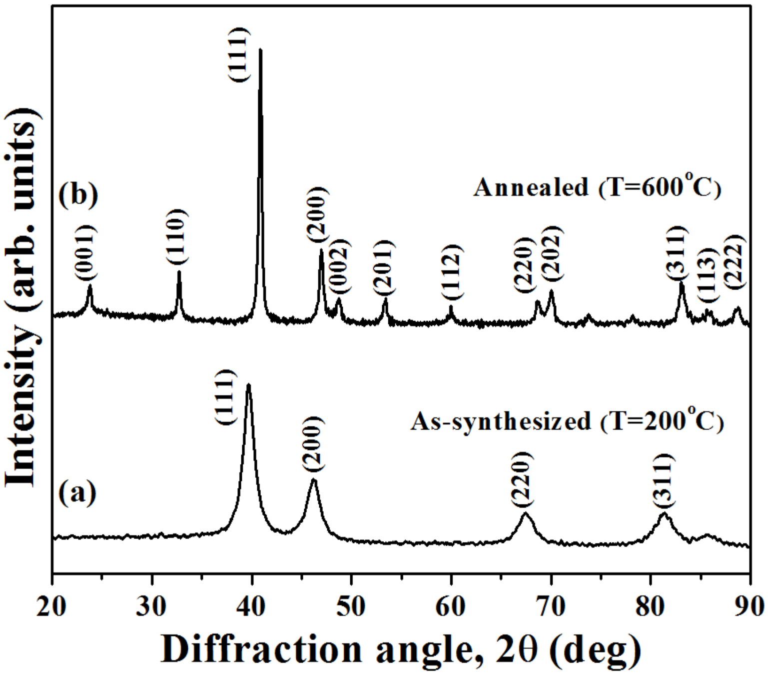

Figure 5.2 XRD patterns of Fe-Pt nanoparticles via route-2, (a) As-synthesized (T=200°C), (b) annealed (T=600°C).

The calculated values of lattice parameters for $L1_0$ Fe-Pt alloy from route-2, i.e. c = 3.7405 Å and a = 3.8656 Å with c/a = 0.9676, matches well with those obtained from route 1, i.e. c = 3.7363 Å and a = 3.8600 Å with c/a = 0.9679. The as-synthesized Fe-Pt alloy nanoparticles from route-2 possess higher crystallinity and size of nanocrystals than materials synthesized via route-1 under similar conditions. The reason may be due to surfactant effects at nucleation and growth stage during the chemical synthesis. However, the results are consistent with the present stated experimental parameters and emphasizes on the novelty of the synthetic strategy.

Table 5.2 Capping agents, annealing conditions, lattice parameters and average crystallite sizes for Fe-Pt alloy nanoparticles.

Materials	Capping agents	Annealing conditions, temp/h (°C/h)	Lattice parameters			Average crystallite size (nm)
			c (Å)	*a* (Å)	*c/a* ratio	
FePt (route-1)	Oleic acid + Oleylamine	600/2	3.7363	3.8600	0.9679	21
FePt (route-2)	Oleic acid + CTAB	600/2	3.7405	3.8656	0.9676	19.5

5.3.1.2 SEM micrographs of Fe-Pt alloy nanoparticles

(A) Route-1

SEM micrographs of the ‘as synthesized’ materials of Fe-Pt(route 1) with 10000X and 50000X magnifications are presented in Figure 5.3 (a) and (b), respectively. A micrograph with 10000X magnification is not showing clear presence of nanostructures. The micrograph with 50000X magnifications shows the presence of Fe-Pt nano-clusters inside some sort of polymer like structures having dimensions of several micrometers.

A SEM micrograph of annealed Fe-Pt(route-1) at 600°C is shown in Figure 5.4 (a) with corresponding SEM particle size distribution in inset. The SEM-EDX pattern of annealed Fe-Pt(route-1) is presented in Figure 5.4 (b). The morphology of the particles appears to be nearly spherical with SEM particle size of 24 nm with narrow distributions of ± 2 nm (Table 5.3). Good agreements are observed between the crystallite sizes obtained from the XRD line broadening, i.e. 21 nm, with those of the corresponding SEM sizes. The EDX spectrum shows the abundance presence of elements: such as: Fe, Pt and O. The presence of oxygen is understood from the fact that annealed Fe-Pt materials are coated with organic matter including oxygen. The EDX analyses confirm the Fe-Pt compositions to be $Fe_{50}Pt_{50}$ for route 1.

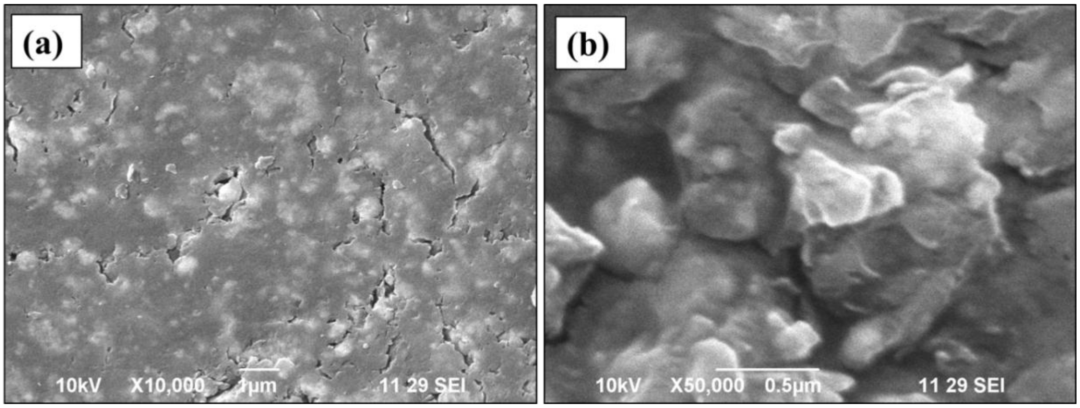

Figure 5.3 SEM micrographs of the as-prepared Fe-Pt alloys via route-1 with various magnifications; (a) 10000X micrograph and (b) 50000X micrograph.

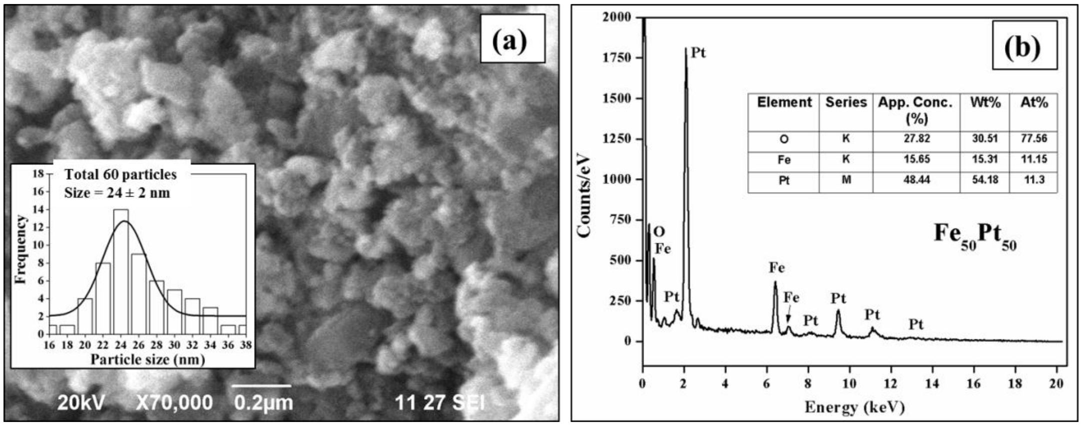

Element	Series	App. Conc. (%)	Wt%	At%
O	K	27.82	30.51	77.56
Fe	K	15.65	15.31	11.15
Pt	M	48.44	54.18	11.3

Figure 5.4 (a) SEM micrographs of the annealed Fe-Pt alloys via route 1 and inset shows particle size distribution. (b) SEM-EDX micrographs of the annealed Fe-Pt alloys via route 1.

(B) Route-2

SEM micrographs of the ‘as-prepared’ materials of Fe-Pt(route-2) with 10000X and 50000X magnifications are presented in Figure 5.5 (a) and (b), respectively. A 10000X micrograph of Fe-Pt(route-2) shows presence of nanostructures in the form of agglomerations. For more clarity 50000X micrograph have been presented. It indicates that as-prepared Fe-Pt(route-2) possesses well defined agglomerated particle like spherical structure of ~ 50 nm.

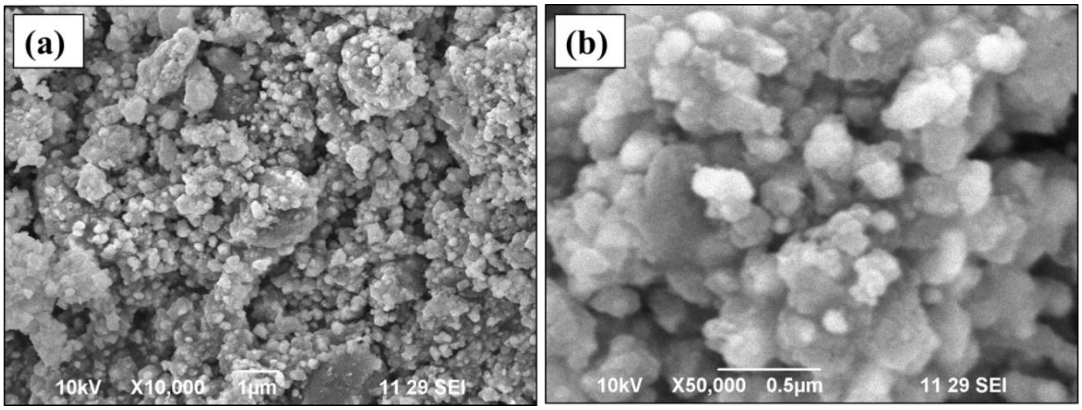

Figure 5.5 SEM micrographs of the as-prepared Fe-Pt alloys via route-2 with various magnifications; (a) 10000X micrograph and (b) 50000X micrograph.

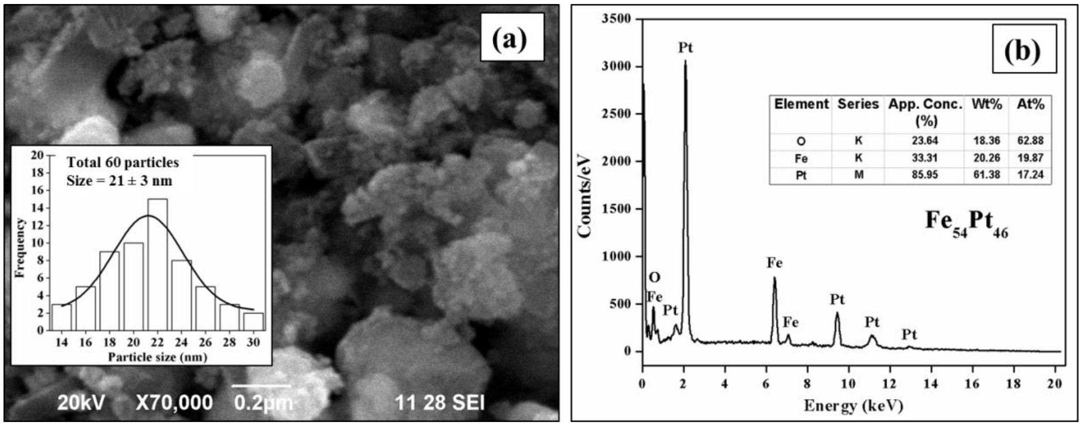

Element	Series	App. Conc. (%)	Wt%	At%
O	K	23.64	18.36	62.88
Fe	K	33.31	20.26	19.87
Pt	M	85.95	61.38	17.24

Figure 5.6 (a) SEM micrographs of the annealed Fe-Pt alloys via route-2 and inset shows particle size distribution. (b) SEM-EDX micrographs of the annealed Fe-Pt alloys via route-2.

A SEM micrograph of the annealed Fe-Pt(route-2) is shown in Figure 5.3 (a) with corresponding SEM particle size distribution in inset. SEM-EDX patterns of the annealed Fe-Pt(route-2) is shown in Figure 5.3 (b). The morphology of the particles appears to be nearly spherical in the agglomerated clusters. Average SEM particle size of annealed Fe-Pt(route-2) was found to be 21 nm with narrow distributions of ± 3 nm (Table 5.3). SEM size is well agrees with observed crystallite size obtained from the XRD for annealed Fe-Pt materials i.e. 19.5 nm. From EDX graph, the presence of oxygen is understood from the fact that annealed Fe-Pt materials are coated with organic matter including oxygen. The composition of Fe-Pt(route-2) from EDX analyses were found to be $Fe_{54}Pt_{46}$.

Table 5.3 Materials, SEM-EDX composition and SEM particle size for annealed Fe-Pt alloy Nanoparticles synthesized via route-1 and route-2.

Materials	SEM-EDX composition, Fe:Pt (At%)	SEM particle size (nm)
Fe-Pt (route-1)	50:50	24 ± 2
Fe-Pt (route-2)	54:46	21 ± 3

5.3.1.3 Magnetic properties of Fe-Pt alloy nanoparticles

5.3.1.3.1 Magnetic properties of as-prepared Fe-Pt alloy nanoparticles via route-1 and route-2

Magnetization vs. Field behavior of the ‘as-prepared’ fcc Fe-Pt nanomaterials synthesized using route 1 and 2 were presented in Figure 5.7 (a) and (b), respectively. The hysteresis curves show ferromagnetic nature with superparamagnetic characteristics at room temperature. This can be inferred from the nearly linear nature of the plots with the increase of applied field and having negligible coercivities. The inset Figure 5.7 shows Langevin fitting of the magnetic data with the following assumption; (i) superparamagnetic particles behave as paramagnet centers, (ii) are spherical in shape with Gaussian size distribution and (iii) finite interactions exists between the particles in presence of weak field [22]. The experimental curve has been superimposed on the fitted curve and compared. It can be seen from the Langevin plot that the theoretical fit deviate much from the experimental data more in the low field region (0-4000 Oe). These results show wider particle size distributions in the ‘as-synthesized’ materials. In addition, this deviation from Gaussian distributions signifies the presence of magnetic particles with larger size. The magnetic moment per particle can be estimated from the fit which has been derived from the following equations:

$$M = M_s \left[coth\left(\frac{PH}{T}\right) - \frac{1}{\left(\frac{PH}{T}\right)} \right] \qquad \text{where, } P = \frac{\mu_o m_p}{k_B} \qquad (5.2)$$

Where, M is magnetization, M_S is Saturation Magnetization, μ_o is permeability of free space, m_p is magnetic moment per particle, k_B is Boltzmann constant, H is field in Oe, and T is absolute temperature [23]. The estimated average magnetic moments for the 'as-prepared' Fe-Pt particles synthesized by route 1 and 2 are estimated to be 753 μ_B and 814 μ_B, respectively.

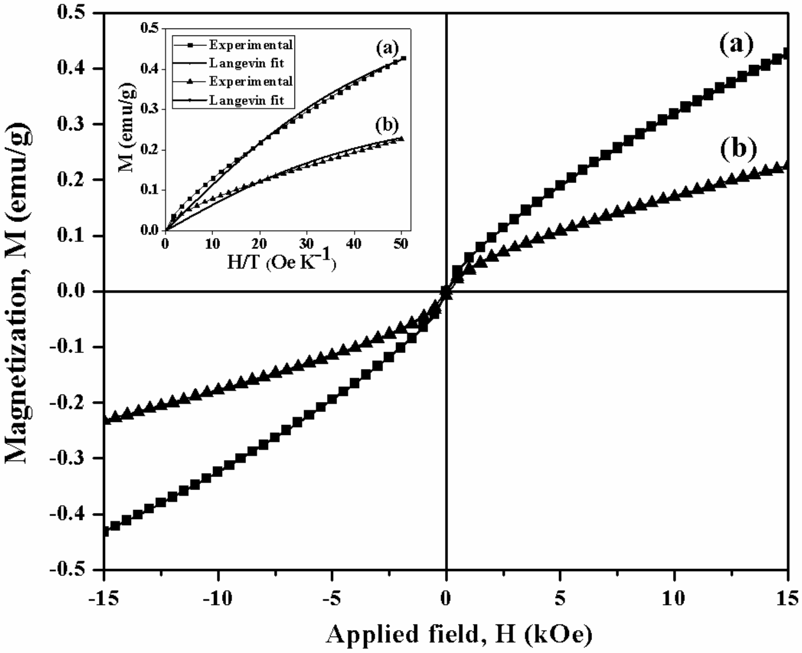

Figure 5.7 A plot of Magnetization vs. Field of the 'as-prepared' fcc Fe-Pt alloys nanoparticles synthesized via (a) route- 1 and (b) route-2. Inset shows corresponding Langevin fitting to experimental data.

In order to establish the size distribution in actual practice using assembly of superparamagnetic fcc Fe-Pt particles, we have fitted the M vs. H plots using lognormal distribution which are shown in Figure 5.8 (a) and (b) for route 1 and 2, respectively. The corresponding estimated size distributions are shown in Inset Figure 5.8 (a) and (b). The average diameters of the Fe-Pt particles are found to be 6 nm and 6.3 nm with size deviations of ~5 nm and ~7.4 nm, for route 1 and 2, respectively. Therefore, fcc Fe-Pt materials synthesized via route 2, indicates wider distribution of size range compared to route 1. Such kind of differences in size distributions in route 1 and 2 are well correlated with average XRD crystallite sizes of 2.3 nm and 6 nm for route 1 and 2, respectively. Considering disordered arrangement of Fe and Pt atoms in the fcc cubic lattice and assuming two Fe atoms per unit cell, one can expect the magnetic moments of 5996 μB and 6818 μB for 6 nm and 6.3 nm (obtained using lognormal distribution fit) Fe-Pt nanoparticles obtained using route 1 and 2, respectively. The drastic reduction (up to 89%) is due to size, surface and organic layer present at the surface of the nanoparticles [24]. Although, the crystallite size of Fe-Pt materials synthesized using route-1, i.e. 2.3 nm, is smaller than that of the route-2, i.e. 6 nm, the values of saturation magnetizations for route-1 is higher than route-2. This seems to be unlikely because of smaller volume of crystalline regions in Fe-Pt synthesized via route-1 is expected to result in smaller value of MS compared to route-2. Further, calculation of M/MS values at various field strengths show higher values for materials synthesized via route-2 when compared with the corresponding values via route-1. These results suggest that Fe-Pt materials synthesized via route-2 contains larger mass fractions of the organic coating layers resulting smaller values of saturation magnetization (Figure 5.7).

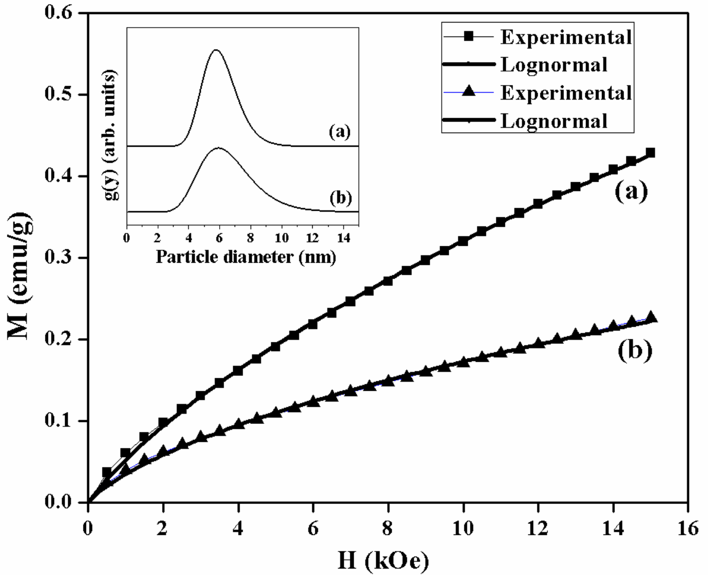

Figure 5.8 Lognormal fitting to M vs. H curves of Fe-Pt alloys nanoparticles synthesized via (a) route- 1 and (b) route-2. Inset shows corresponding lognormal size distribution plots.

5.3.1.3.2 Magnetic properties of annealed Fe-Pt alloy nanoparticles via route-1 and route-2

The Magnetization vs. field plots of Fe-Pt materials obtained by heat treatment of 'as-prepared particles' under the flow (~200 cc) of purified N_2(g) at 600°C are shown in

Figure 5.9. The magnetic parameters are summarized in Table 5.4. As it can be seen the value of saturation magnetization for Fe-Pt materials synthesized via route 2, i.e. 29.6 emu/g, is much larger than that of route 1, i.e. 4.4 emu/g. It has been reported that in Fe_xPt_{100-x} nano-crystalline alloys the values of saturation magnetizations increases from 4.5 emu/g to 44.5 emu/g when x = 30 to 80, respectively [25]. Therefore, one should expect the values of saturation magnetizations in the range of ~15-20 emu/g for the compositions studied in this paper. However, in our study we could get higher value of saturation magnetizations, i.e. 29 emu/g, for route-2 whereas for route-1 significantly lower value of magnetization, i.e. 4.5 emu/g is obtained. Such kind of alteration of saturation magnetizations can be due to several dominant factors; such as: fraction of fct phase, order parameters, size and surface effects etc. [25]. As it can be seen that the average crystallite sizes of Fe-Pt materials synthesized via route-1 and route-2 are estimated to 21 and 19.5 nm, respectively, such link of drastic reduction in M_S for route-1, cannot be explained only by size, surface and order parameters. However, composition of Fe-Pt alloys (Table 5.4) may play a significant role in such an alteration of saturation magnetization. The calculated values of squareness for Fe-Pt materials synthesized via route-1 and route-2 are 0.475 and 0.622, respectively.

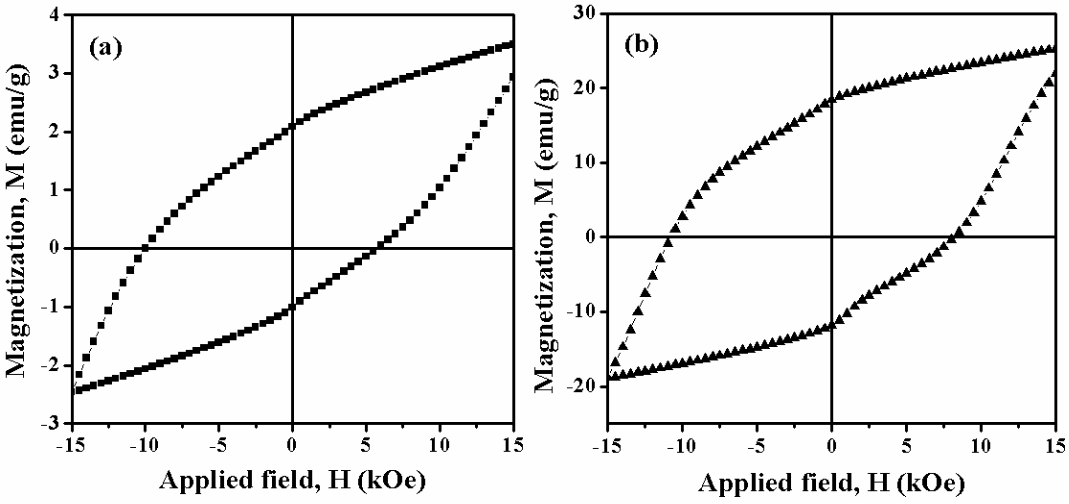

Figure 5.9 Magnetization vs. Field plots of Fe-Pt alloys nanoparticles synthesized via (a) route- 1 and (b) route-2 and annealed under the flow of purified N_2(g) at 600°C for 2 h.

The values of coercivity are found to be 10000 Oe and 10792 Oe, for Fe-Pt materials synthesized via route-1 and route-2, respectively. Comparatively, higher value of coercivity, i.e. 10792 Oe, is observed for $Fe_{54}Pt_{46}$ materials synthesized via route-2. These values can be compared with the literature reported values of 10800 Oe and 9298 Oe, for Fe-Pt nano-materials in thin film and nano-powder form [26, 27]. The observations of higher values of coercivity (~10000 Oe) obtained via both the routes without any post treatment of the materials except post annealing at 600°C under nitrogen gas atmosphere are noteworthy.

Table 5.4 Materials, composition, saturation magnetization and coercivity values for Fe-Pt alloy nanoparticles synthesized via route-1 and route-2.

Materials	Composition, Fe:Pt (At%)	Saturation magnetization, M_S (emu/g)	Coercivity, H_C (Oe)
Fe-Pt (route-1)	50:50	4.4	10000
Fe-Pt (route-2)	54:46	29.6	10792

5.3.2 Characterizations and magnetic properties of Co-Pt alloy nanoparticles via route-1 and route-2

5.3.2.1 XRD studies of Co-Pt alloy nanoparticles

(A) Route-1

The XRD patterns of as-prepared and annealed Co-Pt alloy nanoparticles, prepared via route-1, were represented in Figure 5.10. The materials processing parameters and results from XRD patterns are tabulated in Table 5.5. Co-Pt alloy nanoparticles from route-1 (CTAB coated) possesses disordered fcc crystal structure at as-synthesized stage (Figure 5.10, (a)) with average crystallite size of 6.6 nm. As-prepared Co-Pt alloy nanoparticles were first annealed at 500°C for 2 h. They possess fcc crystal structure even when the processing temperature increases up to 500°C with crystallite sizes of 7.2 nm. The observation of small peak at ~44° may correspond to fcc Co phase. Further annealing at 600°C for 2 h, Co-Pt alloy shows transformation to long range ordered fct ($L1_0$) phase

(ICDD card no. 43-1358). The presence of peaks corresponding to superlattice reflections, i.e. (001), (110), and (200)/(002) doublet peaks in XRD pattern of Co-Pt materials (Figure 5.10, c) [28]. As (200)/(002) peaks splitting is not well separated, calculation of order parameter has not been attempted. Average crystallite size of annealed Fe-Pt alloy (T=600°C) was found to be 7.2 nm. The calculated values of the lattice parameters from (001) and (110) peaks for $L1_0$ Co-Pt were c = 3.6877 Å and a = 3.8008 Å with c/a = 0.9702 (Table 5.4). These lattice parameters are comparable with the literature reported values for pure $L1_0$ Co-Pt alloy, i.e. c = 3.7010 Å and a = 3.8030 Å with c/a = 0.9732 [29], and confirms the formation of $L1_0$ Co-Pt alloy.

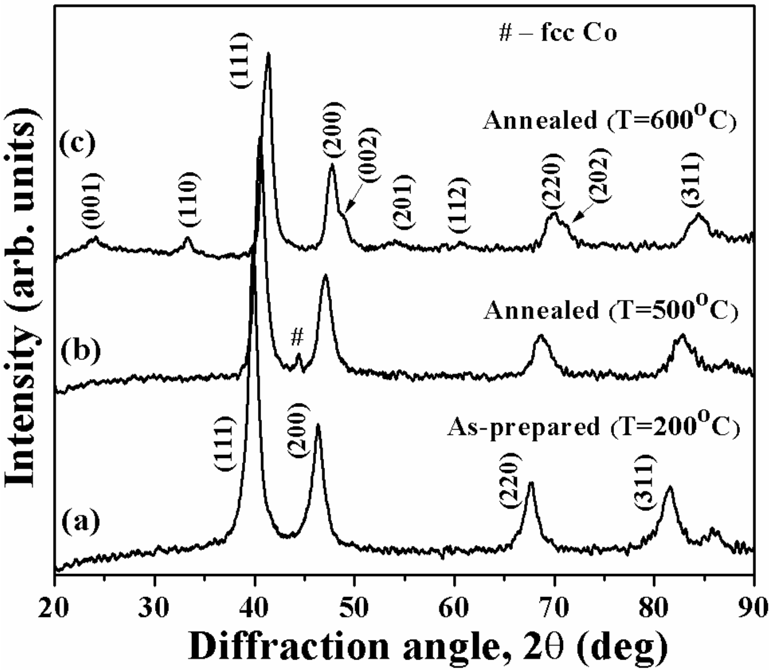

Figure 5.10 XRD patterns of Co-Pt nanoparticles synthesized via route 1; (a) as-prepared, (b) annealed at 500°C/2 h, and (c) annealed at 600 °C/2 h.

(B) Route-2

The XRD patterns of as-prepared and annealed Co-Pt alloy nanoparticles, prepared via route-2, were represented in Figure 5.11. The materials processing parameters and results from XRD patterns are tabulated in Table 5.5. On the other hand, as-prepared Co-Pt alloys from route-2 (Oleic acid and CTAB coated) also crystallize in disordered fcc crystal structure (Figure 5.11 (a)) but has more amorphous nature with crystallite size of 5.8 nm. Annealed Co-Pt alloy of route-2 possess fcc crystal structure even up to 500°C with crystallite sizes of 5.5 nm. The observation of small peak at ~44° may correspond to fcc Co phase. Further annealing at 600°C for 2 h, fcc Co-Pt alloy transformed to long range ordered fct ($L1_0$) phase. Long range order parameters (S) was calculated by using the intensities of (001) and (002) diffraction peaks and found to be 0.5 [20]. After annealing at 600°C for 12 h, order parameter increased to 0.8. The calculated values of the lattice parameters from (001) and (110) peaks for $L1_0$ Co-Pt annealed at 600°C/2h were c = 3.7019 Å and a = 3.8034 Å with c/a = 0.9733 whereas for annealed at 600°C/12h were c = 3.7001 Å and a = 3.8075 Å with c/a = 0.9718 (Table 5.4). These results confirm the formation of $L1_0$ Co-Pt alloy.

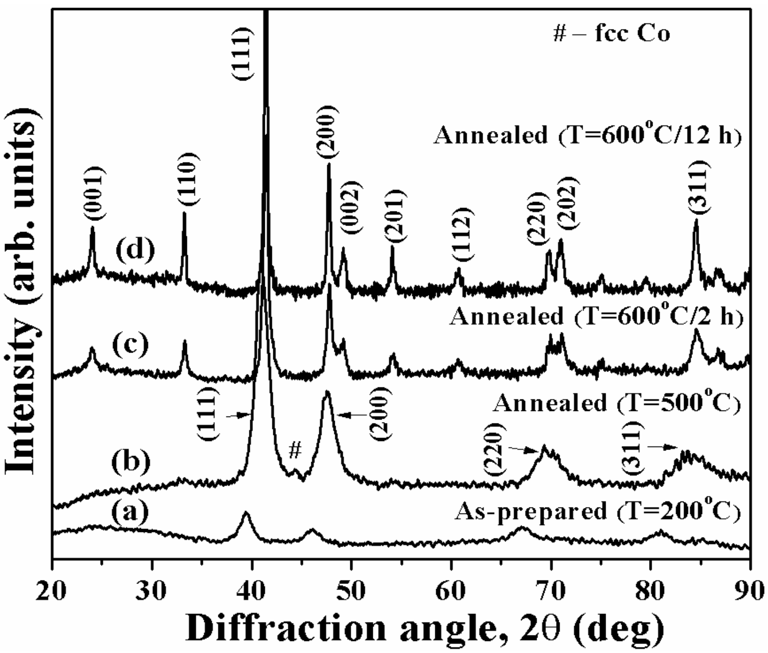

Figure 5.11 XRD patterns of Co-Pt nanoparticles synthesized via route 2; (a) as-prepared, (b) annealed at 500°C/2 h, and (c) annealed at 600°C/2 h, (d) annealed at 600°C/12 h.

Table 5.5 Capping agents, annealing conditions, lattice parameters and average crystallite sizes for Co-Pt alloy nanoparticles synthesized via route-1 and route-2.

Materials	Capping agents	Annealing conditions, temp/h (°C/h)	Lattice parameters			Average crystallite size (nm)
			c (Å)	*a* (Å)	*c/a* ratio	
CoPt (route-1)	CTAB	600/2	3.6877	3.8008	0.9702	7.2
CoPt (route-2)	Oleic acid + CTAB	600/2	3.7019	3.8034	0.9733	13.3
		600/12	3.7001	3.8075	0.9718	22.9

5.3.2.2 SEM microstructural studies of Co-Pt alloy nanoparticles

(A) Route-1

SEM micrographs of low and magnifications for the as-prepared materials of Co-Pt(route-1) are presented in Figure 5.12 (a) and (b). A micrograph with low magnification (15000X) show larger size clusters and nanostructures cannot be distinguished. More clarity was obtained from 55000X micrograph which shows the presence of agglomerated nanoparticles having average diameter of ~38 nm.

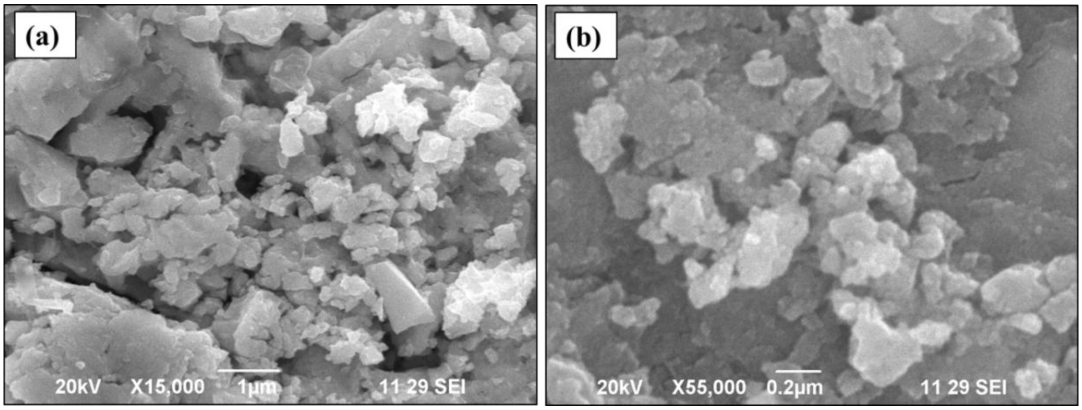

Figure 5.12 SEM micrographs of the as-prepared Co-Pt alloys via route-1 with various magnifications; (a) 15000X micrograph and (b) 55000X micrograph.

A SEM micrograph of the annealed Co-Pt(route-1) (at 600°C) is shown in Figure 5.13 (a) and corresponding SEM particle size distributions as inset. A SEM-EDX pattern of the annealed sample is shown in Figure 5.13 (b). SEM particle size and EDX composition are presented in Table 5.6. The spherical shape nanoparticles which can be easily distinguished from agglomerations are observed in the micrograph. The average SEM particle size was found to be 38 nm distributed over a range of few nm as indicated in the inset of Figure 5.13 (a). The SEM size distribution was observed to be ± 5 nm for Co-Pt(route-1) (Table 5.6). The compositions of Co-Pt(route-1) alloys obtained from the EDX analyses was $Co_{59}Pt_{41}$. The presence of oxygen in EDX spectra indicate that annealed Co-Pt materials are coated with organic matter containing oxygen.

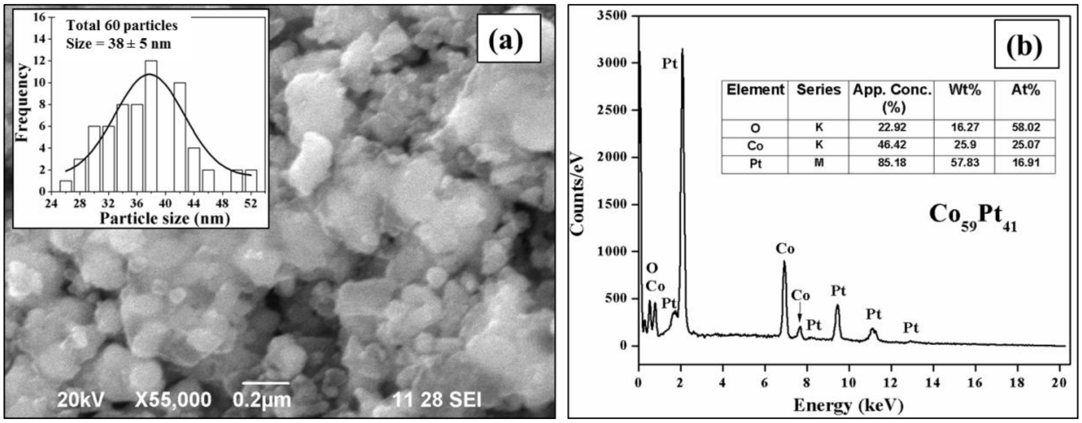

Element	Series	App. Conc. (%)	Wt%	At%
O	K	22.92	16.27	58.02
Co	K	46.42	25.9	25.07
Pt	M	85.18	57.83	16.91

Figure 5.13 (a) SEM micrographs of the annealed Co-Pt alloys via route-1 and inset shows particle size distribution and (b) a representative SEM-EDX micrographs.

(B) Route-2

SEM micrographs of low and high magnifications for as-prepared Co-Pt(route-2) alloys are presented in Figure 5.14 (a) and (b).A micrograph with low magnification (10000X) show the presence of nanoparticles and clusters. While, high magnification micrograph (30000X) contains nano-clusters of ~58 nm inside some sort of polymer like structures. Observation of such kind of results may be due to presence of capping agents at as-prepared state.

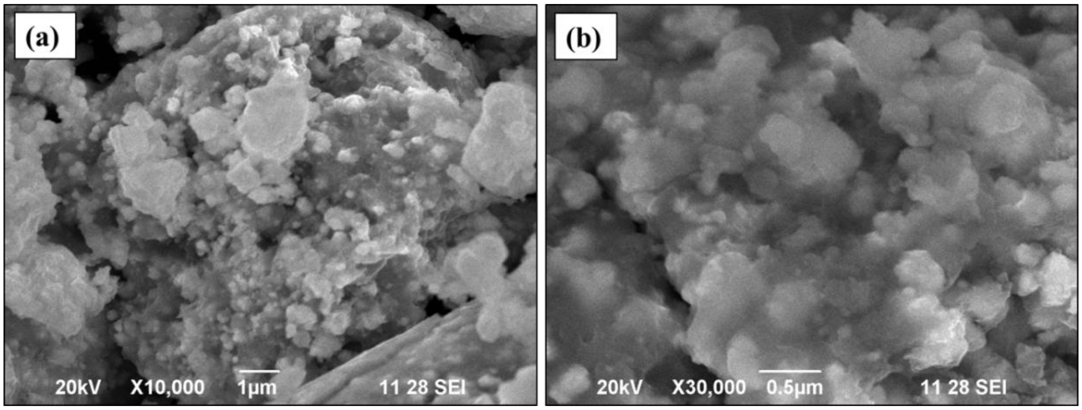

Figure 5.14 SEM micrographs of the as-prepared Co-Pt alloys via route-2 with various magnifications; (a) 10000X micrograph and (b) 30000X micrograph.

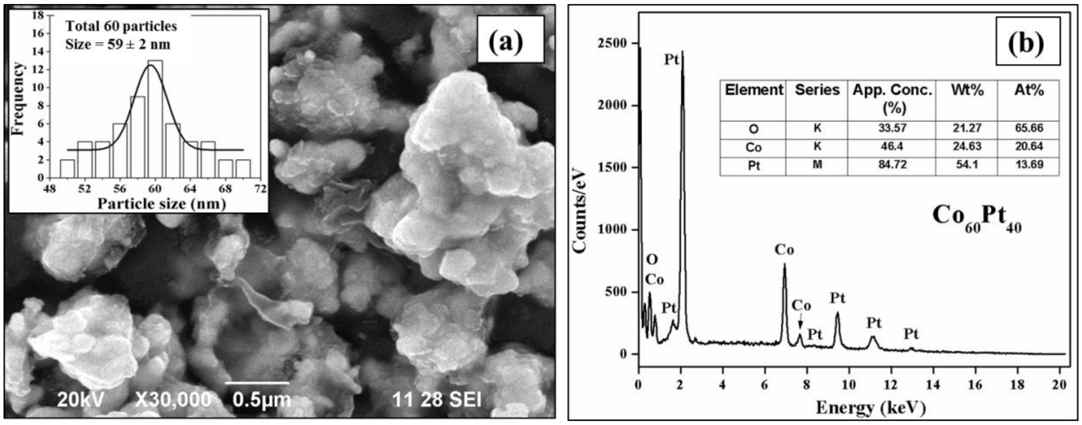

Element	Series	App. Conc. (%)	Wt%	At%
O	K	33.57	21.27	65.66
Co	K	46.4	24.63	20.64
Pt	M	84.72	54.1	13.69

Figure 5.15 (a) SEM micrographs of the annealed Co-Pt alloys route-2 and inset shows particle size distribution and (b) a representative SEM-EDX micrographs.

A SEM micrograph of the annealed Co-Pt(route-2) (at 600°C) is shown in Figure 5.15 (a) and corresponding SEM particle size distributions as inset. SEM-EDX pattern of the annealed Co-Pt(route-2) is shown in Figure 5.15 (b). SEM particle size and EDX composition are presented in Table 5.6. A micrograph indicates the spherical shape nanoparticles present in the agglomerated form. These agglomerations are bigger than Co-Pt(route-1) sample, which may be due to presence of more organic matter compared to route-1 sample. The average SEM particle size was found to be 59 nm with the narrow size distribution of ± 2 nm (Table 5.6). The estimated SEM particle size is larger than the crystallite size, i.e. 13.3 nm, indicates the agglomerations. The composition of Co-Pt(route-2) alloy obtained from the EDX analyses was $Co_{60}Pt_{40}$. The presence of oxygen in EDX spectra indicate that annealed Co-Pt materials are coated with organic matter containing oxygen.

It can be noted that similar composition obtained via route-1 and route-2, i.e. $Co_{59}Pt_{41}$ and $Co_{60}Pt_{40}$ respectively. These results show the effectiveness of superhydride reduction route for controlling compositions accurately.

Table 5.6 Annealing conditions, SEM-EDX composition, and SEM particle size for annealed Co-Pt alloy nanoparticles synthesized via route-1 and route-2.

Materials	Annealing conditions, temp/h (°C/h)	SEM-EDX composition, Co:Pt (At%)	SEM particle size distribution (nm)
Co-Pt (route-1)	600/2	59:41	38 ± 5
Co-Pt (route-2)	600/2	60:40	59 ± 2

5.3.2.3 Studies on magnetic properties of Co-Pt alloy nanoparticles

The Magnetization vs. field plots of Co-Pt nanomaterials, synthesized via route-1 and route-2, are shown in Figure 5.16 and Figure 5.17, respectively. The magnetic parameters for Co-Pt nanoparticles obtained via route-1 and route-2 are summarized in Table 5.7 and Table 5.8, respectively. The values of M_S for Co-Pt(route-1) are found to be 0.9 emu/g, 18.3 emu/g, and 31.4 emu/g whereas H_C values are observed at 428 Oe, 667 Oe, and 1728 Oe, for as-prepared, annealed at 500°C/2h, and annealed at 600°C/2h, respectively. On the other hand, the values of M_S for Co-Pt(route-2) are found to be 1.2 emu/g, 27.5 emu/g, 26.9 emu/g, and 22.5 emu/g whereas H_C values are observed at 870 Oe, 806 Oe, 2525 Oe, and 5027 Oe, for as-prepared, annealed at 500°C/2h, annealed at 600°C/2h, and annealed at 600°C/12h, respectively.

Co-Pt alloys synthesized via route-1 show ferromagnetic nature for as-prepared as well as annealed nanomaterials (Figure 5.16). It has been observed that the values of M_S increase drastically from 0.9 emu/g to 31.4 emu/g with annealing temperatures from 200°C to 600°C, respectively. The values of H_C increases slowly for as-prepared sample to annealed sample at 500°C, i.e. from 428 Oe to 667 Oe, and then large increase is found for sample annealed at 600°C, i.e. 1728 Oe. These results can be understood by increase in the crystallite sizes, volume fraction of fct phase, and order parameter associated with tetragonal phase [30]. However, the observed H_C values for Co-Pt alloys, annealed at 500°C and 600°C, are less than literature reported values i.e. 1.34 kOe and 3.67 kOe, at same temperatures [30]. It may be attributed to the presence of less fraction of fct phase as indicated by poor splitting of (200)/(002) peaks in the XRD pattern (Figure 5.10 (c)). It has been reported that for Co_xPt_{100-x} nano-crystalline alloys, the maximum H_C value can be obtained at around x equal to 50 and decreases for any other values [31]. In our study, Co-Pt(route-1) has SEM-EDX composition of $Co_{59}Pt_{41}$ which may be another reason for less coercivity, i.e. 1728 Oe. This result can be well supported by literature reported H_C value of ~2000 Oe for $Co_{60}Pt_{40}$ [31].

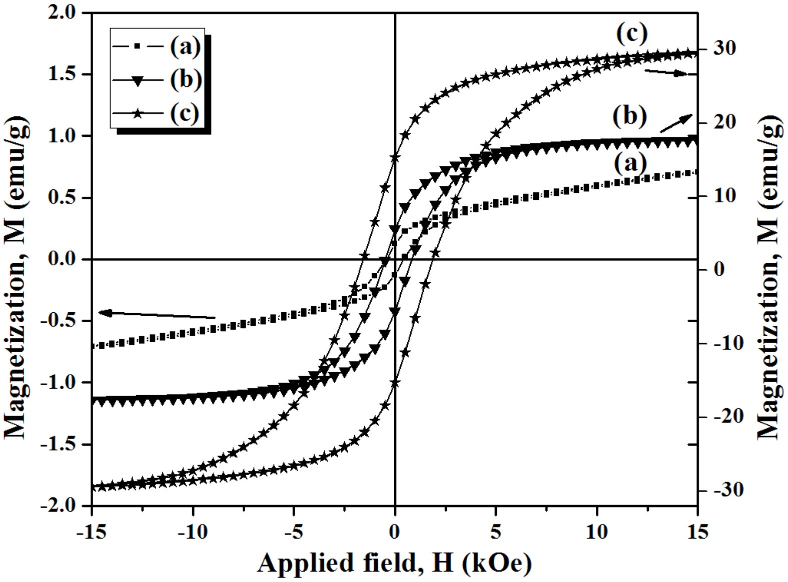

Figure 5.16 Magnetization vs. Field plots of Co-Pt alloys nanoparticles synthesized via route-1, (a) as-prepared, (b) annealed at 500°C/2h and (c) annealed at 600°C/2h under N_2(g) atmosphere.

Table 5.7 Materials, annealing conditions, saturation magnetization and coercivity values for Co-Pt alloys nanoparticles synthesized via route-1.

Materials	Annealing conditions, temp/h (°C/h)	Saturation magnetization, M_S (emu/g)	Coercivity, H_C (Oe)
Co-Pt (route-1)	As-prepared	0.9	428
	500/2	18.3	667
	600/2	31.4	1728

In a similar manner, Co-Pt alloys synthesized via route-2 also show ferromagnetic nature for as-prepared as well as annealed nanomaterials (Figure 5.17). The values of M_S are increasing drastically from 1.2 emu/g to 27.5 emu/g with annealing temperatures from 200°C to 500°C, respectively and thereafter decreasing slightly, i.e. 26.9 emu/g and 22.5 emu/g for annealing at 600°C for 2 h and 12 h, respectively. Initial increase in the H_C values up to 500°C is attributed to increase in the crystallite sizes with annealing at higher temperatures. While later decrease in M_S values at 600°C may be related to increase in fct phase which has slightly lower M_S than fcc CoPt phase. Such kinds of decrease in M_S values have been observed due to decrease in effective magnetic volume at annealing temperatures higher than 600°C [32].

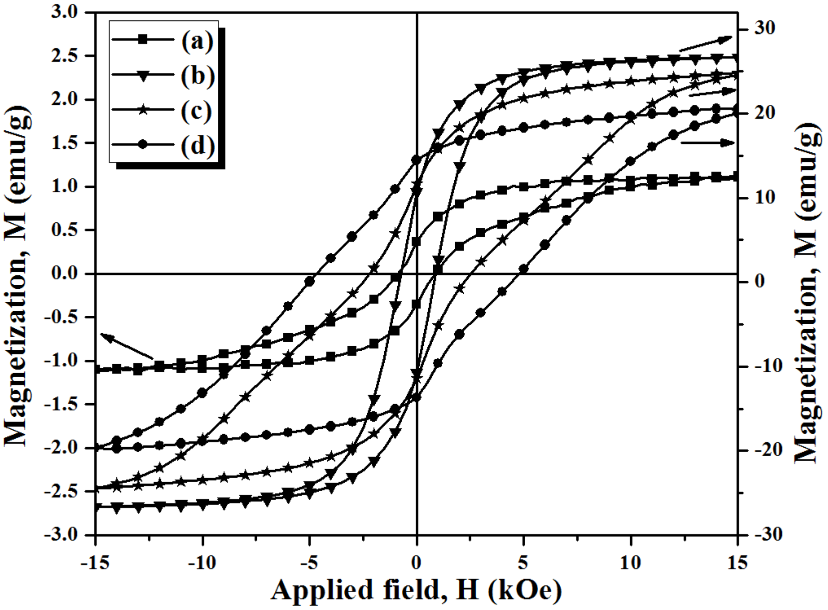

Figure 5.17 Magnetization vs. Field plots of Co-Pt alloys nanoparticles synthesized via route-2, (a) as-prepared, (b) annealed at 500°C/2h, (c) annealed at 600°C/2h and (d) annealed at 600°C/12h under the flow of purified N_2(g).

The value of H_C of annealed sample at 500°C (806 Oe) is less than as-prepared sample (870 Oe) (Table 5.8) and can be supported by corresponding decrease in crystallite size from XRD studies. Further, the large increases in values of H_C were found for samples annealed at 600°C for 2 h and 12 h, i.e. 2525 Oe and 5027 Oe, respectively. These results can be understood by increase in the crystallite sizes, volume fraction of fct phase, and order parameter with annealing at higher temperatures which induces high magnetocrystalline anisotropy [30]. These results are comparable with the literature reported value 3.67 kOe for alloys annealed at 600°C [30]. Co-Pt(route-2) has SEM-EDX composition of $Co_{60}Pt_{40}$ which may be the reason for less coercivity value, i.e. 2525 Oe, than literature reported value. However, observation of larger H_C value i.e. 5027 Oe for $Co_{60}Pt_{40}$ alloy annealed at 600°C for 12 h is interesting and the result can be compared with the reported H_C value of ~2000 Oe for $Co_{60}Pt_{40}$ alloy [31].

Table 5.8 Materials, annealing conditions, saturation magnetization and coercivity values for Co-Pt alloys nanoparticles synthesized via route-2.

Materials	Annealing conditions, temp/h (°C/h)	Saturation magnetization, M_S (emu/g)	Coercivity, H_C (Oe)
Co-Pt (route-2)	As-prepared	1.2	870
	500/2	27.5	806
	600/2	26.9	2525
	600/12	22.5	5027

5.4 Conclusions

We have successfully synthesized nanocrystalline $Fe_{50}Pt_{50}$ and $Fe_{54}Pt_{46}$ alloys via chemical reduction route using superhydride as reducing agent using modified synthetic strategy. Two different combinations of capping structures were designed, namely: oleic acid/oleylamine (route-1) and oleic acid/CTAB (route-2). Fe-Pt alloys were characterized by XRD and SEM techniques in as-prepared and annealed state. The as-prepared Fe-Pt alloys show amorphous disordered fcc crystalline phase with crystallite sizes of 2.3 nm and 6 nm for route-1 and route-2, respectively. After annealing at 600°C, Fe-Pt alloys were transformed to ordered fct phase with crystallite sizes of 21 nm and 19.5 nm for route-1 and route-2, respectively. SEM studies show that as-prepared Fe-Pt nanoparticles were surrounded by capping agents whereas annealed samples have spherical shape morphologies with SEM particle sizes of 24 nm and 21 nm for route-1 and route-2, respectively. As-prepared Fe-Pt alloys are ferromagnetic with presence of superparamagnetic fractions. Langevin fit to M vs. H plots of as-prepared Fe-Pt alloys gives average magnetic moments per particle to be 753 μ_B and 814 μ_B, for route 1 and 2, respectively. The values of saturation magnetization for annealed Fe-Pt alloys were found to be 4.4 emu/g and 29.6 emu/g for route-1 and route 2, respectively. Higher values of coercivities for 10000 Oe and 10792 Oe were obtained for fct Fe-Pt alloys synthesized from route-1 and route-2, respectively. The magnetic properties have been interpreted with the help of observed order parameters, size, surface, and composition effects of the Fe-Pt nanostructured materials.

$Co_{59}Pt_{41}$ and $Co_{60}Pt_{40}$ alloys have been synthesized via superhydride reduction route using two different combinations of capping structures, namely: CTAB (route-1) and oleic acid/CTAB (route-2). Further characterizations were carried out by XRD and SEM techniques in as-prepared and annealed at 500°C and 600°C. As-prepared Co-Pt alloys show amorphous disordered fcc crystalline phase and transformed to ordered fct phase after annealing at 600°C. SEM studies show that annealed Co-Pt nanoparticles have spherical shape morphologies with SEM particle sizes of 38 nm and 59 nm for route-1 and route-2, respectively. The values of M_S for Co-Pt alloys synthesized via route-1 are found to be 0.9 emu/g, 18.3 emu/g, and 31.4 emu/g whereas H_C values are 428 Oe, 667 Oe, and 1728 Oe, for as-prepared, annealed at 500°C/2h, and annealed at 600°C/2h, respectively. The values of M_S for Co-Pt alloys synthesized via route-2 are found to be 1.2 emu/g, 27.5 emu/g, 26.9 emu/g, and 22.5 emu/g whereas H_C values are 870 Oe, 806 Oe, 2525 Oe, and 5027 Oe, for as-prepared, annealed at 500°C/2h, annealed at 600°C/2h, and annealed at 600°C/12h, respectively. The observed magnetic properties have been interpreted with the help of crystallite sizes, order parameters, size, surface, and composition effects of the Co-Pt nanostructured materials.

References

1. E. Grochowski and D. A. Thompson, IEEE Trans. Magn., 30 (1994) 3797-3800.
2. D. N. Lambeth, D. E. Laughlin, S. Charap, L-L. Lee, P. Harllee and L. Tang, Magnetic Hysteresis in Novel Magnetic Materials, G. C. Hadjipanayis, Eds., Kluwer Academic, Dordrecht, 1997.
3. R. Wood, IEEE Trans. Magn., 36 (2000) 36-42.
4. G. Varvaro, S. Laureti and D. Fiorani, J. Magn. Magn. Mater., 368 (2014) 415-420.
5. D. J. Sellmyer, M. Yu and R. D. Kirby, Nanostruct. Mater., 12 (1999) 1021-1026.
6. I. Zafiropoulou, V. Tzitzios, D. Petridis, E. Devlin, J. Fidler, S. Hoefinger and Niarchos, Nanotechnology, 16 (2005) 1603-1607.
7. S. H. Charap, P-L. Lu and Y. He, IEEE Trans. Magn., 33 (1997) 978-983.
8. Y. Gao, X. W. Zhang, Z. G. Yin, S. Qu, J. B. You and N. F. Chen, Nanoscale Res. Lett., 5 (2010) 1-6.
9. S. Sun, C. B. Murray, D. Weller, L. Folks and A. Moser, Science, 287 (2000) 1989-1992.
10. K. Chokprasombat, P. Harding, C. Sirisathitkul, P. Muthitamongkol and S. Pinitsoontorn, Indian J. Eng. Mater. Sci., 19 (2012) 338-342.
11. V. Nandwana, K. E. Elkins and J. P. Liu, Nanotechnology, 16 (2005) 2823-2826.
12. M. Chen, J. P. Liu and S. Sun, J. Am. Chem. Soc., 126 (2004) 8394-8395.
13. A. C. C. Yu, M. Mizuno, Y. Sasaki and H. Kondo, Appl. Phys. Lett., 85 (2004) 6242-6244.
14. C. Srivastava, J. Balasubramanian, C. H. Turner, J. M. Wiest, H. G. Bagaria and G. B. Thompson, J. Appl. Phys., 102 (2007) 104310.
15. C. Srivastava, D. E. Nikles and G. B. Thompson, J. Appl. Phys., 104 (2008) 104314.
16. K. Chokprasombat, C. Sirisathitkul, P. Harding, S. Chandarak and R. Yimnirun Rev. Mex. Fis., 59 (2013) 224–228.
17. P. Gibot, E. Tronc, C. Chaneac, J. P. Jolivet, D. Fiorani and A. M. Testa, J. Magn. Magn. Mater., 290-291 (2005) 555-558.

18. H. M. Lee, S. G. Kim, I. Matsui, T. Iwaki, F. Iskandar, I. W. Lenggoro and K. Okuyama, J. Magn. Magn. Mater., 313 (2007) 62-68.
19. T. J. Klemmer, N. Shukla, C. Liu, X. W. Wu, E. B. Svedberg, O. Mryasov, R. W. Chantrell, D. Weller, M. Tanase and D. E. Laughlin, Appl. Phys. Lett., 81 (2002) 2220-2222.
20. L. Y. Lu, D. Wang, X. G. Xu, Q. Zhan and Y. Jiang, J. Phys. Chem. C, 113 (2009) 19867-19870.
21. M. S. Wellons, W. H. Morris III, Z. Gai, J. Shen, J. Bentley, J. E. Wittig and C. M. Lukehart, Chem. Mater., 19 (2007) 2483-2488.
22. D. Babonneau, G. Abadias, J. Toudert, T. Girardeau, E. Fonda, J. S. Micha and F. Petroff, J. Phys.: Condens. Matter, 20 (2008) 035218.
23. K. L. Pisane, S. Singh and M. S. Seehra, J. Appl. Phys., 117 (2015) 17D708.
24. S. Morup, E. Brok and C. Frandsen, J. Nanomater., 2013 (2013) Article ID 720629.
25. Y. Liu, Y. Jiang, X. Zhang, Y. Wang, Y. Zhang, H. Liu, H. Zhai, Y. Liu, J. Yang and Y. Yan, J. Solid State Chem., 209 (2014) 69-73.
26. H. H. Hsiao, R. N. Panda, J. C. Shih and T. S. Chin, J. Appl. Phys., 91 (2002) 3145-3149.
27. L. Bai, H. Wan and S. C. Street, Colloids Surf. A: Physicochem. Eng. Asp., 349 (2009) 23-28.
28. X. Sun, Z. Y. Jia, Y. H. Huang, J. W. Harrell, D. E. Nikles, K. Sun and L. M. Wang, J. Appl. Phys., 95 (2004) 6747-6749.
29. J. Fang, L. D. Tung, K. L. Stokes, J. He, D. Caruntu, W. L. Zhou and C. J. O'Connor, J. Appl. Phys., 91 (2002) 8816-8818.
30. C. N. Chinnasamy, B. Jeyadevan, K. Shinoda and K. Tohji, J. Appl. Phys., 93 (2003) 7583-7585.
31. A. C. C. Yu, M. Mizuno, Y. Sasaki, H. Kondo and K. Hiraga, Appl. Phys. Lett., 81 (2002) 3768-3770.
32. M. Yu, Y. Liu and D. J. Sellmyer, J. Appl. Phys., 87 (2000) 6959-6961.

CHAPTER VI

Development of newer synthetic routes for Co, Co-Ni and Co-Pt nanoparticles by using modified polyol method and studies on their structural and magnetic properties

6.1 Introduction

This chapter mainly deals with studies on Co based nanomaterials such as Co, Co-Ni and Co-Pt synthesized via novel polyol method. Several Fe and Co based alloys are specifically used in high temperature applications because of soft magnetic characteristics which include: low coercivity to minimize frequency independent losses, high resistivity to minimize frequency dependent eddy current losses, and high magnetization to increase the range of field amplitudes available for use [1]. Further, Co based nanomaterials have more stable magnetic properties in the temperature range of 500-600°C due to their higher Curie temperature, T_C [2]. Co-Pt alloys being hard magnetic materials have major applications in the field of ultrahigh density magnetic storage media because of their high values of H_C and K_u [3]. Polyol method can be performed by using inexpensive and nontoxic chemicals such as: PEG 200 as reducing agent, PVP as stabilizer to control size and shape of nanoparticles, non-aqueous solvents to protect nanoparticles from surface oxidation [3, 4]. Hence, polyol method was selected for the synthesis of Co, Co-Ni, Co-Pt nanomaterials owing to the fact that it is simple, cost effective and nontoxic. On the light of the above mentioned points various reports are available in the literature [5-7] and a few of them are summarized below mentioned paragraph.

Generally, polyol process uses ethylene glycol as reducing agent and sodium hydroxide to facilitate electron transfer from polyol to the ionic species which result in reduction [5]. However, polyol method has lesser control on the growth of the particles [8]. Hence, in order to achieve control on particle growth, development of novel methodologies have become an important topic of research. Synthesis of nanocrystalline Co-Ni alloys with controlled compositions by polyol reduction method was reported without any nucleating agent or protecting agent. [6]. Polyol reduction method has been used for synthesis of morphology controlled nanostructures, e.g. flower like morphology, by a simple one pot polyol process [5]. Modifications in the polyol method were carried out to control size and air stability by varying reaction conditions and additionally using PEG [7].

In earlier reports on synthesis of materials using polyol route, ethylene glycol or polyol was used as both reducing agent and solvent. As polyols have limited solubility for various capping agents or stabilizers, polyol methods are unable to use for the synthesis of capped nanoparticles which have large applications. It is well known that capping agents are helpful for controlling size and morphology of the nanomaterials. In view of above points, novel polyol method have been reported which include DMF as solvent and modified reactions conditions (e.g. temperature, capping agents, materials processing etc.) for synthesis of controlled nanostructures. Polyol reduction method was modified by using PEG-200 as reducing agent, PVP as capping agent and DMF as solvent. PEG and PVP were chosen as these are biocompatible materials and synthesized nanoparticles coated with PVP can be useful for biomedical applications. This chapter focuses on synthesis, magnetic characteristics studies of Co, $Co_{50}Ni_{50}$ and $Co_{50}Pt_{50}$ nanomaterials. Specifically, equiatomic composition of Co-Ni and Co-Pt alloys were chosen because these alloys have more stability compare to other compositions. $Co_{50}Pt_{50}$ has large coercivity than other compositions which is required for magnetic storage applications.

6.2 Experimental

The chemicals used for synthesis of above materials include cobalt chloride hexahydrate ($CoCl_2·6H_2O$), nickel chloride hexahydrate ($NiCl_2·6H_2O$) and Polyethyleneglycol (PEG-200) procured from Molychem, India; N, N dimethylformamide (DMF), sodium hydroxide (NaOH) from Fisher scientific, India; platinum chloride ($PtCl_2$, 73 wt% Pt), polyvinylpyrrolidone (PVP, M.W. = 58000) from Acros organics, USA. The chemicals were of analytical grade and have been used without further purification.

In a typical synthesis, metal salts were added into 20 ml DMF in a 250 ml three neck flask. Thereafter, addition of capping agent, i.e. PVP (1:1 wt/wt ratio with salts) and PEG-200 (2 ml per mmol of salts) were carried out with vigorous stirring using magnetic stirrer at RT. Then, the mixture was heated to 100-110°C for the duration of 5 min. To this solution, NaOH pellets (1 pellet per mmol) were added under vigorous stirring. Black color dispersion of nanoparticles was occurred. Reaction mixture was maintained at this temperature for 15 min and cooled down to RT. 100 ml acetone was added to precipitate solids. The colloid dispersion was separated by centrifugation at 5000 rpm for different time duration (say 5-10 min). These solids were washed with water repeatedly till water shows neutral pH, then with acetone and dried in vacuum at RT (as-prepared materials). The final products were obtained from as-prepared materials using two different drying and processing conditions, i.e. (i) route-1 and (ii) route-2. Route-1 and route-2 represents products without and with traces of NaCl, respectively. In route-1, solids obtained after centrifugation were washed with distilled water (in order to wash out NaOH and NaCl) and finally with acetone. These samples were annealed at 600°C-700^{o}C for 6-12 hrs duration under N_2(g) flow. In route-2, solids obtained after centrifugation were first annealed at 600°C-700^{o}C for 6 h under N_2(g) flow and then materials were washed using distilled water (in order to wash out NaOH and NaCl) followed by final washing with acetone.

Table 6.1 Details of moles and weights of metal salts used in polyol reduction method.

Materials	$CoCl_2{\cdot}6H_2O$		$NiCl_2{\cdot}6H_2O$		$PtCl_2$ (73 wt% Pt)	
	Moles (mmol)	weight (g)	Moles (mmol)	weight (g)	Moles (mmol)	weight (g)
Co	2	0.476	---	---	---	---
$Co_{50}Ni_{50}$	1	0.238	1	0.238	---	---
$Co_{50}Pt_{50}$	0.2	0.049	---	---	0.2	0.053

6.3 Results and Discussion

The synthesized materials (Co, Co-Ni and Co-Pt) synthesized by polyol routes were subjected to different processing parameters and studied for their characterizations, electron microscopy and magnetic properties. The following sub-sections deals with the aforesaid aspects separately utilizing Co, Co-Ni and Co-Pt materials systems.

6.3.1 Characterizations and Magnetic properties of Co nanoparticles synthesized via polyol route

6.3.1.1 XRD studies of Co nanoparticles

The XRD patterns of as-prepared and annealed Co nanoparticles at 600°C for 6 h under N_2(g) atmosphere are presented in Figure 6.1. The values of the lattice parameters and crystallite sizes of Co (route-1) and Co (route-2) have been summarized in Table 6.2. The absence of diffraction peaks in XRD patterns for as-prepared Co nanomaterials, except a very small intensity peak centered on 60° indicates amorphous nature of the as-prepared materials (Figure 6.1 (a)). The small peak at 60° may correspond to CoO formation on the surface as the materials were dried in air. After Annealing of the as prepared precursors at 600°C under inert gas atmosphere via two routes, i.e. route-1 (without NaCl matrix) and route-2 (with NaCl matrix), crystalline products were obtained. Co (route-1) crystallizes in hcp phase (α) whereas Co (route2) crystallizes in fcc (β) phase after post heat treatment. The observed XRD patterns were indexed in accordance with JCPDS # 05-0727 for α-Co and # 15-0806 for β-Co, respectively. [9]. One striking feature in the observed XRD pattern for hcp Co is that intensity of (002) peak is higher than intensity of (100) peak. These results indicate preferential growth of the crystal lattice along (002) plane of *c*-axis [10]. The estimated values of lattice parameters for hcp (α) phase of Co (route-1) are a = 2.4972 Ǻ and c = 4.0734 Ǻ whereas for fcc (β) Co (route-2), a = 3.5403 Ǻ is observed. Average crystallite sizes estimated from XRD line broadening for hcp Co(route-1) and fcc Co(route-2) were found to be 16.4 nm and 37.1 nm, respectively. These estimated average crystallite sizes for annealed Co nanomaterials are comparable with the literature reported values of 19 nm for Co synthesized via polyol method [11]. In case of bulk Co, hcp phase is stable below 450°C while fcc phase is stable at temperatures above 450°C. However, the presence of hcp phase at 600°C in Co (route-1) sample is may be attributed to the fine particle nature of the materials [12]. The observation of only fcc phase for Co (route-2) rather than energetically stable hcp phase is may be due to annealing in presence of crystalline NaCl matrix. Such kind of stabilizations of fcc phase have already been noticed for cobalt in crystalline copper matrix [13]. The values of lattice parameters for hcp Co (i.e. a = 2.4972 Å and c = 4.0734 Å) and fcc Co (i.e. a = 3.5403 Å) phases are in well agreement with reported values of a = 2.5088 Å, c = 4.0762 Å for α-Co and a = 3.5448 Å for β-Co [14].

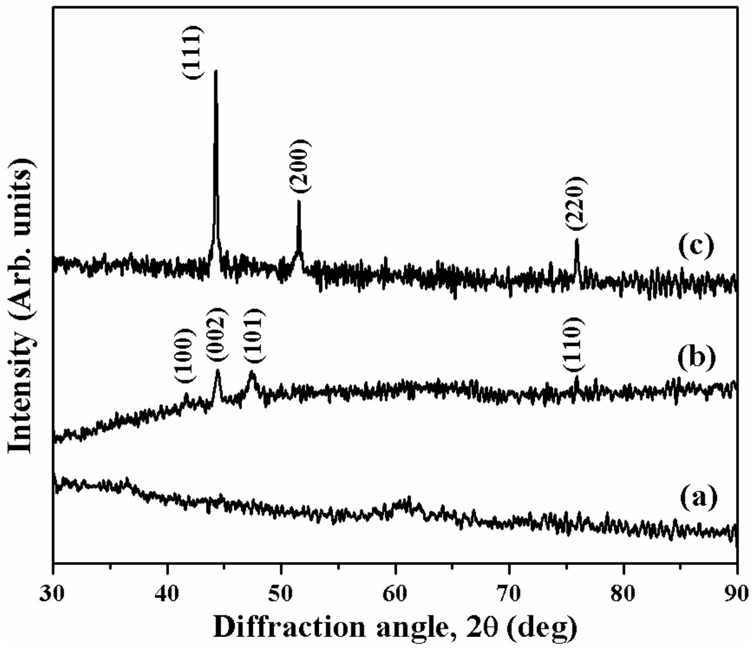

Figure 6.1 Indexed XRD patterns of Co nanoparticles synthesized via polyol process in (a) as-prepared state and (b) annealed via route-1, and (c) route-2, at 600°C/6 h under N_2(g) flow.

Table 6.2 Materials, annealing conditions, crystalline phases, lattice parameters and average crystallite sizes for Co nanoparticles synthesized via route-1 and route-2.

Materials	Annealing conditions, temp/h (°C/h)	Crystalline phase	Lattice parameters		Average crystallite size (nm)
			a (Å)	c (Å)	
Co (route-1)	600/6	hcp	2.4972	4.0734	16.4(±1)
Co (route-2)	600/6	fcc	3.5403	–	37.1(±1)

6.3.1.2 TEM micrographs studies of Co nanoparticles synthesized via polyol route

TEM micrographs for Co annealed at 600°C via route1 and route-2 are shown in Figure 6.2 ((a) and (c)). The corresponding TEM size distribution plots have been shown in Figure 6.2 ((b) and (d)). TEM particle morphologies and sizes are tabulated in Table 6.3.

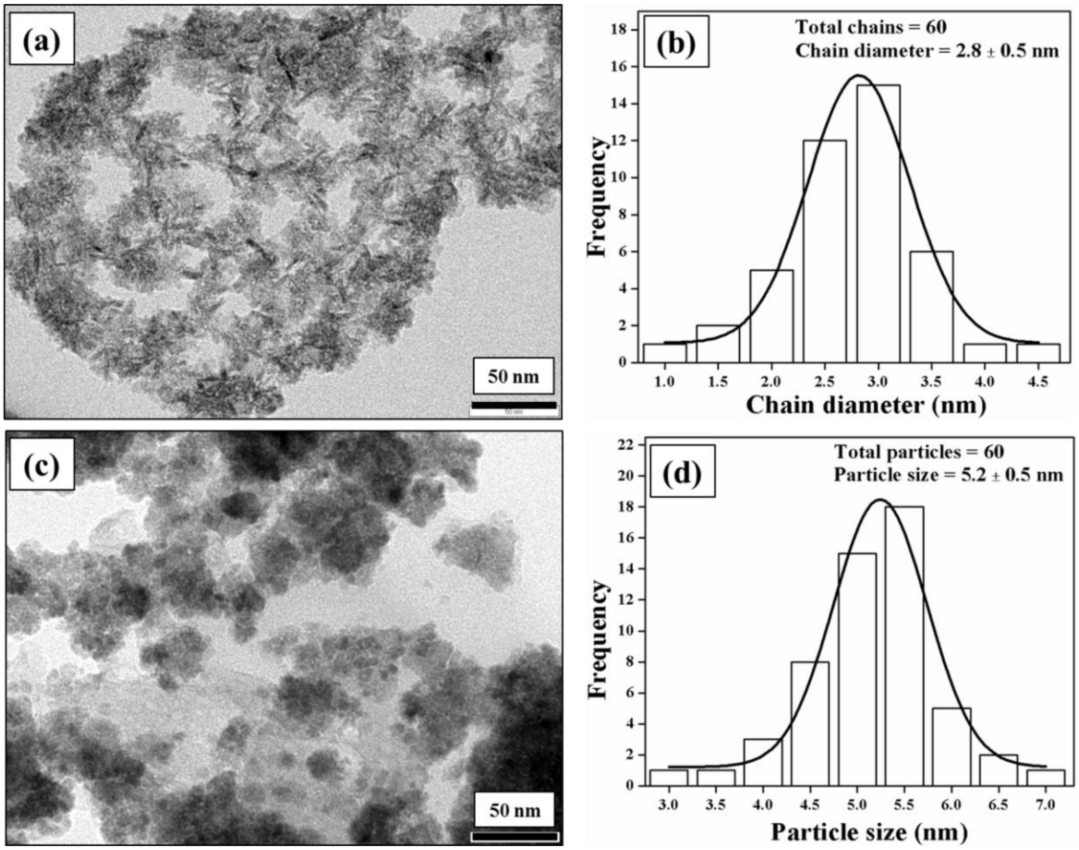

Figure 6.2 TEM micrographs and corresponding size distributions plots of Co nanoparticles synthesized by ((a) and (b)) route-1 and ((c) and (d)) route-2, respectively.

Table 6.3 TEM particle morphology and TEM particle size, of Co (route-1) and Co (route-2) nanomaterials annealed at 600°C for 6 h under N_2(g) atmosphere.

Materials	TEM particle morphology	TEM particle size (nm)
Co (route-1)	Chains	Diameter = 2.8 ± 0.5 Length = 15 to 26
Co (route-2)	Spheres	5.2 ± 0.5

TEM micrograph of Co(route-1) shows chain-like nanostructures having uniform dispersion. The formation of chains may be resulted due to hcp crystal structure having c/*a* ratio of 1.6 as confirmed from XRD studies (Table 6.2). The estimated values of average chain diameter was found to be 2.8 ± 0.5 nm and chain lengths varies from 15-26 nm. TEM micrograph of Co(route-2) shows monodispersed nanostructures with nearly spherical morphologies. Average TEM particle size for Co(route-2) was found to be 5.2 ± 0.5 nm. TEM micrographs results of Co nanomaterials from both the routes show narrow size distributions. The estimated TEM particle sizes are smaller than crystallite sizes, i.e. 16.4 nm and 37.1 nm for Co(route-1) and Co(route-2), respectively. These results might be due to the fact that TEM particle size corresponds to local probe which contains smaller particles only while crystallite size corresponds to the average of the whole mass including larger crystallites [15].

6.3.1.3 Magnetic properties of Co nanoparticles synthesized via polyol route

M vs. H curves for Co (route-1 and route-2), measured at RT and at 100K, are shown in Figure 6.3. The estimated values of the M_S and H_C for Co alloys are tabulated in Table 6.4. Co nanoparticles annealed at 600°C, contain organic coating at the surface. Total wt% of CHN content for Co(route-1) and Co(route-2) were found to be 0.1 % and 10.2 %, respectively. Therefore, two different values of M_S are reported herewith, i.e. one denotes M_S without considering wt% of organic layer and the other, M'_S, after wt% corrections corresponding to total CHN content (Table 6.4). For Co(route-1), the values of M_S, M'_S and H_C were found to be 162.5 emu/g, 162.7 emu/g and 220 Oe, at RT whereas 166.9 emu/g, 167 emu/g and 357 Oe, at 100K respectively. For Co(route-2), the values of M_S, M'_S and H_C were found to be 26.7 emu/g, 29.7 emu/g and 185Oe, at RT whereas 31.4 emu/g, 35 emu/g and 369Oe, at 100K, respectively (Table 6.4).

Corrected values of M_S of Co(route-1) measured at RT, i.e. 162.7 emu/g, is matching well with the value for bulk hcp Co (162 emu/g) whereas M_S values of Co(route-2), i.e. 29.7 emu/g, is less than the value for bulk fcc Co (172 emu/g) [16]. The observation of large reduction in M_S for Co(route-2) sample may be attributed to size, shape, spin canting at the surface, altered crystal anisotropies etc. [17, 18]. These aspects have already been explained in the chapter I, subsection 1.6.4. Further, reduction in M_S in our Co(route-2) may also be due to presence of fcc phase as nanocrystalline fcc Co show reduction in magnetization than bulk value [19]. Possibly, the chain structure observed in TEM micrograph is the responsible factor for larger magnetization in samples produced via route-1. In such kind of materials shape anisotropy plays a very important role along with several other factors described above. Saturation magnetization of Co(route-1) and Co(route-2) measured at 100K show enhancement of 0.06 % and 3.55 % respectively, in the M_S values compare to the values at RT. It has been reported that magnetization of Co increases slowly lowering temperature from 300K to 100K and thereafter increases fast below 100K [20]. Hence our results are in accordance with literature reported data.

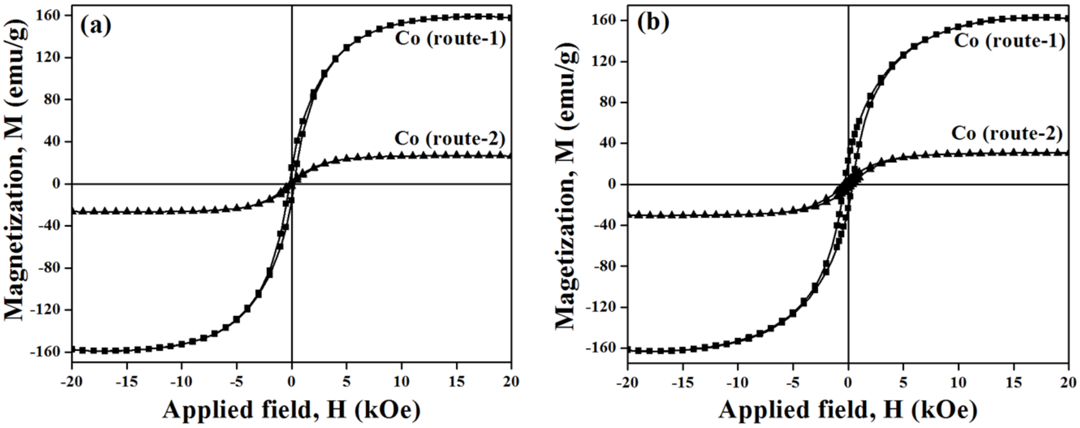

Figure 6.3 Magnetization vs. field plots of Co nanoparticles synthesized via route-1 and route-2, measured at two different temperatures; (a) RT(298K) and (b) 100K.

Table 6.4 Materials, total CHN content, saturation magnetization (M_S), Corrected M_S and Coercivity (H_C) of Co nanocrystals synthesized via route-1 and route-2 at RT and 100K.

Materials	Total CHN content (wt%)	M_S (emu/g)		M'_S(emu/g)		H_C (Oe)	
		RT	100K	RT	100K	RT	100K
Co (route-1)	0.1	162.5	166.9	162.7	167	220	357
Co (route-2)	10.2	26.7	31.4	29.7	35	185	369

It has been reported that hcp Co is magnetically hard phase (H_C > 400 Oe) whereas fcc Co is magnetically soft phase (H_C < 100 Oe) [9, 21]. The H_C value at RT of hcp Co(route1), i.e. 220 Oe, is less than literature reported value of 583 Oe for magnetically hard hcp Co phase with particle size of 10-12 nm [22]. The decrease in H_C values for hcp Co(route-1) sample is attributed to smaller TEM particle size because coercivity of Co nanoparticles decreases with decreasing particle size below critical size of 61 nm [23] (Refer- Chapter I, subsection 1.6.2). Further, the H_C value of fcc Co(route-2) at RT, i.e. 185 Oe, is larger than the values expected for soft magnetic materials. These alterations can be supported by the presence of small ferromagnetic fractions having larger particles, as indicated by particle size distribution studies, can results in larger H_C values for Co nanoparticles. At 100K, the H_C values of Co(route-1) and Co(route-2) increased by 1.6 times and 2.0 times, respectively, compare to the H_C values at RT. Such kind of enhancement in H_C values at low temperatures can be explained by dominance of thermal effects over anisotropy energy barrier according to Kneller's law which is applicable in the temperature range of 0 K to T_B [24, 25].

6.3.2 Characterizations and magnetic properties of $Co_{50}Ni_{50}$ alloy nanoparticles synthesized via polyol route

6.3.2.1 XRD studies of $Co_{50}Ni_{50}$ alloy nanoparticles

XRD patterns of as-prepared and annealed Co-Ni alloy at 600°C via route-1 and route-2 are shown in Figure 6.4. The values of lattice parameters and crystallite sizes of Co-Ni(route-1) and Co-Ni(route-2) have been summarized in Table 6.5.The as-prepared Co-Ni nanomaterials show amorphous nature (Figure 6.4 (a)) whereas annealed Co-Ni alloys via route-1 (without NaCl matrix) and route-2 (with NaCl matrix) crystallize in fcc phase (JCPDS # 04-8490) [26]. The formation of stable fcc crystal phases of Co-Ni alloys annealed via both the routes route-1 and route-2 may be attributed to Ni which stabilizes fcc phase at Co:Ni molar ratio above 1:1 [27]. The values of lattice parameters (*a*) for Co-Ni(route-1) and Co-Ni(route-2) are found to be 3.5328 Ǻ and 3.5282 Ǻ, respectively. These values of lattice parameters are lies in between the values of fcc Co (*a* = 3.5447 Å) and fcc Ni (*a* = 3.5238 Å) [27]. These results confirm the formation of Co-Ni alloys with high homogeneity. Average crystallite sizes for Co-Ni(route-1) and Co-Ni(route-2) were found to be 28.1 nm and 30.4 nm, respectively.

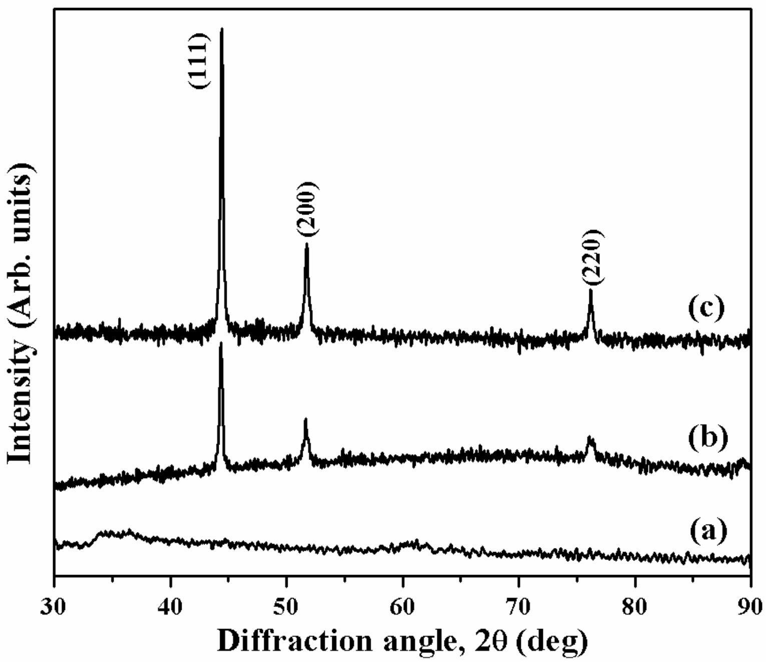

Figure 6.4 Indexed XRD patterns of CoNi nanoparticles synthesized via polyol process in (a) as-prepared state and (b) annealed via route-1, and (c) route-2, at 600°C/6 h under N_2(g) flow.

Table 6.5 Materials, annealing conditions, crystalline phases, lattice parameters and average crystallite sizes for Co-Ni alloy nanoparticles.

Materials	Annealing conditions, temp/h (°C/h)	Crystalline phase	Lattice parameters, *a* (Å)	Average crystallite size (nm)
Co-Ni (route-1)	600/6	fcc	3.5328	28.1(±1)
Co-Ni (route-2)	600/6	fcc	3.5282	30.4(±1)

6.3.2.2 TEM micrographs studies of $Co_{50}Ni_{50}$ alloy nanoparticles synthesized via polyol route

TEM microstructural studies have been carried out for a typical sample of Co-Ni(route-2). TEM micrograph and corresponding TEM size distribution plot for Co-Ni(route-2) are shown in Figure 6.5 (a and b). TEM micrograph of Co-Ni(route-2) shows nanostructures with nearly spherical morphologies. Average TEM particle size for Co-Ni(route-2) was found to be 8±1 nm with narrow size distribution. The observed TEM particle size is smaller than crystallite size, i.e. 30.4 nm, might be due to the fact that estimation of TEM particle size performed on specific area which contains smaller particles only while estimation of crystallite size takes average of the whole mass including larger crystallites. Similar observations have been reported in the literature and have been well demonstrated by Ponrouch et al. for porous Ru nanowires [15].

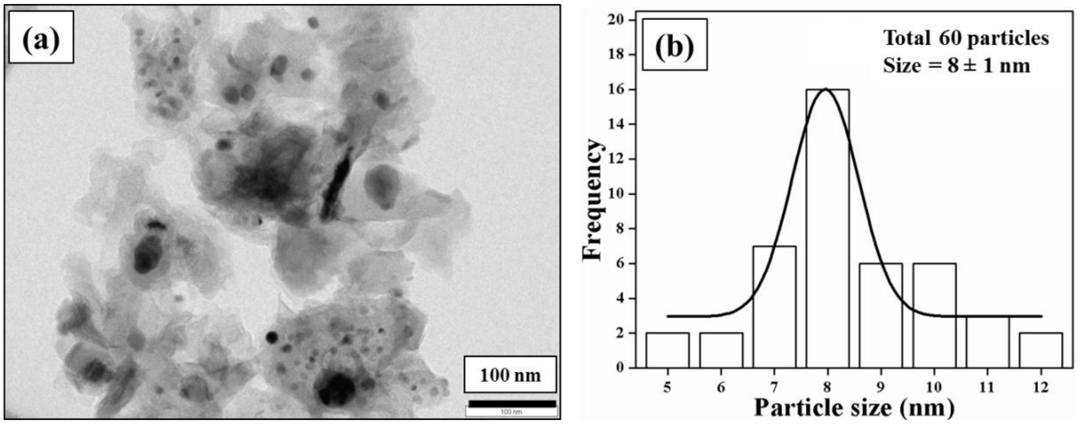

Figure 6.5 (a) A TEM micrograph of Co-Ni(route-2) and (b) its corresponding TEM particle size distribution plot.

6.3.2.3 Magnetic properties of $Co_{50}Ni_{50}$ alloy nanoparticles synthesized via polyol route

M vs. H curves for Co-Ni(route-1 and route-2) alloys measured at RT and at 100K are shown in Figure 6.6 (a) and (b), respectively. The estimated values of the M_S and H_C for Co-Ni alloys are tabulated in Table 6.6. Co-Ni alloys annealed at 600°C, contain organic coating at the surface. Total wt% of CHN content for Co-Ni(route-1) and Co-Ni(route-2) were found to be 0.2 % and 21.5 %, respectively. Therefore, two different values of M_S are reported herewith, i.e. one denotes M_S without considering wt% of organic layer and the other, M'_S , after wt% corrections corresponding to total CHN content. For Co-Ni(route-1), the values of M_S, M'_S and H_C were found to be 116 emu/g, 116.2 emu/g and 86 Oe, at RT whereas 109.7 emu/g, 110 emu/g and 93 Oe, at 100K respectively. For Co-Ni(route-2), the values of M_S, M'_S and H_C were found to be 35.8 emu/g, 45.6 emu/g and

214Oe, at RT whereas 37.2 emu/g, 47.4 emu/g and 324Oe, at 100K, respectively.

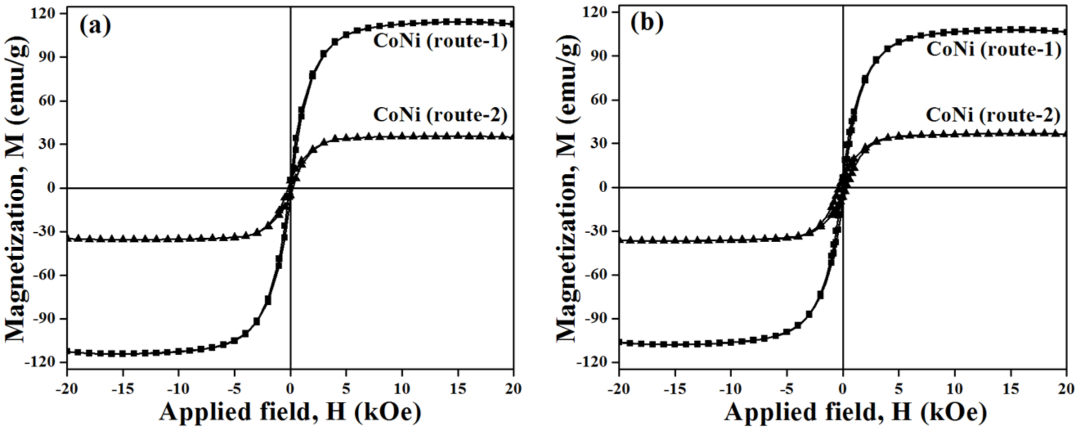

Figure 6.6 Magnetization vs. field plots of Co-Ni nanoparticles synthesized via route-1 and route-2, measured at different temperatures; (a) RT(298K) and (b) 100K.

Table 6.6 Materials, Total CHN content, M_S, corrected M_S and H_C of Co-Ni (route-1) and Co-Ni (route-2) nanomaterials measured at RT and 100K.

Materials	Total CHN content (wt%)	M_S (emu/g)		M'_S(emu/g)		H_C (Oe)	
		RT	100K	RT	100K	RT	100K
Co-Ni (route-1)	0.2	116	109.7	116.2	110	86	93
Co-Ni (route-2)	21.5	35.8	37.2	45.6	47.4	214	324

The corrected M_S value for $Co_{50}Ni_{50}$(route-1) alloy measured at RT, i.e. 116.2 emu/g, is matching well with the value reported for bulk $Co_{50}Ni_{50}$ alloy (110 emu/g) [28]. H_C value for $Co_{50}Ni_{50}$ (route-1) alloy measured at RT, i.e. 86 Oe, is close to superparamagnetic regime. At 100K, one can expect the increase in M_S and H_C values when compared with the values measured at RT. However, it has been observed that M_S value Co-Ni(route-1) sample decreases (i.e. 110 emu/g) whereas H_C value increases slightly (i.e. 93 Oe), at 100K compare to the values at RT. It has been reported in the literature that decrease in magnetization value of superparamagnetic Co nanoparticles with lowering the temperature may be observed due to deviations in anisotropy near saturation of magnetization [29]. Hence, abrupt decrease in M_S value of Co-Ni(route-1) at 100K may be attributed to deviations in anisotropy as superparamagnetic nature of this material can be proved by low coercivity value.

It has been observed that corrected M_S of $Co_{50}Ni_{50}$(route-2), i.e. 45.6 emu/g, is less than the reported value bulk $Co_{50}Ni_{50}$ alloy (110 emu/g) [28]. The reduction in M_S values of Co-Ni(route-2) can be explained on the basis of size and surface effects. At 100K, corrected M_S of $Co_{50}Ni_{50}$(route-2), i.e. 47.4 emu/g is slightly greater than the value at RT. This is in accordance with the literature data where magnetization has been found to increase slowly by lowering temperature from 300K to 100K and thereafter increases drastically below 100K [20]. The observed H_C values for annealed $Co_{50}Ni_{50}$(route-2) at RT and 100K were found to be higher than the typical range for soft magnetic materials. These results may be attributed fine particle size effects in the materials. Further, enhancement in the H_C value is observed at 100K compare to H_C value at RT. These results are in accordance with reported observation of increase in H_C value of Co based nanomaterials with decreasing temperature, goes through maximum and decreases again [20, 30].

6.3.3 Characterizations of the synthesized materials and magnetic properties of fct $L1_o$ Co-Pt alloy nanoparticles

6.3.3.1 XRD studies of Co-Pt alloy nanoparticles

The XRD patterns of as-prepared and annealed Co-Pt alloy nanoparticles via route-1 and route-2 were represented in Figure 6.7. The materials processing parameters, lattice parameters and crystallite sizes are tabulated in Table 6.7. As-prepared Co-Pt alloy nanoparticles show disordered fcc crystal structure (Figure 6.7, (a)) with crystallite size of 2.5 nm. As-prepared Co-Pt alloy nanoparticles were annealed at 700°C for 6 h via two routes, i.e. route-1 (without NaCl matrix) and route-2 (with NaCl matrix). It has been observed that Co-Pt alloy nanoparticles annealed via route-1 possess fcc crystal structure even at 700°C (Figure 6.7, (b)) with lattice parameters (*a*) and average crystallite size equal to 3.7138 Å and 22.6(±1) nm, respectively. However, Co-Pt alloy nanoparticles annealed via route-2 shows transformation to long range ordered fct ($L1_0$) phase (ICDD card no. 43-1358) average crystallite size equal to 24.7(±1) nm. Disordered fcc to ordered fct phase transformation in Co-Pt alloys strongly depends on synthetic routes, crystallinity, grain boundaries and annealing temperature etc. [31, 32]. Hence, absence of fct phase in Co-Pt(route-1) may be attributed to less crystallinity and presence of grain boundaries in the sample whereas these limitations might overcome in Co(route-2) after annealing with NaCl matrix. In Co(route-2), the presence of peaks at 2θ values of 24.1°, 33.4° and 47.4°/49.2° corresponding to superlattice reflections, i.e. (001), (110) and (200)/(002) doublet peaks in XRD pattern of Co-Pt materials (Figure 6.7 (c)) [33]. Long-range order parameters (S) was calculated by using the intensities of (001) and (002) diffraction peaks and found to be 0.9 [34]. The calculated values of the lattice parameters from (001) and (110) peaks for $L1_0$ Co-Pt were c = 3.6984 Å and a = 3.7929 Å with c/a = 0.9702 (Table 5.4). These lattice parameters are comparable with the literature reported values for pure $L1_0$ Co-Pt alloy, i.e. c = 3.7010 Å and a = 3.8030 Å with c/a = 0.9750 [35]. These results confirm the formation of $L1_0$ Co-Pt alloy annealed via route-2. As fct phase is obtained via route-2 successfully, our focus remains on microstructural and magnetic properties of Co-Pt samples in the following sub-sections.

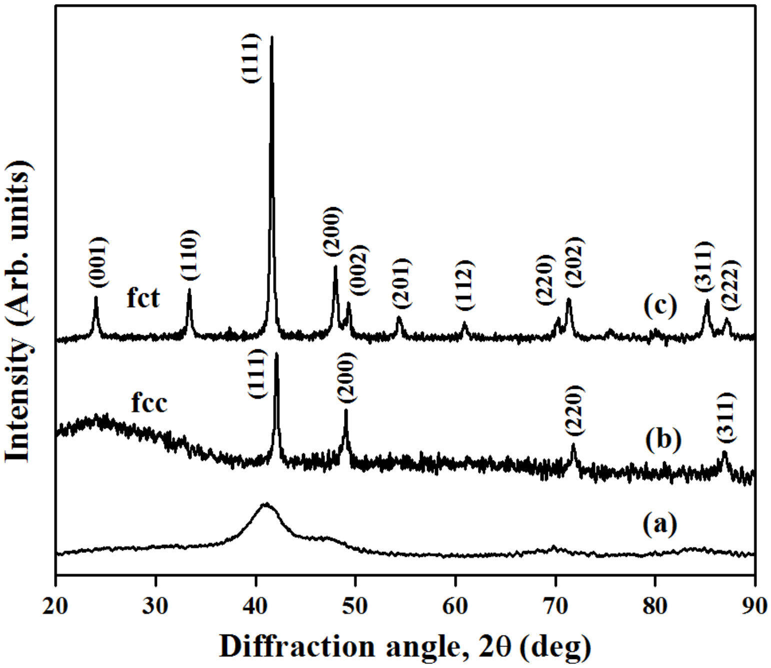

Figure 6.7 Indexed XRD patterns of CoPt nanoparticles synthesized via polyol process in (a) as-prepared state and (b) annealed via route-1, and (c) route-2, at 700°C/6 h under $N_2(g)$ flow. Route-1 and route-2 represents products without and with traces of NaCl.

Table 6.7 Materials, annealing conditions, crystalline phases, lattice parameters and average crystallite sizes for Co-Pt alloy nanoparticles.

Materials	Annealing conditions, temp/h (°C/h)	Crystalline phase	Lattice parameters			Average crystallite size (nm)
			c (Å)	a (Å)	c/a ratio	
CoPt (route-1)	700/6	fcc	–	3.7138	–	22.6(±1)
CoPt (route-2)	700/6	fct	3.6984	3.7929	0.9750	24.7(±1)

6.3.3.2 SEM micrographs studies fct $L1_0$ of Co-Pt alloy nanoparticles synthesized via polyol method (route 2)

SEM microstructural studies were carried out only for Co-Pt alloy annealed via route-2 because it has fct crystal structure and used for magnetic properties study whereas Co-Pt alloy annealed via route-1 has fcc crystal structure. SEM micrograph of Co-Pt alloy nanoparticles annealed via route-2 is shown in Figure 6.8 (a) and inset represents the SEM particle size distribution. SEM-EDX pattern of the annealed sample is shown in Figure 6.8 (b). SEM micrograph shows the presence of spherical shape nanoparticles which can be easily distinguished from agglomeration. The average SEM particle size was found to be 41 nm with narrow size distribution of ± 3 nm. The estimated SEM particle size is larger than the crystallite size, i.e. 24.7 nm. SEM-EDX analysis indicates that the composition of Co-Pt alloy annealed via route-2 was $Co_{58}Pt_{42}$ (Figure 6.8 (b)). The presence of oxygen in EDX spectra has origin from coated organic matter at the surface of annealed Co-Pt materials.

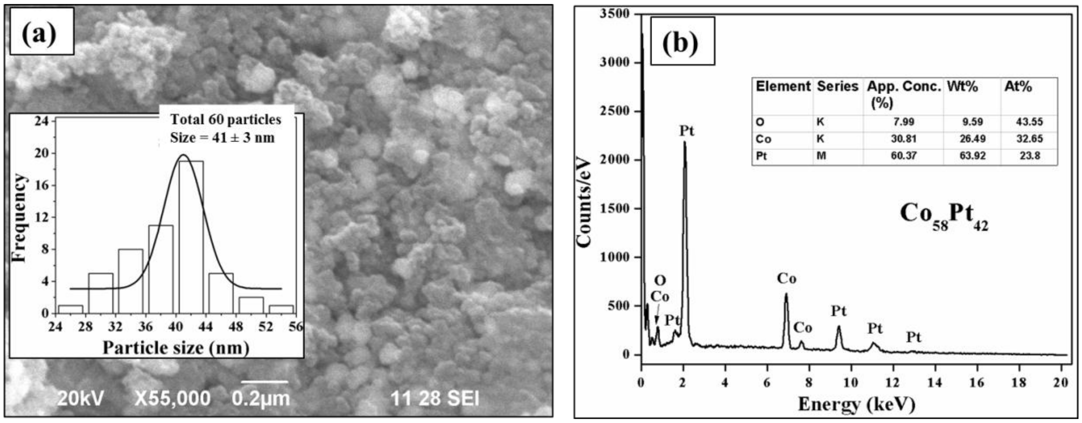

Element	Series	App. Conc. (%)	Wt%	At%
O	K	7.99	9.59	43.55
Co	K	30.81	26.49	32.65
Pt	M	60.37	63.92	23.8

Figure 6.8 (a) SEM micrographs and (b) its corresponding SEM-EDX analysis of the annealed Co-Pt alloys at 700°C via route-2. Inset (Figure (a)) shows particle size distribution plot.

6.3.3.3 Magnetic properties of fct L1$_o$ Co-Pt alloy nanoparticles synthesized via polyol method (route 2)

Magnetic properties studies were carried out only for Co-Pt alloy annealed via route-2. The Magnetization vs. field plot of Co-Pt nanoparticles annealed via route-2 is shown in Figure 6.9. The values of M_S and H_C are found to be 24 emu/g and 6050 Oe, respectively. Co-Pt alloys annealed via route-2 show ferromagnetic nature of the nanomaterials. Further, initial magnetization curve shows that there is slow increase of magnetization with applied field and have not saturated completely up to higher applied field, i.e. 15 kOe. These results indicate the hard magnetic properties of the materials. Observation of high value of H_C, i.e. 6050 Oe, for Co-Pt annealed at 700°C can be understood by increase in the crystallite sizes, volume fraction of fct phase, and order parameter with annealing at higher temperatures which induces high magnetocrystalline anisotropy [36]. The observed coercivity value is higher than reported values i.e. 1.25-3.67 kOe for Co-Pt alloys synthesized via chemical reduction routes [36, 37]. The H_C value for Co-Pt alloy with composition of $Co_{60}Pt_{40}$ is reported to be ~2 kOe after annealing at 600°C in the literature [38]. However, observation of high H_C value i.e. 6050 Oe for $Co_{58}Pt_{42}$ alloy annealed at via route-2 is interesting result and may be attributed to higher order parameter (0.9) obtained after annealing via route-2.

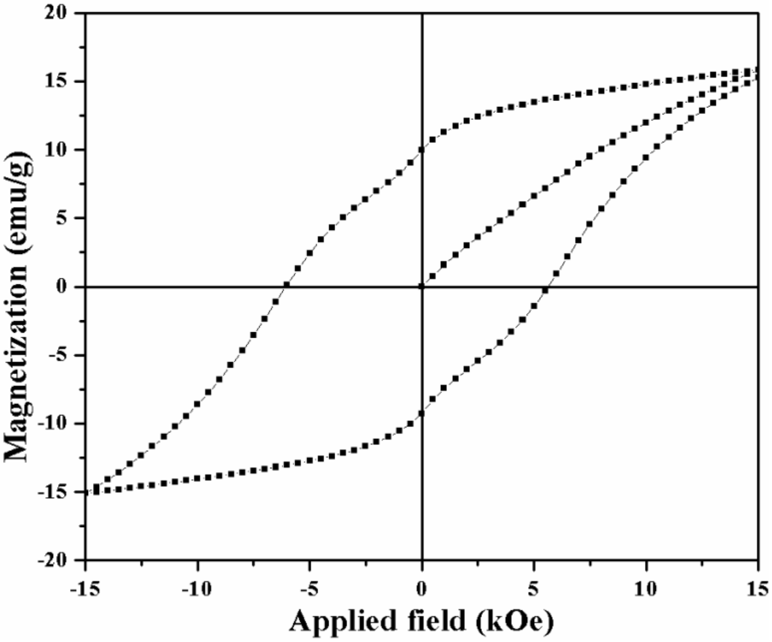

Figure 6.9 Magnetization vs. Field plots of Co-Pt alloys nanoparticles, synthesized via route 2 and annealed at 700°C/6 h under the flow of purified N_2(g).

6.4 Conclusions

In summary, Co, Co-Ni and Co-Pt nanoparticles have been successfully synthesized by modified polyol reduction route using PVP as capping agent. The materials were annealed by two routes, i.e. route-1(without NaCl matrix) and route-2(with NaCl matrix). Results of samples annealed via route-1 and route-2 were different as obtained from characterization and magnetic studies.

Co(route-1) crystallizes in hcp phase with average crystallite size of 16.4 nm even after annealing at 600°C. While Co(route-2) crystallizes in fcc phase with average crystallite size of 37.1 nm at 600°C. The observation of different phases for two routes is attributed to fine particle effects and annealing in presence of crystalline NaCl matrix. A TEM micrograph shows that Co(route-1) has uniformly dispersed chain-like nanostructures whereas Co(route-2) shows monodispersed nanostructures with nearly spherical morphologies. The estimated values of average chain diameter was found to be 2.8 ± 0.5 nm and chain lengths varies from 15-26 nm. Average TEM particle size for Co(route-2) was found to be 5.2 ± 0.5 nm. Co(route-1) nanoparticles have large M_S value of 162.7

emu/g and 167 emu/g at RT and 100K, respectively. While Co(route-2) nanoparticles have small M_S value of 29.7 emu/g and 35 emu/g at RT and 100K, respectively. These alterations in the magnetic properties have been explained with the help of size, shape, spin canting at the surface, altered crystal anisotropies etc. The H_C values at RT of Co(route-1) and Co(route-2) are 220 Oe and 185 Oe, respectively, and difference has been explained on the basis of nano-size effects. However, H_C values measure at 100K of Co(route-1) and Co(route-2) were found to be 1.6 times and 2 times higher than that of RT and indicate the fact that thermal effects dominates over anisotropy effects at 100K.

Co-Ni alloys annealed via both route-1 and route-2 crystallize in pure fcc phase with average crystallite sizes of 28.1 nm and 30.4 nm, respectively. TEM micrograph study was carried for typical sample, i.e. Co-Ni(route-2), and shows presence of nanostructures with nearly spherical morphologies with particle size of 8 ± 1 nm having narrow size distribution. Corrected M_S and H_C values Co-Ni(route-1) were found to be 116.2 emu/g and 86 Oe, at RT whereas 110 emu/g and 93 Oe, at 100K respectively. Abrupt decrease in M_S value of Co-Ni(route-1) at 100K may be attributed to deviations in anisotropy near saturation of magnetization. Corrected M_S and H_C values Co-Ni(route-2) were found to be 45.6 emu/g and 214Oe, at RT whereas 47.4 emu/g and 324Oe, at 100K, respectively. These variations of magnetic parameters with temperature indicate fine particle size effects along with traditional spin wave dependency.

As-prepared Co-Pt alloy nanoparticles crystallize in amorphous disordered fcc phase. Co-Pt alloy nanoparticles annealed via route-1 possess fcc crystal structure even at 700°C whereas Co-Pt alloy nanoparticles annealed via route-2 shows ordered fct ($L1_0$) phase. Microstructural and magnetic properties of fct Co-Pt obtained via route-2 have been studied. SEM studies show that annealed Co-Pt nanoparticles have spherical shape morphologies with SEM particle sizes of 41 ± 3 nm. And SEM EDX composition was found to be $Co_{58}Pt_{42}$. The values of M_S and H_C for Co-Pt(route-2) are found to be 24 emu/g and 6050 Oe, respectively. The observed magnetic properties have been interpreted with the help of crystallite sizes, order parameters, and composition effects of the Co-Pt nanostructured materials.

References

1. T. Kulik, J. Ferenc, A. Kolano-Burian, X. B. Liang, M. Kowalczyk, J. Alloys Compd., 434-435 (2007) 623-627.
2. N. V. Dmitrieva, V. A. Lukshina, E. G. Volkova, A. P. Potapov, V. S. Gaviko and B. N. Filippov, Phys. Met. Metall., 114 (2013) 129-137.
3. V. Tzitzios, D. Niarchos, G. Margariti, J. Fidler and D. Petridis, Nanotechnology, 16 (2005) 287-291.
4. J. Zhu, Y. Wang, X. Wang, X. Yang and L. Lu, Powder Technol., 181 (2008) 249-254.
5. P. Karipoth, A. Thirumurugan and R. J. Joseyphus, J. Colloid Interface Sci., 404 (2013) 49-55.
6. S. Panday, B. S. S. Daniel and P. Jeevanandam, J. Magn. Magn. Mater., 323 (2011) 2271-2280.
7. M. Abbas, Md. N. Islam, B. Parvatheeswara Rao, T. Ogawa, M. Takahashi and C. Kim, Mater. Lett., 91 (2013) 326-329.
8. Z. J. Huba, K. J. Carroll and E. E. Carpenter, J. Appl. Phys., 109 (2011) 07B514.
9. V. M. Maksimovic, N. D. Nikolic, V. B. Kusigerski and J. L. Blanusa, J. Serb. Chem. Soc., 80 (2015) 197-207.
10. Y. P. Ivanov, L. G. Vivas, A. Asenjo, A. Chuvilin, O. Chubykalo-Fesenko and M. Vazquez, Europhys. Lett., 102 (2013) 17009.
11. B. Liu, J-G. Guan, Q. Wang and Q-J. Zhang, Mater. Trans., 46 (2005) 1865-1867.
12. B. Stahl, N. S. Gajbhiye, G. Wilde, D. Kramer, J. Ellrich, M. Ghafari, H. Hahn, H. Gleiter, J. Weibumuller, R. Wurschum and P. Schlossmacher, Adv. Mater., 14 (2002) 24-27.
13. P. Anil Kumar, S. Mitra and K. Mandal, Indian J. Pure Appl. Phys., 45 (2007) 21-26.
14. A. S. Kurlov, A. I. Gusev and A. A. Rempel, Rev. Adv. Mater. Sci., 32 (2012) 52-60.
15. A. Ponrouch, M. P. Bichat, S. Garbarino, C. Maunders, G. Botton, P. L. Taberna, P. Simon and D. Guay, ECS Trans., 25 (2010) 3-11.

16. M-I. Baraton and I. V. Uvarova, Eds., Functional Gradient Materials and Surface Layers Prepared by Fine Particles Technology, Springer, UA, 2001.
17. A. G. Kolhatkar, A. C. Jamison, D. Litvinov, R. C. Willson and T. R. Lee, Int. J. Mol. Sci., 14 (2013) 15977-16009.
18. J. M. D. Coey, Phys. Rev. Lett., 27 (1971) 1140-1142.
19. J. Ahmed, S. Sharma, K. V. Ramanujachary, S. E. Lofland and A. K. Ganguli, J. Colloid Interface Sci., 336 (2009) 814-819.
20. Q-F. Liu, C-J. Jiang, X-L. Fan, J-B. Wang and D-S. Xue, Chin. Phys. Lett., 23 (2006) 1592-1595.
21. C. Osorio-Cantillo, A. N. Santiago-Miranda, O. Perales-Perez and Y. Xin, J. Appl. Phys., 111 (2012) 07B324.
22. K. Srinivasa Rao, T. Balaji, Y. Lingappaa, M. R. P. Reddy and T. L. Prakash, J. Exp. Nanosci., 8 (2013) 162-170.
23. M. D. L. Balela, S. Yagi, Z. Lockman, A. Aziz, A. V. Amorsolo, Jr. and E. Matsubara, J. Electrochem. Soc., 156 (2009) E139-E142.
24. K. Maaz, A. Mumtaz, S. K. Hasanain and M. F. Bertino, J. Magn. Magn. Mater., 322 (2010) 2199-2202.
25. Y. Zhang, Y. Liu, C. Fei, Z. Yang, Z. Lu, R. Xiong, D. Yin and J. Shi, J. Appl. Phys., 108 (2010) 084312.
26. S. Olvera, J. Sanchez-Marcos, F. J. Palomares, E. Salas, E. M. Arce and P. Herrasti, Mater. Charact., 93 (2014) 79-86.
27. Y. D. Li, L. Q. Li, H. W. Liao and H. R. Wang, J. Mater. Chem., 9 (1999) 2675-2677.
28. P. Elumalai, H. N. Vasan, M. Verelst, P. Lecante, V. Carles and P. Tailhades, Mater. Res. Bull., 37 (2002) 353-363.
29. M. Respaud, J. Appl. Phys., 86 (1999) 556-561.
30. J. Zhang, H. Liu, C-B. Rong, H-W. Zhang, S-Y. Zhang, B-G. Shen, Y-Q. Bai and B-H. Li, Appl. Phys. Lett., 83 (2003) 1172-1174.
31. P. Andreazza, C. Mottet, C. Andreazza-Vignolle, J. Penuelas, H. C. N. Tolentino, M. De Santis, R. Felici and N. Bouet, Phys. Rev. B, 82 (2010) 155453.

32. F. Kameche, A-T. Ngo, C. Salzemann, M. Cordeiro, E. Sutter and C. Petit, Phys. Chem. Chem. Phys., 17 (2015) 28162-28170.
33. X. Sun, Z. Y. Jia, Y. H. Huang, J. W. Harrell, D. E. Nikles, K. Sun and L. M. Wang, J. Appl. Phys., 95 (2004) 6747-6749.
34. L. Y. Lu, D. Wang, X. G. Xu, Q. Zhan and Y. Jiang, J. Phys. Chem. C, 113 (2009) 19867-19870.
35. J. Fang, L. D. Tung, K. L. Stokes, J. He, D. Caruntu, W. L. Zhou and C. J. O'Connor, J. Appl. Phys., 91 (2002) 8816-8818.
36. C. N. Chinnasamy, B. Jeyadevan, K. Shinoda and K. Tohji, J. Appl. Phys., 93 (2003) 7583-7585.
37. C-M. Shen, C. Hui, T-Z. Yang, C-W. Xiao, S-T. Chen, H. Ding and H-J. Gao, Chin. Phys. Lett., 25 (2008) 1479-1481.
38. A. C. C. Yu, M. Mizuno, Y. Sasaki, H. Kondo and K. Hiraga, Appl. Phys. Lett., 81 (2002) 3768-3770.

CHAPTER VII

Investigations on magnetic exchange and dipolar interactions in some model nanostructured systems: Co and Ni based metals and alloys

7.1 Introduction

The diluted magnetic nanoparticles systems such as nanoparticles dispersed in porous matrix, coated with non-magnetic capping agents or coated with carbon shell show unique magnetic properties due to magnetic exchange and dipolar interactions through matrix or shell [1]. It has been known that there are several possible drawbacks in pure or uncoated magnetic nanoparticles, such as: agglomerations of nanoparticles, reduction in M_S, alteration in H_C, etc. due to size and surface effects. Recently, various non-conventional diluted magnetic systems are being explored for their interesting magnetic characteristics [2, 3]. Magnetic nanoparticles embedded in matrix possess specific particle sizes and interparticle separations. Such kind of systems show enhancement in magnetizations because of exchange and dipolar interactions takes place through matrix. These magnetic interactions can be more effective when size and interparticle separation is in the order of exchange length [4]. Magnetic exchange length is the distance within which magnetic interactions are effective and it related to domain wall thickness [5]. The desired magnetic properties can be derived from the synthesis and processing parameters; such as: controlled nucleation, growth of nanoparticles within the silica matrix, heat treatment using different inert atmosphere etc.

Magnetic metal or alloys embedded in a suitable matrix not only fundamentally important but also have specific technological applications. As per our knowledge, very less literature are available on the study of magnetic properties of Co-Ni alloys embedded in silica matrix or in carbonaceous matrix even though they have potential technological applications in the area of microwave absorption and catalysis [6-8]. Co-Ni alloys in pure form and emended properly in silica matrix enhances the catalytic activity as well as selectivity [6]. Magnetic nanoparticles coated with carbonaceous matter having high M_S and low H_C improve permeability and microwave absorption capacity of the materials [7]. Moreover, $Co_{50}Ni_{50}$ alloys are more important because of their high values of saturation magnetization and moderate coercivities [9].

We have used chemical reduction route using superhydride as reducing agent for the synthesis of $Co_{50}Ni_{50}$ alloys nanoparticles embedded in silica matrix (KIT-6) or coated with capping agents. Superhydride reduction route is chosen selectively because it gives size controlled nanoparticles uniformly distributed in matrix which may help in order to achieve better magnetic properties. KIT-6 is ordered mesoporous material which has high surface area, narrow pore size distribution and high pore volume and useful for getting dispersion of nanoparticles [10, 11]. Interparticle separation among magnetic nanoparticles is necessary for studying magnetic exchange and dipolar interactions. In this chapter, novel solution based method for the synthesis Ni and $Co_{50}Ni_{50}$ alloys nanoparticles embedded in KIT-6 silica matrix is being reported. In addition, studies on exchange and dipolar interactions in nanomaterials coated with oleic acid/oleylamine and carbonaceous matter (obtained after annealing of materials at higher temperatures) have been carried out. Co-Ni alloys coated with oleic acid/oleylamine synthesized via superhydride route were used. Co, Ni, Fe-Co and Fe-Ni-Co coated with carbonaceous matter were obtained after annealing of as-prepared materials at temperature above ~600°C. Structural characterizations and studies on magnetic interactions were investigated.

7.2 Experimental

7.2.1 Synthesis of Ni/silica and $Co_{50}Ni_{50}$/silica

The chemicals (starting materials) and experimental procedure were similar to superhydride reduction method for Co and Ni (See Chapter IV, subsection 4.2.1). Additional changes in synthetic procedure are described as follows.

Appropriate amounts of KIT-6 matrix (Table 7.1), which is required to obtain 4-12 wt% metal loaded in silica matrix, were added to reaction mass at 100°C after the dissolution of metal chlorides. Reduction of metal salts was carried out using superhydride at temperature of 200°C to form Ni/silica and $Co_{50}Ni_{50}$/silica. Samples were separated by centrifugation and dried at RT in vacuum (~1 Torr) (i.e. as-prepared materials). Ni, $Co_{50}Ni_{50}$ dispersed in silica matrix were annealed at 400°C for 2 h under the atmosphere of N_2(g) flow.

Table 7.1 Details of moles and weights of metal salts and silica matrix used in the synthesis of Ni and $Co_{50}Ni_{50}$ dispersed in silica matrix.

Materials	$CoCl_2 \cdot 6H_2O$		$NiCl_2 \cdot 6H_2O$		Wt. of KIT-6 (g)		
	Moles (mmol)	weight (g)	Moles (mmol)	weight (g)	For 4 wt%	For 8 wt%	For 12 wt%
Ni/silica	---	---	0.5	0.119	0.704	0.337	---
$Co_{50}Ni_{50}$ /silica	0.5	0.119	0.5	0.119	1.411	0.676	0.431

7.2.2 Synthesis of Co-Ni alloys coated with oleic acid and oleylamine

Synthesis of Co_xNi_{100-x} alloys (x = 20, 40, 60, 80), coated with oleic acid and oleylamine, have been already described in Chapter IV, subsection 4.2.3. In summary, $CoCl_2 \cdot 6H_2O$ and $NiCl_2 \cdot 6H_2O$ were dissolved in organic solvent, i.e. diphenyl ether, using oleic acid and oleylamine at 100°C under high purity N_2(g) gas atmosphere. Reduction of metal salts was carried out using superhydride at 200°C to form Co-Ni alloys. Samples were separated by centrifugation and dried at RT in vacuum (i.e. as-prepared materials) and also annealed 400°C in N_2(g) atmosphere for 2 h and used for further characterizations and magnetic studies.

7.2.3 Synthesis of Co, Ni, Fe-Co and Fe-Ni-Co coated with carbonaceous matter

Synthesis Co, Ni and Fe_xCo_{100-x} alloys (x = 40, 60, 80) have been described in Chapter IV, subsection 4.2.1 and 4.2.2. In summary, Metal chlorides were dissolved in diphenyl ether using oleic acid and oleylamine at 100°C under high purity N_2(g) gas atmosphere. Reduction of metal salts was carried out using superhydride at 200°C. Products were separated by centrifugation and dried at RT in vacuum (i.e. as-prepared materials). As-prepared samples were annealed at 600°C in N_2(g) atmosphere for 2 h to decompose coating of oleic acid/oleylamine and form Co, Ni and Fe_xCo_{100-x} alloys coated with carbonaceous matter.

$Fe_xNi_{80-x}Co_{20}$ (x = 20, 40) alloys were synthesized via $NaBH_4$ reduction route in aqueous medium as described in Chapter III, subsection 3.2.2. In summary, stoichiometric amount of metal chlorides were dissolved in 50 mL of 1 M HCl. Reduction was achieved by adding 50 mL 1 M $NaBH_4$ solution at 25-30°C. Products were separated by filtration on drawn in 1 ml PEG-200 for capping. Sample was dried in vacuum desiccator over night at room temperature (i.e. as-prepared sample) and then heated to 600°C in N_2(g) atmosphere for 2 h to decompose PEG coating which produces $Fe_xNi_{80-x}Co_{20}$ coated with carbonaceous matter.

7.3 Characterizations of the synthesized materials

7.3.1 Characterizations of Ni/silica and $Co_{50}Ni_{50}$/silica

7.3.1.1 UV-Visible and FTIR studies

Characterizations using UV-Visible spectroscopy and FTIR spectroscopy were carried out for a typical sample with 8 wt% $Co_{50}Ni_{50}$/silica. Reaction mixture used for UV-Visible study contains $CoCl_2{\cdot}6H_2O$, $NiCl_2{\cdot}6H_2O$, KIT-6 matrix, diphenyl ether, oleic acid and oleylamine. And reaction mixture after reduction contains Co-Ni alloy nanoparticles coated with oleic acid/Oleylamine, KIT-6 matrix and diphenyl ether. Reaction mixture samples for UV-Visible spectroscopy studies were removed from the reaction flask at two stages: (i) after the dissolution of metal salts with the help of capping agents and (ii) after the completion of reduction procedure (i.e. using superhydride as reducing agent).

UV-Visible spectra of reaction mixture obtained before and after chemical reduction are shown in Figure 7.1. An UV-Visible spectrum of sample before reduction shows broad absorption peak centered at ≈660 nm. This peak is at higher wavelength side than the absorption peaks for pure $CoCl_2{\cdot}6H_2O$ and $NiCl_2{\cdot}6H_2O$ corresponding to d-d transitions i.e. 520 nm and 410 nm, respectively [12]. Hence, the peak observed at ≈660 nm may be assigned to the mixture or complex of cobalt chlorides, nickel chlorides, oleic acid and oleylamine. The absence of absorption peak centered at ≈660 nm in UV-Visible spectrum after reduction confirms the complete reduction of cobalt chlorides and nickel chlorides quantitatively forming the solid phase.

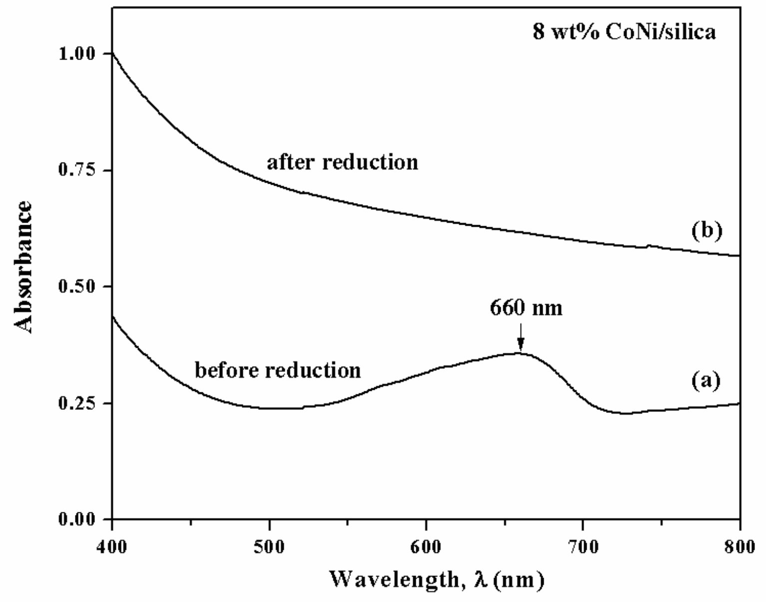

Figure 7.1 UV-Visible spectra of reaction mixtures at two stages, (a) before reduction and (b) after reduction, for 8 wt% CoNi loaded in silica matrix.

The solid precursors obtained after the synthesis and processing (i.e. as-prepared) were subjected to FTIR spectroscopy in order to study bonding and chemical interactions in 8 wt% $Co_{50}Ni_{50}$ alloy nanoparticles embedded in silica matrix (Figure 7.2). The results are summarized in Table 7.2. FTIR spectrum for as-prepared materials shows the dominantly presence of silica matrix (KIT-6) and capping agents (i.e. oleic acid and oleylamine). The peaks present at 460 cm^{-1} and 793 cm^{-1} are assigned to symmetric stretching vibrations of siloxane group (Si-O-Si). However, the broad peak centered at 1080 cm^{-1} and its shoulder are corresponding to asymmetric stretching vibrations of siloxane group (Si-O-Si) [13]. In the FTIR spectra of as-prepared materials, peaks at 1641 cm^{-1} and 3447 cm^{-1} are attributed to the presence of bending and stretching vibrations of O-H group, respectively. These results indicate the adsorption of some molecular water on the surface [13]. The peaks at 2925 cm^{-1} and 2850 cm^{-1} are corresponding to oleyl group which has origin from capping agents present at the surface of nanomaterials. The peaks in the range of 1450-1579 cm^{-1} can be assigned to carboxylate group ($-COO^{-}$).

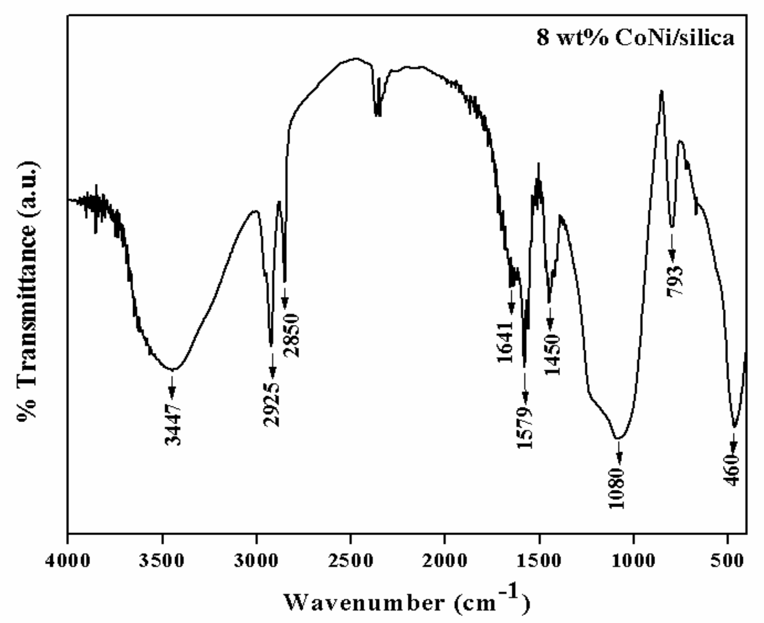

Figure 7.2 FTIR spectrum for as-prepared precursor sample for 8 wt% CoNi loaded in silica matrix. Sample was annealed at 400°C for 2 h under $N_2(g)$ atmosphere.

Table 7.2 Peak positions and assignments of FTIR spectrum obtained for coated 8 wt% CoNi/silica.

Wavenumber, $\bar{\upsilon}$ (cm^{-1})	Assignments
3447 b	O─H stretch
2925 s	asym. CH_2 stretch
2850 m	sym. CH_2 stretch
1641 w	O─H bending
1579 w	asym COO^- stretch
1450 b	sym COO^- stretch
1080 b	asym Si─O─Si stretch
793 s, 460 s	sym Si─O─Si stretch

Abbreviations: b-broad, s-strong, m-medium, w-weak, sym-symmetric, asym-asymmetric.

7.3.1.2 XRD studies of Ni/silica and $Co_{50}Ni_{50}$/silica

XRD patterns for pure Ni and Ni/silica with various loading percentage (4 and 8 wt%) are shown in Figure 7.3. Figure 7.4 shows XRD patterns for pure $Co_{50}Ni_{50}$ and $Co_{50}Ni_{50}$/silica with various loading percentage (4-12 wt%). As-prepared Ni and Co-Ni materials were amorphous in nature and have been explained by XRD studies in Chapter IV, subsections 4.3.1.2 and 4.3.3.2. Therefore, heat treated in an inert atmosphere at optimum temperature of 400°C for evolution of crystalline phase. Lattice parameters and crystallite sizes for all samples (Ni/silica and $Co_{50}Ni_{50}$/silica) are tabulated in Table 7.3.

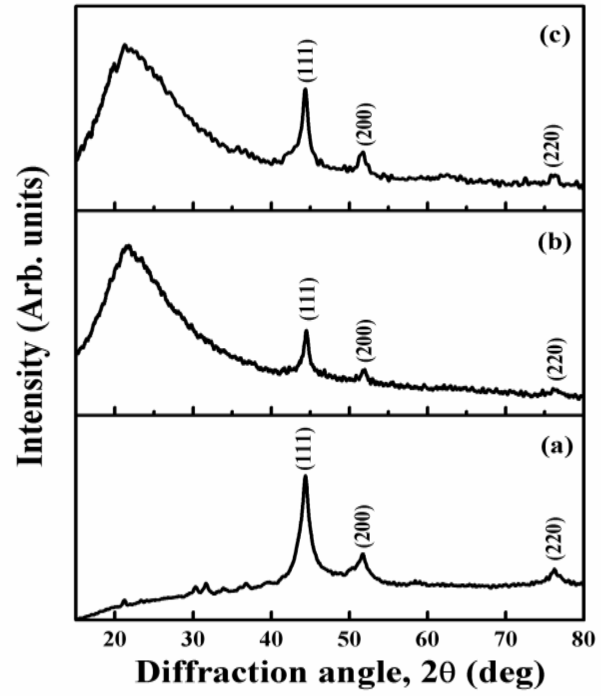

Figure 7.3 Indexed XRD patterns for (a) pure Ni, (b) 4 wt% Ni in silica and (c) 8 wt% Ni in silica matrix and heat treated at 400°C.

Ni nanoparticles (pure and loaded in silica matrix) crystallize in fcc structure. The diffraction patterns of CoNi solid solution were indexed in accordance with the patterns for fcc structure of Co and Ni [14]. Diffraction peaks for Ni/silica and CoNi/silica are relatively lesser intense compared to pure materials which indicate that nanomaterials are embedded in silica matrix. A broad peak, centered on 2θ value of 22^{o}, corresponds to the amorphous nature of silica matrix. The values of lattice parameters were found to be 3.5301 Å, 3.5254 Å and 3.5320 Å for pure Ni, 4 wt% and 8 wt% of Ni in silica matrix, respectively. The crystallite sizes were estimated to be 6.0 nm, 10.4 nm and 10.5 nm, for pure Ni, 4 wt% and 8 wt% Ni in silica, respectively.

Co-Ni alloys (pure and loaded in silica matrix) crystallize in fcc crystal phase. The estimated values of lattice parameters were found to be 3.5413 Å, 3.5319 Å, 3.5365 Å and 3.5356 Å for pure CoNi, 4 wt%, 8 wt% and 12 wt% CoNi in silica, respectively.

These values of the lattice parameters are in agreement with the literature reported values for $Co_{53}Ni_{47}$ alloys, i.e. 3.5343 Å [14]. Estimated average crystallite sizes were found to be 16.3 nm, 15.1 nm, 14.9 nm and 13.6 nm for pure $Co_{50}Ni_{50}$, 4 wt%, 8 wt% and 12 wt% CoNi in silica, respectively.

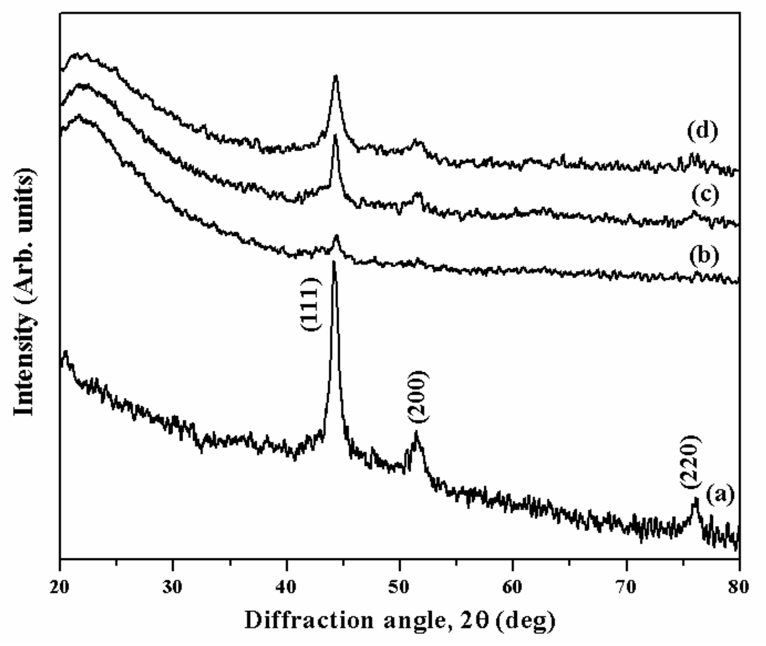

Figure 7.4 Indexed XRD patterns of (a) pure $Co_{50}Ni_{50}$, (b) 4 wt%, (c) 8 wt% and (d) 12 wt% $Co_{50}Ni_{50}$ alloys in silica matrix and heat treated at 400°C.

Table 7.3 Materials, crystalline phases, lattice parameters and crystallite sizes of $Co_{50}Ni_{50}$ alloy nanoparticles in silica matrix with various loading and heat treated at 400°C for 2 h.

Materials	Crystalline phase	Lattice parameters (Å)	XRD Crystallite size (nm)
Pure Ni	fcc	3.5301	6.0(±1)
4 wt% Ni	fcc	3.5254	10.4(±1)
8 wt% Ni	fcc	3.5320	10.5(±1)
Pure $Co_{50}Ni_{50}$	fcc	3.5413	16.3(±1)
4 wt% $Co_{50}Ni_{50}$	fcc	3.5319	15.1(±1)
8 wt% $Co_{50}Ni_{50}$	fcc	3.5365	14.9(±1)
12 wt% $Co_{50}Ni_{50}$	fcc	3.5356	13.6(±1)

7.3.1.3 Sorption studies of $Co_{50}Ni_{50}$/silica

In order to study the possible incorporation of the nanoparticles within the silica matrix, we attempted studies on surface areas and pore structures of few selected model samples (4 and 8 wt% CoNi/silica). BET adsorption-desorption isotherms (using N_2) for pure silica matrix and Co-Ni alloy nanoparticles (4 and 8 wt%) in silica matrix are shown in Figure 7.5. Adsorption-desorption curves for all three samples show Type IV isotherm which is the characteristic of mesoporous materials. The pore size distribution plots are shown in Figure 7.6. The pore diameters were found to be 5.16 nm, 3.61 nm and 3.13 nm whereas the values of the BET surface area (S_{BET}) were found to be 300 m^2/g, 26 m^2/g and 10 m^2/g for pure silica matrix, 4 wt% and 8 wt% Co-Ni alloy nanoparticles in silica matrix, respectively. The decrease of S_{BET} values with increasing loading wt% of Co-Ni alloy nanoparticles in silica matrix confirms the incorporation of Co-Ni alloy materials in the porous structure of silica matrix [15].

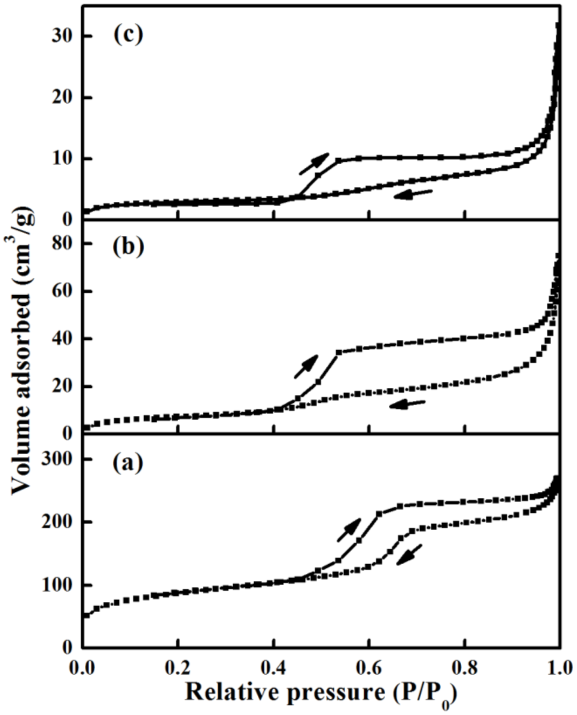

Figure 7.5 BET adsorption-desorption isotherms for (a) pure silica matrix, (b) 4 wt% $Co_{50}Ni_{50}$/silica and (c) 8 wt% $Co_{50}Ni_{50}$/silica using N_2(g) as adsorbent at 78K.

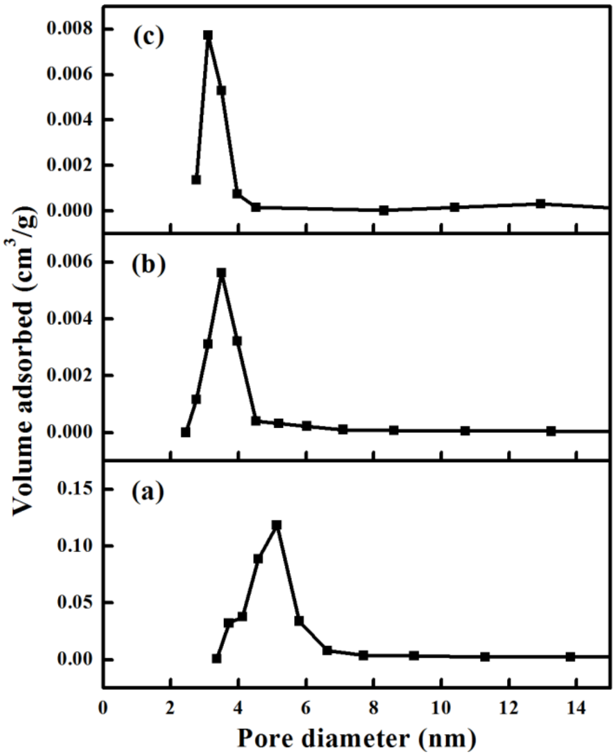

Figure 7.6 Pore size distribution plots for (a) pure silica matrix, (b) 4 wt% $Co_{50}Ni_{50}$/silica and (c) 8 wt% $Co_{50}Ni_{50}$/silica.

7.3.1.4 Electron microscopic studies

7.3.1.4.1 SEM studies of Ni and Ni/silica materials

Morphology and distribution of Ni nanoparticles in silica matrix were studied by SEM. Representative SEM micrographs for pure Ni, 4 wt% and 8 wt% Ni/silica are shown in Figure 7.7 (a, b and c). SEM particle size for pure Ni nanoparticles is found to be 70 nm and is greater than crystallite size (6 nm) indicating agglomeration. In case of Ni embedded in silica matrix, we could not distinguish the two phases (Ni and Silica) even at 40000X magnification (overall agglomerated size is 84 nm).

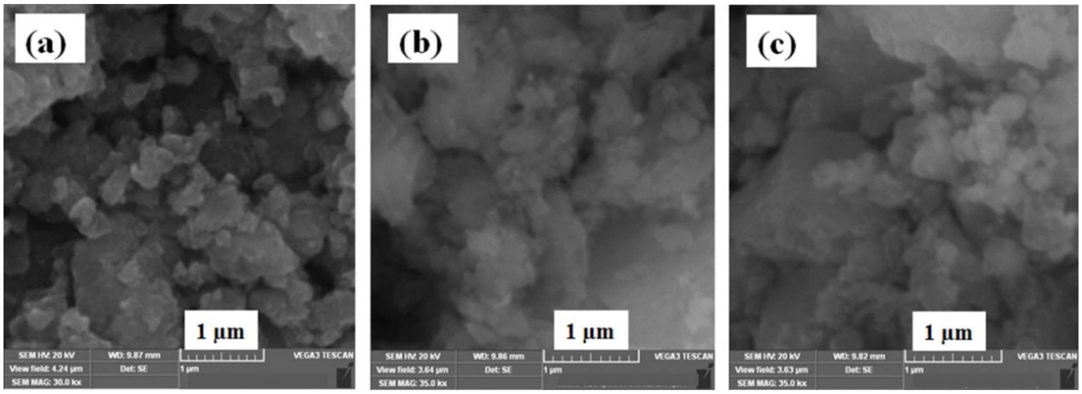

Figure 7.7 SEM photographs of heat treated (400°C/2 h) Ni nano-crystals embedded in silica matrix; (a) pure Ni, (b) 4wt% and (c) 8 wt% of Ni.

7.3.1.4.2 TEM studies of $Co_{50}Ni_{50}$ and $Co_{50}Ni_{50}$/silica materials

In order to carry out microstructural and crystalline structure analysis on $Co_{50}Ni_{50}$ alloys, TEM has been used preferably. TEM micrographs with low and high magnifications for pure $Co_{50}Ni_{50}$ and 8 wt% $Co_{50}Ni_{50}$/silica are shown in Figure 7.8 ((a) (b), (c) and (d)). SAED patterns for pure $Co_{50}Ni_{50}$ and 8 wt% $Co_{50}Ni_{50}$ in silica matrix are shown in Figure 7.8 ((e) and (f)). TEM micrographs with low magnifications show that pure $Co_{50}Ni_{50}$ nanoparticles and 8 wt% $Co_{50}Ni_{50}$/silica have nearly spherical shape morphologies with narrow size distributions. Also, the dispersion of $Co_{50}Ni_{50}$ nanoparticles in silica matrix is confirmed from Figure 7.8 (b). However, higher magnification TEM micrographs have been used for more clarity and particle size determination. TEM particle sizes were estimated to be 13.6 nm and 8.9 nm for pure Co-Ni, 8 wt% Co-Ni in silica matrix, respectively. The estimated TEM particle sizes of 13.6 nm and 8.9 nm for pure Co-Ni and 8 wt% Co-Ni embedded in silica matrix are smaller than the corresponding average crystallite sizes of 16.3 nm and 14.9 nm, respectively. The plausible reason might be due to the fact that TEM particle size corresponds to local probe while crystallite size corresponds to the average of the whole mass employed for diffraction measurements. Evidences on such kind of results indicating a difference of nearly 3 nm has already been reported in metallic ruthenium nanowires and nanotubes [16].

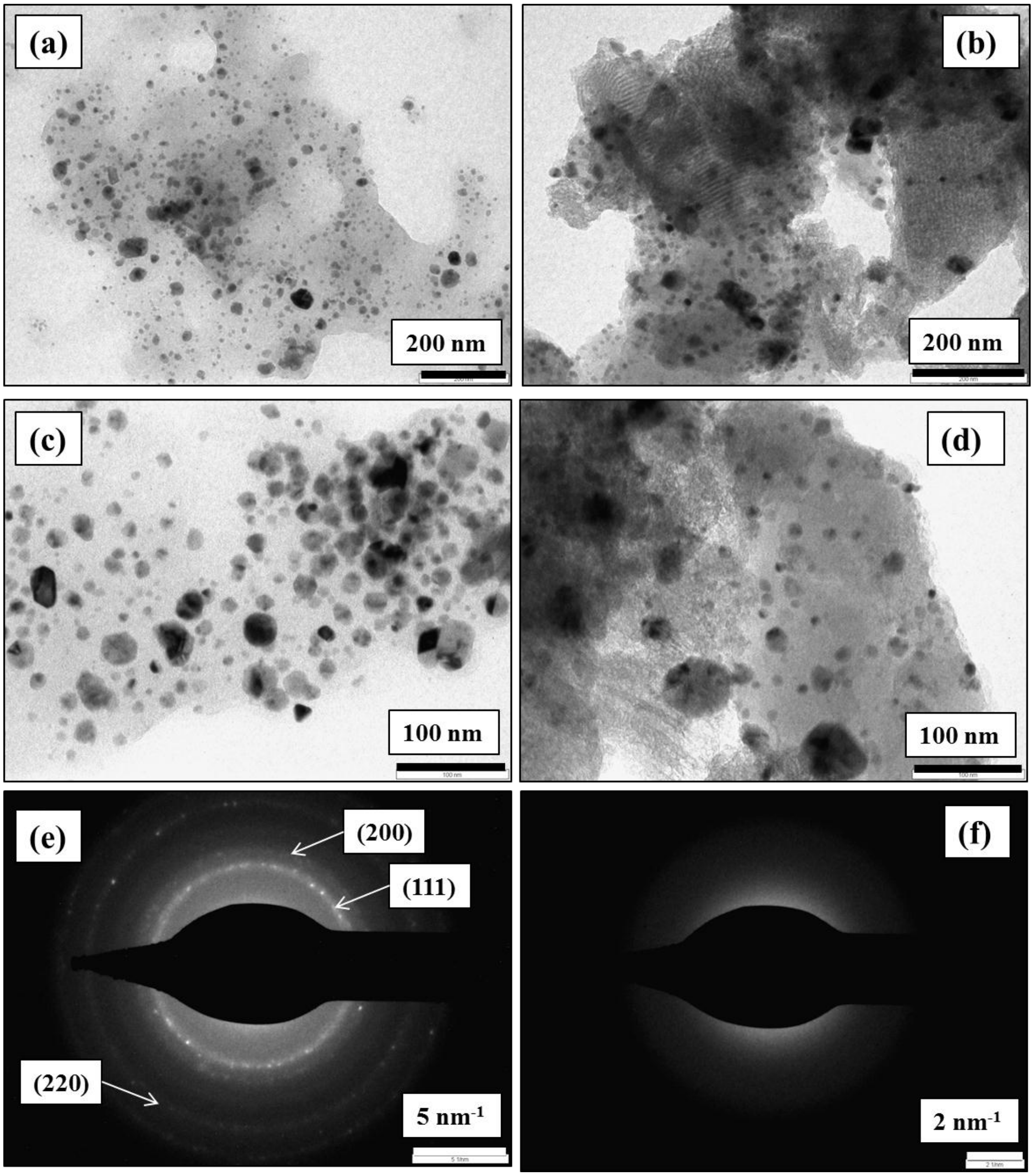

Figure 7.8 TEM micrographs of pure and $Co_{50}Ni_{50}$ loaded in silica matrix with various magnifications; lower magnifications: (a) pure $Co_{50}Ni_{50}$ and (b) 8 wt% $Co_{50}Ni_{50}$/silica and higher magnifications: (c) pure $Co_{50}Ni_{50}$ and (d) 8 wt% $Co_{50}Ni_{50}$/silica and SAED patterns for (e) pure $Co_{50}Ni_{50}$ and (f) 8 wt% $Co_{50}Ni_{50}$/silica.

SAED pattern of pure Co-Ni alloy indicates well intense diffraction rings corresponding to various crystal planes with fcc crystal structure and matches well with the results obtained from XRD measurements. However, SAED pattern of 8 wt% Co-Ni alloy in silica did not show prominent diffraction ring pattern. The observation of the diffused broad rings indicates nearly amorphous structure with the absence of any sharp peak in XRD pattern. The size effect along with the lattice distortion may be the major reason for this finding. In addition, the crystal orientation of the embedded Co-Ni nanomaterials in silica matrix may result in amorphous ring structures in TEM micrographs [17].

7.3.2 Characterizations of Co-Ni alloys coated with oleic acid and oleylamine

Co_xNi_{100-x} alloys (x = 20, 40, 60, 80), coated with oleic acid and oleylamine, were characterized by CHN analysis, FTIR spectroscopy, XRD studies and TEM studies and are discussed previously in Chapter IV, subsection 4.3.3. Summary of the characterizations parameters are presented in Table 7.4.

Table 7.4 Materials, annealing conditions, crystalline phase, crystallite sizes and TEM particle sizes for oleic acid and oleylamine coated Co-Ni alloys nanoparticles.

Composition	Annealing temperature/time (°C/h)	Crystalline phase	Crystallite size (nm)	TEM Particle size (nm)
$Co_{40}Ni_{60}$	As-prepared	fcc	9.0(±4)	7 ± 1
$Co_{20}Ni_{80}$	400/2	fcc	8.0(±4)	9 ± 1
$Co_{40}Ni_{60}$	400/2	fcc	10.0(±3)	11 ± 1
$Co_{60}Ni_{40}$	400/2	fcc	11.0(±4)	10 ±1
$Co_{80}Ni_{20}$	400/2	fcc	11.0(±4)	10 ± 1

7.3.3 Characterizations of Co, Ni, Fe-Co and Fe-Ni-Co coated with carbonaceous matter

Co, Ni and Fe_xCo_{100-x} alloys (x = 40, 60, 80), coated with carbonaceous matter (resulting from heat treatment of coated materials in as-prepared stage), were characterized by CHN analysis, FTIR spectroscopy, XRD studies and TEM studies as discussed previously in Chapter IV, subsection 4.3.1 and 4.3.2. $Fe_xNi_{80-x}Co_{20}$ (x = 20, 40) coated with carbonaceous matter were characterized by XRD studies and TEM studies as discussed previously in Chapter III, subsection 3.3.2. Some of parameters of characterizations of Co, Ni, Fe-Co and Fe-Ni-Co coated with carbonaceous matter are summarized in Table 7.5 for reference.

Table 7.5 Materials, annealing condition, crystalline phase, crystallite sizes and TEM particle sizes for Co, Ni, Fe-Co and Fe-Ni-Co coated with carbonaceous matter.

Composition	Annealing temperature/time (°C/h)	Crystalline phase	Crystallite size (nm)	TEM particle size (nm)
Co	600/2	hcp (53%) + fcc (47%)	15.0	11 ± 2
Ni	600/2	fcc	35.0	10 ± 2
$Fe_{40}Co_{60}$	600/2	bcc	37.9	51 ± 2
$Fe_{60}Co_{40}$	600/2	bcc	26.0	34 ± 2
$Fe_{80}Co_{20}$	600/2	bcc	38.2	24 ± 2
$Fe_{20}Ni_{60}Co_{20}$	600/2	fcc	27.5	15 ± 2
$Fe_{40}Ni_{40}Co_{20}$	600/2	fcc	24.0	22 ± 3

7.4 Magnetic exchange and dipolar interactions studies

This subsection deals with in-depth studies on magnetic exchange couplings and dipolar interactions in the above mentioned Co, Ni, Co-Ni, Fe-Co and Fe-Ni-Co alloys based model systems.

7.4.1 Ni/silica and $Co_{50}Ni_{50}$/silica systems

In order to study magnetic properties of Ni and $Co_{50}Ni_{50}$ alloy nanoparticles loaded in silica matrix, field dependence and temperature dependence of magnetization measurements (for $Co_{50}Ni_{50}$/silica only) using low applied field strength (100 Oe) have been carried out. The magnetization versus applied field (M-H) plots measured at 298 K for pure and materials loaded in silica matrix are presented in Figure 7.9 and Figure 7.10. The values of relative permeability (μ_r) of $Co_{50}Ni_{50}$/silica samples were calculated from initial magnetization (M vs. H) plots. First, susceptibility (χ) was determined which is equal to slope of tangent drawn to initial magnetization curve at origin. Then μ_r in CGS units can be calculated by formula, $\mu_r = 1+4\pi\chi$, as $\mu_0 = 1$ in CGS unit system [18]. Variation of μ_r in the range of applied field (500- 6000 Oe) is shown in the Figure 7.11. The estimated values of saturation magnetization (M_S), coercivity (H_C), remanent magnetization (M_r) and reduced remanent magnetization (M_r/M_S) are tabulated in Table

7.6. The M_S values for pure Ni, 4 wt% and 8 wt% Ni loaded in silica were found to be 15.77 emu/g, 5.08 emu/g and 2.00 emu/g whereas H_C values were 33.72 Oe, 92.47 Oe and 64.70 Oe, respectively. The M_S values are found to be 3.59 emu/g, 1.22 emu/g, 1.96 emu/g and 3.96 emu/g whereas H_C values are 205 Oe, 100 Oe, 175 Oe and 158 Oe for pure, 4 wt%, 8 wt% and 12 wt% $Co_{50}Ni_{50}$ loaded in silica matrix, respectively. Further, the values of M_r are found to be 0.58 emu/g, 0.11 emu/g, 0.37 emu/g and 0.50 emu/g for pure, 4 wt%, 8 wt% and 12 wt% $Co_{50}Ni_{50}$ loaded in silica matrix, respectively.

After correction for wt fraction of silica matrix, the corrected M_S values of Ni and $Co_{50}Ni_{50}$ increases drastically (i.e. 25-127 emu/g for Ni and 24.5-33.0 emu/g for Co-Ni) when compared with the M_S values for pure Ni and $Co_{50}Ni_{50}$ alloy. These results may be directly related to alteration of exchange interactions assuming size and interparticle separation to be in the order of exchange length [4]. With the increase of wt% of Co-Ni in silica matrix, i.e. from 4-12 wt%, an increasing trend in the corrected M_S has been observed (Table 7.6). These results can be understood as dilution effect of Co-Ni nanoparticles in the non-magnetic silica matrix along with alteration of nanomaterials dimensions other than spherical inside the porous structure of silica.

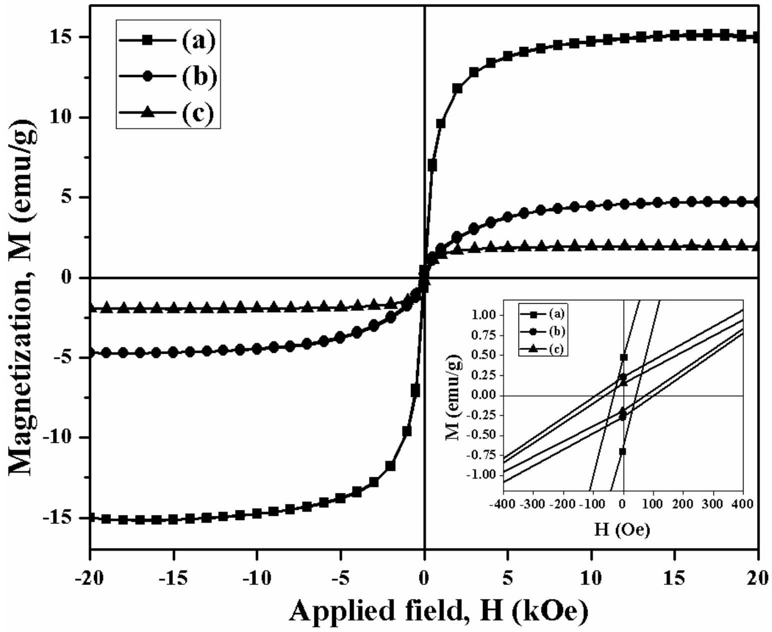

Figure 7.9 Plots of specific magnetization vs. applied field for (a) pure Ni, (b) 4 wt% and (c) 8 wt% Ni embedded in silica matrix. Inset shows zoom out part centered around zero field showing corresponding values of the coercivities.

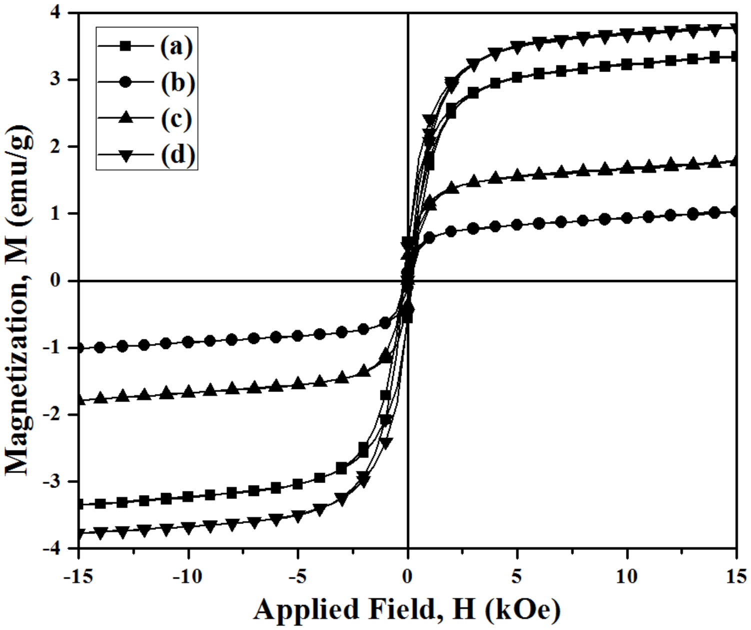

Figure 7.10 Room temperature magnetic hysteresis loops for various wt% of $Co_{50}Ni_{50}$ materials embedded in silica matrix; (a) pure CoNi, (b) 4 wt%, (c) 8 wt% and (d) 12 wt%.

Table 7.6 Materials, Crystalline phases, values of saturation magnetizations (M_S), coecivities (H_C), remanent magnetizations (M_r), and reduced remanent magnetization (M_r/M_S) of $Co_{50}Ni_{50}$ alloy nanoparticles in silica matrix with various wt% of loading.

Materials	Crystalline phase	M_S (emu/g)	Corrected M_S (emu/g)	H_C (Oe)	M_r (emu/g)	M_r/M_S
Pure Ni	fcc	15.77	--	34	0.48	0.03
4 wt% Ni	fcc	5.08	127.0	92	0.23	0.04
8 wt% Ni	fcc	2.00	25.0	65	0.15	0.07
Pure CoNi	fcc	3.59	--	205	0.58	0.16
4 wt% CoNi	fcc	1.22	30.5	100	0.11	0.09
8 wt% CoNi	fcc	1.96	24.5	175	0.37	0.19
12 wt% CoNi	fcc	3.96	33.0	158	0.50	0.12

It is noteworthy that 4 wt% loaded materials exhibit an abrupt enhancement of magnetization as compared to materials with higher wt% loading. The inter-grain exchange interactions mediated by the silica matrix may be a dominant factor for enhancement of magnetization in 4 wt% loaded sample [4]. Further, the aforesaid results can be supported well by a similar literature report on enhancement of magnetic moment up to 41 % by preparing magnetically diluted systems [19]. It should be noted that the critical sizes for Ni and Co-Ni are ~86 nm and ~40 nm, respectively. Reduction in the H_C values for Ni nanoparticles is observed at particle sizes below critical size. Further, the maximum H_C value of 421.8 Oe is reported in the literature for Co-Ni nanoparticles attached on multi-walled carbon nanotubes with particle size of 37 nm [20]. In this study, the values of coercivity for Co-Ni alloy nanoparticles i.e. 100-205 Oe are in the regime of single domain Co-Ni nanoparticles. The coercivity values for Co-Ni alloys nanoparticles loaded in silica matrix with various wt% (4-12) start increasing from 100 Oe to 175 Oe even though there is a smaller variation in crystallite sizes i.e. 15.6 to 13.6 nm. In addition to size and surface effects in Co-Ni nanocrystals, one can expect presence of varying lattice strains in the loaded materials. Reduction in grain size produces lattice volume expansion accompanied by anisotropic lattice strain which results in higher coercivity values [21]. Squareness ratio of magnetic hysteresis loop can be expressed by reduced remanent magnetization, i.e. $M_r/M_{S,}$ which is attributed to size and orientation of magnetic particles. The materials with M_r/M_S value of 0.5 indicate the presence of uniaxial anisotropy and that of 0.8-0.9 indicates cubic anisotropy [22]. In our study, M_r/M_S values for both Ni and Co-Ni alloys lies in the range from 0.03-0.19. These reductions in the M_r/M_S values may be due to the presence of randomly oriented magnetic domains in the nanoparticles which may be assumed to be blocked [23].

The observed values of μ_r for pure $Co_{50}Ni_{50}$ sample are found to be nearly constant (i.e. 1.25-1.05) in the range of applied field, 500-6000 Oe (Figure 7.11). However, the values of μ_r for $Co_{50}Ni_{50}$ alloys, embedded in silica matrix with different loading percentage (4-12 wt%), were found to increase drastically (i.e. 1.95 to 3.72) at lower applied field, i.e. from 2000 Oe to 500 Oe. These results may be attributed to exchange coupling effects that may exist in the Co-Ni alloy nanoparticles embedded in silica matrix in addition to materials deformation [4]. These results support the enhancement of saturation magnetizations of the samples embedded in silica matrix. And can be interpreted in terms of alteration of structural parameters thereby changing the magnetic structures. A similar result has already been reported for ferromagnetic Ni in silica matrix by Peng et al [4].

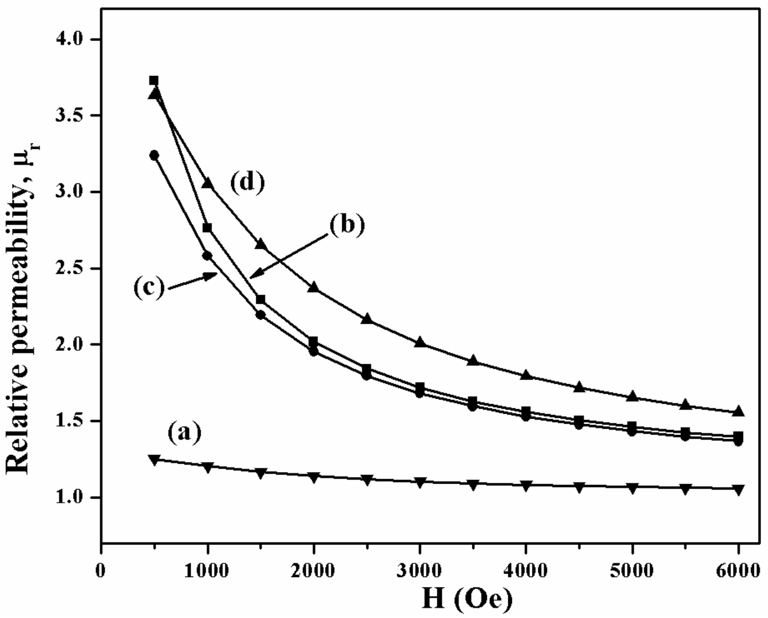

Figure 7.11 Plots for relative permeability versus applied field of (a) pure CoNi, (b) 4 wt%, (c) 8 wt% and (d) 12 wt% $Co_{50}Ni_{50}$/silica matrix.

Further, interparticle interactions and blocking temperature have been studied by FC/ZFC magnetizations plots (Figure 7.12). Typical FC/ZFC plots for pure $Co_{50}Ni_{50}$ and 8 wt% $Co_{50}Ni_{50}$/silica show the blocking temperature (T_B) lies significantly above 300 K for pure $Co_{50}Ni_{50}$ whereas 300 K for 8 wt% $Co_{50}Ni_{50}$/silica. It has been reported that smaller size particles have low T_B value and larger size particles have high T_B value [24]. Hence our results may be attributed to the presence of particle size distribution in the materials. The higher values of FC magnetizations than ZFC magnetizations indicate that $Co_{50}Ni_{50}$ alloys are ferromagnetic up to 300 K. An effective magnetic anisotropy constant (K_{eff}) includes contribution from magnetocrystalline anisotropy and shape anisotropy. Assuming the blocking temperature (T_B) of pure CoNi alloy to be 300 K and using the formula $K_{eff} = 25k_BT_B/V$, K_{eff} value is found to be 280 kJ/m^3 (Refer- Chapter I, subsection 1.6.5). Considering the blocking temperature for 8 wt% of $Co_{50}Ni_{50}$/silica to be 300 K, the estimated K_{eff} value is found to be 78 kJ/m^3. This value is in the comparable range with the magnetocrystalline anisotropy constant (K_V = 150 kJ/m^3) for Co-Ni alloy nanoparticles with 10 nm size [25]. The decrease of K_{eff} value for loaded Co-Ni signifies altered size and magnetic structure at the surface. Also, one can see from FC/ZFC plots pure Co-Ni (Figure 7.12 (a)), the actual T_B lies well above 300 K.

Therefore, we can expect K_{eff} for pure Co-Ni sample to be much higher than the value 280 kJ/m^3. These results indicate very strong dipolar interactions arise for deformed magnetic structure for Co-Ni alloy embedded in silica matrix. Thus, the aforesaid enhancement of the magnetization and alteration of various magnetic parameters may be attributed to size, deformed magnetic structure at the surface and strong dipolar interactions, in addition to usual fine particle size and surface effects.

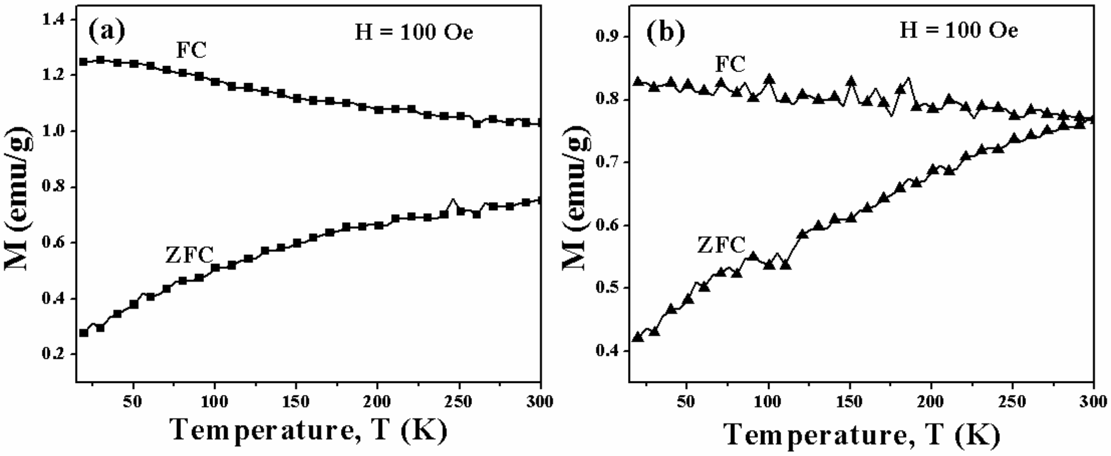

Figure 7.12 FC and ZFC plots for (a) pure $Co_{50}Ni_{50}$ and (b) 8 wt% $Co_{50}Ni_{50}$/silica matrix. Applied magnetic field was kept at 100 Oe.

7.4.2 Co-Ni alloys coated with oleic acid and oleylamine

FC and ZFC plots for as-prepared and annealed Co_xNi_{100-x} alloys (x = 20, 40, 60, 80) show similar magnetic irreversibility below 300 K (Figure 7.13). For all samples, the FC magnetization values are higher than the magnetization measured in ZFC conditions. These results indicate the presence of ferromagnetism in Co_xNi_{100-x} alloys up to at least 300 K. In the ZFC plot of as-prepared $Co_{40}Ni_{60}$ alloy (Figure 7.13 (a)), there is no peak at low temperatures for superparamagnetic blocking. However, the ZFC plots of annealed $Co_{20}Ni_{80}$ and $Co_{40}Ni_{60}$ (Figure 7.13 (b) and (c)) show a broad hump in the region ≈150-200 K. It may correspond to blocking temperature (T_B) below which spins of particles are in superparamagnetically blocked state [26]. However, the ZFC plots of annealed $Co_{60}Ni_{40}$ and $Co_{80}Ni_{20}$ (Figure 7.12 (d) and (e)) show linear increase in ZFC magnetization up to 300 K; indicating the absence of superparamagnetic blocking.

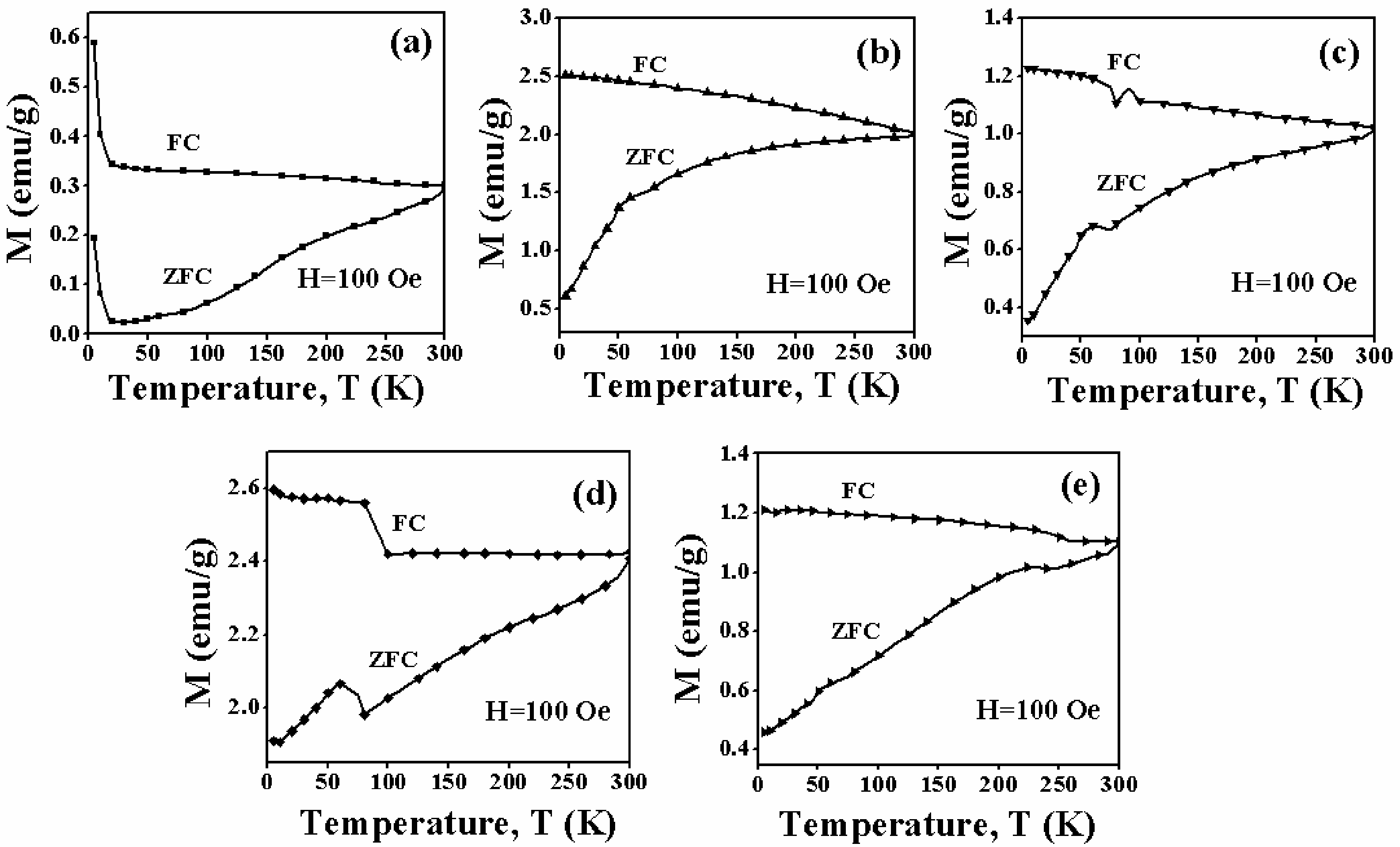

Figure 7.13 Temperature dependence of magnetization curves for (a) as-prepared $Co_{40}Ni_{60}$ and (b) $Co_{20}Ni_{80}$ (c) $Co_{40}Ni_{60}$ (d) $Co_{60}Ni_{40}$ (e) $Co_{80}Ni_{20}$ alloys in FC and ZFC conditions. The applied field used was kept at 100 Oe.

Therefore, we expect the blocking temperature (T_B) to be present well above 300 K [27]. Also, the peak around 60 K is observed in ZFC plots for all Co-Ni alloys which may be due to random freezing of surface spins generally occurred at low temperatures. In all Co-Ni alloys, FC and ZFC curves meet each other at 300 K which can be referred to as an irreversible temperature (T_{irr}). These results may be attributed to the particle size distribution and stronger dipolar interparticle magnetic interactions [26]. At temperatures greater than 300 K, we can expect superimposition of FC/ZFC curves. This result indicates the presence of sufficient fraction of materials in superparamagnetic state. Assuming the particle volume from TEM, the effective anisotropy constants (K_{eff}) of Co_xNi_{100-x} alloys were calculated to be 135-181 kJ/m^3, 57-76 kJ/m^3, 148 kJ/m^{3}and 148 kJ/m^3 for the values of x equal to 20, 40, 60 and 80, respectively (Refer- Chapter I, subsection 1.6.5). These values are in the comparable range with a typical magnetocrystalline anisotropy constant (K_1 = 150 kJ/m^3) for CoNi alloy nanoparticles with 10 nm size, reported in the literature [25]. The variations in the values of K_{eff} for Co-Ni alloys with different compositions may be attributed to alteration of size of the nanoparticles and surface anisotropy contribution.

7.4.3 Co, Ni and Fe-Co alloys coated with carbonaceous matter

FC and ZFC magnetization measurements of Co and Ni nanoparticles coated with carbonaceous materials are presented in Figure 7.14. Magnetization in the FC curves includes contribution from all particles whereas ZFC curves consider magnetization from such nanoparticles whose energy barriers are overcome by thermal energy (k_BT) at that temperature [28]. The FC magnetization values are higher than the ZFC magnetization values and indicate the presence of ferromagnetism in our samples up to at least 300 K. Both Co and Ni show magnetic irreversibility below room temperature (300 K). It is observed that FC magnetization of Co (Figure 7.14 (a)) increases with increase in temperature which is opposite to the expected trend. However, it may be due to lower field (100 Oe) applied during FC measurements. Such kind of exceptional trend has been observed for Co nanoparticles at applied field below 500 Oe [27, 29]. The ZFC magnetization increases rapidly during heating at temperatures below 120 K and 150 K for Co and Ni, respectively. However, initial variation in magnetization in the FC/ZFC curves of Co and Ni at temperatures below 20K may be attributed to some sort of magnetic phase transitions and/or presence of low number of non-interacting particles. The ZFC curve of Ni exhibits a peak at lower temperature, i.e. ~10K, and indicates feature of freezing properties [30, 31]. At higher temperatures, the ZFC magnetization increases less abruptly up to 300 K. At temperatures greater than 300 K, we can expect superparamagnetic behavior of the materials. Assuming blocking temperature (T_B) equal to 300 K and particle volume from TEM, the anisotropy constants (K_{eff}) were calculated as 25 kJ/m^3 and 13 kJ/m^3 for Co and Ni, respectively. These values are less in magnitude compared to the values for bulk Co and Ni, i.e. 430 kJ/m^3 and 80 kJ/m^3, respectively [31, 32]. The decrease in K values can be attributed to fine particle nature of the materials. These results may be compared with the finding of Wang et al [33]. The difference in the slopes of ZFC magnetization at lower temperatures can be due to smaller particles whose blocking temperature would lie below 120 K and 150 K for Co and Ni, respectively. These results also indicate wider particle size range of our materials which may be correlated to TEM study. The magnetic irreversibility of ZFC and FC curves shows frustration processes of magnetic moments in the interacting clusters [27]. Therefore the magnetic behavior can be correlated to dipolar magnetic interactions of particles in the whole temperature range.

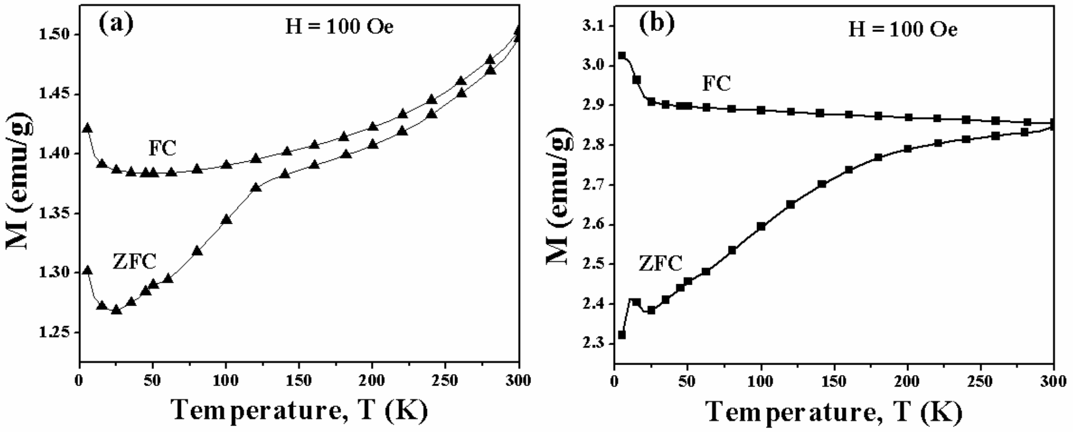

Figure 7.14 Temperature dependence of magnetization curves for (a) Co and (b) Ni in FC and ZFC conditions. The applied field used was kept at 100 Oe.

FC and ZFC magnetization measurements of Fe_xCo_{100-x} alloys (x = 40, 60, 80) (Figure 7.15) show similar behavior with magnetic irreversibility below room temperature (i.e.

300 K). In all Fe-Co alloys, the ZFC magnetization increases rapidly with temperature and is not superimposed with FC curve up to 300 K which indicates that the nanoparticles are in the magnetically blocked state. This blocking of nanoparticles may be attributed to stronger dipolar interparticle magnetic interactions [34]. Strength of such a dipolar interactions increases with increase in particle magnetic moments and decrease in distance between them. In the present study, the observed higher values of coercivity (244-474 Oe) indicate strong dipolar interactions amongst the particles. This is evident from the literature reported results that Fe-Co bulk materials are expected to show reduced coercivity (~10-60 Oe) [34] and with a reduction of particle sizes to a value of 10-60 nm range, moderate increase in the values of H_c (102 Oe) is observed [35]. Hence deviations in the FC/ZFC curves are mainly related to dipolar interactions in adjacent particles. At temperatures greater than 300 K, we can expect superimposition of FC/ZFC curves and hence superparamagnetic behavior of the materials.

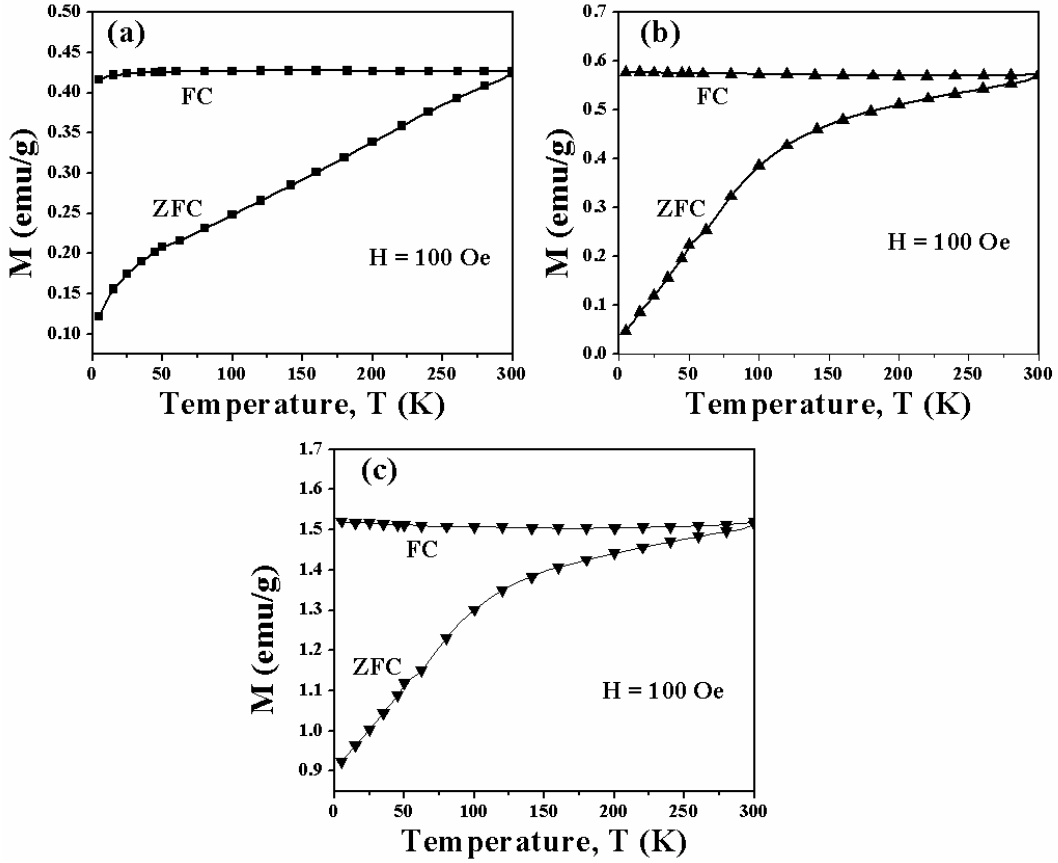

Figure 7.15 Temperature dependence of magnetization curves for (a) $Fe_{40}Co_{60}$, (b) $Fe_{60}Co_{40}$ and (c) $Fe_{80}Co_{20}$ alloys in FC and ZFC conditions. The applied field employed was 100 Oe.

Assuming the value of blocking temperature (T_B) equal to 300 K and the particle volume from TEM, the K_{eff} of Fe_xCo_{100-x} alloys were calculated to be 1.5 kJ/m^3, 4.6 kJ/m^3 and 14.3 kJ/m^3 for the values of x equal to 40, 60 and 80, respectively. To be noted, Peng et al. determined the magnetic anisotropy energy (40 kJ/m^3) for $Fe_{70}Co_{30}$ nanoparticles [36]. Similarly Bansmann et al. [37] obtained a magnetic anisotropy energy of K= 190-200 kJ/m^3 for 10 nm Fe-Co nanoparticles. However, we observed reduction in magnetic anisotropy energy in our Fe-Co compositions compared to the literature reported values for 10 nm Fe-Co alloys. This may be attributed to alteration of size of the nanoparticles and surface anisotropy contribution [38]. Further investigations are needed on the origin and quantification of surface magnetic anisotropy in Fe-Co alloys.

7.4.4 Fe-Ni-Co alloys coated with carbonaceous matter

In Fe-Ni-Co alloys, field cooled (FC) magnetization values are larger than the zero field cooled (ZFC) magnetization values. These observations show the ferromagnetic nature of the materials (Figure 7.16). It has been observed that FC/ZFC plots show thermo-magnetic irreversibility below 300 K and indicate Fe-Ni-Co nanoparticles become superparamagnetic at 300 K. The ZFC magnetization increases rapidly during the heating at temperatures up to 100 K and 130 K for $Fe_{20}Ni_{60}Co_{20}$ and $Fe_{40}Ni_{40}Co_{20}$, respectively. This variation in magnetic behavior may be attributed to the presence of interparticle dipolar magnetic interactions among nanoparticles. Such kind of interpretations has been explained in the literature for Co-Pt nanomaterials dispersed in polymer matrix [39].

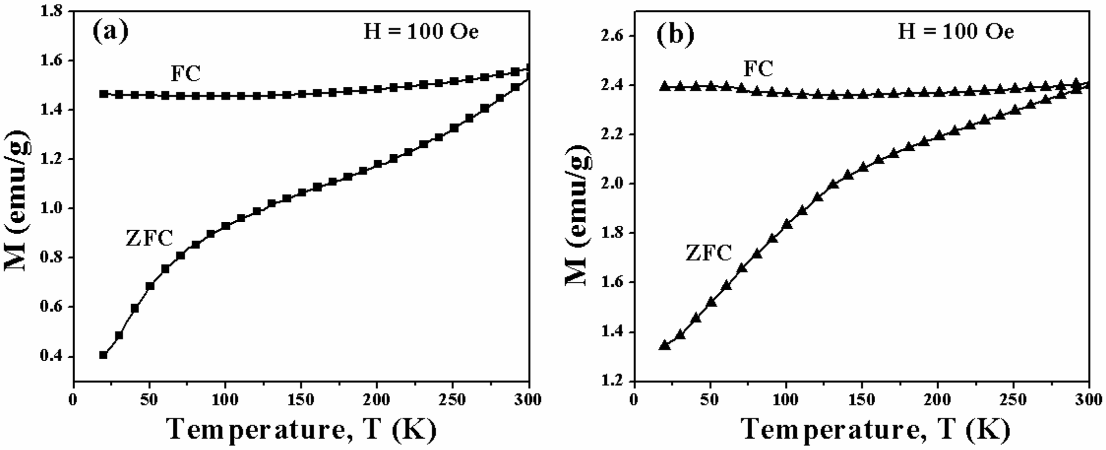

Figure 7.16 Temperature dependence of magnetization curves for (a) $Fe_{20}Ni_{60}Co_{20}$ and (b) $Fe_{40}Ni_{40}Co_{20}$ alloys in FC and ZFC conditions. The applied field employed was 100 Oe.

Assuming the value of blocking temperature (T_B) equal to 300 K and the particle volume from TEM, the effective magnetic anisotropy constants (K_{eff}) for $Fe_{20}Ni_{60}Co_{20}$ and $Fe_{40}Ni_{40}Co_{20}$ were found to be 14 kJm^{-3} and 4.2 kJm^{-3}, respectively. These values are less in magnitude compared the value for Co (25 kJm^{-3}) and Ni (13 kJm^{-3}) as discussed above. K_{eff} values for Fe-Ni-Co alloys are decreases with increasing Fe content and the materials drift towards softer in magnetic behavior with increasing Fe contents.

7.5 Conclusions

Ni/silica and $Co_{50}Ni_{50}$/silica with various loading (4-12 wt%) have been synthesized by novel chemical reduction route. The novelty of synthetic procedure adopted has been established using UV-VIS and FTIR spectroscopy. XRD studies confirm that Ni/silica and $Co_{50}Ni_{50}$/silica form pure fcc phase embedded in amorphous silica matrix with crystallite sizes are in the range of 6-10.5 nm and 13.6-16.3 nm, respectively. TEM microscopy studies show that Co-Ni alloys have nearly spherical shape morphologies and narrow size distributions. TEM particle sizes were estimated to be 13.6 nm and 8.9 nm for pure $Co_{50}Ni_{50}$ and 8 wt% $Co_{50}Ni_{50}$/silica, respectively. Magnetic hysteresis studies at RT indicate the presence of superparamagnetic fractions in the materials. Enhancements in the values of magnetizations of Ni/silica and $Co_{50}Ni_{50}$/silica compared to that of pure materials have been observed with increase in dilution of nanoparticles in matrix. FC/ZFC magnetizations plots show decrease is blocking temperature for $Co_{50}Ni_{50}$/silica compare to pure $Co_{50}Ni_{50}$ which indicates magnetic structure alteration and supports our magnetic results. The observed enhancement in magnetization with low values of coercivity after loading in silica matrix has been explained on the basis of fine particle size, surface effects and dipolar interparticle interactions.

Magnetic interactions in Co_xNi_{100-x} alloys coated by oleic acid and oleyl amine have been studied by low temperature FC/ZFC magnetization measurements. It could be confirmed from the present study that the presence of magnetic irreversibility and superparamagnetic blocking of nanoparticles due to strong dipolar interactions and particle size distribution. Estimated values of effective anisotropy constants of Co-Ni alloys (i.e., 57-181 kJ/m^3) reveal the contribution from the reduced particle size and surface anisotropy. On the above, a structure-property correlation in Co-Ni alloys has been attempted in this investigation.

Also, magnetic interactions in Co, Ni, Fe-Co and Fe-Ni-Co alloys coated by carbonaceous matter have been studied by low temperature FC/ZFC magnetization measurements. The anisotropy constants for Co and Ni were found to be 25 kJ/m^3 and 13 kJ/m^3, respectively. FC/ZFC results show the wider size distributions in Co and Ni. Magnetic irreversible behavior below 300 K was observed in the materials from FC/ZFC curves due to ferromagnetism and dipolar interactions among the particles and result in shifting of blocking temperature above 300 K. FC/ZFC magnetization measurements of Fe_xCo_{100-x} alloys show magnetic irreversibility and blocking of nanoparticles due to strong dipolar interparticle magnetic interactions. Estimated values of K_{eff} of Fe_xCo_{100-x} alloys (i.e. 1.5 kJ/m^3, 4.6 kJ/m^3 and 14.3 kJ/m^3 for x = 40, 60 and 80, respectively) reveal the contribution from the reduced particle size and surface anisotropy. It is observed that Fe-Ni-Co alloys showing thermo-magnetic irreversibility below 300 K and blocking temperature approximately at 300 K. FC and ZFC magnetic characteristics of Fe-Ni-Co alloys are interpreted on the basis of interparticle interactions among magnetic nanoparticles. The values of effective magnetic anisotropy constants (K_{eff}) are found to be 14 kJm^{-3} and 4.2 kJm^{-3} for $Fe_{20}Ni_{60}Co_{20}$ and $Fe_{40}Ni_{40}Co_{20}$, respectively.

References

1. A. Corrias, M. F. Casula, A. Falqui and G. Paschina, Chem. Mater., 16 (2004) 3130-3138.
2. P. P. Mishra, M. Manivel Raja and R. N. Panda, Mater. Res. Bull., 75 (2016) 127-133.
3. M. C. Prestgard, G. P. Siegel and A. Tiwari, Adv. Mat. Lett., 5 (2014) 242-247.
4. K. Peng, L. Zhou, A. Hu, Y. Tang and D. Li, Mater. Chem. Phys., 111 (2008) 34-37.
5. G. S. Abo, Y-K. Hong, J. Park, J. Lee, W. Lee and B-C. Choi, IEEE Trans. Magn., 49 (2013) 4937-4939.
6. L. Li, P. Lu, Y. Yao and W. Ji, Catal. Commun., 26 (2012) 72-77.

7. N. Li, C. Hu and M. Cao, Phys. Chem. Chem. Phys., 15 (2013) 7685-7689.
8. N. A. M. Barakat, M. Motlak, B. H. Lim, M. H. El-Newehy and S. S. Al-Deyab, J. Electrochem. Soc., 161 (2014) F1194-F1201.
9. C. de Julian Fernandez, C. Sangregorio, G. Mattei, C. Maurizio, G. Battaglin, F. Gonella, A. Lascialfari, S. Lo Russo, D. Gatteschi, P. Mazzoldi, J. M. Gonzalez and F. D. Acapito, Nucl. Instrum. Methods. Phys. Res. Sect. B, 175-177 (2001) 479-484.
10. F. Kleitz, S. H. Choi and R. Ryoo, Chem. Commun., (2003) 2136-2137.
11. H. Tuysuz, E. L. Salabas, E. Bill, H. Bongard, B. Spliethoff, C. W. Lehmann and F. Schuth, Chem. Mater., 24 (2012) 2493-2500.
12. O. Metin and S. Ozkar, Int. J. Hydrogen Energy, 36 (2011) 1424-1432.
13. A. Mourhly, M. Khachani, A. E. Hamidi, M. Kacimi, M. Halim and S. Arsalane, *Nanomater. Nanotechnol.* 5 (2015) 35.
14. S. Panday, B. S. S. Daniel and P. Jeevanandam, J. Magn. Magn. Mater., 323 (2011) 2271-2280.
15. N. Wu, W. Zhang, B. Li and C. Han, Microporous. Mesoporous. Mater., 185 (2014) 130-136.
16. A. Ponrouch, M.P. Bichat, S. Garbarino, C. Maunders, G. Botton, P. L. Taberna, P. Simon and D. Guay, ECS Trans., 25 (2010) 3-11.
17. E. I. Suvorova and P. A. Buffat, J. Microsc., 196 (1999) 46-58.
18. B. D. Culity and C. D. Graham, Introduction to Magnetic Materials, 2nd ed., John Wiley & Sons, NJ, 2009.
19. M. C. Prestgard, G. Siegel, Q. Ma and A. Tiwari, Appl. Phys. Lett., 103 (2013) 102409.
20. H. Wu, P. Cao, W. Li, N. Ni, L. Zhu and X. Zhang, J. Alloys Compd., 509 (2011) 1261-1265.
21. N. Lu, X. Song and J. Zhang, Nanotechnology 21 (2010) 115708.
22. C. de Julian Fernandez, C. Sangregorio, C. Innocenti, G. Mattei and P. Mazzoldi, Inorg. Chim. Acta., 361 (2008) 4138-4142.
23. G. Ennas, A. Falqui, S. Marras, C. Sangregorio and G. Marongiu, Chem. Mater., 16 (2004) 5659-5663.

24. R. K. Zheng, H. Gu, B. Xu and X. X. Zhang, J. Phys.: Condens. Matter, 18 (2006) 5905-5910.
25. S. Zhu, K. Sun, Q. Y. Zhang, X. T. Zu, L. M. Wang and R. C. Ewing, J. Appl. Phys., 94 (2003) 5648-5651.
26. S. Sharma, N. S. Gajbhiye and R. S. Ningthoujam, J. Colloid Interface Sci., 351 (2010) 323-329.
27. A. A. El-Gendy, E. M. M. Ibrahim, V. O. Khavrus, Y. Krupskaya, S. Hampel, A. Leonhardt, B. Buchner and R. Klingeler, Carbon, 47 (2009) 2821-2828.
28. J. Kim, J. Kim, J. Kim and K. H. Kim, J. Appl. Phys., 113 (2013) 17A313.
29. G. Cheng, D. Romero, G. T. Fraser and A. R. Hight Walker, Langmuir, 21 (2005) 12055-12059.
30. S. Asthana, Bull. Mater. Sci., 34 (2011) 279-282.
31. G. G. Couto, J. J. Klein, W. H. Schreiner, D. H. Mosca, A. J. A. de Oliveira and A. J. G. Zarbin, J. Colloid Interface Sci., 311 (2007) 461-468.
32. P. M. Paulus, F. Luis, M. Kroll, G. Schmid and L. J. de Jongh, J. Magn. Magn. Mater., 224 (2001) 180-196.
33. H. Wang, L. Zhang, J. Huang and J. Li, J. Nanopart. Res., 13 (2011) 1709-1715.
34. X-W. Wei, G-X. Zhu, Y-J. Liu, Y-H. Ni, Y. Song and Z. Xu, Chem. Mater., 20 (2008) 6248-6253.
35. S. Alikhanzadeh-Arani, M. Salavati-Niasari and M. Almasi-Kashi, J. Magn. Magn. Mater., 324 (2012) 3652-3657.
36. D. L. Peng, Y. Chen, H. She, R. Katoh and K. Sumiyama, J. Alloys Compd., 469 (2009) 276-281.
37. J. Bansmann, A. Kleibert, M. Getzlaff, A. F. Rodriguez, F. Nolting, C. Boeglin and K-H. Meiwes-Broer, Phys. Status Solidi B, 247 (2010) 1152-1160.
38. E. M. M. Ibrahim, S. Hampel, A. U. B. Wolter, M. Kath, A. A. El-Gendy, R. Klingeler, C. Taschner, V. O. Khavrus, T. Gemming, A. Leonhardt and B. Buchner, J. Phys. Chem. C, 116 (2012) 22509-22517.
39. J. Fang, L. D. Tung, K. L. Stokes, J. He, D. Caruntu, W. L. Zhou and C. J. O’Connor, J. Appl. Phys., 91 (2002) 8816-8818.

CHAPTER VIII

Summary and future scope

8.1 Summary of thesis

The nanocrystalline magnetic metals and alloys under this thesis work were synthesized by novel or modified chemical synthetic strategies using reducing agents such as: sodium borohydride, superhydride and polyol. These nanomaterials were characterized for the determination of purity, crystallinity, microstructures, particle sizes etc. Solid state reactivity leading to nano-structure materials formation, elucidation of structural aspects and details of magnetic behavior in materials was studied in detail.

In chapter I, An introduction to transition metals/alloys, their properties, synthesis methods, crystallography of selected crystal structures have been discussed initially in this chapter. In the general introduction to magnetism, different kinds of magnetic ordering in the magnetic materials were discussed and specifically ferromagnetism in the transition metals/alloys has been presented in detail. In fine particle magnetism or nano-magnetism section, the key points such as alterations of magnetic properties in nanomaterials, coercivity, magnetic anisotropy, factors affecting saturation magnetization, superparamagnetism in nanoparticles have been described. Detail literature survey of recent reports on soft and hard magnetic nanomaterials such as Fe, Co, Ni, Fe-Co, Co-Ni, Fe-Pt, Co-Pt and metal/alloy embedded in silica matrix systems were discussed. At the end, definition of the research problems to be executed in this thesis work has been summarized.

Chapter II describes the general aspects of synthesis methodologies and characterization methods. The modified $NaBH_4$ reduction route was used for the synthesis of ultrafine Fe, Co, Ni and Fe-Ni-Co alloy nanoparticles in aqueous medium by encapsulating with PEG-200. In this method, the use of $NaBH_4$ as reducing agent at RT, PEG-200 as capping, air atmosphere and aqueous medium for reaction have advantage for biomedical applications of these kinds of nanomaterials. Processing of the materials was carried out at 600°C under high purity nitrogen atmosphere before attempting for structural, microscopic and magnetic studies. The superhydride reduction method is developed for the synthesis of Co, Ni, Fe-Co, Co-Ni, Fe-Pt and Co-Pt alloys systems. Oleic acid and oleyl amine were used as capping agents for Co, Ni, Fe-Co, and Co-Ni whereas combinations of oleic acid, oleylamine and CTAB were used for Fe-Pt and Co-Pt alloys. Surface functionalization by oleic acid, oleylamine and CTAB on the surface nanomaterials have been successfully achieved by this method. Hence, superhydride method produces stable, monodispersed nanoparticles with narrow size distribution. Crystalline phases of the materials were obtained by annealing at 400-600°C under high purity nitrogen atmosphere. Superhydride method was also applied for the synthesis of Ni and $Co_{50}Ni_{50}$ nanoparticles dispersed in KIT-6 as silica matrix with different loading of 4-12 wt%. The novel and solution based method for dispersion of nanoparticles in silica matrix could give better dispersion of nanoparticles in silica matrix with appropriate interparticle separation. Crystalline phases of the materials were obtained by annealing at 400°C under high purity nitrogen atmosphere. Polyol reduction method was modified by using PEG-200 as reducing agent, PVP as capping agent and DMF as solvent. This method was successfully used for the synthesis of Co, $Co_{50}Ni_{50}$ and $Co_{50}Pt_{50}$ nanomaterials. The materials were annealed by two routes, i.e. route-1(without NaCl matrix) and route-2(with NaCl matrix) at 600-700°C under high purity nitrogen atmosphere. The characterization methods include UV-Visible spectroscopy, FTIR spectroscopy, Surface area analyzer, CHNS analyzer, XRD, SEM, TEM, VSM, SQUID and Mössbauer spectroscopy. The details of instrumental analysis such as principle, block diagram, output data and data interpretation have also been discussed in this chapter.

In chapter III includes Fe, Co, Ni and Fe-Co-Ni systems synthesized via modified $NaBH_4$ route. As-prepared Fe nanoparticles are amorphous in nature and prone to oxidation after annealing due to pyrophoric nature. Co and Ni nanoparticles crystallize in pure fcc phases with lattice parameters 3.54(±1) Å and 3.52(±1) Å whereas crystallite sizes are equal to 42.6(±1) nm and 29.1(±1) nm, respectively. SEM and TEM studies confirm the formation of nano-spheres of Co and Ni by this methodology. Size, shape and surface morphologies of material were studied by SEM and TEM analysis. SEM micrograph shows the particle sizes to be 62±5 nm and 54±3 nm whereas TEM studies confirm the sizes to be 43±4 nm and 48±5 nm for Co and Ni, respectively. These particle sizes are larger than crystallite sizes estimated by XRD studies due to the agglomeration of the nano-particles. Fine particle magnetism in our material is explained by the plot of specific magnetization versus applied field which shows the signature of the size and surface effects. The values of saturation magnetization are 122 and 47 emu/g whereas the coercivity values are 111 and 84 Oe for Co and Ni, respectively. These magnetic parameters indicate excellent soft magnetic behavior with presence of size, surface effects and spin canting at the surface of the ultrafine materials. Nanocrystalline ternary Fe-Ni-Co alloys with compositions $Fe_{20}Ni_{60}Co_{20}$, $Fe_{30}Ni_{50}Co_{20}$, $Fe_{40}Ni_{40}Co_{20}$ and $Fe_{50}Ni_{30}Co_{20}$ alloys have been successfully synthesized via $NaBH_4$ route in aqueous medium. All alloys crystallize in pure fcc phases of the ternary alloys with lattice parameters in the range of 3.546-3.558 Å and crystallite sizes are in the range of 22.8-27.5 nm. The increase in the values of lattice parameters was observed with the increase of Fe content in the ternary alloys. SEM studies indicate the presence of aggregates or clusters consisting of several crystallites. SEM particle sizes of Fe-Ni-Co alloys were in the range of 59±6 nm to 75±5 nm. TEM studies confirm that synthesized materials have spherical morphologies with minute fractions of agglomerations. Estimated values of TEM particle sizes were found to be 15±2 nm and 22±3 nm for $Fe_{20}Ni_{60}Co_{20}$ and $Fe_{40}Ni_{40}Co_{20}$, respectively. The observed values of saturation magnetization for our ternary alloys are in the range of 54.3-41.2 emu/g and coercivity values in the range of 170-122 Oe. The alterations of magnetic characteristics were observed due to fine particle size, surface effects, spin canting at the surface and presence of superparamagnetic fractions in the ultrafine materials.

Chapter IV includes Co, Ni, Fe-Co and Co-Ni materials synthesized via superhydride route. Co crystallizes in mixture of 53% hcp and 47% fcc phase whereas Ni crystallizes in fcc phase. Average crystallite sizes for Co and Ni were found to be 15 nm and 35 nm, respectively. TEM studies indicate the fine particle nature and spherical shape morphologies of synthesized materials. Average TEM particle sizes from TEM micrographs analysis are equal to 11±2 nm and 10±2 nm for Co and Ni, respectively.

Magnetic properties of Co and Ni were studied by field dependence of magnetization plots. Both Co and Ni show ferromagnetic behavior at room temperature. The magnetization-field (M-H) characteristics show the presence of superparamagnetic fractions in the ferromagnetic materials. The M_S values for Co and Ni are found to be 64 and 29 emu/g, respectively. The H_C values for Co and Ni are 436 Oe and 148 Oe, respectively and indicate high magnetocrystalline anisotropy effect and/or the presence of particle size distribution in our materials. Fe_xCo_{100-x} alloys (x = 40, 60, 80) prepared via superhydride route crystallize in pure α-Fe-Co alloy phase. The crystallite sizes were found to be in the range of ≈ 23-38 nm. TEM micrograph studies prove nearly spherical morphologies with narrow particle size distribution of the synthesized Fe-Co alloys. Average particle sizes estimated from TEM micrographs range from 10 nm to 51nm. The values of the M_S for Fe-Co alloys range from 93.1-142.2 emu/g after corrections for organic wt% at the surface of the materials. These values are quite large for Fe-Co materials while considering the small size nature of the materials and may be useful for potential technological applications. Variation of saturation magnetization with compositions was interpreted on the basis of varied compositions, reduction in particle size, altered crystal anisotropies and spin canting at the surface of nanomaterials. Room temperature Mössbauer studies show presence of ferromagnetic sextet and superparamagnetic doublet in Fe-Co materials. The variations in the values of H_{hf} in Fe-Co alloys may be attributed to the change in magnetic structure at the Fe nucleus with composition and disordered magnetic structures at the surface of the nanoparticles. Co_xNi_{100-x} alloys (x = 20, 40, 60, 80) prepared via superhydride route crystallize in pure fcc phase. Average crystallite sizes were found to be in the range of 8-11 nm. TEM micrograph studies show nearly spherical morphologies with narrow particle size distribution for the synthesized Co-Ni alloys. Average TEM particle sizes range from 7-11 nm. As-prepared as well as annealed Co-Ni alloys exhibit ferromagnetic behavior at room temperature with soft magnetic properties. The M_S values for annealed Co-Ni alloys are found to be in the range of 25-59.6 emu/g. The H_C values for annealed Co-Ni alloys (52-314 Oe) were found higher than the typical range for soft magnetic materials. These results were interpreted with the help of size effects, altered crystal anisotropies and spin canting at the surface of nanomaterials.

Chapter V includes Fe-Pt and Co-Pt materials synthesized via superhydride route. Nanocrystalline $Fe_{50}Pt_{50}$ and $Fe_{54}Pt_{46}$ alloys have been successfully synthesized using two different combinations of capping agents, namely: oleic acid/oleylamine (route-1) and oleic acid/CTAB (route-2). Fe-Pt alloys were characterized by XRD and SEM techniques in as-prepared and annealed state. The as-prepared Fe-Pt alloys show amorphous disordered fcc crystalline phase with crystallite sizes of 2.3 nm and 6 nm for route-1 and route-2, respectively. After annealing at 600°C, Fe-Pt alloys were transformed to ordered fct phase with crystallite sizes of 21nm and 19.5 nm for route-1 and route-2, respectively. SEM studies show that as-prepared Fe-Pt nanoparticles were surrounded by capping agents whereas annealed samples have spherical shape morphologies with SEM particle sizes of 24±2 nm and 21±3 nm for route-1 and route-2, respectively. As-prepared Fe-Pt alloys are ferromagnetic with presence of superparamagnetic fractions. Langevin fit to M vs. H plots of as-prepared Fe-Pt alloys gives average magnetic moments per particle to be 753 μ_B and 814 μ_B, for route 1 and 2, respectively. The values of saturation magnetization for annealed Fe-Pt alloys were found to be 4.4 emu/g and 29.6 emu/g for route-1 and route 2, respectively. Higher values of coercivity for 10000 Oe and 10792 Oe were obtained for fct Fe-Pt alloys synthesized from route-1 and route-2, respectively. $Co_{59}Pt_{41}$ and $Co_{60}Pt_{40}$ alloys have been synthesized via superhydride reduction route using two different combinations of capping structures, namely: CTAB (route-1) and oleic acid/CTAB (route-2). Further characterizations were carried out by XRD and SEM techniques in as-prepared and annealed at 500°C and 600°C. As-prepared Co-Pt alloys show amorphous disordered fcc crystalline phase and transformed to ordered fct phase after annealing at 600°C. SEM studies show that annealed Co-Pt nanoparticles have spherical shape morphologies with SEM particle sizes of 38±5 nm and 59±2 nm for route-1 and route-2, respectively. The values of M_S for Co-Pt alloys synthesized via route-1 are found to be 0.9 emu/g, 18.3 emu/g, and 31.4 emu/g whereas H_C values are 428 Oe, 667 Oe, and 1728 Oe, for as-prepared, annealed at 500°C/2h, and annealed at 600°C/2h, respectively. The values of M_S for Co-Pt alloys synthesized via route-2 are found to be 1.2 emu/g, 27.5 emu/g, 26.9 emu/g, and 22.5 emu/g whereas H_C values are

870 Oe, 806 Oe, 2525 Oe, and 5027 Oe, for as-prepared, annealed at 500°C/2h, annealed at 600°C/2h, and annealed at 600°C/12h, respectively. The observed magnetic properties have been interpreted with the help of crystallite sizes, order parameters, size, surface, and composition effects of the nanostructured materials.

Chapter VI includes Co, $Co_{50}Ni_{50}$ and Co-Pt alloys synthesized via polyol method. Co(route-1) crystallizes in hcp phase with average crystallite size of 16.4 nm even after annealing at 600°C. While Co(route-2) crystallizes in fcc phase with average crystallite size of 37.1 nm at 600°C. The observation of different phases for two routes is attributed to fine particle effects and annealing in presence of crystalline NaCl matrix. A TEM micrograph shows that Co(route-1) has uniformly dispersed chain-like nanostructures whereas Co(route-2) shows monodispersed nanostructures with nearly spherical morphologies. The estimated values of average chain diameter was found to be 2.8 ± 0.5 nm and chain lengths varies from 15-26 nm. Average TEM particle size for Co(route-2) was found to be 5.2 ± 0.5 nm. Co(route-1) nanoparticles have large M_S value of 162.7 emu/g and 167 emu/g while those of Co(route-2) have small M_S value of 29.7 emu/g and 35 emu/g at RT and 100K, respectively. These alterations in the magnetic properties have been explained with the help of size, shape, spin canting at the surface, altered crystal anisotropies etc. The H_C values at RT of Co(route-1) and Co(route-2) are 220 Oe and 185 Oe, respectively, and indicates the particle size effects on coercivity. However, H_C values measure at 100K of Co(route-1) and Co(route-2)were found to be 1.6 times and 2 times higher than that of RT and indicate thermal effects dominates over anisotropy effects at 100K. A typical composition of $Co_{50}Ni_{50}$ alloy has been synthesized via modified polyol method and annealed via both route-1 and route-2 crystallize in pure fcc phase with average crystallite sizes of 28.1 nm and 30.4 nm, respectively. TEM micrograph study was carried for typical sample, i.e. Co-Ni(route-2), and shows presence of nanostructures with nearly spherical morphologies with particle size of 8±1 nm having narrow size distribution. Corrected M_S and H_C values Co-Ni(route-1) were found to be 116.2 emu/g and 86 Oe, at RT whereas 110 emu/g and 93Oe, at 100K respectively. Abnormal decrease in M_S value of Co-Ni(route-1) at 100K may be attributed to deviations in anisotropy near saturation of magnetization. Corrected M_S and H_C values Co-Ni(route-2) were found to be 45.6 emu/g and 214 Oe, at RT whereas 47.4 emu/g and 324 Oe, at 100K, respectively. These magnetic properties show fine particle size effects and temperature effects in the materials. $Co_{58}Pt_{42}$ alloy nanoparticles have synthesized via modified polyol method. As-prepared Co-Pt alloy nanoparticles crystallize in amorphous disordered fcc phase. Co-Pt alloy nanoparticles annealed via route-1 possess fcc crystal structure even at 700°C whereas Co-Pt alloy nanoparticles annealed via route-2 shows ordered fct ($L1_0$) phase. Microstructural and magnetic properties of fct Co-Pt obtained via route-2 have been studied. SEM studies show that annealed Co-Pt nanoparticles have spherical shape morphologies with SEM particle sizes of 41±3 nm. And SEM EDX composition was found to be $Co_{58}Pt_{42}$. The values of M_S and H_C for Co-Pt(route-2) are found to be 24 emu/g and 6050 Oe, respectively. The observed magnetic properties have been interpreted with the help of crystallite sizes, order parameters, and composition effects of the Co-Pt nanostructured materials.

Chapter VII describes magnetic exchange and dipolar interactions studies in Ni/silica, $Co_{50}Ni_{50}$/silica, Co-Ni, Co, Ni, Fe-Co and Fe-Ni-Co systems. Ni/silica and $Co_{50}Ni_{50}$/silica with various loading (4-12 wt%) have been synthesized by novel chemical reduction route. The novelty of synthetic procedure adopted has been established using UV-VIS and FTIR spectroscopy. XRD studies confirm that both the materials form pure fcc phase embedded in amorphous silica matrix. XRD crystallite sizes for Ni/silica and $Co_{50}Ni_{50}$/silica are in the range of 6-10.5 nm and 13.6-16.3 nm, respectively. TEM microscopy studies show that CoNi alloys have nearly spherical shape morphologies and narrow size distributions. TEM particle sizes were estimated to be 13.6 nm and 8.9 nm for pure CoNi and 8 wt% CoNi materials loaded in silica matrix, respectively. Magnetic hysteresis studies at RT indicate the presence of superparamagnetic fractions in the materials. Enhancements in the values of magnetizations of Ni/silica and $Co_{50}Ni_{50}$/silica compared to that of pure materials have been observed with increase in dilution of nanoparticles in matrix. FC/ZFC magnetizations plots show decrease is blocking temperature for $Co_{50}Ni_{50}$/silica compare to pure $Co_{50}Ni_{50}$ which indicates magnetic structure alteration and supports our magnetic results. The observed enhancement in magnetization with low values of coercivity after loading in silica matrix has been explained on the basis of fine particle size, surface effects and dipolar interparticle interactions. Magnetic interactions in Co_xNi_{100-x} alloys coated by oleic acid and oleyl amine have been studied by low temperature FC/ZFC magnetization measurements. It could be confirm the presence of magnetic irreversibility and superparamagnetic blocking of nanoparticles due to strong dipolar interactions and particle size distribution. Estimated values of effective anisotropy constants of Co-Ni alloys (i.e., 57-181 kJ/m^3) reveal the contribution from the reduced particle size and surface anisotropy. On the above, a structure-property correlation in Co-Ni alloys has been attempted in this investigation. Also, magnetic interactions in Co, Ni, Fe-Co and Fe-Ni-Co alloys coated by carbonaceous matter have been studied by low temperature FC/ZFC magnetization measurements. The anisotropy constants for Co and Ni were found to be 25 kJ/m^3 and 13 kJ/m^3, respectively. FC/ZFC results show the wider size distributions in Co and Ni. Magnetic irreversible behavior below 300 K was observed in the materials from FC/ZFC curves due to ferromagnetism and dipolar interactions among the particles and result in shifting of blocking temperature value above 300 K.FC/ZFC magnetization measurements of Fe_xCo_{100-x} alloys show magnetic irreversibility and blocking of nanoparticles due to strong dipolar interparticle magnetic interactions. Estimated values of K_{eff} of Fe_xCo_{100-x} alloys (i.e. 1.5 kJ/m^3, 4.6 kJ/m^3 and 14.3 kJ/m^3 for x = 40, 60 and 80, respectively) reveal the contribution from the reduced particle size and surface anisotropy. It is observed that Fe-Ni-Co alloys showing thermo-magnetic irreversibility below 300 K and blocking temperature approximately at 300 K. FC and ZFC magnetic characteristics of Fe-Ni-Co alloys are interpreted on the basis of interparticle interactions among magnetic nanoparticles. The values of effective magnetic anisotropy constants (K_{eff}) are found to be 14 kJm^{-3} and 4.2 kJm^{-3}for $Fe_{20}Ni_{60}Co_{20}$ and $Fe_{40}Ni_{40}Co_{20}$, respectively.

8.2 Future scope of research work

The modified $NaBH_4$ reduction route can be used for synthesis of PEG coated nanocrystalline metals/alloys at ambient conditions like air atmosphere, room temperature and aqueous medium. This method has advantage in field of biomedical research, provided stabilization of the nanostructure including surface oxidation is achieved. The modified superhydride route and polyol methods have fine control on nanoparticle size, their distribution and coating on the surface in organic medium. These alterations in materials morphology may help in designing materials for specific applications. The materials such as Co, Ni, Fe-Co, Co-Ni alloys show soft magnetic properties and have important applications in magnetic recording field, MRI contrast agents, cancer therapy, drug delivery agents, microwave absorption materials and catalysis. Basic study as well as applications oriented research of above materials can be extended. Synthesis of nanomaterials embedded in silica matrix using solution based method is a new approach and may be useful for future research. Also, synthesis of materials with controlled interparticle separations is useful for deep study of magnetic exchange and dipolar interactions among nanoparticles. In summary, there is ample scope of the future work based on stabilization, functionalization of the nano-materials with tunable structural and magnetic properties for possible potential applications.

10. **S. B. Dalavi**, J. Theerthagiri, M. Manivel Raja and R. N. Panda, Synthesis, characterization and magnetic properties of nanocrystalline FexNi80−xCo20 ternary alloys, J. Magn. Magn. Mater., 344 (2013) 30–34.

Publications apart from thesis work

1. J. Theerthagiri, **S. B. Dalavi**, M. Manivel Raja and R.N. Panda, Magnetic properties of nanocrystalline ε-Fe_3N and Co_4N phases synthesized by newer precursor route, Mater. Res. Bull., 48 (2013) 4444-4448.
2. Rabi N. Panda, **S. B. Dalavi** and J. Theerthagiri, Synthesis of High Surface Area W_2N and Co–W–N Nitrides by Chemical Routes, Adsorpt. Sci. Technol., 30 (2012) 345-354.

Conferences

International (03) and National (03)

1. **S. B. Dalavi** and R. N. Panda, Magnetic Properties of nano-structured Co and Ni Synthesized by Modified $NaBH_4$ Reduction Route, ‘International Conference on Powder, Granule and Bulk Solids: Innovations and Applications (PGBSIA)’, Thapar University, Patiala, 2013.
2. **S. B. Dalavi**, M. Manivel Raja and R. N. Panda, Chemical Synthesis, Characterizations and Magnetic Properties of Nanocrystalline $Fe_{50}Co_{50}$ Alloy, ‘58th DAE Solid State Physics Symposium (DAE-SSPS-2013)’, Thapar University, Patiala, 2013.
3. **S. B. Dalavi** and R. N. Panda, Studies on Fine Particle Magnetism in $Fe_xNi_{80-x}Co_{20}$ (x = 20, 40) Ternary Alloys Synthesized by Chemical Route, ‘International Symposium for Research Scholars – 2014 (ISRS 14)’, IIT Madras, Chennai, 2014.

4. **S. B. Dalavi**, M. Manivel Raja and R. N. Panda, Magnetic Properties of Ni Nanoparticles Embedded in Silica Matrix (KIT-6) Synthesized via Novel Chemical Route, '59th DAE Solid State Physics Symposium (DAE-SSPS-2014)', VIT University, Vellore**,** 2014.
5. **S. B. Dalavi** and R. N. Panda, Development of novel chemical methods for synthesis of Co and Ni nanoparticles and studies on their magnetic properties, 'National Conference on Frontiers in Chemical and Material Sciences (FCMS)', Shivaji University, Kolhapur, 2015.
6. **S. B. Dalavi** and R. N. Panda, Enhancement Of Magnetic Moment In Co-Ni Alloy Nanoparticles Dispersed In Silica Matrix Synthesized By Novel Chemical Route, 'International Conference on Magnetic Materials and Applications (ICMAGMA-2015)', VIT University, Vellore, 2015.

Bio-data of candidate

Personal detail

Name:	**DALAVI SHANKAR BALU**
Gender and Marital Status:	**Male, Unmarried**
Date of Birth:	**01/06/1986**
Nationality:	**Indian**

E-mail: **shankardalavi@gmail.com, p2012013@goa.bits-pilani.ac.in**

Education

2007-2009	**M.Sc. in Physical Chemistry** (70.13 %, First class) Shivaji University, Kolhapur, Maharashtra.
2004-2007	**B.Sc. in Chemistry** (81.04 %, First class) Shivaji University, Kolhapur, Maharashtra.

Professional Experience

06/2009-11/2011	**Worked as Asst. R&D officer in organic research lab** of Gharda Chemicals Ltd. Dombivli, Thane, Maharashtra.

Honors and Awards

11/2011-11/2013	**'JRF'** in CSIR funded project entitled "Magnetic Properties of Metallic Nanoparticles." with Prof. Rabi Narayan Panda (PI) Department of Chemistry, BITS, Pilani-K. K. Birla Goa Campus, Zuarinagar, Goa-403726, India.

11/2013-07/2014	**‘SRF’** in CSIR funded project entitled “Magnetic Properties of Metallic Nanoparticles.” with Prof. Rabi Narayan Panda (PI) Department of Chemistry, BITS, Pilani-K. K. Birla Goa Campus, Zuarinagar, Goa-403726, India.
02/2013	**Qualified SET** (for lectureship), Maharashtra, India.
03/2011	**Qualified GATE**

Publications during Ph. D.

Publications and conferences are listed in Appendix I.

Bio-data of supervisor

Name Prof. Rabi Narayan Panda

Current position Associate Professor
Department of Chemistry
Birla Institute of Technology and Science-Pilani,
K. K. Birla Goa Campus
Zuarinagar-403726, State-Goa, India.

Date of Birth 01/09/1970

Education Ph. D. in Chemistry: IIT Kanpur (1998).
M. Sc. In Chemistry: Sambalpur University (1993).

Areas of research (i) Magnetics, Mossbauer of Ultrafine Ferrite and related materials and their bio-applications.
(ii) Magnetic Properties of Metal/Alloy nano-particles.
(iii) Synthesis and Electronic Properties of semiconductor quantum dots (ZnS, CdS and related).
(iv) Size and shape induced magnetic and electronic properties.
(v) Solid-gas reactions-Generation of nono-dimensional transition metal nitrides.
(vi) Hydroxy-apatite related Bio-materials.
(vii) Correlation of physical properties with materials structure at the surface along with microstructure.
(viii) Coated and embedded nano-structured for Bio- and magnetic applications.

No. of Sponsored Research Projects

As PI 02 (CSIR, DST)

No. of Publications in International Journals 42 (SCI Journals)

(h-index: 16 , i-10-index: 20)

No. of Conference Proceedings	21
No. of Invited Talk and Seminars	13

Honors and Awards

2000-2002	Awarded a post-doctoral fellowship from National Science Council, Taiwan, to do research in the field of Material Science at National Tsing Hua University, Taiwan.
2003	Awarded Alexander Von Humboldt Fellowship, in order to conduct research in nano-materials at the Institute of nanotechnology, Forschungszentrum Karlsruhe (Now KIT), Germany.
2005-2005	Awarded a post-doctoral fellowship from National Science Council, Taiwan, to do research in the area of Spintronics at Department of Physics, National Taiwan University, Taipei, Taiwan.

Reviewer and Editor

Reviewer	International Journals: Nano-Scale Research Letter, Materials Science and Engg, B, Materials Lett. , Journal of Magn. Magn. Mater., Dalton transactions, etc.
Guest Editor	J. Nanomaterials (2014-15), Special Issue: Advanced Nanoporous Materials: Synthesis, properties and applications.

Publications

1. P. P. Mishra and **R. N. Panda**, Mater. Res. Bull., 86 (2017) 241-247.
2. S. B. Dalavi and **R. N. Panda**, J. Magn. Magn. Mater., 438 (2017) 306-312.
3. S. B. Dalavi and **R. N. Panda**, J. Nanosci. Nanotechnol., 17 (2017) 2589-2595.
4. S. B. Dalavi and **R. N. Panda**, J. Mater. Res., 31 (2016) 2430-2437.
5. P. P. Mishra, M. Manivel Raja and **R. N. Panda**, J. Supercond. Nov. Magn., 29 (2016) 1347-1356.

6. P. P. Mishra, M. Manivel Raja and **R. N. Panda**, Mater. Res. Bull., 75 (2016) 127-133.
7. S. B. Dalavi, M. Manivel Raja and **R. N. Panda**, New J. Chem., 39 (2015) 9641-9649.
8. S. B. Dalavi, M. Manivel Raja and **R. N. Panda**, AIP Conf. Proc., 1665 (2015) 050071.
9. S. B. Dalavi and **R. N. Panda**, Trans. Indian Inst. Met., 68 (2015) 253-257.
10. P. P. Mishra and **R. N. Panda**, AIP Conf. Proc., 1665 (2015) 050030.
11. S. B. Dalavi and **R. N. Panda**, J. Magn. Magn. Mater., 374 (2015) 411-416.
12. S. B. Dalavi and **R. N. Panda**, Part. Sci. Technol., 33 (2015) 97-101.
13. P. P. Mishra, J. Theerthagiri and **R. N. Panda**, Adsorpt. Sci. Technol., 32 (2014) 465-474.
14. S. B. Dalavi, M. Manivel Raja and **R. N. Panda**, AIP Conf. Proc., 1591 (2014) 241-243.
15. J. Theerthagiri, S. B. Dalavi, M. Manivel Raja and **R. N. Panda**, Mater. Res. Bull., 48 (2013) 4444-4448.
16. S. B. Dalavi, J. Theerthagiri, M. Manivel Raja and **R. N. Panda**, J. Magn. Mag. Mater., 344 (2013) 30-34.
17. **R. N. Panda,** S. B. Dalavi and J. Theerthagiri, Adsorpt. Sci. Technol., 30 (2012) 345-354.
18. R. S. Ningthoujam, **R. N. Panda** and N. S. Gajbhiye, Mater. Chem. Phys., 134 (2012) 377-381.
19. **R. N. Panda**, J. Surface. Sci. Technol., 27 (2011) 125-134.
20. P. Krawiec, **R. N. Panda**, E. Kockrick, D. Geiger and S. Kaskel, J. Solid State Chem., 181 (2008) 935-942.
21. **R. N. Panda**, G. Balaji, P. K. Pandey and N. S. Gajbhiye, Hyperfine Interact., 184 (2008) 659-664.
22. **R. N. Panda** and S. Kaskel, J. Mater. Sci., 41 (2006) 2465-2470.
23. K. De, R. Ray, **R. N. Panda**, S. Giri, H. Nakamura and T. Kohara, J. Magn. Magn. Mater., 288 (2005) 339-346.

24. N. S. Gajbhiye, **R. N. Panda**, R. S. Ningthoujam and S. Bhattacharyya, Phys. Stat. Sol. c, 1 (2004) 3252-3259.
25. R. J. Chung , M. F. Hsieh, **R. N. Panda** and T. S. Chin, Surf. Coat. Tech., 165 (2003) 194-200.
26. **R. N. Panda**, J. C. Shih and T. S. Chin, J. Magn. Magn. Mater., 157 (2003) 79-86.
27. **R. N. Panda**, M. F. Hsieh, R. J. Chung and T. S. Chin, J. Phys. Chem. Solids, 64 (2003) 193-199.
28. **R. N. Panda** and A. Pradhan, Mater. Chem. Phys., 78 (2002) 313-317.
29. Md. N. Islam, **R. N. Panda**, A. Pradhan and S. Kumar, Phys. Rev. B, 65 (2002) 033314(1-4).
30. **R. N. Panda**, G. Balaji and N. S. Gajbhiye, Hyperfine Interact., 141 (2002) 187-191.
31. H. H. Hsiao, **R. N. Panda**, J. C. Shih and T. S. Chin, J. Appl. Phys., 91 (2002) 3145-3149.
32. **R. N. Panda**, M-F. Hsieh, R-J. Chung and T-S. Chin, Jap. J. Appl. Phys., 40 (2001) 5030-5035.
33. B. V. Laxmi, **R. N. Panda**, M. S. Nair, A. Rastogi, D. K. Mittal, A. Agarwal and A. Pradhan, Lasers Life Sci., 9 (2001) 229-243.
34. **R. N. Panda**, N. S. Gajbhiye and G. Balaji, J. Alloy Compd., 326 (2001) 50-53.
35. **R. N. Panda**, A. Agarwal and A. Pradhan, Asian J. Phys., 8 (1999) 179-184.
36. **R. N. Panda** and N. S. Gajbhiye, J. Magn. Magn. Mater., 195 (1999) 396-405.
37. **R. N. Panda** and N. S. Gajbhiye, J. Appl. Phys., 86 (1999) 3295-3302.
38. **R. N. Panda** and N. S. Gajbhiye, J. Cryst. Growth, 191 (1998) 92-96.
39. **R. N. Panda** and N. S. Gajbhiye, J. Magn. Soc. Japan, 22S1 (1998) 209-211.
40. **R. N. Panda** and N. S. Gajbhiye, IEEE Trans. Mag., 34 (1998) 542-548.
41. **R. N. Panda** and N. S. Gajbhiye, J. Appl. Phys., 81 (1997) 335-339.
42. **R. N. Panda** and N. S. Gajbhiye, J. Alloy Compd., 256 (1997) 102-107.

Studies on Nano-magnetism of Fe, Co, Ni and Pt based Ferromagnetic Metal and Alloy Nanoparticles Synthesized via Novel Chemical Routes

THESIS

Submitted in partial fulfillment
of the requirements for the degree of

DOCTOR OF PHILOSOPHY

by

DALAVI SHANKAR BALU

Under the Supervision of

Prof. RABI NARAYAN PANDA

BIRLA INSTITUTE OF TECHNOLOGY AND SCIENCE, PILANI

2017

CHAPTER VIII

Summary and future scope

8.1 Summary of thesis

The nanocrystalline magnetic metals and alloys under this thesis work were synthesized by novel or modified chemical synthetic strategies using reducing agents such as: sodium borohydride, superhydride and polyol. These nanomaterials were characterized for the determination of purity, crystallinity, microstructures, particle sizes etc. Solid state reactivity leading to nano-structure materials formation, elucidation of structural aspects and details of magnetic behavior in materials was studied in detail.

In chapter I, An introduction to transition metals/alloys, their properties, synthesis methods, crystallography of selected crystal structures have been discussed initially in this chapter. In the general introduction to magnetism, different kinds of magnetic ordering in the magnetic materials were discussed and specifically ferromagnetism in the transition metals/alloys has been presented in detail. In fine particle magnetism or nano-magnetism section, the key points such as alterations of magnetic properties in nanomaterials, coercivity, magnetic anisotropy, factors affecting saturation magnetization, superparamagnetism in nanoparticles have been described. Detail literature survey of recent reports on soft and hard magnetic nanomaterials such as Fe, Co, Ni, Fe-Co, Co-Ni, Fe-Pt, Co-Pt and metal/alloy embedded in silica matrix systems were discussed. At the end, definition of the research problems to be executed in this thesis work has been summarized.

Chapter II describes the general aspects of synthesis methodologies and characterization methods. The modified $NaBH_4$ reduction route was used for the synthesis of ultrafine Fe, Co, Ni and Fe-Ni-Co alloy nanoparticles in aqueous medium by encapsulating with PEG-200. In this method, the use of $NaBH_4$ as reducing agent at RT, PEG-200 as capping, air atmosphere and aqueous medium for reaction have advantage for biomedical applications of these kinds of nanomaterials. Processing of the materials was carried out at 600°C under high purity nitrogen atmosphere before attempting for structural, microscopic and magnetic studies. The superhydride reduction method is developed for the synthesis of Co, Ni, Fe-Co, Co-Ni, Fe-Pt and Co-Pt alloys systems. Oleic acid and oleyl amine were used as capping agents for Co, Ni, Fe-Co, and Co-Ni whereas combinations of oleic acid, oleylamine and CTAB were used for Fe-Pt and Co-Pt alloys. Surface functionalization by oleic acid, oleylamine and CTAB on the surface nanomaterials have been successfully achieved by this method. Hence, superhydride method produces stable, monodispersed nanoparticles with narrow size distribution. Crystalline phases of the materials were obtained by annealing at 400-600°C under high purity nitrogen atmosphere. Superhydride method was also applied for the synthesis of Ni and $Co_{50}Ni_{50}$ nanoparticles dispersed in KIT-6 as silica matrix with different loading of 4-12 wt%. The novel and solution based method for dispersion of nanoparticles in silica matrix could give better dispersion of nanoparticles in silica matrix with appropriate interparticle separation. Crystalline phases of the materials were obtained by annealing at 400°C under high purity nitrogen atmosphere. Polyol reduction method was modified by using PEG-200 as reducing agent, PVP as capping agent and DMF as solvent. This method was successfully used for the synthesis of Co, $Co_{50}Ni_{50}$ and $Co_{50}Pt_{50}$ nanomaterials. The materials were annealed by two routes, i.e. route-1(without NaCl matrix) and route-2(with NaCl matrix) at 600-700°C under high purity nitrogen atmosphere. The characterization methods include UV-Visible spectroscopy, FTIR spectroscopy, Surface area analyzer, CHNS analyzer, XRD, SEM, TEM, VSM, SQUID and Mössbauer spectroscopy. The details of instrumental analysis such as principle, block diagram, output data and data interpretation have also been discussed in this chapter.

In chapter III includes Fe, Co, Ni and Fe-Co-Ni systems synthesized via modified $NaBH_4$ route. As-prepared Fe nanoparticles are amorphous in nature and prone to oxidation after annealing due to pyrophoric nature. Co and Ni nanoparticles crystallize in pure fcc phases with lattice parameters 3.54(±1) Å and 3.52(±1) Å whereas crystallite sizes are equal to 42.6(±1) nm and 29.1(±1) nm, respectively. SEM and TEM studies confirm the formation of nano-spheres of Co and Ni by this methodology. Size, shape and surface morphologies of material were studied by SEM and TEM analysis. SEM micrograph shows the particle sizes to be 62±5 nm and 54±3 nm whereas TEM studies confirm the sizes to be 43±4 nm and 48±5 nm for Co and Ni, respectively. These particle sizes are larger than crystallite sizes estimated by XRD studies due to the agglomeration of the nano-particles. Fine particle magnetism in our material is explained by the plot of specific magnetization versus applied field which shows the signature of the size and surface effects. The values of saturation magnetization are 122 and 47 emu/g whereas the coercivity values are 111 and 84 Oe for Co and Ni, respectively. These magnetic parameters indicate excellent soft magnetic behavior with presence of size, surface effects and spin canting at the surface of the ultrafine materials. Nanocrystalline ternary Fe-Ni-Co alloys with compositions $Fe_{20}Ni_{60}Co_{20}$, $Fe_{30}Ni_{50}Co_{20}$, $Fe_{40}Ni_{40}Co_{20}$ and $Fe_{50}Ni_{30}Co_{20}$ alloys have been successfully synthesized via $NaBH_4$ route in aqueous medium. All alloys crystallize in pure fcc phases of the ternary alloys with lattice parameters in the range of 3.546-3.558 Å and crystallite sizes are in the range of 22.8-27.5 nm. The increase in the values of lattice parameters was observed with the increase of Fe content in the ternary alloys. SEM studies indicate the presence of aggregates or clusters consisting of several crystallites. SEM particle sizes of Fe-Ni-Co alloys were in the range of 59±6 nm to 75±5 nm. TEM studies confirm that synthesized materials have spherical morphologies with minute fractions of agglomerations. Estimated values of TEM particle sizes were found to be 15±2 nm and 22±3 nm for $Fe_{20}Ni_{60}Co_{20}$ and $Fe_{40}Ni_{40}Co_{20}$, respectively. The observed values of saturation magnetization for our ternary alloys are in the range of 54.3-41.2 emu/g and coercivity values in the range of 170-122 Oe. The alterations of magnetic characteristics were observed due to fine particle size, surface effects, spin canting at the surface and presence of superparamagnetic fractions in the ultrafine materials.

Chapter IV includes Co, Ni, Fe-Co and Co-Ni materials synthesized via superhydride route. Co crystallizes in mixture of 53% hcp and 47% fcc phase whereas Ni crystallizes in fcc phase. Average crystallite sizes for Co and Ni were found to be 15 nm and 35 nm, respectively. TEM studies indicate the fine particle nature and spherical shape morphologies of synthesized materials. Average TEM particle sizes from TEM micrographs analysis are equal to 11±2 nm and 10±2 nm for Co and Ni, respectively.

Magnetic properties of Co and Ni were studied by field dependence of magnetization plots. Both Co and Ni show ferromagnetic behavior at room temperature. The magnetization-field (M-H) characteristics show the presence of superparamagnetic fractions in the ferromagnetic materials. The M_S values for Co and Ni are found to be 64 and 29 emu/g, respectively. The H_C values for Co and Ni are 436 Oe and 148 Oe, respectively and indicate high magnetocrystalline anisotropy effect and/or the presence of particle size distribution in our materials. Fe_xCo_{100-x} alloys (x = 40, 60, 80) prepared via superhydride route crystallize in pure α-Fe-Co alloy phase. The crystallite sizes were found to be in the range of ≈ 23-38 nm. TEM micrograph studies prove nearly spherical morphologies with narrow particle size distribution of the synthesized Fe-Co alloys. Average particle sizes estimated from TEM micrographs range from 10 nm to 51nm. The values of the M_S for Fe-Co alloys range from 93.1-142.2 emu/g after corrections for organic wt% at the surface of the materials. These values are quite large for Fe-Co materials while considering the small size nature of the materials and may be useful for potential technological applications. Variation of saturation magnetization with compositions was interpreted on the basis of varied compositions, reduction in particle size, altered crystal anisotropies and spin canting at the surface of nanomaterials. Room temperature Mössbauer studies show presence of ferromagnetic sextet and superparamagnetic doublet in Fe-Co materials. The variations in the values of H_{hf} in Fe-Co alloys may be attributed to the change in magnetic structure at the Fe nucleus with composition and disordered magnetic structures at the surface of the nanoparticles. Co_xNi_{100-x} alloys (x = 20, 40, 60, 80) prepared via superhydride route crystallize in pure fcc phase. Average crystallite sizes were found to be in the range of 8-11 nm. TEM micrograph studies show nearly spherical morphologies with narrow particle size distribution for the synthesized Co-Ni alloys. Average TEM particle sizes range from 7-11 nm. As-prepared as well as annealed Co-Ni alloys exhibit ferromagnetic behavior at room temperature with soft magnetic properties. The M_S values for annealed Co-Ni alloys are found to be in the range of 25-59.6 emu/g. The H_C values for annealed Co-Ni alloys (52-314 Oe) were found higher than the typical range for soft magnetic materials. These results were interpreted with the help of size effects, altered crystal anisotropies and spin canting at the surface of nanomaterials.

Chapter V includes Fe-Pt and Co-Pt materials synthesized via superhydride route. Nanocrystalline $Fe_{50}Pt_{50}$ and $Fe_{54}Pt_{46}$ alloys have been successfully synthesized using two different combinations of capping agents, namely: oleic acid/oleylamine (route-1) and oleic acid/CTAB (route-2). Fe-Pt alloys were characterized by XRD and SEM techniques in as-prepared and annealed state. The as-prepared Fe-Pt alloys show amorphous disordered fcc crystalline phase with crystallite sizes of 2.3 nm and 6 nm for route-1 and route-2, respectively. After annealing at 600°C, Fe-Pt alloys were transformed to ordered fct phase with crystallite sizes of 21nm and 19.5 nm for route-1 and route-2, respectively. SEM studies show that as-prepared Fe-Pt nanoparticles were surrounded by capping agents whereas annealed samples have spherical shape morphologies with SEM particle sizes of 24±2 nm and 21±3 nm for route-1 and route-2, respectively. As-prepared Fe-Pt alloys are ferromagnetic with presence of superparamagnetic fractions. Langevin fit to M vs. H plots of as-prepared Fe-Pt alloys gives average magnetic moments per particle to be 753 μ_B and 814 μ_B, for route 1 and 2, respectively. The values of saturation magnetization for annealed Fe-Pt alloys were found to be 4.4 emu/g and 29.6 emu/g for route-1 and route 2, respectively. Higher values of coercivity for 10000 Oe and 10792 Oe were obtained for fct Fe-Pt alloys synthesized from route-1 and route-2, respectively. $Co_{59}Pt_{41}$ and $Co_{60}Pt_{40}$ alloys have been synthesized via superhydride reduction route using two different combinations of capping structures, namely: CTAB (route-1) and oleic acid/CTAB (route-2). Further characterizations were carried out by XRD and SEM techniques in as-prepared and annealed at 500°C and 600°C. As-prepared Co-Pt alloys show amorphous disordered fcc crystalline phase and transformed to ordered fct phase after annealing at 600°C. SEM studies show that annealed Co-Pt nanoparticles have spherical shape morphologies with SEM particle sizes of 38±5 nm and 59±2 nm for route-1 and route-2, respectively. The values of M_S for Co-Pt alloys synthesized via route-1 are found to be 0.9 emu/g, 18.3 emu/g, and 31.4 emu/g whereas H_C values are 428 Oe, 667 Oe, and 1728 Oe, for as-prepared, annealed at 500°C/2h, and annealed at 600°C/2h, respectively. The values of M_S for Co-Pt alloys synthesized via route-2 are found to be 1.2 emu/g, 27.5 emu/g, 26.9 emu/g, and 22.5 emu/g whereas H_C values are

870 Oe, 806 Oe, 2525 Oe, and 5027 Oe, for as-prepared, annealed at 500°C/2h, annealed at 600°C/2h, and annealed at 600°C/12h, respectively. The observed magnetic properties have been interpreted with the help of crystallite sizes, order parameters, size, surface, and composition effects of the nanostructured materials.

Chapter VI includes Co, $Co_{50}Ni_{50}$ and Co-Pt alloys synthesized via polyol method. Co(route-1) crystallizes in hcp phase with average crystallite size of 16.4 nm even after annealing at 600°C. While Co(route-2) crystallizes in fcc phase with average crystallite size of 37.1 nm at 600°C. The observation of different phases for two routes is attributed to fine particle effects and annealing in presence of crystalline NaCl matrix. A TEM micrograph shows that Co(route-1) has uniformly dispersed chain-like nanostructures whereas Co(route-2) shows monodispersed nanostructures with nearly spherical morphologies. The estimated values of average chain diameter was found to be 2.8 ± 0.5 nm and chain lengths varies from 15-26 nm. Average TEM particle size for Co(route-2) was found to be 5.2 ± 0.5 nm. Co(route-1) nanoparticles have large M_S value of 162.7 emu/g and 167 emu/g while those of Co(route-2) have small M_S value of 29.7 emu/g and 35 emu/g at RT and 100K, respectively. These alterations in the magnetic properties have been explained with the help of size, shape, spin canting at the surface, altered crystal anisotropies etc. The H_C values at RT of Co(route-1) and Co(route-2) are 220 Oe and 185 Oe, respectively, and indicates the particle size effects on coercivity. However, H_C values measure at 100K of Co(route-1) and Co(route-2)were found to be 1.6 times and 2 times higher than that of RT and indicate thermal effects dominates over anisotropy effects at 100K. A typical composition of $Co_{50}Ni_{50}$ alloy has been synthesized via modified polyol method and annealed via both route-1 and route-2 crystallize in pure fcc phase with average crystallite sizes of 28.1 nm and 30.4 nm, respectively. TEM micrograph study was carried for typical sample, i.e. Co-Ni(route-2), and shows presence of nanostructures with nearly spherical morphologies with particle size of 8±1 nm having narrow size distribution. Corrected M_S and H_C values Co-Ni(route-1) were found to be 116.2 emu/g and 86 Oe, at RT whereas 110 emu/g and 93Oe, at 100K respectively. Abnormal decrease in M_S value of Co-Ni(route-1) at 100K may be attributed to deviations in anisotropy near saturation of magnetization. Corrected M_S and H_C values Co-Ni(route-2) were found to be 45.6 emu/g and 214 Oe, at RT whereas 47.4 emu/g and 324 Oe, at 100K, respectively. These magnetic properties show fine particle size effects and temperature effects in the materials. $Co_{58}Pt_{42}$ alloy nanoparticles have synthesized via modified polyol method. As-prepared Co-Pt alloy nanoparticles crystallize in amorphous disordered fcc phase. Co-Pt alloy nanoparticles annealed via route-1 possess fcc crystal structure even at 700°C whereas Co-Pt alloy nanoparticles annealed via route-2 shows ordered fct ($L1_0$) phase. Microstructural and magnetic properties of fct Co-Pt obtained via route-2 have been studied. SEM studies show that annealed Co-Pt nanoparticles have spherical shape morphologies with SEM particle sizes of 41 ± 3 nm. And SEM EDX composition was found to be $Co_{58}Pt_{42}$. The values of M_S and H_C for Co-Pt(route-2) are found to be 24 emu/g and 6050 Oe, respectively. The observed magnetic properties have been interpreted with the help of crystallite sizes, order parameters, and composition effects of the Co-Pt nanostructured materials.

Chapter VII describes magnetic exchange and dipolar interactions studies in Ni/silica, $Co_{50}Ni_{50}$/silica, Co-Ni, Co, Ni, Fe-Co and Fe-Ni-Co systems. Ni/silica and $Co_{50}Ni_{50}$/silica with various loading (4-12 wt%) have been synthesized by novel chemical reduction route. The novelty of synthetic procedure adopted has been established using UV-VIS and FTIR spectroscopy. XRD studies confirm that both the materials form pure fcc phase embedded in amorphous silica matrix. XRD crystallite sizes for Ni/silica and $Co_{50}Ni_{50}$/silica are in the range of 6-10.5 nm and 13.6-16.3 nm, respectively. TEM microscopy studies show that CoNi alloys have nearly spherical shape morphologies and narrow size distributions. TEM particle sizes were estimated to be 13.6 nm and 8.9 nm for pure CoNi and 8 wt% CoNi materials loaded in silica matrix, respectively. Magnetic hysteresis studies at RT indicate the presence of superparamagnetic fractions in the materials. Enhancements in the values of magnetizations of Ni/silica and $Co_{50}Ni_{50}$/silica compared to that of pure materials have been observed with increase in dilution of nanoparticles in matrix. FC/ZFC magnetizations plots show decrease is blocking temperature for $Co_{50}Ni_{50}$/silica compare to pure $Co_{50}Ni_{50}$ which indicates magnetic structure alteration and supports our magnetic results. The observed enhancement in magnetization with low values of coercivity after loading in silica matrix has been explained on the basis of fine particle size, surface effects and dipolar interparticle interactions. Magnetic interactions in Co_xNi_{100-x} alloys coated by oleic acid and oleyl amine have been studied by low temperature FC/ZFC magnetization measurements. It could be confirm the presence of magnetic irreversibility and superparamagnetic blocking of nanoparticles due to strong dipolar interactions and particle size distribution. Estimated values of effective anisotropy constants of Co-Ni alloys (i.e., 57-181 kJ/m^3) reveal the contribution from the reduced particle size and surface anisotropy. On the above, a structure-property correlation in Co-Ni alloys has been attempted in this investigation. Also, magnetic interactions in Co, Ni, Fe-Co and Fe-Ni-Co alloys coated by carbonaceous matter have been studied by low temperature FC/ZFC magnetization measurements. The anisotropy constants for Co and Ni were found to be 25 kJ/m^3 and 13 kJ/m^3, respectively. FC/ZFC results show the wider size distributions in Co and Ni. Magnetic irreversible behavior below 300 K was observed in the materials from FC/ZFC curves due to ferromagnetism and dipolar interactions among the particles and result in shifting of blocking temperature value above 300 K.FC/ZFC magnetization measurements of Fe_xCo_{100-x} alloys show magnetic irreversibility and blocking of nanoparticles due to strong dipolar interparticle magnetic interactions. Estimated values of K_{eff} of Fe_xCo_{100-x} alloys (i.e. 1.5 kJ/m^3, 4.6 kJ/m^3 and 14.3 kJ/m^3 for x = 40, 60 and 80, respectively) reveal the contribution from the reduced particle size and surface anisotropy. It is observed that Fe-Ni-Co alloys showing thermo-magnetic irreversibility below 300 K and blocking temperature approximately at 300 K. FC and ZFC magnetic characteristics of Fe-Ni-Co alloys are interpreted on the basis of interparticle interactions among magnetic nanoparticles. The values of effective magnetic anisotropy constants (K_{eff}) are found to be 14 kJm^{-3} and 4.2 kJ$m^{-3}$for $Fe_{20}Ni_{60}Co_{20}$ and $Fe_{40}Ni_{40}Co_{20}$, respectively.

8.2 Future scope of research work

The modified $NaBH_4$ reduction route can be used for synthesis of PEG coated nanocrystalline metals/alloys at ambient conditions like air atmosphere, room temperature and aqueous medium. This method has advantage in field of biomedical research, provided stabilization of the nanostructure including surface oxidation is achieved. The modified superhydride route and polyol methods have fine control on nanoparticle size, their distribution and coating on the surface in organic medium. These alterations in materials morphology may help in designing materials for specific applications. The materials such as Co, Ni, Fe-Co, Co-Ni alloys show soft magnetic properties and have important applications in magnetic recording field, MRI contrast agents, cancer therapy, drug delivery agents, microwave absorption materials and catalysis. Basic study as well as applications oriented research of above materials can be extended. Synthesis of nanomaterials embedded in silica matrix using solution based method is a new approach and may be useful for future research. Also, synthesis of materials with controlled interparticle separations is useful for deep study of magnetic exchange and dipolar interactions among nanoparticles. In summary, there is ample scope of the future work based on stabilization, functionalization of the nano-materials with tunable structural and magnetic properties for possible potential applications.